

# **A MULTI-TIME-SCALE WALL MODEL FOR LARGE EDDY SIMULATION OF NON-EQUILIBRIUM FLOWS**

**by**

**Mitchell S. Fowler**

**A dissertation submitted to Johns Hopkins University  
in conformity with the requirements for the degree of  
Doctor of Philosophy**

**Baltimore, Maryland**

**November, 2023**

**© 2023 by Mitchell Fowler**

**All rights reserved**

# Abstract

The prohibitive cost of resolving near-wall flow features has led to the usage of wall models for Large Eddy Simulation (LES) of wall bounded turbulent flows. Wall models typically rely on simplified equations to model, as opposed to resolve, the underlying physics such that the computational overhead is reduced. The equilibrium wall model (EQWM) remains the most popular wall model due to its simplicity and relatively good performance over many flows. However it is conceptually only valid for equilibrium flows while many wall-bounded turbulent flows occur far from equilibrium. This motivates developing the Lagrangian relaxation towards equilibrium (LaRTE) model, a new pathway for non-equilibrium wall modeling. The LaRTE model utilizes the unsteady RANS equations and a momentum integral approach to isolate quasi-equilibrium wall-stress dynamics from non-equilibrium responses to time- and spatial-varying LES inputs. Non-equilibrium physics can then be modeled separately, such as (1) the laminar Stokes layers that form in the viscous region and generate rapid wall-stress responses to fast changes in the pressure gradient or (2) turbulent velocity fluctuations and how they correlate with wall-stress fluctuations. The total modeled wall-stress thus includes contributions from various processes operating at different time scales (i.e.,

the LaRTE quasi-equilibrium plus laminar and turbulent non-equilibrium wall-stresses) and is called the multi-time-scale wall model (MTSWM).

The MTSWM is applied in LES of turbulent flows with both temporal and spatial non-equilibrium. Wall-parallel homogeneous flows tested include canonical stationary channel flow, channel flow with a sudden spanwise pressure gradient (SSPG), and pulsating and linearly accelerating channel flow for several forcing frequencies and acceleration rates, respectively. Streamwise developing flows tested include the canonical zero-pressure-gradient (ZPG) flat plate developing boundary layer over a wide range of Reynolds numbers and a separated boundary layer flow induced by a suction and blowing transpiration boundary condition. Results obtained with the MTSWM show improvement, relative to the EQWM, for flows with high temporal non-equilibrium while still showing good agreement with direct numerical simulation data for canonical flows (or flows with weak non-equilibrium) where the EQWM performance is also good. Both the MTSWM and EQWM show similar good performance for the separated flow case but more testing for spatial non-equilibrium flows is needed.

# **Thesis Committee**

## **Readers**

Charles Meneveau (Primary Advisor)  
Professor  
Department of Mechanical Engineering  
Johns Hopkins Whiting School of Engineering

Tamer Zaki (Secondary Advisor)  
Professor  
Department of Mechanical Engineering  
Johns Hopkins Whiting School of Engineering

Dennice Gayme  
Associate Professor  
Department of Mechanical Engineering  
Johns Hopkins Whiting School of Engineering

# Acknowledgments

I would first like thank my advisors, Professor Charles Meneveau and Professor Tamer Zaki, for their invaluable support and expertise. I came into the lab with little fluids and research background, and I am fortunate Charles and Tamer saw something in me to give me the opportunity to work on such an interesting and practical problem as LES wall modeling for my PhD project. Charles and Tamer are not only knowledgeable experts within their fields but also are always encouraging creative solutions for complex research questions, a skill I will take with me wherever I go. I would also like to thank my other professors and mentors for their guidance throughout my PhD. Thanks to Professor Dennice Gayme for serving as a dissertation reader and for the great insight and sarcastic humor in weekly group meetings. Thanks to Professors Gregory Eyink and Anand Gnanadesikan for serving on my final GBO/defense committee and for the excellent questions regarding extending my work. Thanks to Professors Gretar Tryggvason, Rajat Mittal, Jung-Hee Seo, and Yannis Kevrekidis for challenging me in courses and for introducing me to the fascinating world of fluids.

I would like to thank my friends and family for always being there for me, especially during times of difficulty. Thanks to my parents and my siblings

for providing a loving home I always looked forward to returning to. Thanks to my partner, Priya, for being my best friend - someone I never tire talking to, someone to explore the world with, someone to share experiences during the highs and lows of life - and without whom I surely would not have been able to complete my PhD. Thanks to Ghanesh for being such a great friend, roommate, and research collaborator whom I've spent countless days and nights discussing research ideas on our apartment whiteboard. Thanks to Srivaths for being the friend I could always count on for fun plans away from the academic realm. Thanks to Karthik and Aaron for the many biking and hiking adventures we've gone on together. Thanks to Ben and Gen for playing Jungle Speed with or without me. Thanks to all of my soccer friends, both inside the department and outside the department in pick-up soccer, which always provided a fun escape from research. Finally, thanks to all my other friends and classmates for making my experience at Hopkins so memorable. I hope and expect our journey will not end here.

Thanks to the Office of Naval Research for their financial support for this research. Thanks to the advanced research computing center at Hopkins for providing the computing resources needed to carrying out this work.

# Table of Contents

<b>Abstract</b>	ii
<b>Thesis Committee</b>	iv
<b>Acknowledgments</b>	v
<b>Table of Contents</b>	vii
<b>List of Tables</b>	x
<b>List of Figures</b>	xi
<b>1 Introduction</b>	1
1.1 Background/Motivation . . . . .	1
1.2 Objectives and outline . . . . .	4
<b>2 The Lagrangian Relaxation Towards Equilibrium (LaRTE) model</b>	10
2.1 Derivation . . . . .	10
2.2 Discussion . . . . .	18
2.3 Closure for the total stress at the wall-model height . . . . .	20

2.4	A-priori analysis of quasi-equilibrium dynamics in channel flow	24
2.5	Discretization of the LaRTE evolution equation . . . . .	27
<b>3</b>	<b>The laminar non-equilibrium (lamNEQ) model</b>	<b>29</b>
3.1	Derivation . . . . .	29
3.2	Evaluating the temporal convolution integral . . . . .	33
3.3	Verification of the accuracy of the SOE method . . . . .	36
<b>4</b>	<b>Applications of the LaRTE+lamNEQ wall model to equilibrium and non-equilibrium channel flows</b>	<b>39</b>
4.1	Summary of the LaRTE+lamNEQ wall model . . . . .	39
4.1.1	Pressure gradient decomposition . . . . .	40
4.1.2	LaRTE+lamNEQ length and time scales . . . . .	42
4.2	Statistically stationary channel flow . . . . .	43
4.3	Channel flow with a sudden spanwise pressure gradient (SSPG)	56
4.4	Summary . . . . .	63
<b>5</b>	<b>The multi-time-scale wall model (MTSWM)</b>	<b>67</b>
5.1	Turbulent non-equilibrium . . . . .	67
5.2	Modifications to the original LaRTE model . . . . .	70
5.2.1	Revisiting the equilibrium stress closure for the LaRTE model . . . . .	70
5.2.2	Velocity correction to the LES input . . . . .	73
5.3	Summary of the MTSWM . . . . .	75

<b>6 The MTSWM applied to horizontally homogeneous flows</b>	<b>79</b>
6.1 Revisiting stationary channel flow and SSPG . . . . .	79
6.2 Pulsating channel flow . . . . .	85
6.3 Linearly accelerating channel flow . . . . .	102
6.4 The MTS wall model in the limit of instantaneous relaxation .	116
6.5 Summary . . . . .	123
<b>7 The MTSWM applied to streamwise developing flows</b>	<b>127</b>
7.1 Introduction . . . . .	127
7.2 Code development . . . . .	129
7.2.1 Fringe region . . . . .	129
7.2.2 Rescale-recycle method . . . . .	132
7.3 Zero pressure gradient flat plate turbulent boundary layer .	134
7.4 Separation induced by suction and blowing . . . . .	141
7.5 Summary . . . . .	160
<b>8 Summary, conclusions, and future directions</b>	<b>165</b>
<b>9 Appendix</b>	<b>174</b>
9.1 Fits for $f(\Delta^+)$ , cell thickness scales, and $Re_{\tau\Delta}$ . . . . .	174
9.2 Sum of exponentials (SOE) constants used for the lamNEQ model	180
9.3 ZPGBL velocity field initialization and fits . . . . .	180
<b>Bibliography</b>	<b>185</b>

# List of Tables

4.1	Stationary channel flow Reynolds numbers and corresponding $\Delta^+$ . . . . .	45
6.1	Pulsating channel flow forcing frequencies . . . . .	88
6.2	The acceleration/ramp rates for linearly accelerating channel flow and the flow regime classification . . . . .	106
7.1	Summary of the different regions within the separated flow .	144
9.1	SOE constants for $N_{exp} = 48$ . . . . .	180

# List of Figures

2.1	Sketch of LaRTE velocity profile and stresses acting in the near-wall fluid layer	12
2.2	A-priori test of the relaxation time scale	26
3.1	SOE error analysis for the lamNEQ model	37
4.1	Length and time scale schematic for the LaRTE+lamNEQ model	43
4.2	Mean velocity profiles for stationary channel flow over a wide range of Reynolds numbers	47
4.3	Mean Reynolds stresses for stationary channel flow	48
4.4	Time signals of the LaRTE relaxation terms	49
4.5	Time signals of terms in the LaRTE evolution equation for stationary channel flow	50
4.6	Snapshots of the LaRTE+lamNEQ wall stress components for $Re_\tau = 1,000$	51
4.7	Contour plots of the streamwise wall stress with Lagrangian vs Eulerian relaxation	53
4.8	Wall stress PDFs for the original LaRTE+lamNEQ wall model	55

4.9	Time signals of each spanwise pressure gradient component for the SSPG flow . . . . .	57
4.10	Mean spanwise wall stress after the SSPG . . . . .	59
4.11	Mean streamwise wall stress after the SSPG . . . . .	59
4.12	Mean spanwise velocity profiles after the SSPG . . . . .	61
4.13	Contours of the LaRTE wall stress fluctuations after the SSPG	62
4.14	Plane-averaged pressure gradient and wall stress angles after the SSPG . . . . .	62
5.1	Turbulent non-equilibrium schematic . . . . .	69
5.2	Schematic of the velocity profiles for the LaRTE, lamNEQ, and turbNEQ models . . . . .	77
5.3	Schematic of the MTSWM length and time scales . . . . .	78
6.1	Wall stress PDFs for stationary channel flow revisited . . . . .	81
6.2	Mean streamwise and spanwise wall stress after the SSPG . .	83
6.3	Contours of the wall stress fluctuations for the MTSWM after the SSPG . . . . .	84
6.4	Time evolution of the periodic centerline velocity for pulsating channel flow . . . . .	90
6.5	Time averaged mean velocity profiles and Reynolds stresses for pulsating channel flow . . . . .	92
6.6	Amplitude and phase lead of the periodic velocity . . . . .	93
6.7	Time evolution of the periodic wall stress . . . . .	95

6.8	Time evolution of the MTSWM periodic wall stress components	96
6.9	The periodic wall stress amplitude and phase . . . . .	97
6.10	The periodic wall stress amplitude and phase for each of the MTSWM components . . . . .	98
6.11	The time evolution of $\widetilde{u'v'}$ at different phases of the wave cycle	99
6.12	Amplitude and phase lead of $\widetilde{u'v'}$ . . . . .	100
6.13	Amplitude and phase lead of $\widetilde{u'u'}$ . . . . .	100
6.14	Amplitude and phase lead of $\widetilde{v'v'}$ . . . . .	101
6.15	Amplitude and phase lead of $\widetilde{w'w'}$ . . . . .	101
6.16	Time signals of budget terms for $\omega_f^+ = 0.01$ in the integrated, phase-averaged x-momentum equation for different integration heights . . . . .	103
6.17	Time signals of the pressure gradient forcing and the mean Reynolds number for different acceleration ramp rates . . . . .	106
6.18	The mean velocity profiles and Reynolds stresses before acceler- ation and after acceleration once the flow has achieved its new steady state. . . . .	107
6.19	Time signals of the skin friction coefficient for different acceler- ation ramp rates . . . . .	110
6.20	Time signals of the MTSWM wall-stress components for differ- ent acceleration ramp rates . . . . .	113

6.21	Time signals at a representative single point of the different modeling components of the LES velocity for several acceleration ramp rates . . . . .	115
6.22	Time signals of the velocity perturbation (from the initial condition) at several heights for (a) $T^* = 0.1$ and (b) $T^* = 5.0$ . . . . .	116
6.23	Single period time evolution of the periodic streamwise wall-stress for several forcing frequencies with the EQMTSWM . . . . .	119
6.24	Single period time evolution of the EQMTSWM periodic streamwise wall-stress components for several forcing frequencies . . . . .	120
6.25	Time signals of the skin friction coefficient for different acceleration ramp rates with the EQMTSWM . . . . .	121
7.1	Contour plot of the instantaneous streamwise velocity field for the ZPG boundary layer . . . . .	128
7.2	Contour plot of the instantaneous streamwise velocity field for the separated boundary layer . . . . .	129
7.3	Schematic of the modified rescaling-recycling method and the fringe region. . . . .	131
7.4	Mean velocity profiles over a wide range of Reynolds numbers	136
7.6	$C_f$ and $U_\infty^+$ vs $Re_\theta$ for all Reynolds numbers . . . . .	138
7.7	Mean pressure gradient contour plots for simulation A0 . . . . .	138
7.9	Mean velocity on the top surface of the domain . . . . .	145
7.10	Different boundary layer thicknesses . . . . .	147
7.11	$C_f$ , $C_p$ , and $\gamma_r$ . . . . .	149

7.12 Velocity profile evolution . . . . .	150
7.13 Velocity and Reynolds shear stress profiles at ZPG regions . .	151
7.14 Velocity and Reynolds shear stress profiles in the suction and blowing region . . . . .	151
7.15 Wall stress mean and RMS . . . . .	152
7.16 Wall stress PDFs for the MTSWM . . . . .	154
7.17 Wall stress PDFs for the EQWM . . . . .	155
7.18 Instantaneous total wall stress contour for the EQWM and MTSWM . . . . .	156
7.19 Instantaneous wall stress contour plots for the MTSWM with each of its wall stress components . . . . .	157
7.20 MTWSM time scales . . . . .	158
7.21 MTWSM pressure gradients . . . . .	159
7.22 Time signals lamNEQ pressure gradient at select streamwise locations . . . . .	159
7.23 Inputs and outputs for the LaRTE model versus streamwise location . . . . .	161
7.24 Time signals of the inputs and outputs for the LaRTE model at select streamwise locations . . . . .	162
9.1 Numerical evaluation of the cell displacement thickness, cell momentum thickness, cell shape factor and their corresponding fits. . . . .	177

# Chapter 1

## Introduction

### 1.1 Background/Motivation

Simulations of wall-bounded turbulence at high Reynolds numbers are computationally challenging because they must resolve a vast range of scales. For example, in the near-wall region the velocity scales with the viscous length scale which at high Reynolds numbers requires a very fine mesh near the wall. In Large Eddy Simulations (LES), “wall models” are deployed to model rather than resolve these small near-wall length scales. Wall models for LES have been reviewed in Piomelli and Balaras (2002), Piomelli (2008), Larsson et al. (2016), and Bose and Park (2018). We here concentrate on “wall-stress models” in which the LES domain extends all the way to the wall, where the wall-stress is applied as a boundary condition. The simplest and most commonly used wall-stress model is the equilibrium wall model (EQWM) (briefly reviewed in chapter 2) which assumes that the velocity profile follows some known functional form, an equilibrium velocity profile such as the log-law (Deardorff, 1970; Piomelli et al., 1989; Schumann, 1975). While strictly

such profiles tend to be valid after long-time averaging under full equilibrium conditions, applications of EQWM in LES usually assume such profiles to be valid locally and instantaneously. This enables us to use the LES velocity known at the wall-model height to determine the local friction-velocity and thus the local wall-stress. However, the application of a model derived from pure equilibrium assumptions to situations in highly non-equilibrium conditions poses conceptual and practical problems. One difficulty is that it combines both quasi-equilibrium and non-equilibrium effects in a single model formulation, where non-equilibrium effects tend to be clouded by the underlying quasi-equilibrium dynamics. Alternative recent wall models such as the dynamic slip wall models impose a slip velocity boundary condition (Bose and Moin (2014); Bae et al. (2019)). Close connections between slip-velocity and equilibrium wall models have been pointed out in X. Yang et al. (2016).

Existing wall models tend to model non-equilibrium and quasi-equilibrium effects in a single formulation. A popular method for incorporating non-equilibrium effects is to solve the full thin boundary-layer equations in a near-wall mesh (Balaras et al., 1996). Although this method includes all non-equilibrium terms in the momentum balance, its computational cost can approach that of wall-resolved LES since a refined near-wall mesh must be used. Chung and Pullin (2009) developed a model based on the wall-normal integrated thin boundary-layer equations within the near-wall region and a law of the wall assumption for the velocity profile. Certain non-equilibrium effects can be captured since all terms are included in the momentum balance

and because the horizontal Reynolds-stress gradients are evaluated using the SGS stresses at the wall model height. Nevertheless the model assumes a plug-flow profile for the advection term. In order to account for the velocity profile below the wall model height, X. Yang et al. (2015) developed another wall model (called iWMLES) based on the integrated momentum equations. They assume the near-wall velocity profile is linear in the viscous sublayer above which it obeys the log law with an additional linear term to capture non-equilibrium effects. Tests using iWMLES in non-equilibrium flows such as flow over cubed roughness elements in X. Yang et al. (2015) and the sudden spanwise pressure gradient flow in Lozano-Durán et al. (2020) have shown that the model properly captures some non-equilibrium effects. However, iWMLES models non-equilibrium solely through modifying the assumed velocity profile, while still assuming that non-equilibrium dynamics can be captured via an only slightly modified equilibrium velocity profile. Thus, equilibrium and non-equilibrium effects are mixed together in a single formulation and it remains unclear how to proceed for more complex flows where the modeling assumption of a near-equilibrium velocity profile is expected to break down.

This motivated the development of a new formal approach to separate equilibrium, quasi-equilibrium and highly non-equilibrium conditions for wall modeling which is the primary focus of this dissertation. The formalism decomposes LES information into contributions from different time scales and models each component separately. Quasi-equilibrium is assumed to hold for time scales slow enough so that the corresponding velocity profile

satisfies the law of the wall. An evolution equation for the friction-velocity vector is derived which may be described as a ‘Lagrangian relaxation towards equilibrium’, or LaRTE for short. This LaRTE model then captures solely the quasi-equilibrium dynamics, leaving non-equilibrium dynamics to be modeled separately. Consequently, the LaRTE equation is supplemented with two non-equilibrium components: (1) a laminar non-equilibrium (lamNEQ) component which captures the laminar, near-wall Stokes layer behavior arising from fast changes in the pressure gradient and (2) a turbulent non-equilibrium (turbNEQ) component motivated by the wall attached eddy hypothesis to correlate LES velocity fluctuations with wall stress fluctuations. The resulting model thus includes three separate parts (LaRTE, lamNEQ and turbNEQ), and is termed the multi-time-scale wall model (MTSWM) since it models the full spectrum of time scales in the near-wall region.

## 1.2 Objectives and outline

The objectives of this dissertation are to (1) outline the theory behind the MTSWM, (2) to apply the MTSWM for a wide range of non-equilibrium flows and compare performance against existing wall models (such as the EQWM) and the “truth” (DNS or experimental data), and (3) to motive the usefulness of this wall modeling approach. The dissertation is outlined as follows:

We begin by describing the LaRTE model in chapter 2. The LaRTE model is first derived in §2.1. The derivation begins with RANS equations governing the slow quasi-equilibrium velocity assumed to follow the law of the wall. The law of the wall is then substituted and vertically integrated from the

wall to the wall model height. This results in a governing equation for the friction velocity vector. In §2.2, a simplified form of the governing equation for the LaRTE model is then discussed to understand the behavior of the LaRTE friction velocity evolution. This simplified form shows that the friction velocity and wall stress relaxes in a Lagrangian manner to the total shear stress at the wall model height, at a rate corresponding to a formally derived relaxation time scale,  $T_s$ . §2.3 outlines how closure is achieved for the LaRTE model using the ideas behind the EQWM. This closure, combined with the behavior of the governing equation for the friction velocity vector, lead to the name “Lagrangian Relaxation Towards Equilibrium” (LaRTE) for the wall model. An a-priori test is then done in §2.4 to see if the relaxation time scale is consistent with the concepts underlying quasi-equilibrium. DNS velocity profiles are filtered at different time scales to see which collapse onto the law of the wall. Finally, §2.5 shows how the Lagrangian time derivative of the friction velocity vector is discretized for the LaRTE model. An explicit, first-order bilinear interpolation scheme is used.

Chapter 3 motivates and outlines the laminar non-equilibrium (lamNEQ) model. Again the chapter begins with a derivation. It’s shown that the lamNEQ velocity has the same form as the unsteady heat equation which allows for analytical solutions to be formed for this velocity. The corresponding wall stress is found to follow a convolution-type integral of the lamNEQ pressure gradient with a slow temporal  $t^{-1/2}$  kernel. This is related to the Caputo fractional derivative. In §3.2, it is shown that this type of fractional derivative can be evaluated efficiently using a “sum-of-exponentials” (SOE) method

where the kernel is replaced by a series of exponential term, thus allowing the fractional derivative to be computed recursively. This significantly reduces the storage and work (number of computations) requirements. The accuracy of the SOE method is tested in §3.3 using a standard pressure gradient signal from LES and compared against the more costly, but well established “L1 method”.

In chapter 4, the “LaRTE+lamNEQ” wall model (called such because the wall stress is the superposition between these two models) is applied to two channel flows. But before applying the model, a few details regarding implementation must be clarified. First in §4.1.1, the evaluation of the various pressure gradient inputs to the model is described. Then §4.1.2 introduces a length and time scale schematic of the model to (1) clarify the dynamics being captured by the model and (2) highlight the range of of time scales being captured by the model. In §4.2, the LaRTE+lamNEQ model is applied to canonical, statistically stationary channel flow to document its various properties and confirm it gives good baseline statistics. Figures shown include mean velocity profiles and Reynolds stresses for several Reynolds numbers, time signals of various LaRTE terms and variables, snapshot contours of the instantaneous wall stress for each component of the LaRTE+lamNEQ model, contour plots of wall stress for Eulerian vs Lagrangian wall stress, and probability density functions of the LaRTE+lamNEQ wall stress. Then in §4.3, the LaRTE+lamNEQ model is applied to the first non-equilibrium studied here: steady channel flow with a large spanwise pressure gradient suddenly applied (called SSPG). The performance of the model is assessed

by comparing the wall stress evolution against DNS and the EQWM. The behavior of the model is shown through the evolution of each component of LaRTE+lamNEQ wall stress, contour plots of the LaRTE wall stress fluctuation after the SSPG, and the time evolution of the spanwise components after the SSPG.

Chapter 5 introduces the final ingredients needed for the MTSWM. First in §5.1, the turbulent non-equilibrium (turbNEQ) wall model is motivated and introduced. A turbulent non-equilibrium velocity fluctuations is defined and then connected to the wall stress via a modeled “linear + plug flow” velocity profile. After the turbNEQ model is introduced, in §5.2 the modifications to the LaRTE model are discussed. This includes the pressure gradient and velocity inputs to equilibrium stress closure for the stress at the model height. The velocity is “corrected” to account for the contribution of the laminar Stokes layer to the LES velocity. This velocity correction model is developed in §5.2.2. Finally, the full MTSWM is summarized in §5.3 which now includes LaRTE, lamNEQ, and turbNEQ components. An updated model velocity profile schematic and length and time scale schematic are shown to highlight the various of dynamics and time scales modeled by the MTSWM.

The MTSWM is then applied to horizontally homogeneous (channel) flows for a wide range of unsteady non-equilibrium conditions in chapter 6. First the wall stress PDFs for stationary channel flow are revisited in §6.1 to show how the added turbNEQ model and modifications to the LaRTE model affect the wall stress fluctuations. Then the SSPG flow is revisited to again see how the additions and changes affect model performance. In §6.2, the MTSWM is

applied to pulsating channel flow where a wide range of pressure gradient forcing frequencies are tested. The model is compared against the EQWM and DNS, and the contribution of different wall stress components is analyzed for each of the forcing frequencies. In §6.3, the MTSWM is applied to linearly accelerating channel flow for several different acceleration rates. Finally, the MTSWM is analyzed in the limit of “instantaneous relaxation”, i.e. a vanishingly small relaxation time scale. In this limit, the friction velocity is equal to its equilibrium value and the turbNEQ wall stress vanishes. A model can be formed based on this limit and is called the equilibrium MTS wall model or EQMTSWM for short. This model is then tested and compared against the EQWM and regular MTSWM for the pulsating and linearly accelerating channel flows.

The last set of simulations in this dissertation are streamwise developing flows, discussed in chapter 7. This includes zero pressure gradient (ZPG) turbulent boundary layers over a wide range of Reynolds numbers and a separated turbulent boundary layer induced by a suction and blowing transpiration boundary condition. The MTSWM is applied to these flows to see how it performs under spatial non-equilibrium as opposed to temporal non-equilibrium like the flows considered in chapter 7. But before discussing results, some details outlining code development is needed to explain how the numerical code used in prior sections had to be modified to handle streamwise developing flows like a ZPG turbulent boundary layer. This is done in §7.2 and includes the implementation of a fringe region to force the flow to the desired inflow velocity and the use of a modified rescale-recycle method to

specify the target inflow velocity. Then in §7.3, the results for ZPG turbulent boundary layers over a wide range of Reynolds numbers is discussed to verify that the code works properly for this canonical flow, similar to the stationary channel flow in §4.2 and §6.1. This includes plots of velocity profiles, turbulence intensity profiles, and skin friction vs  $Re_\theta$  for all the Reynolds numbers simulated. Lastly, in §7.4 the performance of the MTSWM is tested for a separated boundary layer. The MTSWM is compared against the EQWM and DNS in terms of the the skin friction, the wall pressure coefficient, and velocity profiles at different streamwise locations. Then the MTSWM properties are explored by examining plots of each component of the MTSWM for the mean wall stress, wall stress RMS, wall stress PDFs at each stremwise location, and instantaneous wall stress contour plots. Different LaRTE model terms are also analyzed by studying time signals and how mean and fluctuating quantities vary as suction and blowing is applied.

The dissertation finishes with conclusions and future directions in chapter 8. An appendix is included as chapter 9 and includes various fits used by the models as well as a table showing the SOE constants used by the lamNEQ model. Content in chapters 2-4 is mostly from the published work Fowler et al. (2022) and content in chapters 5-6 comes from the published work Fowler et al. (2023). Chapter 7 is unpublished at the time of writing this dissertation.

# Chapter 2

## The Lagrangian Relaxation Towards Equilibrium (LaRTE) model

### 2.1 Derivation

This chapter begins by deriving the Lagrangian Relaxation Towards Equilibrium (LaRTE) wall model. Following the ideas underlying the integral wall model (X. Yang et al., 2015) we assume that between the wall and the wall model height (an LES grid point at a distance  $\Delta$  away from the wall there exists a quasi-equilibrium mean velocity profile (see figure 2.1(a)). An overline denotes the corresponding averaging operation, which may be interpreted as a horizontally grid filtered quantity at the LES scale in the wall-parallel plane, and additional (implicit) temporal averaging whose properties will become apparent from the derivation itself. The key assumption underlying the proposed wall model is that in the horizontal (wall parallel,  $x - z$ ) plane, the mean velocity  $\bar{u}_s = \bar{u} \hat{i} + \bar{w} \hat{k}$  ( $\hat{i}$  and  $\hat{k}$  are the two unit vectors on the wall)

can be written according to

$$\bar{\mathbf{u}}_s(x, y, z, t) = \mathbf{u}_\tau(x, z, t) f(y^+), \quad (2.1)$$

where  $\mathbf{u}_\tau(x, z, t)$  is the friction velocity vector and is a slowly varying function of the horizontal positions  $x, z$  and time  $t$ . The characteristic time-scale characterizing what is termed “slow” evolution is not prescribed a-priori but will be shown to arise directly from the assumption of quasi-equilibrium. The inner similarity function  $f(y^+)$  with  $y^+ = y u_\tau / \nu$  is the assumed velocity profile in inner units, and  $u_\tau = |\mathbf{u}_\tau|$ . Typically  $f(y^+)$  includes a linear region near the wall merging with a logarithmic portion above the buffer layer but the precise shape of  $f(y^+)$  is not important at initial stages of development. We remark that in the present work we deal exclusively with smooth planar walls.

The full quasi-steady velocity is then given by

$$\bar{\mathbf{u}} = \bar{\mathbf{u}}_s + \bar{v} \hat{\mathbf{j}}, \quad (2.2)$$

where  $\bar{v}$  is the wall-normal velocity and  $\hat{\mathbf{j}}$  the unit vector in the  $y$ -direction. The friction velocity vector  $\mathbf{u}_\tau = u_{\tau x} \hat{\mathbf{i}} + u_{\tau z} \hat{\mathbf{k}}$  is defined such that the (kinematic) wall stress vector  $\bar{\boldsymbol{\tau}}_w$  (its two components in the wall plane) is given by

$$\bar{\boldsymbol{\tau}}_w = u_\tau \mathbf{u}_\tau, \quad (2.3)$$

i.e.  $\bar{\mathbf{u}}_s$  and  $\mathbf{u}_\tau$  are in the same direction as  $\bar{\boldsymbol{\tau}}_w$ . This direction will be represented by unit vector  $\mathbf{s}$  (that also can depend on  $x, z, t$ ), i.e.  $\mathbf{u}_\tau = u_\tau \mathbf{s}$  and  $\bar{\mathbf{u}}_s = u_\tau f(y^+) \mathbf{s}$  (figure 2.1(a)).

Next, we aim to derive an evolution equation for the friction velocity vector

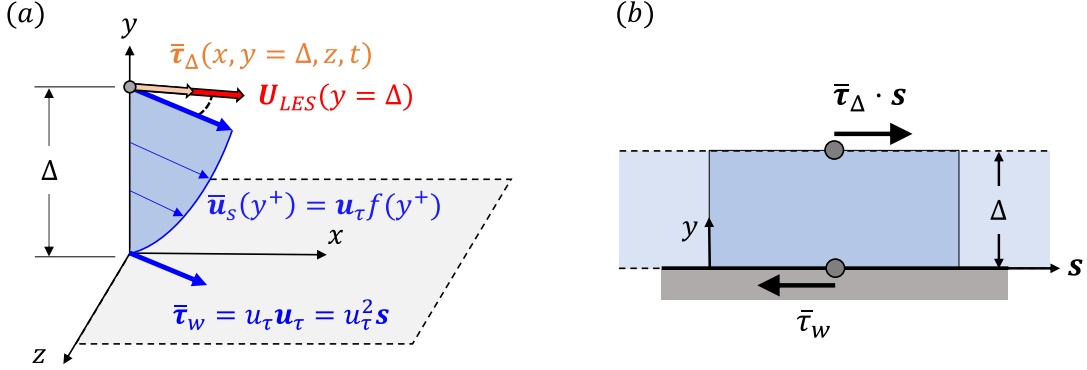


**Figure 2.1:** (a) Sketch of assumed inner velocity profile (in blue) representing a quasi-equilibrium RANS solution in the inner layer, responding to an outer “applied” total shear stress  $\bar{\tau}_\Delta$  at the wall model height at  $y = \Delta$ . (b) Sketch of stresses acting on the fluid layer between  $y = 0$  and  $y = \Delta$ , leading to inertia term with response time-scale  $T_s$  proportional to  $\Delta$ .

$u_\tau(x, z, t)$  that is consistent with the RANS evolution for  $\bar{u}$ :

$$\frac{\partial \bar{u}}{\partial t} + \nabla \cdot (\bar{u} \bar{u}) = -\frac{1}{\rho} \nabla \bar{p} + \nabla \cdot \left[ (\nu + \nu_T) (\nabla \bar{u} + \nabla \bar{u}^\top) \right], \quad (2.4)$$

where  $\nu_T(x, y, z, t)$  is the position-dependent eddy viscosity associated with the RANS model being considered and  $\bar{p}(x, z, t)$  is the quasi-equilibrium pressure with no wall-normal dependence, consistent with boundary layer approximations. The momentum equation for the wall-parallel velocity  $\bar{u}_s$  (2 components) reads

$$\begin{aligned} \frac{\partial \bar{u}_s}{\partial t} + \nabla_h \cdot (\bar{u}_s \bar{u}_s) + \partial_y (\bar{v} \bar{u}_s) &= -\frac{1}{\rho} \nabla_h \bar{p} + \frac{\partial}{\partial y} \left[ (\nu + \nu_T) \frac{\partial \bar{u}_s}{\partial y} \right] \\ &\quad + \nabla_h \cdot \left[ (\nu + \nu_T) (\nabla_h \bar{u}_s + \nabla_h \bar{u}_s^\top) \right], \end{aligned} \quad (2.5)$$

where  $\nabla_h = \partial_x \hat{i} + \partial_z \hat{k}$  represents the horizontal gradients on the  $x - z$  wall plane, and diffusion cross terms involving the (small) vertical velocity  $\bar{v}$  have been neglected. Into this equation we replace the main ansatz (2.1). And,

following the logic of Chung and Pullin (2009) and the integral wall model by X. Yang et al. (2015), we integrate from  $y = 0$  to the wall-model height at  $y = \Delta$ . We first illustrate this idea with the Eulerian time derivative  $\partial_t \bar{u}_s$ . The key steps for the time derivative read as follows:

$$\begin{aligned} \frac{\partial}{\partial t} \int_0^\Delta \bar{u}_s \, dy &= \frac{\partial}{\partial t} \left[ s \int_0^\Delta u_\tau f \left( \frac{yu_\tau}{\nu} \right) \, dy \right] \\ &= s \int_0^\Delta \frac{\partial u_\tau}{\partial t} \left( f(y^+) + u_\tau f'(y^+) \frac{y}{\nu} \right) \, dy + \frac{\partial s}{\partial t} \int_0^\Delta u_\tau f(y^+) \, dy. \end{aligned} \quad (2.6)$$

As recognized by Chung and Pullin (2009) in their derivation of an integral boundary layer equation-based wall model, the first integral on the RHS can be rewritten with  $d/dy^+ [y^+ f(y^+)]$  as integrand, resulting in

$$\begin{aligned} \frac{\partial}{\partial t} \int_0^\Delta \bar{u}_s \, dy &= s \frac{\partial u_\tau}{\partial t} \int_0^{\Delta^+} \frac{d}{dy^+} [y^+ f(y^+)] \, dy^+ \frac{\nu}{u_\tau} + u_\tau \frac{\partial s}{\partial t} \int_0^\Delta f(y^+) \, dy \\ &= s \frac{\partial u_\tau}{\partial t} \Delta f(\Delta^+) + u_\tau \frac{\partial s}{\partial t} \int_0^\Delta f(y^+) \, dy \\ &= \frac{\partial(u_\tau s)}{\partial t} \Delta f(\Delta^+) + u_\tau \frac{\partial s}{\partial t} \left( \int_0^\Delta [f(y^+) - f(\Delta^+)] \, dy \right). \end{aligned} \quad (2.7)$$

The last term motivates definition of a “cell displacement thickness”

$$\begin{aligned} \delta_\Delta^* &\equiv \int_0^\Delta \left( 1 - \frac{\bar{u}_s(y)}{\bar{u}_s(\Delta)} \right) \, dy \\ \frac{\delta_\Delta^*}{\Delta} &= \frac{1}{\Delta^+} \int_0^{\Delta^+} \left( 1 - \frac{f(y^+)}{f(\Delta^+)} \right) \, dy^+, \end{aligned} \quad (2.8)$$

analogous to the boundary-layer displacement thickness but integrated only

up to  $y = \Delta$ . Finally, the Eulerian time derivative term can be written according to

$$\frac{\partial}{\partial t} \int_0^\Delta \bar{u}_s dy = \Delta f(\Delta^+) \frac{\partial u_\tau}{\partial t} - u_\tau f(\Delta^+) \delta_\Delta^* \frac{\partial s}{\partial t}. \quad (2.9)$$

The derivation for the advective term will now be done in index notation leading to inclusion of an additional term which was not included in the original derivation in Fowler et al. (2022). The horizontal momentum equation (equation 2.5) re-written in index notation is given by

$$\begin{aligned} & \frac{\partial \bar{u}_{si}}{\partial t} + \partial_j (\bar{u}_{si} \bar{u}_{sj}) + \partial_y (\bar{v} \bar{u}_{si}) \\ &= -\rho^{-1} \partial_i \bar{p} + \frac{\partial}{\partial y} \left[ (\nu + \nu_T) \frac{\partial \bar{u}_{si}}{\partial y} \right] + \partial_j [(\nu + \nu_T) (\partial_i \bar{u}_{sj} + \partial_j \bar{u}_{si})] \end{aligned} \quad (2.10)$$

where indices correspond with the horizontal directions, i.e.  $i = 1, 3$ , and the horizontal velocity follows the law of the wall, i.e.  $\bar{u}_{si} = u_\tau s_i f(y^+) = u_\tau s_i f(\Delta^+)$ . The continuity equation is

$$\partial_i \bar{u}_{si} + \partial_y \bar{v} = \partial_s \bar{u}_s + \bar{u}_s (\partial_i s_i) + \partial_y \bar{v} = 0 \quad (2.11)$$

where we have used the relation  $\partial_s = s_i \partial_i$ . Equation 2.11 can be integrated to obtain the vertical velocity at the wall-model height

$$\begin{aligned} \bar{v}(\Delta) &= - \int_0^\Delta \partial_i \bar{u}_{si} dy = - \int_0^\Delta \partial_i (u_\tau s_i f) dy \\ &= -(\partial_s u_\tau) \int_0^\Delta [f + y^+ f'] dy - u_\tau (\partial_i s_i) \int_0^\Delta f dy \\ &= -(\partial_s u_\tau) \Delta f_\Delta - u_\tau (\partial_i s_i) \int_0^\Delta f dy, \end{aligned} \quad (2.12)$$

where  $f_\Delta \equiv f(\Delta^+)$  and the term proportional to  $\partial_i s_i$  was omitted in Fowler

et al. (2022). The advection term in equation 2.10 is now vertically integrated from the wall to the wall model height. The non-linear advection term is then

$$\int_0^\Delta [\partial_j(\bar{u}_{si}\bar{u}_{sj}) + \partial_y(\bar{v}\bar{u}_{si})] dy = \int_0^\Delta \partial_j(\bar{u}_{si}\bar{u}_{sj}) dy + \bar{v}(\Delta)u_\tau s_i f_\Delta. \quad (2.13)$$

The first term requires expanding, which after some manipulation can be written as

$$\int_0^\Delta \partial_j(\bar{u}_{si}\bar{u}_{sj}) dy = u_{\tau i}(\partial_s u_\tau) \Delta f_\Delta^2 + [u_\tau(\partial_s u_{\tau i}) + u_\tau^2 s_i (\partial_j s_j)] \int_0^\Delta f^2 dy. \quad (2.14)$$

Substituting equations 2.14 and 2.12 into equation 2.13 yields the integrated advection term

$$\begin{aligned} & \int_0^\Delta [\partial_j(\bar{u}_{si}\bar{u}_{sj}) + \partial_y(\bar{v}\bar{u}_{si})] dy \\ &= \Delta f_\Delta V_{\tau j}(\partial_j u_{\tau i}) - \Delta u_\tau f_\Delta^2 (\partial_j s_j) \left( \frac{\theta_\Delta}{\Delta} \right) u_{\tau i} \end{aligned} \quad (2.15)$$

which returning to Gibbs notation (and replacing  $f_\Delta \rightarrow f(\Delta^+)$ ) gives

$$\begin{aligned} & \int_0^\Delta [\nabla_h \cdot (\bar{\mathbf{u}}_s \bar{\mathbf{u}}_s) + \partial_y(\bar{v} \bar{\mathbf{u}}_s)] dy \\ &= \Delta f(\Delta^+) \mathbf{V}_\tau \cdot \nabla_h \mathbf{u}_\tau - \Delta u_\tau f(\Delta^+)^2 (\nabla_h \cdot \mathbf{s}) \left( \frac{\theta_\Delta}{\Delta} \right) \mathbf{u}_\tau \end{aligned} \quad (2.16)$$

where

$$\mathbf{V}_\tau \equiv \left( 1 - \frac{\delta_\Delta^*}{\Delta} - \frac{\theta_\Delta}{\Delta} \right) f(\Delta^+) \mathbf{u}_\tau \quad (2.17)$$

is the advective velocity and a “cell momentum thickness”

$$\begin{aligned}\theta_\Delta &\equiv \int_0^\Delta \frac{\bar{u}_s(y)}{\bar{u}_s(\Delta)} \left(1 - \frac{\bar{u}_s(y)}{\bar{u}_s(\Delta)}\right) dy \\ \frac{\theta_\Delta}{\Delta} &= \frac{1}{\Delta^+} \int_0^{\Delta^+} \frac{f(y^+)}{f(\Delta^+)} \left(1 - \frac{f(y^+)}{f(\Delta^+)}\right) dy^+, \end{aligned}\quad (2.18)$$

has been introduced arising from the integrals of quadratic advection terms. Equation 2.16 completes the derivation of the advection term where the second term (proportional to the divergence of  $s$ ) is the term missed in the original derivation.

Next we derive the expressions needed for the diffusion term. The integral of the vertical diffusion term is obvious and simply becomes

$$\int_0^\Delta \frac{\partial}{\partial y} \left[ (\nu + \nu_T) \frac{\partial \bar{u}_s}{\partial y} \right] dy = \bar{\tau}_\Delta - u_\tau u_\tau \quad (2.19)$$

where  $u_\tau u_\tau$  is the LaRTE wall stress and

$$\bar{\tau}_\Delta \equiv (\nu + \nu_T) \frac{\partial \bar{u}_s}{\partial y} \Big|_{y=\Delta} \quad (2.20)$$

is the total (molecular viscous + turbulent viscous) shear stress at  $y = \Delta$ . The integral of the horizontal diffusion term is less obvious and its derivation is presented before for completeness, even if we expect it to be far less important than the vertical term and will be neglected in practice. We focus our attention on one term, namely

$$D_{\tau\nu} = \int_0^\Delta \nu \left[ \nabla_h \bar{u}_s + (\nabla_h \bar{u}_s)^\top \right] dy, \quad (2.21)$$

i.e. the contribution to  $\mathbf{D}_\tau = \mathbf{D}_{\tau v} + \mathbf{D}_{\tau T}$  from the constant (molecular) viscosity. Using again  $\bar{\mathbf{u}}_s = \bar{u}_s(y) \mathbf{s}$  and  $\nabla_h = \mathbf{s} \partial_s$ , we consider

$$\begin{aligned} & \nu \int_0^\Delta \mathbf{s} \partial_s [\bar{u}_s(y) \mathbf{s}] \, dy \\ &= \nu \int_0^\Delta \partial_s [u_\tau f(y^+)] \, dy (\mathbf{s} \mathbf{s}) + \nu u_\tau \int_0^\Delta f(y^+) \, dy \left( \mathbf{s} \frac{\partial \mathbf{s}}{\partial s} \right). \end{aligned} \quad (2.22)$$

Since  $\int_0^\Delta \partial_s [u_\tau f(y^+)] \, dy = \Delta f(\Delta^+) \partial u_\tau / \partial s$ , we obtain

$$\begin{aligned} \nu \int_0^\Delta \mathbf{s} \partial_s [\bar{u}_s(y) \mathbf{s}] \, dy &= \nu \Delta f(\Delta^+) \frac{\partial u_\tau}{\partial s} (\mathbf{s} \mathbf{s}) + \nu u_\tau \int_0^\Delta f(y^+) \, dy \left( \mathbf{s} \frac{\partial \mathbf{s}}{\partial s} \right) \\ &= \nu \Delta f(\Delta^+) \mathbf{s} \frac{\partial(u_\tau \mathbf{s})}{\partial s} - \nu u_\tau \delta_\Delta^* \left( \mathbf{s} \frac{\partial \mathbf{s}}{\partial s} \right). \end{aligned} \quad (2.23)$$

Adding the transpose and writing  $s_i \partial s_j + s_j \partial s_i = \partial(s_i s_j)$  as  $\partial_s(\mathbf{s} \mathbf{s}) = \mathbf{s} \cdot \nabla_h(\mathbf{s} \mathbf{s})$  we obtain, finally,

$$\mathbf{D}_{\tau v} = \nu \Delta f(\Delta^+) \left[ \nabla_h \mathbf{u}_\tau + (\nabla_h \mathbf{u}_\tau)^\top \right] - \nu \delta_\Delta^* \mathbf{u}_\tau \cdot \nabla_h (\mathbf{s} \mathbf{s}). \quad (2.24)$$

The first term is in the form of standard horizontal diffusion proportional to viscosity and the symmetric part of the friction velocity horizontal gradient tensor. The last term is non-standard and represents spatial direction changes. However, since  $\delta^*$  is expected to be typically much smaller than  $\Delta f(\Delta^+)$  this term can be expected to be small (similarly to the term in the Eulerian time derivative proportional to  $\delta_\Delta^*$  in equation 2.9). The case of  $y$ -dependent eddy viscosity to determine  $\mathbf{D}_{\tau T}$  can be developed similarly but includes more complicated expressions. In the simulations presented in this dissertation the horizontal diffusion terms are not explicitly included while some horizontal diffusion is provided by the low-order discretization method employed to

solve the Lagrangian advection part of the equation efficiently.

Finally, we collect all terms from the vertically integrated horizontal momentum equation (equations 2.9, 2.16, 2.19, 2.24), divide the entire equation by  $\Delta f(\Delta^+)$  (the coefficient for the  $\partial_t \mathbf{u}_\tau$  terms) and the evolution equation for the friction velocity vector can now be written according to

$$\begin{aligned} \frac{\partial \mathbf{u}_\tau}{\partial t} + \mathbf{V}_\tau \cdot \nabla_h \mathbf{u}_\tau &= \frac{1}{T_s} \left[ \frac{1}{u_\tau} \left( -\frac{\Delta}{\rho} \nabla_h \bar{p} + \bar{\tau}_\Delta \right) - \mathbf{u}_\tau \right] + u_\tau \frac{\delta_\Delta^*}{\Delta} \frac{\partial \mathbf{s}}{\partial t} \\ &\quad + u_\tau f_\Delta (\nabla_h \cdot \mathbf{s}) \left( \frac{\theta_\Delta}{\Delta} \right) \mathbf{u}_\tau + \frac{1}{\Delta f(\Delta^+)} \nabla_h \cdot \mathbf{D}_\tau \end{aligned} \quad (2.25)$$

where  $T_s$  is given by

$$T_s = f(\Delta^+) \frac{\Delta}{u_\tau}. \quad (2.26)$$

It represents a time-scale that arises from the derivation of equation (2.25) and does not require additional ad-hoc assumptions. When coupled with appropriate models for  $\bar{\tau}_\Delta$ ,  $f(\Delta^+)$ ,  $\delta_\Delta^*$ ,  $\theta_\Delta$ , and  $\mathbf{D}_\tau$ , we refer to equation (2.25) as the evolution equation underlying the LaRTE wall model.

## 2.2 Discussion

For the sake of initial discussion, it is instructive to consider a simplified form for the (e.g.) streamwise  $x$ -component of equation (2.25) and for now neglecting the pressure gradient, diffusive terms, the  $(\nabla_h \cdot \mathbf{s})$  term, as well as the direction change term  $\partial \mathbf{s} / \partial t$ . Under these simplifying conditions, equation (2.25) can be written as

$$\frac{d_s u_{\tau x}}{dt} = \frac{1}{T_s} (\bar{\tau}_{\Delta x} / u_\tau - u_{\tau x}), \quad (2.27)$$

with  $d_s/dt = \partial_t + \mathbf{V}_\tau \cdot \nabla_h$  representing a Lagrangian time derivative on the surface. In this form, it becomes apparent that the model represents a Lagrangian relaxation dynamics, with  $T_s$  serving as the relaxation time-scale for how the friction velocity component  $u_{\tau x}$  approaches the stress at the wall-model grid point in LES ( $\bar{\tau}_{\Delta x}$ ) (the latter divided by the friction velocity magnitude  $u_\tau$ ). For the present discussion, neglecting  $\bar{\tau}_{wz}$ , i.e. with  $\bar{\tau}_{wx} = u_\tau u_{\tau x} = u_{\tau x}^2$ , we see by multiplying (2.27) by  $u_{\tau x}$  that in terms of the wall stress the Lagrangian relaxation equation can equivalently be written as

$$\frac{d_s \bar{\tau}_{wx}}{dt} = \frac{2}{T_s} (\bar{\tau}_{\Delta x} - \bar{\tau}_{wx}), \quad (2.28)$$

showing that for the stress the relaxation time-scale is  $T_s/2$ . This time scale was originally derived by Chung and Pullin (2009) where they also showed the wall stress tends (in an Eulerian sense) towards its steady state value at a rate corresponding to this time scale (in the work of Chung and Pullin (2009), the quantity denoted as  $1/(\Lambda \tilde{\eta}_0)$  is equivalent to  $T_s/2$  shown here).

It can be seen from equation (2.9) that the relaxation time scale  $T_s$  arises from integrating the assumed velocity profile between  $y = 0$  and  $y = \Delta$  (this integral is similar to the term  $\partial L/\partial t$  that arises in the iWMLES approach by X. Yang et al., 2015). As a result of the analysis,  $T_s$  is proportional to the volume per unit area ( $\Delta$ ) in the fluid layer under consideration, between the wall and the wall-model height  $y = \Delta$ . It represents the inertia of the fluid in that layer and can be seen to cause a time-delay between the stress at  $y = \Delta$  and at the wall, under unsteady conditions. The thicker the layer (large  $\Delta$ ), the more the time delay due to added fluid inertia. Conversely, the stronger the

turbulence (large  $u_\tau$ ), the faster the relaxation leading to a smaller time-delay. We note that in X. Yang et al. (2015) for the iWMLES approach, an explicit time-filtering at a time-scale  $\sim \Delta/\kappa u_\tau$  was introduced, operationally similar but shorter than  $T_s$  by a factor  $\kappa f(\Delta^+) = \kappa \bar{u}(\Delta)/u_\tau$ . Here, such temporal relaxation behavior has been derived formally from the momentum equation (unsteady RANS) and the assumed validity of a quasi-equilibrium velocity profile (equation 2.1).

Also, for the full vector problem with two stress components, we remark that when attempting to write the relaxation equation in terms of wall-parallel components  $\bar{\tau}_{wx}$  and  $\bar{\tau}_{wz}$  instead of friction velocity vector components  $u_{\tau x}$  and  $u_{\tau z}$  (or  $\mathbf{u}_\tau$ ), the resulting equation is far less intuitive compared to the relatively simple form of equation (2.25). The latter resembles a standard transported vector field equation with a relaxation source term and a diffusion term (only the  $\partial \mathbf{s}/\partial t$  and  $\nabla_h \cdot \mathbf{s}$  terms are non-standard) and is therefore much preferable.

Finally, we note that when including the pressure gradient term  $\nabla_h \bar{p}$ , equation (2.25) shows that the implied relaxation dynamics is for how  $\mathbf{u}_\tau$  approaches the total cell forcing (vector) term  $(-\rho^{-1} \nabla_s \bar{p} \Delta + \bar{\boldsymbol{\tau}}_\Delta)/u_\tau$ .

## 2.3 Closure for the total stress at the wall-model height

The LaRTE model requires specification of the total (molecular viscous + turbulent) stress  $\bar{\boldsymbol{\tau}}_\Delta$  at  $y = \Delta$  as function of known LES quantities there, such as the LES velocity  $\mathbf{U}_{\text{LES}}$  at the wall-model point. I.e. we denote  $\tilde{\mathbf{u}}(y = \Delta) =$

$\mathbf{U}_{\text{LES}}$ , where  $\tilde{\mathbf{u}}(\mathbf{x}, t)$  is the velocity field being solved in LES. We argue that introducing a closure model for the total stress there ( $\bar{\tau}_\Delta$ ) is more appropriate than closing the stress at the wall, since the wall is at a different position than the position at which the LES velocity is known. For now the simplest approach, which we shall adopt in this paper, is to use a standard “equilibrium” RANS closure to relate the known velocity  $\mathbf{U}_{\text{LES}}(y = \Delta)$  to the total (viscous plus turbulent) shear stress  $\bar{\tau}_\Delta$  at the same position. In this way, we can connect the new LaRTE wall model to the traditional equilibrium wall model: the latter is obtained simply by letting  $T_s \rightarrow 0$ , in which case the wall stress is set equal to the total stress at  $y = \Delta$ . This equality of stresses would be justified under full equilibrium conditions, i.e. if the turbulence small-scale unresolved motions operated on much shorter time-scales than the macroscopic variables (time-scale separation) and  $T_s \rightarrow 0$  would be appropriate. However, for turbulence that lacks scale separation under quasi-equilibrium conditions with temporal and spatial variations and pressure gradient effects, the assumption that  $T_s \rightarrow 0$  and equality of stresses are not formally justified. Then the relaxation equation can be solved instead.

Next, we describe the proposed closure for the stress  $\bar{\tau}_\Delta$ . We use the approach developed in Meneveau (2020) in which an equilibrium layer partial differential equation is numerically integrated and various fitting functions are developed for the numerical solution. The model of Meneveau (2020) is expressed in the form of a friction Reynolds number that depends on a  $U_{\text{LES}}$ -based Reynolds number and a dimensionless pressure gradient parameter via

a dimensionless fitting function:

$$\frac{\langle u_\tau \rangle \Delta}{\nu} = Re_{\tau\Delta}^{\text{pres}}(Re_\Delta, \psi_p) \quad (2.29)$$

where

$$Re_\Delta = \frac{U_{\text{LES}} \Delta}{\nu} \quad \text{and} \quad \psi_p = \frac{1}{\rho} (\nabla_h P \cdot \hat{e}_u) \frac{\Delta^3}{\nu^2}. \quad (2.30)$$

The superscript “pres” indicates that the fit includes pressure gradient dependence. This fit is repeated in appendix 9.1 for completeness (algorithm 1). Also,  $\hat{e}_u = \mathbf{U}_{\text{LES}} / |\mathbf{U}_{\text{LES}}|$  is the unit vector in the  $\mathbf{U}_{\text{LES}}$  direction. The pressure gradient  $\nabla_h P$  represents a steady or very low-frequency background pressure gradient, included in the full equilibrium part of the dynamics. Details of how  $\nabla_h P$  is determined in simulations are provided later, in §4.1.1. The fit for  $Re_{\tau\Delta}^{\text{pres}}(Re_\Delta, \psi_p)$  provided in Meneveau (2020) was obtained by numerically integrating the simple steady 1D RANS equations that, unlike equation 2.4 did not include time-dependence and can thus be characterized as a “fully equilibrium model” (as opposed to quasi-equilibrium) assumption. The friction velocity  $\langle u_\tau \rangle$  is the corresponding “full equilibrium” friction velocity. Under these conditions, the full equilibrium vertically integrated momentum equation implies that  $0 = -\Delta \nabla_h P / \rho + \bar{\tau}_\Delta - \langle u_\tau \rangle^2$ , i.e.  $\langle u_\tau \rangle^2$  obtained from applying equation 2.29 represents a model for the combined  $\bar{\tau}_\Delta - \Delta \nabla_h P / \rho$ .

Following usual practice of equilibrium wall models, we assume that the total stress modeled by the fitted equilibrium expression is aligned with the LES velocity at the first grid point and write

$$\bar{\tau}_\Delta - \frac{1}{\rho} \Delta \nabla_h P = \frac{1}{2} c_f^{\text{wm}} U_{\text{LES}}^2 \hat{e}_u = \left( Re_{\tau\Delta}^{\text{pres}} \frac{\nu}{\Delta} \right)^2 \hat{e}_u \quad (2.31)$$

where  $Re_{\tau\Delta}^{\text{pres}} = Re_{\tau\Delta}^{\text{pres}}(Re_\Delta, \psi_p)$  is the fit. Note that the latter is related to the “equilibrium wall model friction factor”  $c_f^{\text{wm}}$  according to  $c_f^{\text{wm}} = 2(Re_{\tau\Delta}^{\text{pres}}/Re_\Delta)^2$ .

Finally then, the two-dimensional PDE governing the evolution of the friction velocity vector in the LaRTE model reads as follows:

$$\begin{aligned} \frac{\partial \mathbf{u}_\tau}{\partial t} + \mathbf{V}_\tau \cdot \nabla_h \mathbf{u}_\tau \\ = \frac{1}{T_s} \left[ \frac{1}{u_\tau} \left( -\frac{\Delta}{\rho} \nabla_h \bar{p}' + (Re_{\tau\Delta}^{\text{pres}} \nu / \Delta)^2 \hat{\mathbf{e}}_u \right) - \mathbf{u}_\tau \right] + u_\tau \frac{\delta_\Delta^* \partial s}{\Delta \partial t}, \end{aligned} \quad (2.32)$$

where  $\bar{p}'$  is the pressure fluctuation that excludes the very slow background pressure gradient based on  $P$  and is further described in §4.1.1. Also note that we have neglected the  $\nabla_h \cdot s$  term (expected to be small) and the horizontal diffusion term in writing this equation (further discussion of horizontal diffusion is provided in §2.5). The solution to equation 2.32 is then used to determine the quasi-equilibrium part of the wall stress  $\bar{\tau}_w = u_\tau \mathbf{u}_\tau$ .

In practice for flows such as channel flow or zero pressure gradient boundary layers that do not display major non-equilibrium effects, one would not expect to see noticeably different results in overall flow statistics, whether one applies the equilibrium wall model instantaneously at the wall as is usually done, or if one applies the proposed Lagrangian time relaxation, i.e. with some time delay and temporal smoothing. However, the new formulation enables us to operationally separate the model self-consistently into a part that genuinely represents quasi-equilibrium dynamics, and a remainder for which additional modeling is needed. As introduced later in chapter 3, the total modeled wall stress may also include a non-equilibrium component  $\tau_w''$ ,

representing additional contributions to the wall stress that do not arise from the quasi-equilibrium dynamics encapsulated in equations 2.25 and 2.32. For example, in chapter 3 we introduce an additional term  $\tau_w''$  intended to capture the non-equilibrium laminar response to a rapidly changing pressure gradient in the viscous sublayer. But first, in the next section we present an a-priori data analysis to provide empirical evidence that the time scale  $T_s$  is appropriate for quasi-equilibrium.

## 2.4 A-priori analysis of quasi-equilibrium dynamics in channel flow

Here we examine channel flow DNS data at  $Re_\tau = 1,000$  to show that the time-scale  $T_s$  identified in equation 2.26 provides a self-consistent decomposition of the flow into quasi-equilibrium and non-equilibrium (the remainder) components. DNS data were obtained from the Johns Hopkins Turbulence Database (JHTDB, 2021) for the channel flow  $Re_\tau = 1,000$  dataset (Graham et al., 2016). The velocity data was Gaussian filtered horizontally at scale  $\Delta_x^+ = \Delta_z^+ = 196$ , commensurate to the LES grid resolution for simulations considered later in this chapter 4. The velocity was collected for all times available,  $0 \leq tu_\tau/h \leq 0.3245$ , at a single point,  $(x_0, z_0)$ , over a wall-normal height  $0 \leq y^+ \leq \Delta^+ \approx 34$ , close to the height of the first LES grid point that will serve as the wall-model height.

The DNS velocity is then temporally filtered below  $y = \Delta$  using a one-sided exponential time filter, computed as  $\tilde{u}^n = \epsilon u^n + (1 - \epsilon)\tilde{u}^{n-1}$ , where  $\epsilon = \delta t/T$ ,  $\delta t$  is the time-step size,  $n$  is the time step index, and  $T$  is the averaging time

scale. Three different averaging time scales are considered to see which time scale is most consistent with quasi-equilibrium assumptions. Quasi-equilibrium is satisfied when the filtered velocity profile collapses to  $\tilde{u} = u_{\tau,l}f(yu_{\tau,l}/\nu)$  for all time, where  $u_{\tau,l}(x,z,t)$  is the local friction velocity. The local friction velocity is computed using  $u_{\tau,l} = \nu/\Delta Re_{\tau}^{fit}(U_{LES}\Delta/\nu)$  where  $Re_{\tau}^{fit}$  is the inverted law of the wall fit from Meneveau (2020) and  $U_{LES} = \tilde{u}(x,y = \Delta, z, t)$  is the filtered velocity at the wall-model height. In the limit  $T \rightarrow \infty$ , the velocity profile is static and thus full equilibrium is achieved. In this limit the local friction velocity tends towards the global friction velocity, computed as  $u_{\tau,g} = \sqrt{(h/\rho)(-d\langle p \rangle/dx)}$  where  $d\langle p \rangle/dx$  is the bulk pressure gradient forcing for channel flow. Inner units normalization of the velocity profile using  $u_{\tau,g}$  is shown in the top row of figure 2.2 whereas normalization with  $u_{\tau,l}$  is shown in the bottom row of figure 2.2. In order, from left to right in figure 2.2, the averaging time scales considered are: panels (a, d): no temporal filtering, i.e. entirely local; panels (b, e): intermediate time scale  $T_1 = \Delta/u_{\tau,g}$ ; and panels (c, f): LaRTE predicted time-scale  $T_s = \Delta f(\Delta u_{\tau,g}/\nu)/u_{\tau,g}$ . Note that  $T_1$  is similar to what is used in X. Yang et al. (2015), however off by a factor  $\theta/\kappa$  with  $\theta = 1$  used for their work. They also mentioned that a longer time scale may be needed, even suggesting a minimum of  $\theta = 5$  which yields a coincidentally rather similar time scale as  $T_s$  for  $\Delta^+ = 34$ . We stress that here  $T_s$  is derived based on a momentum balance and does not require tunable parameters as was the case in X. Yang et al. (2015).

From figure 2.2(f) it is clear that filtering with the relaxation time scale  $T_s$  most closely satisfies quasi-equilibrium assumptions, as it almost completely

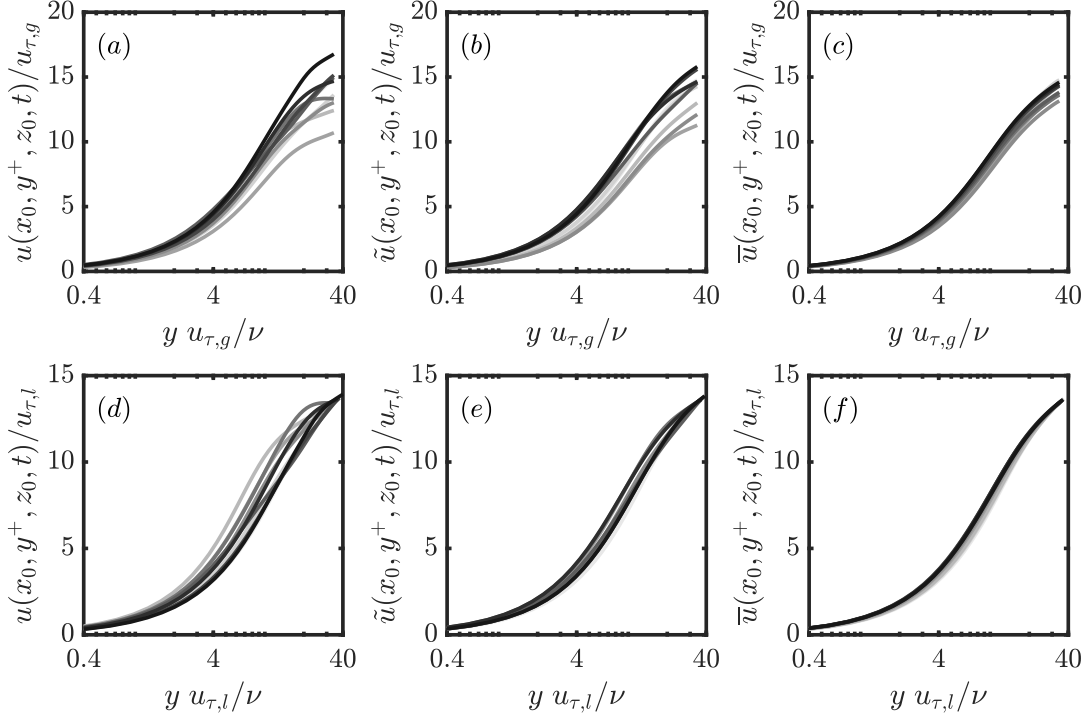


**Figure 2.2:** Velocity profiles at a single point  $(x_0, z_0)$  at various times, from a-priori tests from DNS data, Gaussian filtered in the horizontal directions at  $\Delta_x^+ = \Delta_z^+ = 196$ . Different lines represent different times, lighter line color corresponds to earlier time, separated by  $tu_{\tau,g}/h = 0.13$ . Profiles are normalized using the global friction velocity  $u_{\tau,g}$  in (a – c) while (d – f) use the local friction velocity  $u_{\tau,l}$  as averaged over the same time filtering scale as used for the profile. (a, d): no time filter; (b, e): exponentially time filtered with  $T_1 = \Delta/u_{\tau,g}$  time filter; (c, f): exponentially time filtered using  $T_s = \Delta f(\Delta u_{\tau,g}/\nu)/u_{\tau,g}$  consistent with the LaRTE approach. The  $y^+$  dependence in the vertical axis matches that of the horizontal axis (i.e.  $y^+ = yu_{\tau,g}/\nu$  for (a – c) and  $y^+ = yu_{\tau,l}/\nu$  for (d – f)).

collapses to the law of the wall when normalized with the local friction velocity. This a-priori test therefore provides justification that the relaxation towards equilibrium wall model, which responds within the relaxation time scale  $T_s$  as discussed in §2.2, is consistent with quasi-equilibrium assumptions.

## 2.5 Discretization of the LaRTE evolution equation

The full model embodied by equation (2.25) is a nonlinear PDE for  $\mathbf{u}_\tau(x, y, t)$ , with an elliptic diffusion term, advective term, and a couple of non-standard source terms. Following the logic of the Lagrangian dynamic model implementation (Meneveau et al., 1996) and acknowledging the approximate nature of various modeling assumptions to be made, we opt for efficiency over high-order numerical accuracy in the proposed numerical implementation, while aiming to maintain the main features of the model. We discretize the LaRTE evolution equation using a forward Euler method such that the friction velocity vector may be solved for explicitly. This requires evaluating all terms, including the Lagrangian time derivative, at the previous time step  $t_{n-1} = t_n - \delta t$  (with  $n$  the time step index) where all terms are known. We then propose to discretize the Lagrangian derivative at time  $t_{n-1}$  using a semi-Lagrangian scheme (Staniforth & Côté, 1991):

$$\begin{aligned} \left[ \frac{\partial \mathbf{u}_\tau}{\partial t} + \mathbf{V}_\tau \cdot \nabla_h \mathbf{u}_\tau \right] (x'_i, z'_k, t_{n-1}) &= \left[ \frac{d_s \mathbf{u}_\tau}{dt} \right] (x'_i, z'_k, t_{n-1}) \\ &\approx \frac{1}{\delta t} [\mathbf{u}_\tau(x_i, z_k, t_n) - \mathbf{u}_\tau(x'_i, z'_k, t_{n-1})], \end{aligned} \quad (2.33)$$

where  $x'_i = x_i - V_{\tau x} \delta t$  and  $z'_k = z_k - V_{\tau z} \delta t$  (with  $i$  and  $k$  position indices), and  $\mathbf{V}_\tau$  is evaluated from equation 2.17 using  $\mathbf{u}_\tau(x_i, z_k, t_{n-1})$ . Replacing into the equation  $[\mathbf{u}_\tau(x_i, z_k, t_n) - \mathbf{u}_\tau(x'_i, z'_k, t_{n-1})] / \delta t = \mathbf{RHS}(x'_i, z'_k, t_{n-1})$ , where **RHS** is the entire right-hand-side of equation 2.32 yields

$$\mathbf{u}_\tau(x_i, z_k, t_n) = \mathbf{u}_\tau(x'_i, z'_k, t_{n-1}) + \delta t \mathbf{RHS}(x'_i, z'_k, t_{n-1}). \quad (2.34)$$

The entire right-hand-side of equation 2.34 at the upstream position ( $x_i - V_{\tau x} \delta t, z_k - V_{\tau z} \delta t$ ) at the time  $t_{n-1}$  is obtained using first-order bilinear spatial interpolation of the grid values on the plane, as was done in 3D in Meneveau et al. (1996). The additional numerical diffusion associated with the low-order interpolation reduces the need to include the horizontal diffusion term  $\nabla_h \cdot \mathbf{D}_\tau$  which would require additional modeling and numerical cost associated with solving an elliptic problem. Thus, we neglect the term  $\nabla_h \cdot \mathbf{D}_\tau$  altogether in practical implementations in our LES. We also neglect the  $\nabla_h \cdot \mathbf{s}$  term which is expected to be small. Finally, evaluation of **RHS** requires the  $\partial_t \mathbf{s}$  term. It is discretized using backward differencing, as  $\partial_t \mathbf{s}|_{n-1} = (\mathbf{s}|_{n-1} - \mathbf{s}|_{n-2}) / \delta t$  all evaluated at the interpolated position ( $x_i - V_{\tau x} \delta t, z_k - V_{\tau z} \delta t$ ).

# Chapter 3

## The laminar non-equilibrium (lamNEQ) model

### 3.1 Derivation

So far we have developed a model for  $\bar{\tau}_w$ , the quasi-equilibrium part of the wall stress, which responds to external conditions (changes in velocity and pressure gradients at the wall-model height) at a time-scale  $T_s$  consistent with the assumption of quasi-equilibrium. In order to supplement the quasi-equilibrium Lagrangian relaxation model with additional physics, we now focus on the rapid response of the inner-most part of the boundary layer, the viscous sublayer. The response of near-wall structures of turbulence to rapidly changing pressure gradients has been studied extensively in the past. W. J. Jung et al. (1992), Karniadakis and Choi (2003), Quadrio and Ricco (2003), Ricco et al. (2012), and Yao et al. (2019) studied spanwise wall-oscillations due to its drag-reducing capabilities. Vardy and Brown (2003) and Vardy et al. (2015) attempt to understand the wall shear stress for water hammer pipe flows. Experimental and numerical studies of pulsatile flows

have been performed by Scotti and Piomelli (2001), S. Tardu and da Costa (2005), F. S. Tardu and Maestri (2010), Weng et al. (2016), Sundstrom and Cervantes (2018a), and Cheng et al. (2020). Streamwise accelerating flows were considered by He and Jackson (2000), Greenblatt and Moss (2004), He et al. (2008a), He, Ariyaratne, and Vardy (2011), He and Ariyaratne (2011), He and Seddighi (2013), He and Seddighi (2015), S. Y. Jung and Chung (2012), S. Y. Jung and Kim (2017), Sundstrom and Cervantes (2017), and Sundstrom and Cervantes (2018c). Then there are studies with step changes in either the wall boundary condition or in the pressure forcing such as the sudden spanwise wall movement of Coleman et al. (1996), Tang and Akhavan (2016), and Abe (2020), the sudden spanwise pressure gradient of Moin et al. (1990) and Lozano-Durán et al. (2020), or a change in the direction of the pressure gradient forcing (for a variety of directions) as done in de Wiart et al. (2018). One of the common observations amongst all of these flows is the existence of a laminar Stokes layer near the wall. For pulsatile flows, the wall stress deviation from its steady state value follows the solution to Stokes's second problem exactly for high frequency oscillations (Weng et al. (2016)). For streamwise accelerating flows, the wall stress deviation from its initial value follows the solution to Stokes's first problem during the first stage of the acceleration (He and Seddighi (2015), S. Y. Jung and Kim (2017), Sundstrom and Cervantes (2018c)). Sundstrom and Cervantes (2018b) even showed that the wall stress for low frequency pulsations follows the Stokes solution during the acceleration phase of the pulse. They further showed the similarity of the wall stress during the acceleration phase of pulsatile flows with the initial phase of streamwise accelerating flows. For the sudden spanwise wall

movement and sudden spanwise pressure gradient, the spanwise velocity and wall stress follows Stokes's first problem during the early response (Abe, 2020; Coleman et al., 1996; Lozano-Durán et al., 2020).

We here use concepts inspired by these prior works to complement the quasi-equilibrium LaRTE model presented in chapter 2. We decompose the velocity  $\tilde{u}$  (this velocity is spatially filtered in the 2D horizontal plane but not time filtered, and so it may still contain strong time and  $y$ -dependent deviations from the quasi-equilibrium profile  $\bar{u}$ ) according to  $\tilde{u} = \bar{u} + \tilde{u}''$  where  $\tilde{u}''$  is the non-equilibrium velocity to be modeled here. The deviations from the quasi-equilibrium velocity distribution  $\bar{u}$ , such as the deviations visible in figures 2.2(a) and (d), can arise from a variety of sources such as time-dependent turbulent fluctuations and pressure gradients. The fastest changing pressure gradient fluctuations can induce oscillatory flow conditions even in the viscous sublayer, not unlike those involved in the Stokes first and second problems. Since for the quasi-laminar part of the flow in the viscous sublayer an analytical solution can be developed, we aim now to model that part of the non-equilibrium wall stress arising directly from the response of the laminar sublayer to rapid pressure gradient fluctuations. We denote the corresponding laminar velocity response as  $\tilde{u}_l''$  where subscript "l" stands for laminar component.

In the viscous sublayer the linear terms of the Navier-Stokes equation dominate and hence we argue that  $\tilde{u}_l''$  obeys

$$\frac{\partial \tilde{u}_l''}{\partial t} = -\frac{1}{\rho} \nabla_h \tilde{p}'' + \nu \frac{\partial^2 \tilde{u}_l''}{\partial y^2} \quad (3.1)$$

where as before subscript h represents the horizontal directions  $x$  and  $z$ . The boundary conditions are  $\tilde{u}_l''(y = 0, t) = 0$  and  $\partial\tilde{u}_l''/\partial y(y \rightarrow \infty, t) = 0$  with the initial condition  $\tilde{u}_l''(y, t_0) = 0$ . To simplify the problem, it is useful to define a “non-equilibrium free stream velocity”,  $\tilde{u}_\infty''$ , defined as the velocity that would exist as an inviscid response to the non-equilibrium pressure gradient:

$$\frac{\partial\tilde{u}_\infty''}{\partial t} = -\frac{1}{\rho}\nabla_h\tilde{p}'' , \quad \rightarrow \quad \tilde{u}_\infty''(t) = \int_{t_0}^t -\frac{1}{\rho}\nabla_h\tilde{p}'' dt' . \quad (3.2)$$

We can then use this velocity to eliminate the pressure gradient using the variable transformation  $\hat{u}(y, t) = \tilde{u}_\infty''(t) - \tilde{u}_l''(y, t)$ . The problem then reduces to the generalized Stokes problem where the wall velocity is  $\tilde{u}_\infty''(t)$ . From Schlichting and Gersten (2017) this has the solution

$$\hat{u}(y, t) = \int_{t_0}^t \frac{\partial\tilde{u}_\infty''}{\partial t'} \operatorname{erfc}\left(\frac{y}{2\sqrt{\nu(t-t')}}\right) dt' . \quad (3.3)$$

Rewriting in terms of  $\tilde{u}_l''$  and  $\nabla_h\tilde{p}''$  gives

$$\tilde{u}_l''(y, t) = \int_{t_0}^t \left(-\frac{1}{\rho}\nabla_h\tilde{p}''\right) \operatorname{erf}\left(\frac{y}{2\sqrt{\nu(t-t')}}\right) dt' \quad (3.4)$$

from which the stress contribution can be obtained by differentiation, evaluation at  $y = 0$  and multiplication by  $\nu$ , and reads as follows:

$$\tau_w''(t) = \sqrt{\nu/\pi} \int_{t_0}^t -\frac{1}{\rho}\nabla_h\tilde{p}''(t') (t-t')^{-1/2} dt' . \quad (3.5)$$

Interestingly, we can use  $\tilde{u}_\infty''$  to relate the non-equilibrium wall stress with the Caputo fractional derivative:

$$\tau_w'' = -\sqrt{\nu/\pi} \Gamma(1/2) D_t^{1/2}(\tilde{u}_\infty''), \quad (3.6)$$

where the Caputo fractional derivative of order  $\alpha$  of a signal  $v(t)$  is defined as

$$D_t^\alpha v(t) = \frac{1}{\Gamma(1-\alpha)} \int_{t_0}^t \frac{v^{(1)}(t')}{(t-t')^\alpha} dt' \quad (3.7)$$

In the equation above  $0 < \alpha < 1$  is the order of the fractional derivative. The rapid wall stress model uses  $\alpha = 1/2$ . Relating the wall stress with the Caputo fractional derivative is useful because an efficient numerical evaluation of this type of non-local integral operator is possible, as described in §3.2.

## 3.2 Evaluating the temporal convolution integral

Jiang et al. (2017) developed a method for “fast evaluation of the Caputo fractional derivative” which significantly reduces storage and computational cost requirements thus making the computation of the convolution integral practical. To summarize, their method decomposes the integral into a local and history parts where the history contribution is evaluated efficiently by making a sum-of-exponentials approximation to the kernel. An exponential kernel has the advantage that the current value of the convolution depends only on the previous time-step value of the convolution and a local term, as exploited in many applications where time filtering is needed (as e.g. in Meneveau et al. (1996) and in other instances of exponential time filtering applied in this dissertation).

Since the sum-of-exponentials approximation algorithm is critical for the model, we will describe here the basic details of it pertaining to our application with  $\alpha = 1/2$ . Our task is to find an efficient way of computing the convolution integral in equation 3.5. To simplify notation we let  $G(t) \equiv -\rho^{-1} \nabla_h \tilde{p}''(t)$ .

Then the non-equilibrium wall stress is given by

$$\boldsymbol{\tau}_w''(t_n) = \sqrt{\nu/\pi} \int_{t_0}^{t_n} \mathbf{G}(t')(t_n - t')^{-1/2} dt' \quad (3.8)$$

where  $t_n$  is the current time and  $n$  is, as before, the time step index. The sum-of-exponentials (SOE) approximation for the kernel reads:

$$(t_n - t')^{-1/2} \approx \sum_{m=1}^{N_{\text{exp}}} \omega_m e^{-s_m(t_n - t')} \quad (3.9)$$

where the constants  $\omega_m$  and  $s_m$  are determined a priori as a function of the time-step size for the SOE approximation,  $\delta t$ , the time duration considered,  $T$ , and the desired maximum error for the SOE approximation of the kernel,  $\epsilon$ . According to Jiang et al. (2017), the number of exponential terms,  $N_{\text{exp}}$ , is also a function of these parameters and can be estimated by the expression

$$N_{\text{exp}} = \mathcal{O} \left( \log \frac{1}{\epsilon} \left( \log \log \frac{1}{\epsilon} + \log \frac{T}{\delta t} \right) + \log \frac{1}{\delta t} \left( \log \log \frac{1}{\epsilon} + \log \frac{1}{\delta t} \right) \right). \quad (3.10)$$

$\epsilon$  is the error associated with the approximation in equation 3.9 (not to be confused with the error from discretizing equation 3.8). The simulations in chapter 4 will mostly use  $\delta t \sim 4 \times 10^{-4}$  and so the constants were computed using  $\delta t = 4 \times 10^{-4}$ . Also, it was found that in order to guarantee good accuracy in all cases considered, we required  $\epsilon = 10^{-9}$ . We used  $T = 1$  although this parameter was seen to affect the coefficients very little as long as  $T \gg \delta t$ . The optimization approach by Jiang et al. (2017) yields  $N_{\text{exp}} = 48$  although fewer terms (obtained by using larger  $\epsilon$ ) could be used while still yielding reasonable accuracy. §3.3 provides information about the computed constants as well as a more detailed verification of the numerical method.

The integral is divided into local and history parts (in time)

$$\boldsymbol{\tau}_w'' = \boldsymbol{\tau}_{w,l}'' + \boldsymbol{\tau}_{w,h}'' \quad (3.11)$$

where

$$\begin{aligned} \boldsymbol{\tau}_{w,l}''(t_n) &\equiv \sqrt{\nu/\pi} \int_{t_{n-1}}^{t_n} \mathbf{G}(t')(t_n - t')^{-1/2} dt' \\ \boldsymbol{\tau}_{w,h}''(t_n) &\equiv \sqrt{\nu/\pi} \int_{t_0}^{t_{n-1}} \mathbf{G}(t')(t_n - t')^{-1/2} dt'. \end{aligned} \quad (3.12)$$

The local part is evaluated using the “L1 method” (Li & Zeng, 2015):

$$\boldsymbol{\tau}_{w,l}'' \approx 2\mathbf{G}(t_{n-1/2}) \sqrt{\frac{\nu \Delta t_n}{\pi}} \quad (3.13)$$

where  $\Delta t_n = t_n - t_{n-1}$  and  $\mathbf{G}(t_{n-1/2}) = 0.5(\mathbf{G}(t_n) + \mathbf{G}(t_{n-1}))$ . The history part is evaluated by replacing the kernel with a sum-of-exponential approximation from equation 3.9. This sum-of-exponentials approximation is useful because it allows the integral to be computed recursively. The history term can then be computed using

$$\boldsymbol{\tau}_{w,h}'' \approx \sqrt{\nu/\pi} \sum_{m=1}^{N_{exp}} \omega_m \mathbf{I}_m(t_n) \quad (3.14)$$

where

$$\begin{aligned} \mathbf{I}_m(t_n) &= \int_{t_0}^{t_{n-1}} \mathbf{G}(t') e^{-s_m(t_n - t')} dt' \\ &= e^{-s_m(t_n - t_{n-1})} \mathbf{I}_m(t_{n-1}) + \int_{t_{n-2}}^{t_{n-1}} \mathbf{G}(t') e^{-s_m(t_n - t')} dt' \\ &\approx e^{-s_m \Delta t_n} \left[ \mathbf{I}_m(t_{n-1}) + \frac{\mathbf{G}(t_{n-3/2})}{s_m} (1 - e^{-s_m \Delta t_{n-1}}) \right]. \end{aligned} \quad (3.15)$$

The total non-equilibrium wall stress can then be computed using equation 3.11 together with equations 3.13, 3.14, and 3.15. The advantage of this method is that it requires  $O(N_{exp})$  storage and  $O(N_T N_{exp})$  computational work whereas a direct method requires storing the entire time evolution, i.e.  $O(N_T)$  storage and  $O(N_T^2)$  work which becomes unwieldy for long simulations.

### 3.3 Verification of the accuracy of the SOE method

We now validate the accuracy of the sum-of-exponentials (SOE) method presented in §3.2 by comparing it with the more costly, but well established “L1 method” (Li & Zeng, 2015). A typical pressure gradient signal from real flow simulations for  $Re_\tau = 1000$  and  $\Delta = h/30$  is used for the comparison. The SOE constants  $\omega$  and  $s$  and the number of exponential terms,  $N_{exp}$ , are functions of the error of the SOE approximation,  $\epsilon$ , the time step size,  $\delta t$ , and the length of time considered,  $T$ . The method guarantees that  $|t^{-1/2} - \sum_{m=1}^{N_{exp}} \omega_m \exp(-s_m t)| \leq \epsilon$  but it does not guarantee that the error in computing the integral in 3.8 is below a desired value. Therefore, we simply compare the SOE method with the L1 method to show that the errors between the two are insignificant despite the significant computational cost differences between the two numerical methods. The results are presented in figure 3.1. (a) shows the input signal and (b) shows the output signal. The time step size used for computing the SOE constants matches the time step size of the pressure gradient signal, thus error in the approximation of the kernel is guaranteed. Visually, the differences between the two methods are not noticeable.

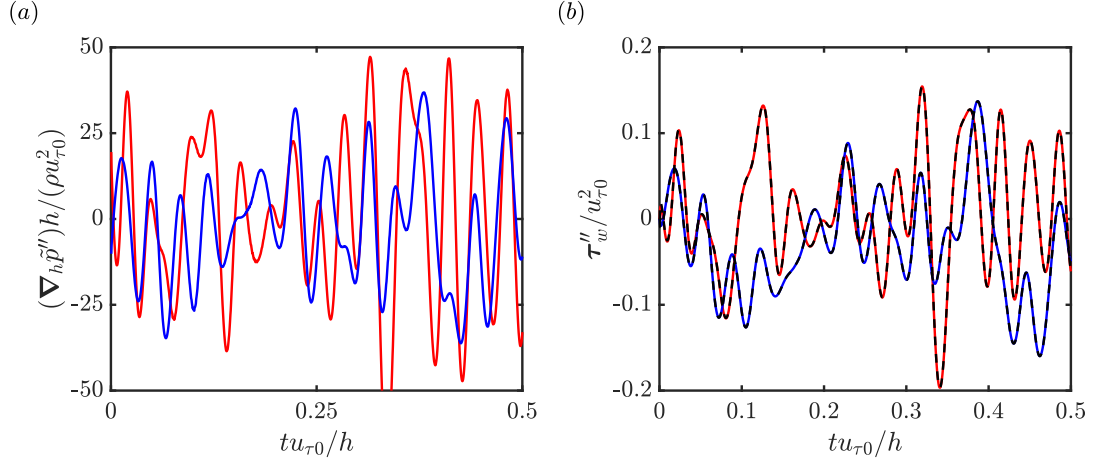


**Figure 3.1:** (a) representative non-equilibrium pressure gradient signal and (b) corresponding non-equilibrium wall stress. Red and blue curves correspond with the x and z components, respectively. For (b), solid lines are computed using the L1 method and dashed black lines are computed using the SOE method. The SOE constants are computed using  $\delta t = 4 \times 10^{-4}$ ,  $\epsilon = 10^{-9}$ , and  $T = 1$  (yielding  $N_{\text{exp}} = 48$ ).

Quantitatively the root-mean-sum (RMS) difference between the methods, normalized with  $u_{\tau 0}^2$ , is less than 0.021 in the x-direction and less than 0.011 in the y-direction. Therefore, differences between the two methods are shown to be small enough to be neglected for current applications. The L1 method requires  $O(N_T)$  computations per time step and  $O(N_T)$  terms to be stored. The SOE method on the other hand requires  $O(N_{\text{exp}})$  computations per time step and  $(N_{\text{exp}})$  terms to be stored where  $N_{\text{exp}}$  can be estimated from equation 3.10. For a large number of time steps  $N_{\text{exp}} \sim O(\log N_T)$  which in practice is held constant to avoid a dynamic storage size. Therefore, the SOE method has been shown to be significantly cheaper (with a non-dynamic storage size) relative to the L1 method while still providing accurate results.

The SOE constants,  $\omega$  and  $s$ , used in all simulations in chapter 4 are included in the appendix in table 9.1. Dr. Shidong Jiang kindly provided the

source code for computing these coefficients.

# Chapter 4

## Applications of the LaRTE+lamNEQ wall model to equilibrium and non-equilibrium channel flows

### 4.1 Summary of the LaRTE+lamNEQ wall model

The LaRTE+lamNEQ wall model will be summarized here and results using this wall model will follow in this chapter. In chapter 2, we developed a model governing slow, quasi-equilibrium wall stress dynamics responding to applied stresses at a rate corresponding with the formally derived relaxation time scale,  $T_s$ . This model was termed the Lagrangian Relaxation Towards Equilibrium (LaRTE) wall model based on the behavior of its governing equation for the friction velocity vector. Then, in chapter 3, we developed a non-equilibrium model to supplement the LaRTE model which captures the near-wall laminar Stokes layer dynamics due to rapid changes in the pressure gradient, termed the lamNEQ model. These two models are linked through the pressure gradient since the lamNEQ model responds to the fast fluctuating components of the LES pressure gradient and the LaRTE model is

assumed to respond to the remaining, slower components of the LES pressure gradient. This decomposition has not yet been specified and will be done in the following section 4.1.1.

### 4.1.1 Pressure gradient decomposition

In this section we discuss the various pressure gradient inputs to the model:  $\nabla_h P$ ,  $\nabla_h \bar{p}'$  and  $\nabla_h \tilde{p}''$ . The first ( $\nabla_h P$ ) is used in evaluating the fully equilibrium fitted part to evaluate the turbulent stress as input to the LaRTE equation.  $\nabla_h \bar{p}'$  is the fluctuating pressure gradient input that directly affects the LaRTE dynamics. The last term  $\nabla_h \tilde{p}''$  is the forcing term for the non-equilibrium laminar response model described in §3.1. We begin from the pressure gradient available from LES, which corresponds to the pressure gradient horizontally filtered to the size of the LES grid, denoted by  $\nabla_h \tilde{p}$ , where  $\tilde{p} = p_{\text{LES}}$  at  $y = \Delta$ . We decompose it according to these three contributions:

$$\nabla_h \tilde{p} = \nabla_h P + \nabla_h \bar{p}' + \nabla_h \tilde{p}'' = \nabla_h \bar{p} + \nabla_h \tilde{p}'', \quad (4.1)$$

where  $\nabla_h \bar{p} = \nabla_h P + \nabla_h \bar{p}'$ .

The “fully-equilibrium pressure gradient”,  $\nabla_h P$  is to be used in the fitting function to model the turbulent stress at  $y = \Delta$ . It is obtained by temporal filtering  $\nabla_h \tilde{p}$  at a long time scale  $n T_s$  where  $n$  is some constant sufficiently greater than one and  $T_s$  is the relaxation time scale of the LaRTE model. We thus write

$$\nabla_h P = \nabla_h \langle \tilde{p} \rangle_{nT_s}, \quad (4.2)$$

where the brackets indicate one-sided exponential time filtering and the subscript denotes the corresponding filtering time-scale. The rationale for this choice is that the equilibrium time scale should be greater than the quasi-equilibrium time scale,  $T_s$ , such that only very slow pressure changes are included in the fitted full-equilibrium model. We chose  $n = 3$  as a practical compromise that works well in applications to be shown later, and results appear to be quite insensitive to this choice.

The laminar Stokes layer that develops near the wall is caused by the high-frequency components (fastest changing) pressure gradient fluctuations. Therefore we define the non-equilibrium pressure gradient input to be a high-pass temporally filtered version of the pressure gradient. This is achieved in practice by subtracting from the LES pressure gradient another low-pass filtered signal, but low-pass filtered at a high frequency. Specifically, we write

$$\nabla_h \tilde{p}'' = \nabla_h \tilde{p} - \nabla_h \langle \tilde{p} \rangle_{t_v}, \quad (4.3)$$

where  $\langle \cdot \rangle_{t_v}$  represents a temporal low-pass filter at time scale  $t_v$ . For  $t_v$ , the appropriate filtering time scale should be the diffusion time from the wall to the edge of the Stokes layer ( $y = l_s$ ). We define this time scale to be  $t_v \equiv l_s^2 / \nu$ . Then rewriting the Stokes layer thickness in inner units, the time scale becomes

$$t_v = \frac{(l_s^+)^2 \nu}{u_\tau^2}. \quad (4.4)$$

The Stokes layer is assumed to be confined to the viscous sublayer, therefore as an approximation we let  $l_s^+ \approx 12$  and  $u_\tau$  is obtained from the LaRTE model.

With  $\nabla_h P$  and  $\nabla_h \tilde{p}''$  so determined, the input to the LaRTE transport

equation is the “band-pass filtered” version of the pressure gradient equal to

$$\nabla_h \bar{p}' = \nabla_h \langle \tilde{p} \rangle_{t_v} - \nabla_h \langle \tilde{p} \rangle_{3T_s}, \quad (4.5)$$

recalling that  $\tilde{p} = p_{\text{LES}}$  is the pressure available from LES at the first wall model point away from the wall.

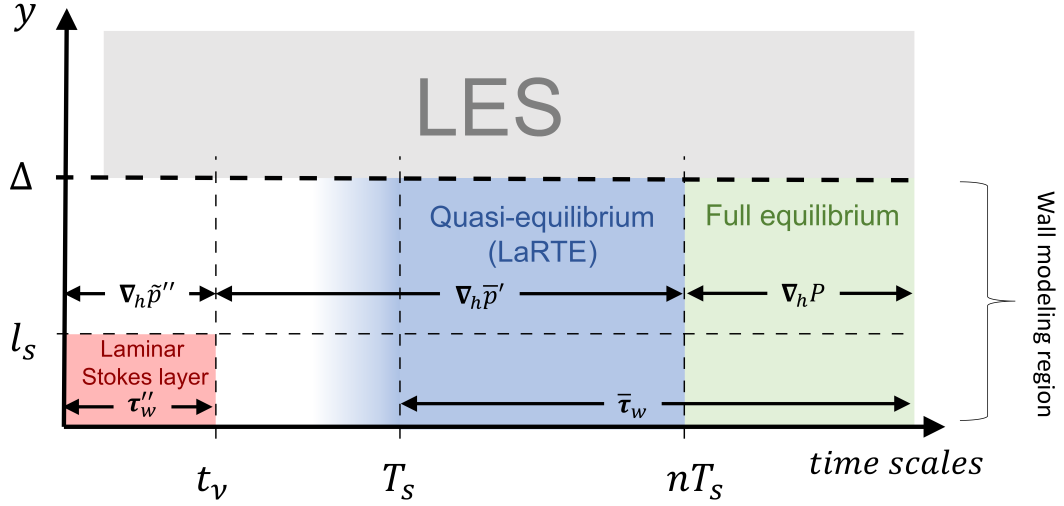
#### 4.1.2 LaRTE+lamNEQ length and time scales

Figure 4.1 shows the different time scales and wall distances considered for the wall modeling region beneath  $y = \Delta$ . The laminar Stokes layer is confined to the fastest time scale,  $t_v$ , and smallest wall distance,  $l_s$ , considered. The quasi-equilibrium and full equilibrium regions on the other hand, correspond with the the largest time scales considered ( $T_s$  and  $nT_s$ , respectively). Note that the LaRTE model has some high frequency content coming from  $\nabla_h \bar{p}'$  and  $\bar{\tau}_\Delta$ , thus the blue region extends somewhat further left than  $T_s$ . The remaining region left in white corresponds to the turbulent portion in the wall-modeled region, below  $y = \Delta$ , at scales faster than  $T_s$  but slower than the viscous time-scale  $t_v$ . The response of turbulence in this region (e.g. reduction of turbulent stresses due to scrambling) requires separate modeling not yet included in the present chapter (but introduced later in chapter 5).

The final wall stress for the LaRTE+lamNEQ wall model is then simply the superposition between these two components

$$\boldsymbol{\tau}_w = \bar{\boldsymbol{\tau}}_w + \boldsymbol{\tau}_w'' \quad (4.6)$$

where  $\bar{\boldsymbol{\tau}}_w \equiv u_\tau \boldsymbol{u}_\tau$  is the LaRTE wall stress governed by equation 2.32 (and



**Figure 4.1:** Schematic of the various time scales and wall-normal distances considered for modeling. Different colored regions identify the corresponding wall modeling components.

numerically evaluated according to equation 2.34) and  $\tau''_w$  is the lamNEQ wall stress governed by equation 3.5 (and numerically evaluated according to equation 3.11). The superposition of stresses is allowed due to the separation of time scales between the two models, as seen in figure 4.1. The rest of this chapter uses equation 4.6 to provide the wall stress boundary condition for the WMLES (except of course when using the EQWM to compare models).

## 4.2 Statistically stationary channel flow

First, the LaRTE+lamNEQ wall model is implemented in a simulation of statistically steady state channel flow at various Reynolds numbers. This is a flow in which the traditional equilibrium wall model typically provides good results. The objective is thus mainly to ensure that similarly good results are obtained using the new model as well as to document its various features,

such as typical orders of magnitudes of the terms appearing in the Lagrangian relaxation transport equation for the friction-velocity vector. Simulations use LESGO, an open-source, parallel, mixed pseudo-spectral and centered finite difference LES code available on Github (LESGO, 2021). The Lagrangian scale-dependent dynamic subgrid stress model (Bou-Zeid et al., 2005) is used in the bulk of the flow. The near-wall region is modeled using the new wall models proposed here: the LaRTE model governed by equation 2.25 (with closure and simplifications according to equation 2.32) and the laminar non-equilibrium model governed by equation 3.5. A wall stress boundary condition is applied consisting of the superposition between the two models (i.e.  $\tilde{\tau}_w = \bar{\tau}_w + \tau''_w$ ).

First, simulations are performed with friction Reynolds numbers based on the half channel height of  $Re_\tau = 1,000$  and  $5,200$ . The domain size, number of grid points, and grid size are  $(L_x, L_y, L_z)/h = (8\pi, 2, 3\pi)$ ,  $(N_x, N_y, N_z) = (128, 30, 48)$ , and  $(\Delta_x, \Delta_y, \Delta_z)/h = (0.196, 0.067, 0.196)$ , respectively. In inner units the grid size for  $Re_\tau = 1,000$  and  $5,200$  are  $(\Delta_x^+, \Delta_y^+, \Delta_z^+) = (196, 67, 196)$  and  $(\Delta_x^+, \Delta_y^+, \Delta_z^+) = (1021, 347, 1021)$ , respectively. Several additional simulations are performed at even higher Reynolds numbers ( $Re_\tau = \{0.2, 1, 5\} \times 10^5$ ) using the same number of grid points in order to ensure applicability at arbitrarily high Reynolds numbers. As can be seen these are very coarse WMLES, very different from the much finer resolutions required for WRLES.

In LESGO the wall model takes information from the first grid point away from the wall (i.e.  $\Delta = \Delta_y/2$ ). The wall model heights for all friction Reynolds numbers considered are summarized in table 4.1. These wall-model heights lie within the log-layer. The proposed new wall model is applied using the

$Re_\tau$	$\Delta^+$
$1.0 \times 10^3$	33
$5.2 \times 10^3$	173
$2.0 \times 10^4$	667
$1.0 \times 10^5$	3333
$5.0 \times 10^5$	16667
$3.17 \times 10^3$	106

**Table 4.1:** Wall model height in inner units  $\Delta^+$  for all friction Reynolds numbers simulated.  $Re_\tau = 3170$  corresponds with the steady state friction Reynolds number long after the application of the spanwise pressure gradient presented in §4.3.

LES data at  $y = \Delta$ . A “ $2\Delta$  spatial filter”, like that used in Bou-Zeid et al. (2005), is applied to the LES velocity at  $y = \Delta$  which is provided as the velocity input to equation 2.29 to model the turbulent stress at that position. This is primarily done to reduce log-layer mismatch (X. I. A. Yang et al., 2017) without causing an excessively sluggish response in the wall stress which would occur if the velocity was time filtered instead. The pressure gradient, on the other hand, is not spatially filtered but instead is temporally filtered with the single-sided exponential filter with the decomposition and filtering time scales described in §4.1.1.

Additional simulations are carried out using the traditional equilibrium wall model (without pressure gradient effects) in order to separate wall modeling dependencies from other dependencies such as grid resolution, SGS modeling, or the numerical discretizations used in the code. The equilibrium wall model used here computes the wall stress using the fitting function  $Re_{\tau\Delta}^{\text{fit}}(Re_\Delta)$  from Meneveau (2020) which is also summarized in algorithm 1 presented in §9.1. Then the wall stress vector is computed using  $\boldsymbol{\tau}_w = (\nu\Delta^{-1}Re_{\tau\Delta}^{\text{fit}})^2 \hat{\mathbf{e}}_u$  with  $\hat{\mathbf{e}}_u = \mathbf{U}_{\text{LES}} / |\mathbf{U}_{\text{LES}}|$ .

First we show mean velocity profiles for the five Reynolds numbers tested (figure 4.2) and mean Reynolds stresses for  $Re_\tau = 1,000$  and  $Re_\tau = 5,200$  (figure 4.3). For the two lowest Reynolds numbers, the WMLES using the new wall model, with combined LaRTE and laminar non-equilibrium parts, is compared with the DNS of M. Lee and Moser (2015) and the WMLES using the equilibrium wall model. The equilibrium wall model results are nearly indistinguishable from the new wall model results. All velocity profiles follow the expected law-of-the-wall but with a slight log-layer undershoot for  $Re_\tau = 1,000$  and an overshoot of the profile in the wake-region at the center of the channel. The LES Reynolds stresses generally follow the same trends as the DNS but with an overpredicted spanwise variance and underpredicted streamwise variance in the near wall region. Similar trends have been obtained in WMLES using different codes and SGS models (X. Yang et al., 2015), and are likely attributable to simulation details (i.e. grid resolution or SGS modeling) other than the wall model. The agreement between the two WMLES with completely different wall models further supports this claim. Wang et al. (2020) showed the effect of different choices in SGS modeling, wall modeling, and grid resolution on various turbulence statistics. Their primary finding is that various one-point statistics in the outer region are not significantly affected by the wall model, but sensitive to the SGS model. As shown in the recent wall-model independent analysis by Lozano-Durán and Bae (2019), LES accuracy in the outer region of wall bounded flows is highly sensitive to details of the ratio of grid resolution compared to outer length-scale (rather than Reynolds number). We therefore conclude that the wall model is unlikely to be the cause for the observed level of differences between the LES and

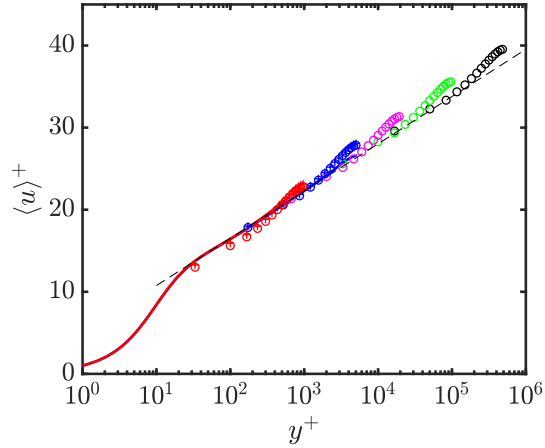


**Figure 4.2:** Open circles: mean velocity profiles from WMLES using the LaRTE and non-equilibrium wall model for  $Re_\tau = 1,000$  (red), 5,200 (blue), 20,000 (magenta),  $10^5$  (green) and  $5 \times 10^5$  (black). Plus signs: mean velocity profiles for WMLES using the equilibrium wall model at  $Re_\tau = 1,000$  (red) and 5,200 (blue). Lines: DNS from M. Lee and Moser (2015) at  $Re_\tau = 1,000$  (red line), 5,200 (blue line), and log-law  $\langle u \rangle^+ = \ln(y^+)/0.4 + 5.0$  (dashed line).

DNS statistics and find that the new wall model, when applied to a standard equilibrium channel flow, performs similarly well as the classic equilibrium wall model.

Next, we illustrate by means of time signals at a representative point on the wall the various terms in equation 2.25 that is being solved at each point following the implementation described in §2.5. In figure 4.4 we show, in cyan, signals of the input stress vector  $\bar{\tau}_\Delta$  at  $y = \Delta$ , evaluated using the fitted equilibrium model in equation 2.29. The stress is divided by  $u_\tau$ , the magnitude of the obtained friction velocity. The gray line shows the same, but with the horizontal pressure gradient added, the quantity towards which the friction velocity vector  $u_\tau$  relaxes, with relaxation time scale  $T_s$ . The cyan and gray lines are generally close, showing that the effect of the pressure gradient is smaller but not negligible compared to the imposed turbulent stress. The

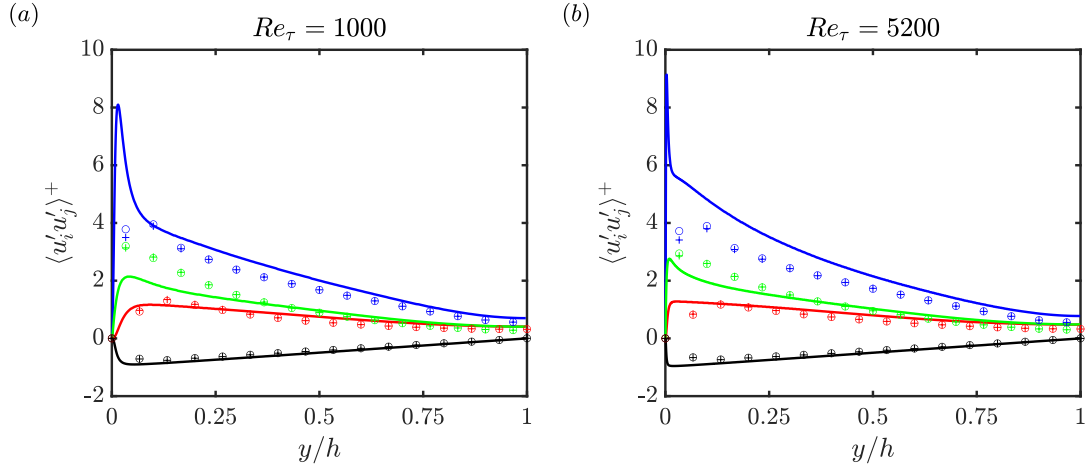


**Figure 4.3:** Mean Reynolds stresses for (a)  $Re_\tau = 1,000$  and (b)  $Re_\tau = 5,200$ . Colors correspond with  $\langle u'u' \rangle$  (blue),  $\langle v'v' \rangle$  (red),  $\langle w'w' \rangle$  (green), and  $\langle u'v' \rangle$  (black). Open circles: WMLES using the new wall model with LaRTE and laminar non-equilibrium parts. Plus signs: WMLES using the equilibrium wall model. Lines: DNS from M. Lee and Moser (2015).

blue line in figure 4.4 shows the friction velocity resulting from the LaRTE solution. In this flow, the characteristic mean value of  $T_s$  can be estimated as  $T_s \langle u_\tau \rangle / h = (\Delta/h) f(\Delta^+) = (1/30) f(1000/30) \approx 0.45$ . As is evident, major fluctuations of  $u_\tau$  occurring at time scales smaller than  $T_s$  have been filtered out almost entirely. Only low frequency variability is left, internally consistent with the notion of quasi-equilibrium that underlies the assumption of the profile scaling in inner units. Note that if an equilibrium model were used the wall stress would fluctuate at levels comparable with the cyan signal.

Next, signals of the individual terms in equation 2.25 are presented in figure 4.5. The Eulerian time derivative shown in black displays some anti-correlated trend with the advective term shown in red. This is expected for transported quantities, and leads to smaller magnitudes of the Lagrangian time derivative as compared to the Eulerian time derivative. The blue line

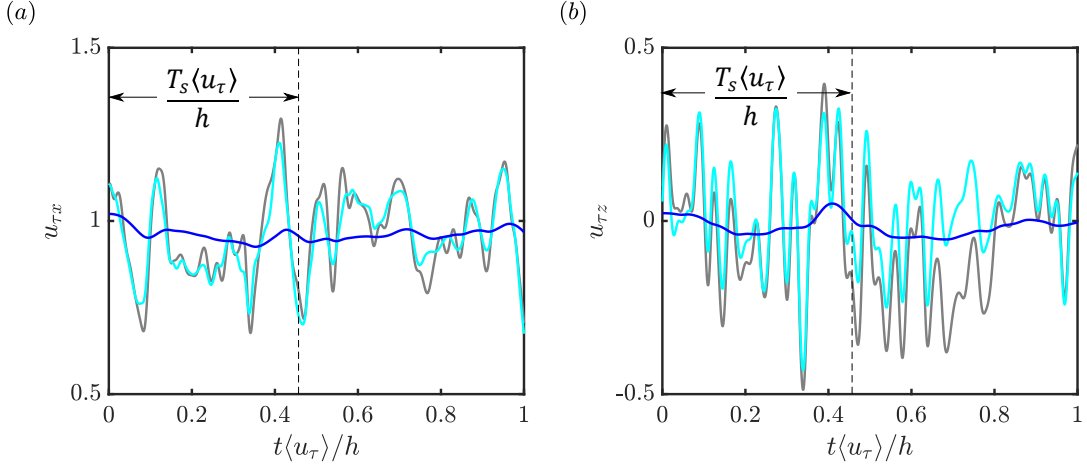


**Figure 4.4:** Time signals of relevant terms in the LaRTE model at some arbitrary representative point at the wall from LES or channel flow at  $Re_\tau=1,000$  and  $\Delta/h = 1/30$ . Time signals shown are for the terms  $\bar{\tau}_\Delta/u_\tau$  (cyan),  $(-\Delta \nabla_h \bar{p}/\rho + \bar{\tau}_\Delta)/u_\tau$  (black) and  $u_\tau$  (blue). Panel (a) shows the  $x$ -component and (b) the  $z$ -component terms. The vertical dashed line shows the relaxation time scale  $T_s \langle u_\tau \rangle / h \approx 0.45$ .

shows the entire relaxation towards equilibrium term which essentially drives the rate of change of the friction velocity vector. The non-standard term with the Eulerian time derivative of the orientation vector  $s$  is negligible in the  $x$ -direction while it shows some contribution in the spanwise direction.

Wall stress contours for  $Re_\tau = 1,000$  are presented in figure 4.6 for a single snapshot of one of the LES realizations. As can be seen from the top row, the LaRTE quasi-equilibrium stress shows elongated structures that extend over relatively long distances downstream. The fluctuations occur, as expected around a value of  $\bar{\tau}_{wx} \approx 1$ . The spanwise stress component  $\bar{\tau}_{wz}$  has zero mean and fluctuations that appear to occur at smaller scales, generally consistent with elongated structures that display larger variability in the transverse direction than in the streamwise direction. The middle row shows the contribution from the laminar non-equilibrium portion of the

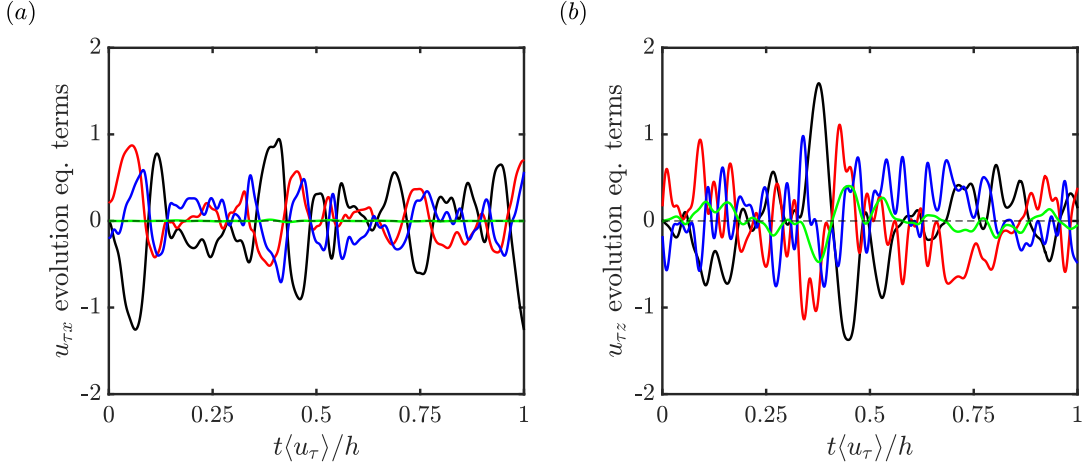


**Figure 4.5:** Time signals of terms in the evolution equation for  $u_\tau$ , equation 2.25 at some arbitrary representative point at the wall from LES or channel flow at  $Re_\tau=1,000$  and  $\Delta/h = 1/30$ . Time signals shown are for the terms  $\partial u_\tau / \partial t$  (—),  $V_\tau \cdot \nabla_h u_\tau$  (—),  $-T_s^{-1} [u_\tau^{-1} (-\Delta \nabla_h \bar{p} / \rho + \bar{\tau}_\Delta) - u_\tau]$  (—), and  $-u_\tau (\delta_\Delta^*/\Delta) \partial \bar{s} / \partial t$  (—).

model. In spite of the backward time integration that should smooth signals to some degree, these fields display much smaller-scale fluctuations. These reflect fluctuations in pressure gradients in both streamwise and spanwise directions that tend to occur at scales similar to the LES grid scale. The bottom row shows contours of the sum of both contributions, combining the streamwise elongated structure and the smaller-scale fluctuations from the laminar non-equilibrium part of the model.

It is of interest to explore further the qualitative differences between an Eulerian and a Lagrangian time derivative in applying the LaRTE model. To this effect, we select some time during the LES using the LaRTE approach and denote that time as  $t = 0$ . Then we continue the LES using the Lagrangian version of LaRTE and perform another simulation that continues using the Eulerian version, i.e. simply omitting the advective derivative  $V_\tau \cdot \nabla_h u_\tau$ .

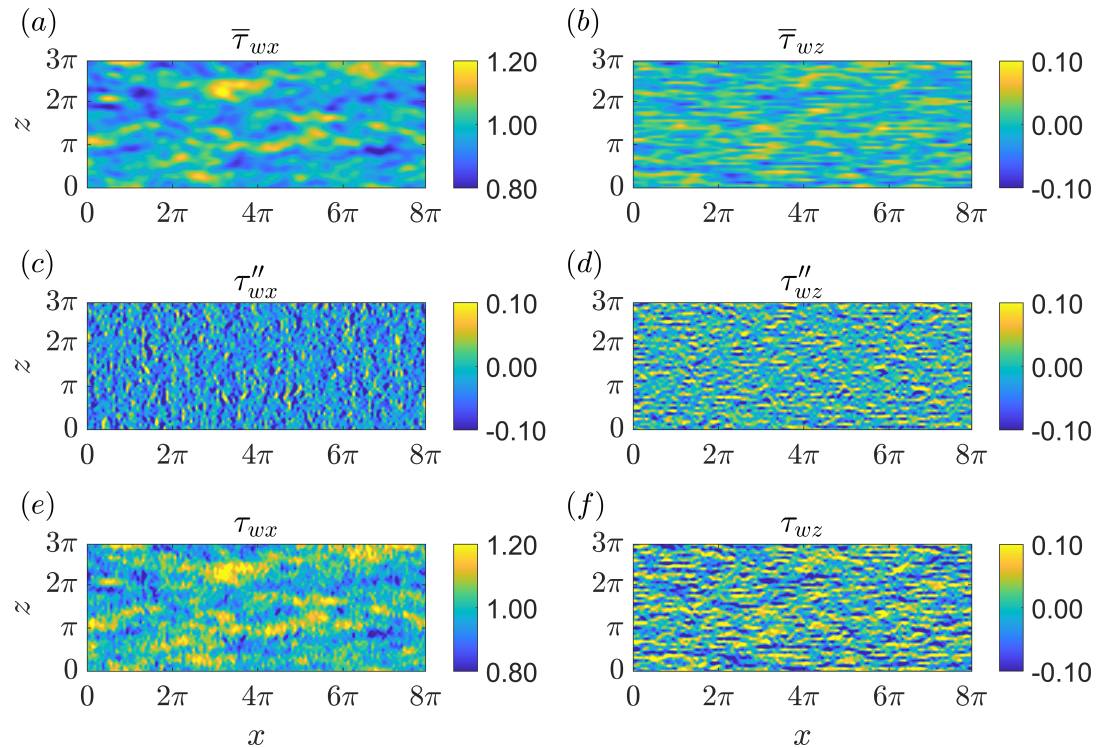


**Figure 4.6:** Snapshots of the wall stress for  $Re_\tau = 1,000$ . (a,b) shows the quasi-equilibrium stress from the LaRTE model for both streamwise and spanwise components, (c,d) shows the laminar layer non-equilibrium portion, and (e,f) shows the total stress ( $\tau_w = \bar{\tau}_w + \tau''_w$ ).

from the evolution equation. Figure 4.7 shows the results in the form of contour plots of the x-component of the modeled wall stress,  $\bar{\tau}_{wx} = u_\tau u_{\tau x}$ . By construction they both agree at  $t = 0$  but begin to differ at later times, significantly. As confirmed by examining animations, the Eulerian version “pins” fluctuations at the wall while perturbations from imposed stress at  $y = \Delta$  travel downstream. The time filtering implicit in the relaxation equation then “smears” and elongates the structures excessively in the streamwise direction. In the Lagrangian version shown to the left, perturbations are allowed to travel downstream, including the time-filtered versions that therefore maintain their more compact integrity as time progresses. We conclude that the Lagrangian version appears more physically reasonable. We remark, however, that we have no “true” distribution (e.g. from DNS) to compare with, since we would need to evaluate either Eulerian and Lagrangian time averaging from the DNS, and similar differences would be obtained, without necessarily indicating which one is “better” or “true”. Having seen significant differences in predicted stress distribution between Eulerian and Lagrangian versions of the model, and the latter being directly motivated by the underlying integral momentum equation, we continue using the Lagrangian version for the rest of this paper.

More quantitative characterization of the stress fluctuations is provided by the probability density function (PDF) of each component of the wall stress. The PDFs obtained from the  $Re_\tau = 1,000$  and 5,200 could be compared to filtered DNS data at the same Reynolds numbers. LES data were collected over five separate uncorrelated simulations to obtain better convergence of

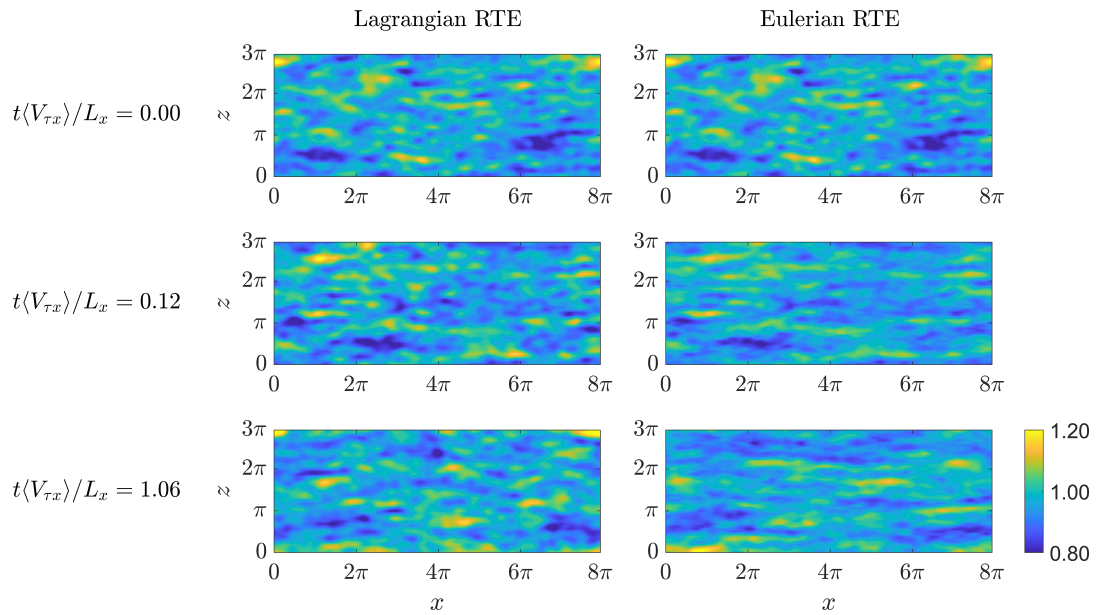


**Figure 4.7:** Streamwise wall stress,  $\bar{\tau}_{wx}$ , contours for several time instances for  $Re_\tau = 1,000$ . Compares Lagrangian RTE (left column) with Eulerian RTE (right column) where the advection term is excluded. Both models are initialized with the same data as shown in the top row. Time is non-dimensionalized with  $\langle V_{\tau x} \rangle \approx 7.93 \langle u_\tau \rangle$  and  $L_x = 8\pi h$ .

statistics. DNS data were obtained from a public database (JHTDB, 2021) and the instantaneous local wall stress was spatially filtered horizontally using a Gaussian filter at the same scale as the LES grid. The PDFs are shown in figure 4.8. The PDF from the filtered DNS (dashed line) peaks around  $\bar{\tau}_{wx} = 1$  and  $\bar{\tau}_{wz} = 0$ . The quasi-equilibrium (LaRTE) part of the model (blue lines) peaks at the same expected values, but display significantly narrower distributions owing to the time filtering that reduces the fluctuations consistent with the notion of quasi-equilibrium. The laminar Stokes layer model that only models the fast laminar response in the viscous sublayer provides additional fluctuations. However, for the streamwise directions, these fluctuations are of smaller magnitude than those for the filtered DNS. This shows that the model is still missing significant parts of the streamwise stress fluctuations. Additional modeling is needed to account for these additional fluctuations that belong neither to the quasi-equilibrium nor the rapid laminar sublayer response parts of the dynamics. This motivated the development of a turbulent non-equilibrium model presented later in §5.1 of this dissertation. We note that in the spanwise direction, the PDFs agree better, in fact slightly overestimating the fluctuations for the  $Re_\tau = 1,000$  case but predicting the spanwise fluctuations PDF for the  $Re_\tau = 5,200$  case very well. From figure 4.8 we can also see that as the Reynolds number increases, the PDFs of the non-equilibrium components (red curves) narrow. As can be expected from equation 3.5 that shows the laminar non-equilibrium portion of the stress to be proportional to  $\nu^{1/2}$ , the stress contribution from the laminar Stokes layer near the wall in fact vanishes in the limit of infinite Reynolds number, unlike fluctuations expected to occur due to turbulence in the wall layer. These

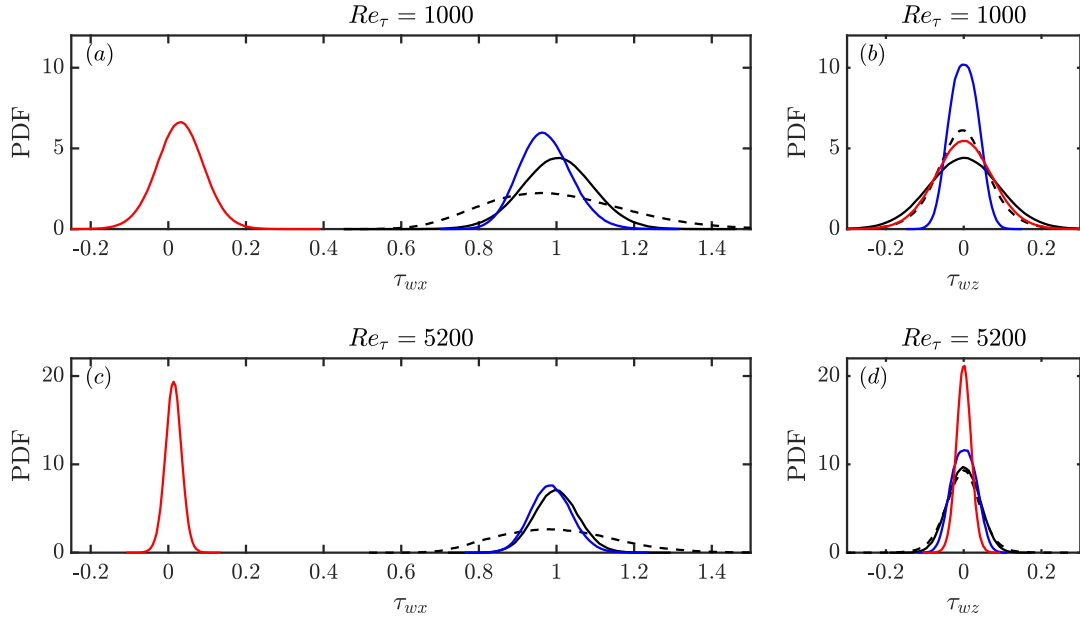


**Figure 4.8:** PDFs for  $\tau_{wx}$  and  $\tau_{wz}$ ; (a, b)  $Re_\tau = 1000$ ; (c, d)  $Re_\tau = 5200$ . The PDF curves correspond with the filtered DNS (---), the LaRTE model (—), the non-equilibrium model (—), and the composite model (LaRTE + non-equilibrium) (—). DNS data obtained from the Johns Hopkins Turbulence Database Graham et al.; JHTDB (2016, 2021). The DNS PDFs are obtained from the Gaussian filtered wall stress where the filtering size is the same as the LES mesh size in the horizontal directions.

contributions are not included in the model version used in this section but will be introduced far later in additional developments presented in §5.1.

We also note that when using the single-sided exponential filter with a fluctuating and short filtering time scale such as  $t_v$ , some undesirable trends can be obtained such as that the mean (in space or time) of a variable may not be exactly equal to the mean of the filtered variable. Because of this feature, the PDF of the non-equilibrium model has a non-zero mean as seen in figure 4.8. This should be kept in mind whenever using the temporal exponential filter with a time-dependent averaging time-scale.

### 4.3 Channel flow with a sudden spanwise pressure gradient (SSPG)

Next we discuss a highly non-equilibrium test case following the work of Lozano-Durán et al. (2020). A large spanwise pressure gradient,  $\partial p_\infty / \partial z$ , is applied to a statistically steady turbulent channel base flow after  $t = 0$ . Particularly, we follow the case presented in their wall modeling results section in which the initial flow ( $t = 0$ ) is standard channel flow with  $Re_\tau = 1,000$  after which ( $t > 0$ ) a spanwise pressure gradient is suddenly applied with strength  $\partial p_\infty / \partial z = 10 \partial p_\infty / \partial x = 10 \rho u_{\tau 0}^2 / h$  (where  $u_{\tau 0}$  is the mean friction velocity of the initial condition and  $h$  the channel half-height). The flow is initialized with the results from §4.2. The results presented in this section use the same code with the same mesh, subgrid scale and wall model, etc.. We should note that dynamic time stepping is used in order to maintain a constant CFL. The time step size stays within the range  $1 \times 10^{-4} \leq \delta t u_{\tau 0} / h \leq 4 \times 10^{-4}$  from steady state to long after the application of the SSPG.

First, in figure 4.9(a, b) we show pressure gradient signals at an arbitrary point corresponding to the LES pressure gradient input  $\partial \tilde{p} / \partial z$  (black line), and its three constituent parts consistent with the discussion of §4.1.1: the long-time average pressure gradient  $\partial P / \partial z$  (green line) entering into the full equilibrium fitted model, the band-pass filtered fluctuating pressure gradient  $\partial \bar{p}' / \partial z$  (blue line) that enters the quasi-equilibrium LaRTE equation, and the rapid non-equilibrium  $\partial \tilde{p}'' / \partial z$  (red line) that affects mostly the viscous sublayer if sufficiently fast. As is evident in figure 4.9(a),  $\partial \tilde{p}'' / \partial z$  captures the majority of the LES pressure gradient fluctuations,  $\partial P / \partial z$  captures only the

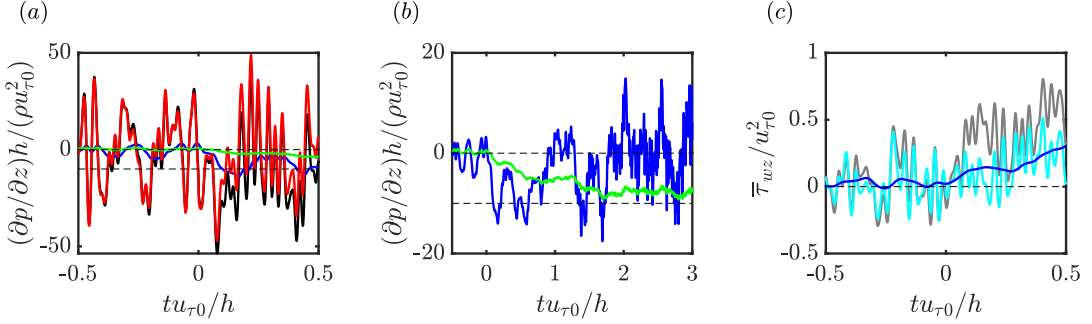


**Figure 4.9:** Time signals at some arbitrary representative horizontal point for (a, b) spanwise pressure gradient components and (c) spanwise quantities in the LaRTE model relevant for  $\bar{\tau}_{wz}$ . (a, b): LES pressure gradient  $\partial\tilde{p}/\partial z$  (—), non-equilibrium pressure gradient  $\partial p''/\partial z$  (—), band-pass filtered pressure gradient  $\partial\bar{p}'/\partial z$  (—), and equilibrium pressure gradient  $\partial P/\partial z$  (—) all normalized with  $h/(\rho u_{\tau0}^2)$ . (c): quasi-equilibrium spanwise wall stress  $\bar{\tau}_{wz}$  (—),  $-\Delta(\partial\bar{p}/\partial z)/\rho + \bar{\tau}_{\Delta z}$  (—), and  $\bar{\tau}_{\Delta z}$  (—) all normalized with  $u_{\tau0}^2$ . Thin dashed horizontal lines indicate steady-state values before and after the SSPG.

“equilibrium” or very slowly varying pressure gradient, and  $\partial\bar{p}'/\partial z$  captures any remaining fluctuations. Figure 4.9(b) shows more clearly that at the onset of the SSPG ( $t=0$ ) the equilibrium pressure gradient slowly relaxes to its new steady state value and that the strength of the quasi-equilibrium pressure gradient fluctuations grows. Both of these pressure gradient signals are inputs to the LaRTE model whose wall stress and relevant relaxation terms are shown in figure 4.9(c). Here we can see the importance of the quasi-equilibrium pressure gradient in the LaRTE model grows upon application of the SSPG.

Next we present the plane-averaged wall stress response to the SSPG. Figure 4.10 shows the spanwise wall stress after the SSPG has been applied compared with the DNS of Lozano-Durán et al. (2020). Panel (a) shows the wall stress decomposition after the initial transient and (b) shows the wall stress behavior long after the SSPG was applied. The trends are in agreement with expectations. For a brief time ( $0 \leq tu_{\tau0}/h \leq 0.05$ ) the wall stress follows

the laminar solution closely, during which the non-equilibrium component is dominant compared with the quasi-equilibrium component. Afterwards the balance is reversed. Note that the LaRTE model responds faster than the relaxation time scale which is  $T_s u_{\tau 0} / h \approx 0.45$ . This is due to the inclusion of the band-pass filtered pressure gradient,  $\nabla_h \bar{p}'$ , in the LaRTE model. Without this pressure gradient,  $\bar{\tau}_{wz}$  is delayed by a time of order  $T_s$ . On the contrary, if no high-pass filtering is done,  $\nabla_h p'' = 0$ ,  $\bar{\tau}_{wz}$  is nearly linear initially and unable to capture the  $\sqrt{t}$  trend corresponding to the laminar Stokes layer. Therefore, low-pass filtering is needed to prevent the overly sluggish behavior of the quasi-equilibrium model and high-pass filtering plus the inclusion of the laminar non-equilibrium model is needed to get the correct  $\sqrt{t}$  behavior initially. Finally, note the new wall model has a closer agreement to the DNS than the equilibrium wall model which gives a linear response to the SSPG. We can attribute the faster wall stress response to the laminar non-equilibrium model whereas the quasi-equilibrium model has a slow initial response which approaches the equilibrium wall model curve long after the SSPG. We should also note that the equilibrium wall model performance shown here is closer to the DNS than that reported in Lozano-Durán et al. (2020) for their implementation of the equilibrium wall model. We have verified that the difference is because the wall model height used here is smaller than that of Lozano-Durán et al. (2020) which leads to a faster wall stress response.

The streamwise wall stress response to the SSPG is shown in figure 4.11. As can be seen, the wall model is unable to capture the slight initial decrease in  $\tau_{wx}$

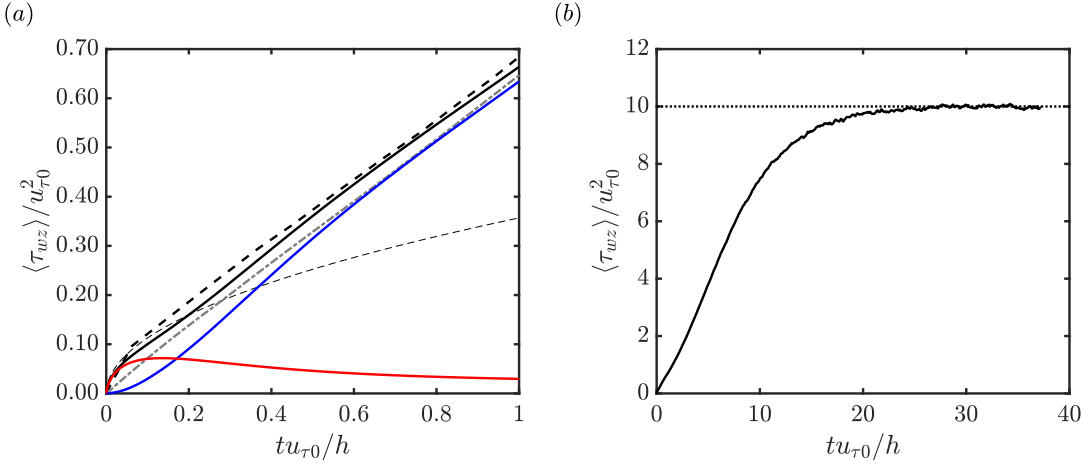


**Figure 4.10:** Spanwise wall stress after sudden spanwise pressure gradient (a) after a short period and (b) after a long period. (a): DNS from Lozano-Durán et al. (2020) (---), composite wall stress  $\langle \bar{\tau}_{wz} \rangle + \langle \tau''_{wz} \rangle$  (—), quasi-equilibrium wall stress  $\langle \bar{\tau}_{wz} \rangle$  (blue), non-equilibrium wall stress  $\langle \tau''_{wz} \rangle$  (red), equilibrium wall model (···), and laminar solution for Stokes's first problem (····). Dotted line in (b) indicates the steady state value after the SSPG. Angled brackets indicates ensemble averaging over the horizontal plane and five separate simulations for (a) and ensemble averaging over the horizontal plane for (b).  $Re_{\tau 0} = 1000$  and  $\partial p_{\infty} / \partial z = 10 \partial p_{\infty} / \partial x$  for  $t > 0$ .

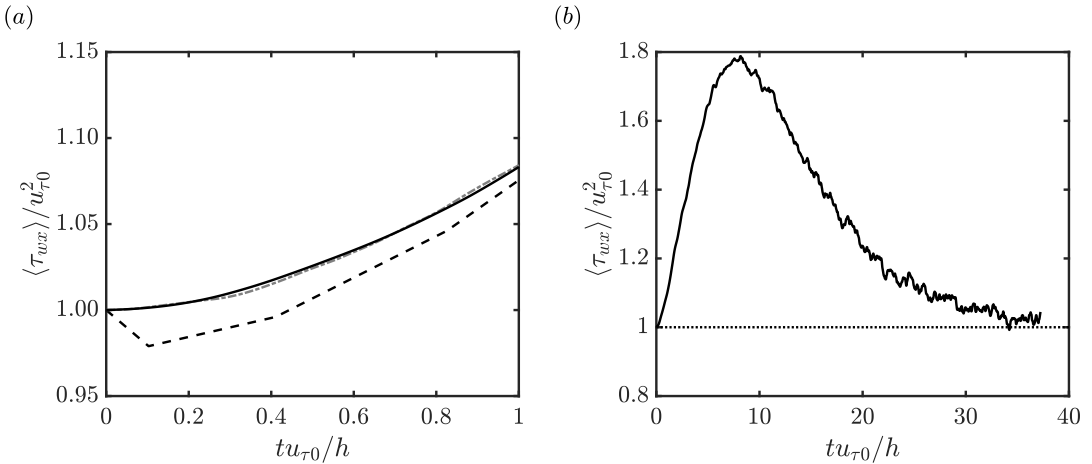


**Figure 4.11:** Streamwise wall stress after sudden spanwise pressure gradient (a) after a short period and (b) after a long period. (a): DNS from Lozano-Durán et al. (2020) (---), composite wall stress  $\langle \bar{\tau}_{wx} \rangle + \langle \tau''_{wx} \rangle$  (—), and equilibrium wall model (···). Dotted line in (b) indicates the steady state value after the SSPG. Angled brackets indicates ensemble averaging over the horizontal plane and five separate simulations for (a) and ensemble averaging over the horizontal plane for (b).  $Re_{\tau 0} = 1000$  and  $\partial p_{\infty} / \partial z = 10 \partial p_{\infty} / \partial x$  for  $t > 0$ .

due to a complex three-dimensional mechanism discussed in Lozano-Durán et al. (2020). The reason is that the scrambling of momentum transporting turbulent structures due to the sudden spanwise pressure gradient is not included in any part of the present model. Significantly more sophisticated modeling of the eddy viscosity in the RANS model used to derive the LaRTE equation would be required. In this case, however, the difference is less than 1-2% of  $u_{\tau 0}$ . The model correctly relaxes towards the DNS trend for  $tu_{\tau 0}/h > 1$ . The increase in  $\tau_{wx}$  may be attributed to the increase in Reynolds number as the mean pressure gradient increases in magnitude even as its alignment rotates away from the x-axis. This behavior is “slow” and thus is expected to be captured well by the LaRTE model. This also means that the equilibrium wall model is able to capture this behavior well, as evident from the similarity between the equilibrium and quasi-equilibrium curves in figure 4.11. After a long time, the new equilibrium condition is reached in which the x-component of the pressure gradient must be balanced by the wall stress and thus the wall stress reduces back to unity as shown in figure 4.11(b).

Figure 4.12 shows mean spanwise velocity profiles after the SSPG for several different time instances. Generally, the LES agrees with the DNS for both wall models quite well. This is consistent with the results reported in Lozano-Durán et al. (2020) where all wall models considered produced good spanwise velocity profiles upon application of the SSPG. This is also consistent with the notion that one-point statistics are less sensitive to the wall model relative to other simulation parameters, as argued earlier in this section.

Figure 4.13 shows contours of fluctuations of the quasi-equilibrium stress

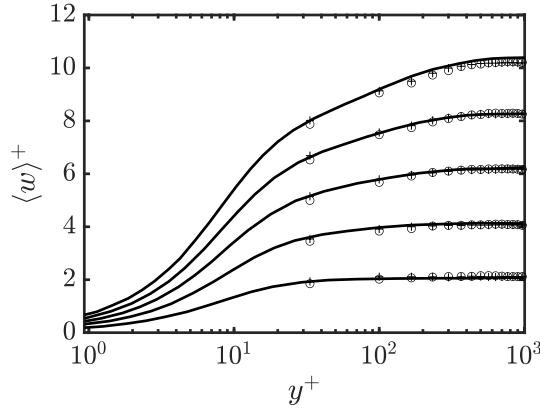


**Figure 4.12:** Mean spanwise velocity profiles at  $tu_{\tau_0}/h = 0.21, 0.405, 0.615, 0.825$ , and  $1.02$  from bottom to top. Open circles: WMLES with composite LaRTE and laminar non-equilibrium components. Plus signs: WMLES with the equilibrium wall model. Lines: DNS from Lozano-Durán et al. (2020).

$\bar{\tau}_w$ . Specifically we show contours of  $\bar{\tau}'_{ws} = \bar{\tau}_w \cdot \langle s \rangle - \langle \bar{\tau}_w \rangle \cdot \langle s \rangle$ , where  $\langle s \rangle$  is the plane averaged unit vector, i.e. in the direction of the mean LaRTE wall stress. The contours represent the wall stress fluctuations aligned with the plane-averaged mean quasi-equilibrium wall stress direction. As a reference, the dashed lines shown are aligned with the total wall stress and thus include the contributions from the laminar boundary layer developing due to the application of the SSPG. The application of the SSPG disrupts the orientation and shape of the structures as the mean flow rotates towards the  $z$  direction. At later times after the SSPG is applied, subfigures  $(b, d, f)$  show that the structures have had enough time to orient and advect themselves with the mean wall stress direction, albeit with a reduced size.

Figure 4.14 shows the evolution of the angle (with respect to the  $x$  axis) of the pressure gradients (dashed lines) and resulting plane averaged total (black line) and quasi-equilibrium (blue line) wall stress. As expected, the quasi-equilibrium component of the wall stress has a delayed and smoothed

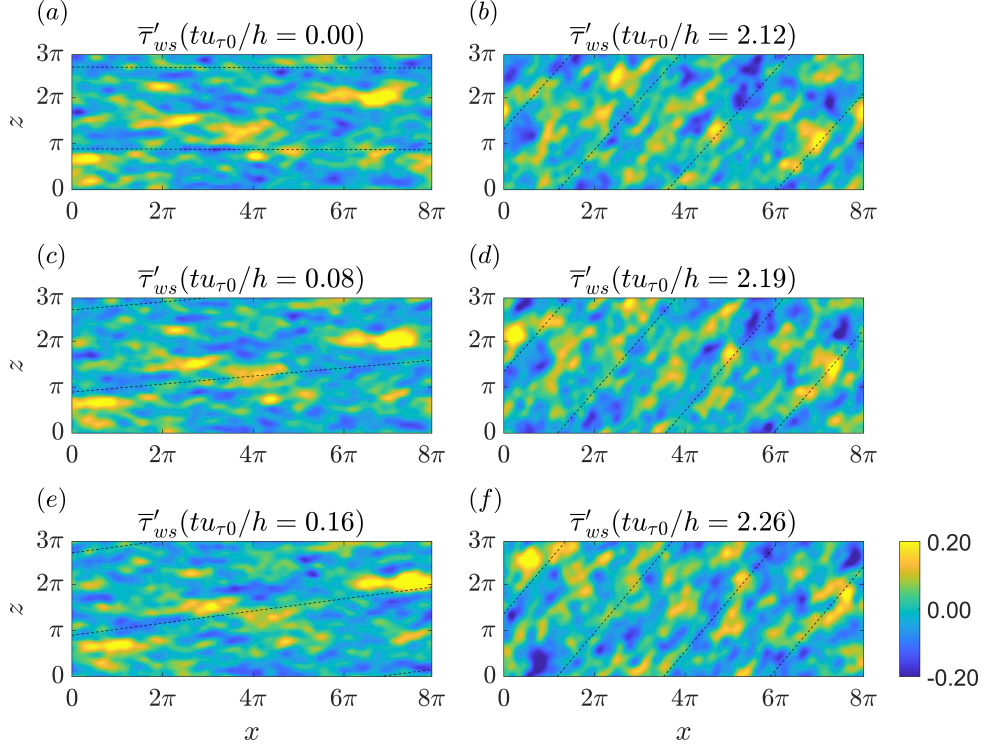


**Figure 4.13:** Contours of the quasi-equilibrium  $s$ -component wall stress ( $s$  introduced in chapter 2) with the plane-averaged mean subtracted,  $\bar{\tau}'_{ws}$ , for various times after the SSPG. (a, c, e): immediately after SSPG; (b, d, f): later times after SSPG. Dashed lines are aligned with the plane-averaged total wall stress angle (includes both quasi-equilibrium and non-equilibrium components).

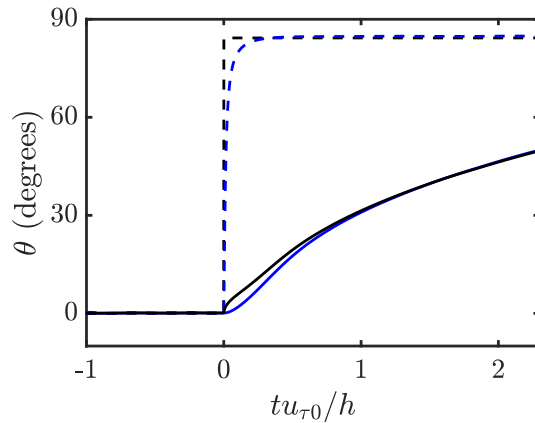


**Figure 4.14:** Plane-averaged pressure gradient and wall stress angles after the SSPG.  $\langle \nabla_h \bar{p} \rangle$  (---),  $\langle \nabla_h p_\infty \rangle$  (- - -),  $\langle \bar{\tau}_w \rangle$  (—),  $\langle \bar{\tau}_w \rangle + \langle \tau''_w \rangle$  (—) where angled brackets indicate plane averaging.

response to the SSPG, while at the initial transient the non-equilibrium component dominates the plane averaged wall stress response. After some adjustment time the quasi-equilibrium component becomes more dominant, again in establishing the trends of the plane averaged wall stress components such as its direction. At large times, the angle tends to the same angle as the net applied pressure gradient.

## 4.4 Summary

In chapter 2 we introduce the Lagrangian Relaxation Towards Equilibrium (LaRTE) wall model, representing quasi-equilibrium dynamics. The LaRTE model consists of an evolution equation for the friction velocity (and thus the wall stress) by using a method similar to that introduced in Chung and Pullin (2009) where the law of the wall is utilized to rewrite the unsteady term as  $\partial u_\tau / \partial t$ . Also similar to Chung and Pullin (2009) and X. Yang et al. (2015), the LaRTE model is based on the vertically integrated RANS-like thin boundary layer equations. Remarkably, it is found that generalization to include the advection terms leads to a Lagrangian form rather than an Eulerian one. Moreover, the right-hand side of this equation is in the form of a term describing relaxation towards the stress at the wall model height, with a relaxation time scale  $T_s$ . A-priori testing based on DNS channel flow data shows that the relaxation time scale is consistent, whereas use of shorter time scales would be inconsistent, with the assumption of quasi-equilibrium.

The proposed formalism allows for separate modeling of non-equilibrium

effects not captured by the LaRTE model. In chapter 3 we introduce a non-equilibrium wall model to capture quick transient pressure gradient effects. The approach is well suited for modeling the laminar Stokes layer observed in the literature for flows with a rapidly changing pressure gradient.

In chapter 4, the LaRTE plus laminar non-equilibrium (LaRTE+lamNEQ) model is tested for (a) simple channel flow with a constant pressure gradient and (b) the sudden spanwise pressure gradient test case introduced in Lozano-Durán et al. (2020). These two cases were selected in order to verify that the LaRTE model elements indeed exhibit quasi-equilibrium behaviour, develop intuition regarding the model performance, and examine its response in a case where the non-equilibrium effects are known to follow the Stokes laminar solution. Time signals, wall stress contour plots, and wall stress PDFs reveal interesting and useful physical insight as to how the model operates. For example, time signals of the LaRTE-predicted wall stress are consistent with the idea that the friction velocity relaxes towards its equilibrium value at the relaxation time scale. Wall stress contour plots show that the structures in the LaRTE model are rather large, of length on the order of or larger than the channel half-width. LaRTE thus implicitly averages out the turbulence leaving only large-scale fluctuations that are internally consistent with “quasi-equilibrium”, i.e. under conditions that are sufficiently averaged so that using the locally determined friction velocity one may assume the law of the wall to hold.

A comparison between Lagrangian versus Eulerian versions of the relaxation towards equilibrium model show the Lagrangian version tends to

advect wall stress structures whereas the Eulerian version tends to thin out and elongate structures in the streamwise direction. Wall stress PDFs show the distribution of wall stress fluctuations of each component and how the non-equilibrium model diminishes in importance as Reynolds number increases. Differences between PDFs from the wall model and filtered DNS show that additional ingredients will be required to fully capture the turbulent fluctuations in wall stress, especially in the streamwise direction. For the sudden spanwise pressure gradient test case, time signals of the plane-averaged mean spanwise and streamwise wall stress show the model is in good agreement with the DNS data of Lozano-Durán et al. (2020) and that long after the application of the SSPG the model approaches the correct steady state values.

In the LaRTE approach, closure for the total stress  $\bar{\tau}_\Delta$  at the wall-model height is required. Also, the pressure gradient decomposition into various time-scales involves some modeling choices. While a number of other options exist and could be explored, the corresponding choices used in this chapter were justified through physical interpretation and the model's ability to yield good results for the test cases considered here. In chapter 5 changes and additions to the model are made to further improve the wall model's performance, thus allowing it to handle even more complex flows.

In summary, the proposed LaRTE model represents a new framework for wall modeling. Specifically, the formal identification of quasi-equilibrium dynamics enables us to model the remainder non-equilibrium parts more rigorously, like the lamNEQ model introduced in chapter 3. The choice of model for the turbulence stress at the wall-model height, the pressure gradient

decompositions, completing the picture for the length and time scale schematic (the white region in figure 4.1), and testing the wall model for additional, more complex non-equilibrium flows will be covered in the following chapters.

# Chapter 5

## The multi-time-scale wall model (MTSWM)

### 5.1 Turbulent non-equilibrium

The wall model physics described so far capture the slow, quasi-equilibrium behavior from the LaRTE model (chapter 2) and the fast, laminar non-equilibrium behavior caused by fast changes in the pressure gradient (lamNEQ model, chapter 3). The wall stress PDFs from §4.2 (figure 4.8) show the wall stress fluctuations are significantly underpredicted by the LaRTE+lamNEQ model. The length and time scale schematic for the LaRTE+lamNEQ model (figure 4.1) shows that there is an empty, unmodeled region for turbulence operating at time scales between the laminar, viscous time scale  $t_v$  and the slow, LaRTE relaxation time scale,  $T_s$ . We posit that the turbulent velocity fluctuations operating between those time scales are directly responsible for the missing wall stress fluctuations in the PDFs. Motivated by this, in this section we now model the corresponding wall stress resulting from velocity fluctuations at the wall model height operating at these intermediate time scales. The LaRTE

model allows us to define this velocity fluctuation in a straightforward fashion. In the LaRTE model, the LES velocity  $\mathbf{U}_{LES}$  creates an applied stress at the wall model height,  $\bar{\tau}_\Delta$ , which in turn creates a wall stress response delayed (at a rate corresponding to the relaxation time scale,  $T_s$ ) due to fluid inertia in the layer between the wall and  $y = \Delta$ . The LaRTE model assumes this inertial fluid layer follows the law of the wall, thus the velocity associated with LaRTE response at the wall model height is  $u_\tau f(\Delta^+)$ . The velocity fluctuation can then be defined as

$$u'_\Delta = \bar{u}_\Delta - u_\tau f(\Delta^+) \quad (5.1)$$

where  $\bar{u}_\Delta$  in equation 5.1 is similar but not quite equal to  $\mathbf{U}_{LES}$ . It is in fact the LES velocity “corrected” to account for the velocity associated with the laminar Stokes layer. The LES velocity correction is an additional model ingredient, introduced later in §5.2, whose understanding is not necessary for the development of the model presented here.

The fluctuating velocity vector  $u'_\Delta$  (shown later by the thick green vector in figures 5.1 and 5.2) represents the turbulence that is left out and not included yet in the wall model. While this velocity can be computed during LES based on equation 5.1, what remains is to determine the contribution to the wall-stress from turbulent flow structures that are associated with the velocity fluctuation  $u'_\Delta$ . For this purpose, we invoke the attached eddy hypothesis of Townsend (1976) and that has been further refined in various more recent works (Marusic & Monty, 2019; Mathis et al., 2009; Smits et al., 2011). Based on the attached eddy hypothesis,  $u'_\Delta$  may be viewed as a turbulent velocity fluctuation caused by the large, wall-attached eddies of height on the order of

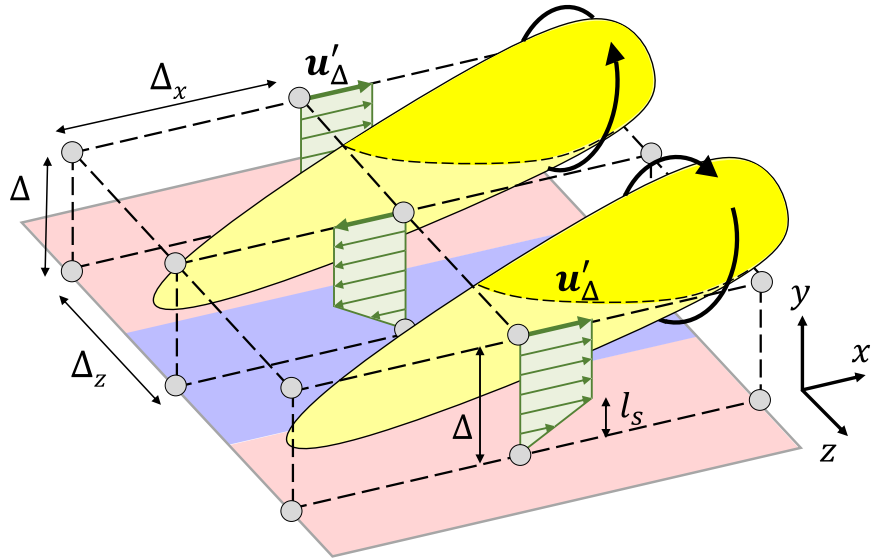


**Figure 5.1:** A schematic of the turbulent non-equilibrium velocity profiles resulting from two counter-rotating wall-attached eddies. Circles indicate the LES grid points and the blue surface indicates a possible region of negative velocity fluctuation (green arrows) induced between wall-attached eddies (yellow) that can only be partially resolved on the LES resolution.

$\Delta$  as portrayed in figure 5.1. We are only interested in the wall-stress filtered to the LES resolution, i.e., the local average of effects of eddies over the LES resolution. It is that local average which is associated with the velocity fluctuation  $u'_\Delta$ . The contribution of eddies smaller than  $\Delta x \times \Delta \times \Delta z$  is neglected. In the absence of additional information or any further assumptions, we model the resulting flow structures as consisting of streamwise elongated high and low-speed regions in which the velocity profile is approximated as mostly plug flow. When approaching the wall, one assumes there is a linear shear layer connecting the profile to the no-slip boundary condition on the smooth wall. We assume that this layer has the thickness of the viscous sublayer (same as that assumed for the Stokes layer,  $l_s$ ). The turbulent non-equilibrium

velocity is then

$$\mathbf{u}' = \mathbf{u}'_\Delta \frac{y}{l_s} \quad \text{for } 0 \leq y \leq l_s \quad (5.2)$$

$$\mathbf{u}' = \mathbf{u}'_\Delta \quad \text{for } y \geq l_s$$

where  $l_s = l_s^+ \nu / u_\tau$  with  $l_s^+ = 12$ , and the friction-velocity  $u_\tau$  comes from the LaRTE model. The wall-stress is then computed as

$$\tau'_w \equiv \nu \frac{\partial \mathbf{u}'}{\partial y} \Big|_0 = \frac{u_\tau \mathbf{u}'_\Delta}{l_s^+}. \quad (5.3)$$

Very recently, Hansen et al. (2023) have shown that very similar vertical profiles can be obtained from POD analysis showing that the most important (energetic) modes of the unresolved turbulence can be described by plug flow with a viscous layer towards the wall starting at  $y^+ \sim 12$ , consistent with our simple model.

The model governed by equation 5.3 is hereafter referred to as the turbulent non-equilibrium (turbNEQ) model and is included as an additional non-equilibrium model to supplement the existing LaRTE and lamNEQ models.

## 5.2 Modifications to the original LaRTE model

### 5.2.1 Revisiting the equilibrium stress closure for the LaRTE model

The total shear stress at  $y = \Delta$ ,  $\bar{\tau}_\Delta$ , is the primary term to be closed in equation 2.25. The LaRTE wall model uses an equilibrium closure for evaluating the total stress. The total stress closure is based on the full equilibrium momentum

balance, where the unsteady and advection terms are set to zero. The smooth-walled, full equilibrium solution is found by solving the ODE

$$0 = -\frac{1}{\rho} \nabla_h \bar{p} + \frac{d}{dy} \left( (\nu + \nu_T) \frac{d\bar{u}^{\text{eq}}}{dy} \right) \quad (5.4)$$

with boundary conditions

$$\bar{u}^{\text{eq}}(0) = \mathbf{0}, \quad \bar{u}^{\text{eq}}(\Delta) = \bar{u}_\Delta \quad (5.5)$$

where  $\Delta$  is the wall model height and the eddy viscosity is assumed to be unaffected by the pressure gradient and is evaluated as  $\nu_T(y) = [D(y)\kappa y]^2 \|d\bar{u}^{\text{eq}}/dy\|$  where  $D(y)$  is the van Driest damping function (van Driest, 1956). The evaluation of the velocity and pressure gradient inputs,  $\bar{u}_\Delta$  and  $\nabla_h \bar{p}$ , are specifically what differ from the original LaRTE wall model.

Recalling §4.1.1, in the new implementation of the LaRTE model, the “band-pass filtered” pressure gradient  $\nabla_h \bar{p}'$  is set to zero and thus the entire quasi-equilibrium pressure gradient goes into the equilibrium fit (i.e.  $\nabla_h \bar{p} = \nabla_h P = \langle \nabla_h p_{LES} \rangle_{t_v}$ ). Numerically the LaRTE quasi-equilibrium pressure gradient is evaluated as

$$\nabla_h \bar{p}^n = \frac{\delta t^n}{t_v} \nabla_h p_{LES}^n + \left( 1 - \frac{\delta t^n}{t_v} \right) \nabla_h \bar{p}^{n-1} \quad (5.6)$$

where  $n$  is the time step index,  $\delta t$  is the time step size,  $\nabla_h p_{LES}$  is the LES pressure gradient at the location  $(x, \Delta, z)$ , and  $t_v$  is the viscous diffusion time scale associated with the laminar Stokes layer (first introduced with the lamNEQ model in chapter 3). The lamNEQ pressure gradient is the same as before and

is evaluated as

$$\nabla_h p'' = \nabla_h p_{\text{LES}} - \nabla_h \bar{p}. \quad (5.7)$$

The idea is to remove the laminar Stokes layer dynamics from the inputs to the equilibrium closure for  $\bar{\tau}_\Delta$ , otherwise the equilibrium fit does not predict the total stress at the wall model height correctly. This input correction is done for the LES velocity input as well, as explained in §5.2.2 below.

Returning to equation 5.4, and integrating between  $y = 0$  and  $y = \Delta$  one obtains

$$0 = -\frac{\Delta}{\rho} \nabla_h \bar{p} + \bar{\tau}_\Delta - \bar{\tau}_w^{\text{eq}}, \quad \text{where } \bar{\tau}_w^{\text{eq}} \equiv \nu \left. \frac{d\bar{u}^{\text{eq}}}{dy} \right|_0 \quad (5.8)$$

The equilibrium wall-stress,  $\bar{\tau}_w^{\text{eq}}$ , is the viscous stress at the wall involving the solution  $\bar{u}^{\text{eq}}(y)$  to equation (5.4). The obtained equilibrium wall-stress, appropriately non-dimensionalized, was fitted for general use in Meneweau (2020) expressing the result in terms of a wall model friction factor  $c_f^{\text{wm,eq}}(Re_\Delta, \psi_p) \equiv 2\bar{\tau}_w^{\text{eq}}/\bar{u}_\Delta^2$ , or equivalently, a wall friction Reynolds number  $Re_{\tau_\Delta}^{\text{pres}}(Re_\Delta, \psi_p) \equiv \Delta(\bar{\tau}_w^{\text{eq}})^{1/2}/\nu$ , where the inputs to the fit are  $Re_\Delta \equiv \bar{u}_\Delta \Delta / \nu$  and  $\psi_p \equiv \frac{1}{\rho} (\nabla_h \bar{p} \cdot \hat{e}_u) \Delta^3 / \nu^2$  and where  $\hat{e}_u \equiv \bar{u}_\Delta / \bar{u}_\Delta$  is the velocity input unit vector. Both are related via  $c_f^{\text{wm,eq}} = 2 [Re_{\tau_\Delta}^{\text{pres}} / Re_\Delta]^2$ . Full equilibrium implies that we may use the equilibrium wall model of  $\bar{\tau}_w^{\text{eq}}$  as a model for the total forcing at  $y = \Delta$ , namely we replace

$$-\frac{\Delta}{\rho} \nabla_h \bar{p} + \bar{\tau}_\Delta = \bar{\tau}_w^{\text{eq}} = \frac{1}{2} c_f^{\text{wm,eq}}(Re_\Delta, \psi_p) \bar{u}_\Delta^2 \hat{e}_u \quad (5.9)$$

in equation 2.25. The final governing equation for the updated LaRTE model

(again neglecting the small  $\nabla_h \cdot s$  and horizontal diffusion terms) is then

$$\frac{\partial \mathbf{u}_\tau}{\partial t} + \mathbf{V}_\tau \cdot \nabla_h \mathbf{u}_\tau = \frac{1}{T_s} [\bar{\boldsymbol{\tau}}_w^{\text{eq}} / u_\tau - \mathbf{u}_\tau] + u_\tau \frac{\delta_\Delta^*}{\Delta} \frac{\partial s}{\partial t} \quad (5.10)$$

where now relaxation towards the friction velocity's equilibrium value is much more obvious.

### 5.2.2 Velocity correction to the LES input

During LES of flows under strong non-equilibrium conditions, we have found that simply using the LES velocity  $\mathbf{U}_{\text{LES}}$  as the input to the stress closure for  $\bar{\boldsymbol{\tau}}_w^{\text{eq}}$  (i.e., using  $Re_\Delta = U_{\text{LES}}\Delta/\nu$ ) yields incorrect results during periods of high non-equilibrium forcing. For example, if the flow were to be accelerated in the streamwise direction by a sudden increase in the pressure gradient, a shear layer grows near the wall and the velocity outside the shear layer increases. If we were to use the LES velocity as the input, equation 5.9 incorrectly attributes the increase in velocity with an increase in the turbulence and the wall-stress. Ample evidence from the literature (Greenblatt & Moss, 2004; He & Jackson, 2000; He & Seddighi, 2013; He et al., 2008b; Joel Sundstrom & Cervantes, 2018; Vardy et al., 2015) show that the stress outside of this shear layer remains unchanged for some time after application of the sudden change in the pressure gradient, consistent with the concept of “frozen turbulence”. To mimic this effect while also keeping the simplicity of the equilibrium wall model, we correct the LES velocity by subtracting from it the anticipated increase in velocity due to rapid changes in pressure gradient. This velocity correction is denoted as  $u''_\Delta$  and is modeled as the solution to the model

equation

$$\frac{\partial \mathbf{u}_\Delta''}{\partial t} = -\frac{1}{\rho} \nabla_h p'' - \frac{\mathbf{u}_\Delta''}{T_\Delta} \quad (5.11)$$

where  $T_\Delta = t_v + \Delta/\kappa u_\tau$  represents the time scale associated with the destruction of the laminar Stokes layer as it diffuses away from the wall. In the absence of mean shear, the fluid acceleration is equal to the pressure gradient. However, because the underlying flow has shear, the laminar Stokes layer above  $l_s$  weakens and becomes turbulent as it diffuses away from the wall. The characteristic time for this diffusive process to take place,  $T_\Delta$ , is modeled as the time it takes for the laminar Stokes layer to diffuse to the edge of the viscous sublayer,  $t_v$ , plus the eddy turnover time at the wall model height,  $\Delta^2/\nu_T(\Delta) = \Delta/\kappa u_\tau$ . In figures 5.3 and 5.2, the dark red region corresponds with the laminar Stokes layer near the wall which diffuses to the edge of the viscous sublayer,  $l_s$ , by time  $t_v$ . The Stokes layer's growth is then interrupted by the turbulent flow which further diffuses it over an eddy turnover time. This is represented by the light red region in figures 5.3 and 5.2. The pressure gradient  $\nabla_h p''$  is same as the lamNEQ pressure gradient in equation 5.7. Equation 5.11 effectively models the changes in the LES velocity due to fast changes in the pressure gradient. Note the similarities between equation 5.11 and equation 3.1 from the lamNEQ model. Equation 5.11 is essentially a model for equation 3.1 evaluated at the wall model height  $\Delta$  where the viscous term is replaced by a modeled destruction term.

The velocity input used in 5.9 is then given by

$$\bar{\mathbf{u}}_\Delta = \mathbf{U}_{LES} - \mathbf{u}_\Delta''. \quad (5.12)$$

The velocity correction  $\mathbf{u}_\Delta''$  is shown schematically with the thick red vector in figure 5.2 and the resulting corrected velocity input  $\bar{\mathbf{u}}_\Delta$  is shown by the light gray vector. During non-equilibrium events,  $\mathbf{u}_\Delta''$  cancels the changes in the LES velocity which ultimately leads to a delayed response by  $\bar{\tau}_\Delta$ . In the previous applications of the LaRTE wall model in chapter 4,  $\mathbf{U}_{LES}$  was filtered using a  $2\Delta$  spatial filter to remove LES velocity fluctuations that would otherwise lead to an over predicted wall-stress (Bou-Zeid et al., 2005). However, we have found that the velocity correction eliminates the need to filter the LES velocity since it inherently removes the high frequency content in  $\mathbf{U}_{LES}$ . Therefore, the LES velocity remains spatially unfiltered when using the velocity correction model.

### 5.3 Summary of the MTSWM

We now have all the ingredients needed to describe the final multi-time-scale wall model highlighted in this dissertation. In §5.1, a new turbulent non-equilibrium model was developed motivated by the need to complete the “missing piece” in the length and time scale schematic (figure 2.1) for the LaRTE+lamNEQ model. The turbNEQ model connects measured turbulent velocity fluctuations (equation 5.1) with corresponding wall stress fluctuations. Then §5.2 outlines the modifications made to the LaRTE model, particularly the changes to the inputs for the equilibrium stress closure through the pressure gradient and the introduction of a velocity correction model. The total wall-stress for the MTSWM is then evaluated as the superposition of the three

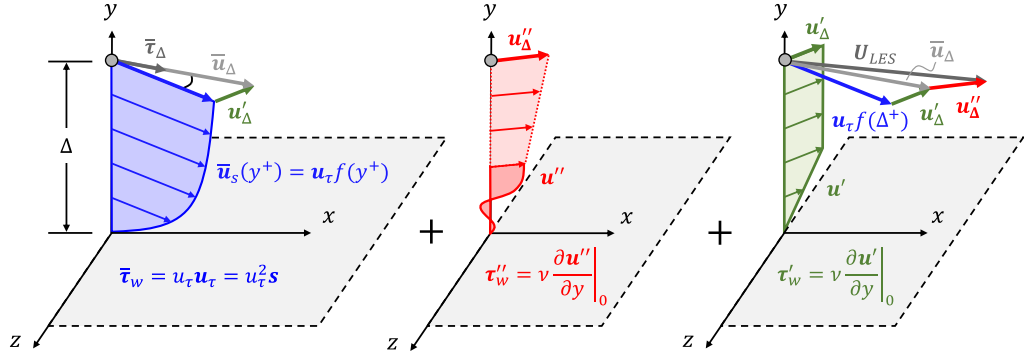
components according to

$$\boldsymbol{\tau}_w(x, z, t) = \bar{\boldsymbol{\tau}}_w(x, z, t) + \boldsymbol{\tau}_w''(x, z, t) + \boldsymbol{\tau}_w'(x, z, t). \quad (5.13)$$

where  $\bar{\boldsymbol{\tau}}_w = u_\tau \boldsymbol{u}_\tau$  is the quasi-equilibrium/LaRTE wall-stress governed by equation 5.10,  $\boldsymbol{\tau}_w''$  is the lamNEQ wall-stress governed by equation 3.5, and  $\boldsymbol{\tau}_w'$  is the turbNEQ wall-stress governed by equation 5.3.

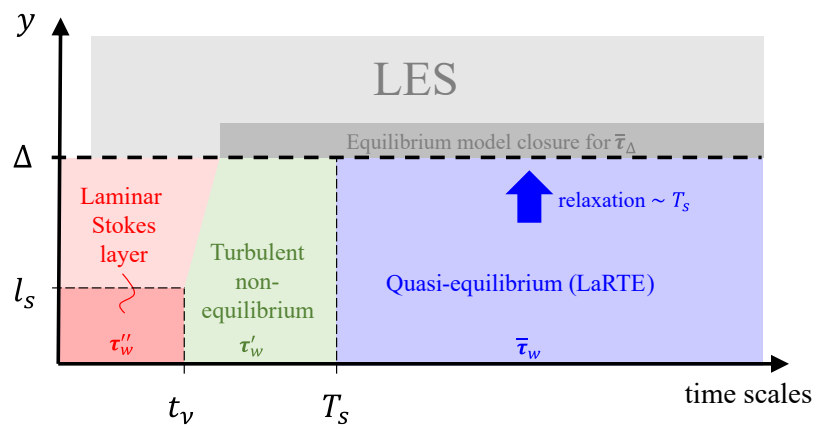
Figure 5.2 shows the three velocity profiles assumed by the LaRTE, lam-NEQ, and turbNEQ models. The left figure shows the law of the wall velocity profile assumed by the LaRTE model, driven by the stress  $\bar{\boldsymbol{\tau}}_\Delta$ . This stress is computed via an equilibrium model closure with the “corrected LES velocity”,  $\bar{\boldsymbol{u}}_\Delta$  (governed by equation 5.12), and the quasi-equilibrium pressure gradient  $\nabla_h \bar{p}$  (evaluated according to equation 5.6) used as inputs. This allows us to define a turbulent velocity fluctuation  $\boldsymbol{u}'_\Delta$  which drives the turbNEQ velocity profile shown on the right in figure 5.2. In the middle of figure 5.2, is a schematic of the laminar Stokes layer that forms near the wall, responding to fast changes in the pressure gradient. This Stokes layer diffuses away from the wall until it interacts with the turbulence outside of the viscous sublayer. This generates a corresponding velocity fluctuation,  $\boldsymbol{u}''_\Delta$  (modeled according to equation 5.11) and subtracted from the LES velocity to give the corrected LES velocity.

Figure 5.3 now shows the updated length and time scale schematic for the MTSWM. It highlights the full spectrum of time scales captured in this approach. The LaRTE model captures the slow, quasi-equilibrium behavior of the wall-stress thus enabling separate modeling of faster, non-equilibrium



**Figure 5.2:** A schematic of the velocity profiles for the LaRTE (left), laminar non-equilibrium (middle), and turbulent non-equilibrium (right) components.

dynamics. These faster dynamics include a laminar, near-wall Stokes layer which responds to fast changes in the pressure gradient and turbulent velocity fluctuations at the wall model height which may be explained by the attached eddy hypothesis. The lamNEQ and turbNEQ models then connect these dynamics with corresponding wall stress responses. The MTSWM thus is expected to properly model dynamics occurring from full equilibrium to highly non-equilibrium flows. To put this theory to the test, several flows are tested using the MTSWM. Chapter 6 deals with wall-parallel homogeneous flows (i.e. channel flow) with various strategies for modifying the pressure gradient forcing such that temporal non-equilibrium state is achieved. Chapter 7 then deals with streamwise developing flows such as the canonical ZPG turbulent boundary layer and a separated boundary layer to test the MTSWM for flows with spatial non-equilibrium.



**Figure 5.3:** Schematic of the MTSWM length and time scales

# Chapter 6

## The MTSWM applied to horizontally homogeneous flows

### 6.1 Revisiting stationary channel flow and SSPG

The wall-stress probability density functions (PDFs) in equilibrium channel flow as well as the sudden spanwise pressure gradient (SSPG) flow studied in chapter 4 are revisited here, in order to discuss how the addition of the non-equilibrium turbulent model (and the other model changes) affect the results. The same grid and subgrid-scale model as in the original SSPG test are used. The first grid point is used for the wall model height. Major differences between the LaRTE+lamNEQ and the newly proposed MTS wall model include: (1) treatment of the pressure gradient in the LaRTE relaxation term, (2) introducing velocity correction to the LES velocity input for computing the equilibrium stress, and (3) addition of the turbNEQ wall model, as was discussed in chapter 5.

First, we consider equilibrium channel flow at  $Re_\tau = 1000$  and 5200, repeating figure 4.8 but using the MTSWM. Results are shown in figure 6.1 and

are compared with DNS (dashed black line). Compared to the model version used in chapter 4, it is evident that the addition of the turbNEQ portion of the model in the MTSWM approach yields very realistic PDFs of the streamwise component of the wall-stress as compared to filtered DNS, but overestimates the level of variability of the spanwise wall-stress component. A simple explanation is that the current LES over-predicts the spanwise velocity fluctuations in the near-wall region, as can be seen in figure 6.5(b) and 6.18(b, d) for low Reynolds numbers and figure 4.3 for high Reynolds numbers. Since the turb-NEQ wall-stress is proportional to the LES velocity fluctuations at the wall model height, this directly leads to over-predicted wall-stress fluctuations. Still, the improved prediction of streamwise fluctuation levels represents a strength of adding the turbNEQ portion of the model.

Next we examine the sudden spanwise pressure gradient (SSPG) flow. The evolution of the predicted spatially averaged mean wall-stress is shown in figure 6.2. For the streamwise wall-stress, the MTS wall model has a slightly more delayed response compared with the LaRTE+lamNEQ results in chapter 4. This delayed response is likely caused by differences (1) and (2) stated above. However we deem this behavior acceptable since these differences to the DNS are small relative to the total wall-stress change after the SSPG is introduced. The spanwise wall-stress, shown in figure 6.2(b), is very similar to that shown in figure 4.11 despite the significantly slower response of the LaRTE model shown by the blue curve. For the spanwise direction, the LaRTE model is slower primarily due to the treatment of the pressure gradient in the relaxation term ( $\nabla_h \bar{p}$  in equation 5.10). In both chapter 4 and the present

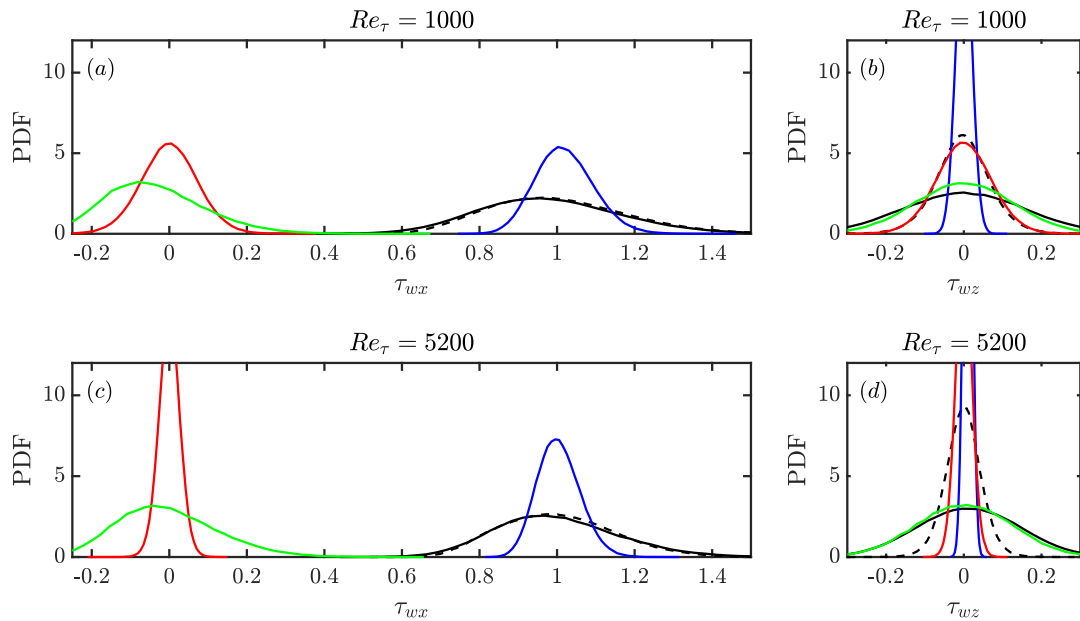


**Figure 6.1:** PDFs for  $\tau_{wx}$  and  $\tau_{wz}$ ; (a, b)  $Re_\tau = 1000$ ; (c, d)  $Re_\tau = 5200$ . The PDF curves correspond with the filtered DNS (dashed black lines), the LaRTE model (blue lines), the non-equilibrium laminar model (red lines), the non-equilibrium turbulent term (green lines) and the MTS model (solid black lines). DNS data obtained from the Johns Hopkins Turbulence Database Graham et al.; JHTDB (2016, 2021). The DNS PDFs are obtained from the Gaussian filtered wall-stress where the filtering size is the same as the LES mesh size in the horizontal directions.

chapter, the quasi-equilibrium pressure gradient is evaluated as the filtered LES pressure gradient with the filtering time scale  $t_\nu$ . However, in chapter 4, part of this pressure gradient is brought into the equilibrium stress closure (equation 5.9) and part of it is left in the relaxation term as a “band-pass filtered pressure gradient” (see §4.1.1 for more information). In the present chapter, all of  $\nabla_h \bar{p}$  is brought into the equilibrium stress closure and therefore there is no leftover relaxation term. When changes in the pressure gradient are large (as is the case with the SSPG flow), this term can become quite significant and speeds up the response of the LaRTE model. We chose to keep all of the quasi-equilibrium pressure gradient in the equilibrium stress closure since the LaRTE model now truly relaxes to its “equilibrium stress” while the turbNEQ model makes up for the delayed response of the LaRTE model.

The turbNEQ wall model, by design, assumes a wall-stress is generated if the LES velocity (with velocity correction) responds more quickly than the quasi-equilibrium velocity,  $u_\tau f(\Delta^+)$ . The green curve in figure 6.2(b) shows that initially the difference between these two velocities is small. It then reaches a peak around  $tu_{\tau p,i}/h = 0.5$ , subsequently decaying until the flow reaches a new quasi-equilibrium state long after the SSPG is applied. Other wall-stress trends for the LaRTE and lamNEQ models discussed in chapter 4 are also observed here (e.g. the fast initial response of the lamNEQ model). Overall the MTS wall model agrees well with the DNS results with improvement over the popular EQWM.

Figure 6.3 shows contour plots of the wall-stress fluctuations for each component of the MTSWM after the SSPG is applied. Only one time instance

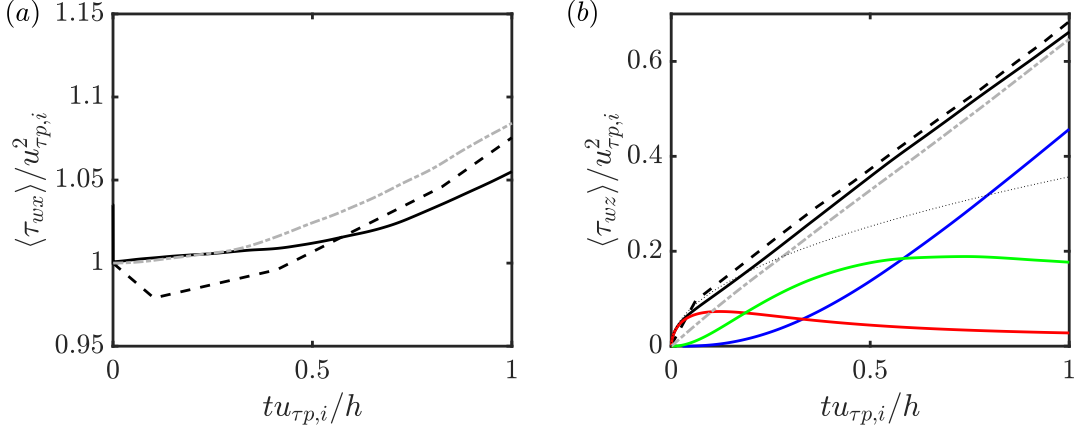


**Figure 6.2:** (a) Streamwise and (b) spanwise wall-stress after a suddenly applied spanwise pressure gradient. Line types correspond with the DNS of Lozano-Durán et al. (2020) (thick dashed black lines), LES with the EQWM (dashed-dot gray lines), and the total wall-stress for LES with the MTSWM (solid black lines). In panel (b), wall-stresses for the LaRTE, lamNEQ, and turbNEQ components of the MTS wall model are shown with blue, red, and green lines, respectively. The thin dotted line in panel (b) corresponds with the Stokes solution wall-stress. Angled brackets represent ensemble averaging over the horizontal plane and over five independent simulations.

$tu_{\tau p,i}/h = 2.22$  is shown in the figure here. From the figure it is clear the turb-NEQ wall model is the primary contributor to wall-stress fluctuations. This is generally true for all conditions from quasi-equilibrium to non-equilibrium. The LaRTE model tends to capture slow large scale wall-stress fluctuations which appear as elongated turbulent streaks in panels (a, b). Similar to what was reported in chapter 4, we observe a break-up of the LaRTE wall-stress streaks initially after the SSPG is applied which then eventually re-align themselves with the mean wall-stress direction as the flow asymptotically approaches its new quasi-equilibrium state. We stress that these streaks are very large, corresponding to the response time  $T_s$  which is significantly larger than the large-eddy turnover time  $\Delta/u_\tau$  (by a factor  $f(\Delta^+)$ ).

For this particular flow, the lamNEQ wall-stress fluctuations are small in

$$tu_{\tau p,i}/h = +2.22$$

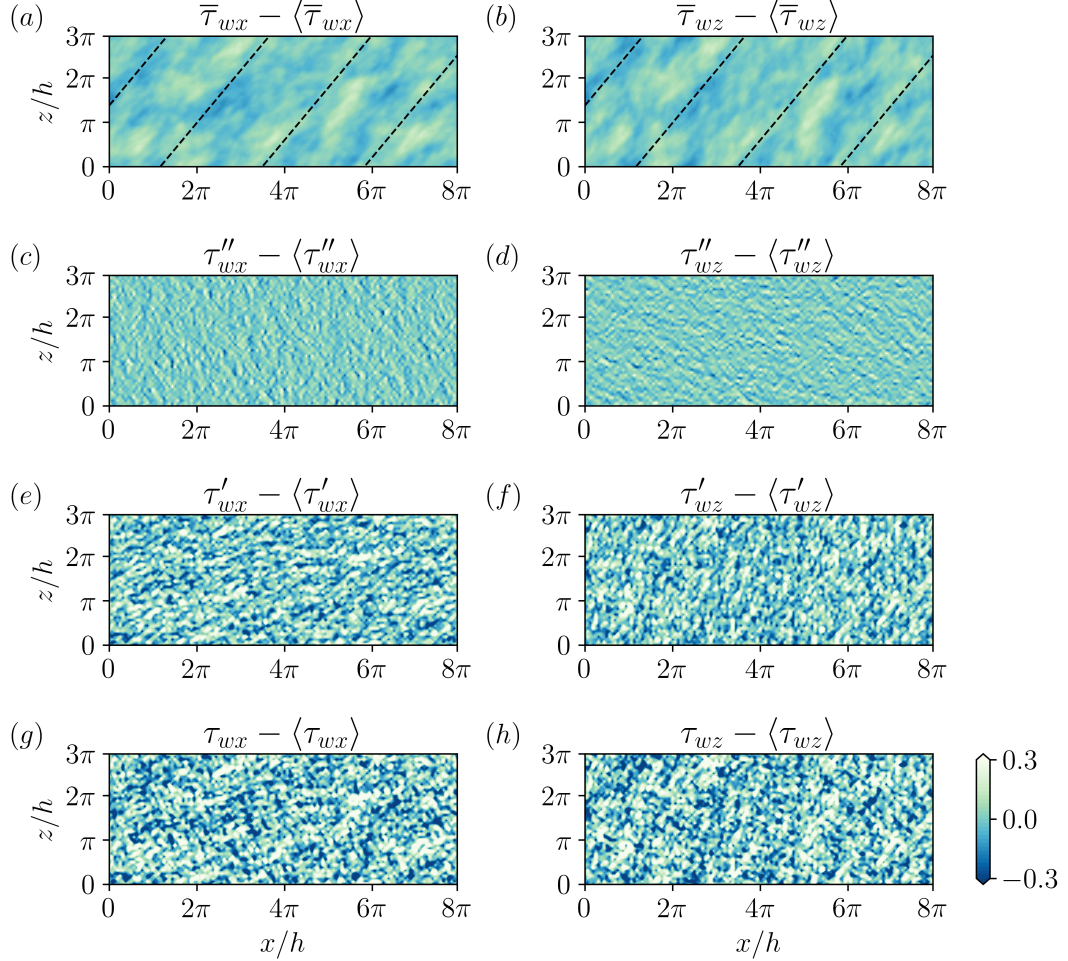


**Figure 6.3:** Contour plots of the wall-stress fluctuations (both streamwise and spanwise directions) for each component in the MTSWM after the SSPG is applied. These components include (a, b) LaRTE, (c, d) lamNEQ, (e, f) turbNEQ, and (g, h) the total MTS wall-stress. The dashed lines in panels (a, b) represent the total wall-stress angle. Angled brackets represent averaging over the horizontal plane.

magnitude, although with large spatial variability, relative to the turbNEQ wall-stress fluctuations. Generally, the lamNEQ wall-stress fluctuations relative to the turbNEQ fluctuations decrease as Reynolds number increases. This is because  $\tau''_w/u_\tau^2$  scales with  $Re_\tau^{-1/2}$  whereas  $\tau'_w/u_\tau^2$  scales with  $u'_\Delta/u_\tau$  which increases with Reynolds number. For  $Re_\tau = 1000$ , the Reynolds number is large enough such that turbulent velocity fluctuations are the dominant contributor to wall-stress fluctuations.

## 6.2 Pulsating channel flow

Large eddy simulations of pulsating channel flow, with an oscillating streamwise pressure gradient forcing, were conducted with the MTSWM and with the classical EQWM. These results are compared with the DNS of Weng et al. (2016) upon which the simulation setup is largely based. As in Weng et al. (2016), we adopt a triple decomposition where any variable,  $F(\mathbf{x}, t)$ , may be written as

$$F(\mathbf{x}, t) = \langle F \rangle_t(y) + \tilde{F}(y, t) + F'(\mathbf{x}, t) \quad (6.1)$$

where  $\langle F \rangle_t$  is the steady, time and horizontally averaged field;  $\tilde{F}$  is the periodic component caused by the oscillatory pressure gradient; and  $F'$  corresponds with turbulent fluctuations. Note that the turbulent fluctuations are the only cause for variability in the  $x$  and  $z$  directions for channel flow. Also note that a single prime in this section is not to be confused with a turbulent non-equilibrium quantity unless otherwise specified. The time and horizontally

averaged component is computed as

$$\langle F \rangle_t(y) = \frac{1}{(t_{N_t} - t_0)L_zL_x} \int_{t_0}^{t_{N_t}} \int_0^{L_z} \int_0^{L_x} F(\mathbf{x}, t) \, dx \, dz \, dt \quad (6.2)$$

where  $t_0$  and  $t_{N_t}$  are the initial and final times, respectively, over which time averaging is done. The periodic component is found by subtracting the time averaged flow field from the phase average:

$$\tilde{F}(y, t) \equiv \frac{1}{N_p L_x L_z} \sum_{n=1}^{N_p} \int_0^{L_z} \int_0^{L_x} F(\mathbf{x}, t + (n-1)T_f) \, dx \, dz - \langle F \rangle_t(y), \quad (6.3)$$

where  $T_f$  is the pressure gradient forcing period and  $N_p$  is the total number of periods over which phase averaging is done.

Simulations are performed using LESGO (an open-source, mixed pseudo-spectral and finite difference code available on github, [LESGO \(2021\)](#)) with a steady friction Reynolds number of  $\langle Re_\tau \rangle_t = u_{\tau p} h / \nu = 350$ , where  $h$  is the channel half-height and  $u_{\tau p} \equiv \sqrt{-h\rho^{-1}(\partial_x \langle p \rangle_t)}$  is the friction-velocity based on the steady pressure gradient. The Lagrangian scale-dependent dynamic subgrid stress model ([Bou-Zeid et al., 2005](#)) is used in the bulk of the flow. The domain size, number of grid points, and grid size are  $(L_x, L_y, L_z)/h = (8\pi, 2, 3\pi)$ ,  $(N_x, N_y, N_z) = (128, 30, 48)$ , and  $(\Delta_x, \Delta_y, \Delta_z)/h = (0.196, 0.067, 0.196)$ , respectively. The third grid point is used for the wall model height (i.e.  $\Delta = 5\Delta_y/2$ ) because for low-Reynolds-number simulations the first grid point falls beneath the log layer where the SGS model lacks accuracy. This underperformance causes an incorrect velocity to be fed into the wall model which in turn produces an incorrect wall-stress. Choosing a point further away allows a more accurately computed velocity to be fed into the wall

model. It is also in agreement with the recommendations made by Larsson et al. (2016). Time advancement is done using an Adams-Bashforth method with a varying time step size to achieve a constant CFL value of 0.05. On average this gives a time step size around  $\delta t \approx 4.2 \times 10^{-4}h/u_{\tau p}$  which is two orders smaller than the fastest forcing time scale. This assures all dynamics are well resolved temporally.

Sinusoidal flow variation is caused by the time-periodic streamwise pressure gradient forcing

$$\frac{\partial \langle p \rangle}{\partial x} = \frac{\partial \langle p \rangle_t}{\partial x} [1 + \beta \cos(\omega_f t)] \quad (6.4)$$

where  $\partial \langle p \rangle_t / \partial x$  is the steady pressure gradient forcing and  $\omega_f$  and  $\beta$  are the pressure gradient forcing frequency and amplitude, respectfully. In our simulations we use a sine function instead of a cosine function to avoid a discontinuous change in the pressure gradient forcing at  $t = 0$  when the forcing starts, however, we adopt the nomenclature of Weng et al. (2016) which uses a cosine function. Therefore, all phases reported are consistent with a cosine pressure gradient forcing. A wide range of forcing frequencies are tested which cover the full range of possible flow types. This is summarized in table 6.1. The forcing frequency determines the extent to which the Stokes layer penetrates into the flow. Similarly, the Stokes length scale provides an estimate of this penetration depth and is related to the frequency through  $l_f = \sqrt{2\nu/\omega_f}$  or in inner units  $l_f^+ = \sqrt{2/\omega_f^+}$  where inner units normalization is done with the friction-velocity  $u_{\tau p}$  and the kinematic viscosity  $\nu$ . If the Stokes layer stays within the viscous sublayer then it doesn't interact with the

$\omega_f^+$	$\langle T_f \rangle_t u_{\tau p} / h$	$l_f^+$	$l_f / h$	flow regime
0.001	18.0	44.7	0.1278	quasi-equilibrium frequency
0.003	6.0	25.8	0.0738	low frequency
0.006	3.0	18.3	0.0522	intermediate frequency
0.01	1.8	14.1	0.0404	intermediate frequency
0.02	0.9	10.0	0.0286	intermediate frequency
0.04	0.45	7.1	0.0202	high frequency
0.2	0.09	3.2	0.0090	very high frequency
1.0	0.018	1.4	0.0040	very high frequency

**Table 6.1:** The forcing frequencies  $\omega_f^+$  and periods and their corresponding Stokes lengths  $l_f$  in inner units and outer units and the flow regime classification. For comparison, the relevant wall modeling time scales are  $\langle T_s \rangle_t u_{\tau p} / h = 2.57$ ,  $\langle t_v \rangle_t u_{\tau p} / h = 0.41$  and  $\langle T_\Delta \rangle_t u_{\tau p} / h = 0.83$ .

turbulence and the flow remains ‘quasi-laminar.’ This is estimated to occur when  $\omega_f^+ > 0.04$  or  $l_f^+ < 7$  (Weng et al., 2016). Several of the other frequencies tested are in the so-called ‘intermediate frequency range’  $0.006 < \omega_f^+ < 0.04$  where the wall-stress amplitude is actually less than the amplitude from the Stokes solution. Finally, a couple low frequency cases are tested where the flow is in a quasi-steady state. In other words, the flow has time to adjust to the instantaneous pressure gradient.

Following Weng et al. (2016), the pressure gradient forcing amplitude is set to give a constant ratio for the periodic centerline velocity amplitude over the mean centerline velocity. This is done by fixing  $a_{cl} \equiv |\tilde{u}_{cl}| / U_{cl} = 0.1$  where  $U_{cl}$  is the centerline velocity of the laminar flow with the same flow rate as the turbulent mean flow. The relationship between  $\beta$  and  $a_{cl}$  can be determined by finding an analytical expression for the periodic centerline velocity,  $\tilde{u}_{cl}$ . This is obtained by writing the momentum balance at the center of the channel and then neglecting the total periodic stress —a valid assumption if the Stokes

layer is far from the center of the channel. The periodic centerline velocity is then found to be

$$\tilde{u}_{cl} = |\tilde{u}_{cl}| \cos(\omega_f t + \phi_{\tilde{u}_{cl}}) \quad (6.5)$$

where

$$|\tilde{u}_{cl}| = \frac{\beta u_{\tau p}^2}{\omega_f h}, \quad \phi_{\tilde{u}_{cl}} = -\pi/2. \quad (6.6)$$

Combining the amplitude shown in equation (6.6) and the definition of  $a_{cl}$ ,  $\beta$  can be found using

$$\beta = a_{cl} \omega_f^+ Re_{cl} \quad (6.7)$$

where  $Re_{cl} \equiv U_{cl}h/\nu \approx 9078$  for  $Re_\tau = 350$  and  $a_{cl}$  is set to a constant value of 0.1.

For the figures throughout this paper, the line type and color of the various models/data has the form: DNS has dashed black lines, LES with the MTS wall model has solid black lines, and LES with the EQWM has dashed-dot gray lines. For vertical profiles, open circles and plus symbols correspond with the location of LES grid points for LES with the MTS wall model and EQWM, respectively. Extraneous lines, such as analytical laminar solutions, are shown with thin dotted lines. The different wall-stress components of the MTS wall model are shown with different colors: total wall-stress is black, LaRTE wall-stress is blue, lamNEQ wall-stress is red, and turbNEQ wall-stress is green.

Figure 6.4 shows the periodic centerline velocity for a wide range of pressure gradient forcing frequencies. For the intermediate and high frequencies, the LES is nearly indistinguishable from the DNS whereas for

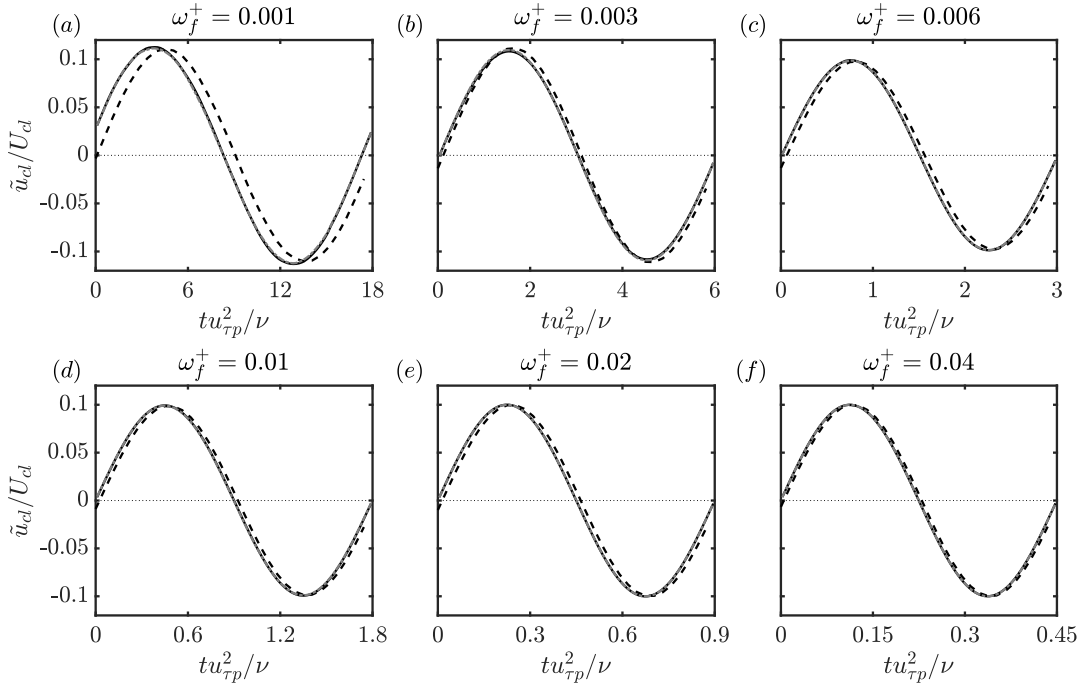


**Figure 6.4:** The time evolution of the periodic centerline velocity  $\tilde{u}_{cl}$  for several forcing frequencies,  $\omega_f^+ = 0.001, 0.003, 0.006, 0.01, 0.02, 0.04$  (subplots (a-f), respectively). Line types correspond with LES using the multi-timescale wall model (thick solid black), LES using the EQWM (thick dashed-dot gray), and DNS from Weng et al. (2016) (thick dashed black). The phase within the cycle is based on the imposed pressure gradient forcing.

For  $\omega_f^+ = 0.001, 0.003$  there are some discrepancies. These differences may be attributed to the LES's overprediction of the mean velocity in the center of the channel (see figure 6.5), which only becomes important for low frequencies when the Stokes layer interacts with the turbulence near the center of the channel. However, for the intermediate and high frequencies the centerline velocity agrees quite well with equations (6.5) & (6.6) and the target periodic centerline velocity amplitude ( $a_{cl} = 0.1$ ) has been met.

Figure 6.5 shows the time-averaged mean velocity profiles and Reynolds stresses for the MTS wall model and for the EQWM compared with the DNS of

Weng et al. (2016). The MTS wall model and the EQWM give nearly identical first and second-order statistics. This indicates the mean behavior of the LES is largely unaffected by the wall model choice. As discussed in Fowler et al. (2022), there is a slight overshoot in the mean velocity profile in the wake region. However, this overshoot is attributed to simulation details other than the wall model, such as subgrid model and numerical effects. Additionally, for these low Reynolds number simulations, the SGS model tends to underpredict the subgrid stress beneath the log layer, thus leading to an overpredicted velocity. This is evident from the first grid point in figure 6.5. The Reynolds shear stress agrees well with DNS as expected from momentum conservation and the streamwise normal stress is also well predicted (except for the near-wall peak that is unresolved in LES). The spanwise and wall normal diagonal Reynolds stress profiles are overpredicted by the LES, but in equal measure by all the wall models, pointing to remaining limitations of the SGS closure and not the wall models.

The governing equation for the periodic component of the streamwise velocity is found by subtracting the time-averaged streamwise momentum equation from the phase-averaged streamwise momentum equation:

$$\frac{\partial \tilde{u}}{\partial t} = -\frac{1}{\rho} \frac{\partial \tilde{p}}{\partial x} + \nu \frac{\partial^2 \tilde{u}}{\partial y^2} - \frac{\partial \tilde{u}' v'}{\partial y} \quad (6.8)$$

Laminar analytical solutions to equation 6.8 can be found by setting the Reynolds stress term to zero and using  $\partial_x \tilde{p} = \beta(\partial_x \langle p \rangle_t) \cos(\omega_f t)$ . For the frequencies considered in table 6.1, the frequencies are high enough such that the Stokes solution is similar to the laminar channel flow solution since  $l_f \ll h$

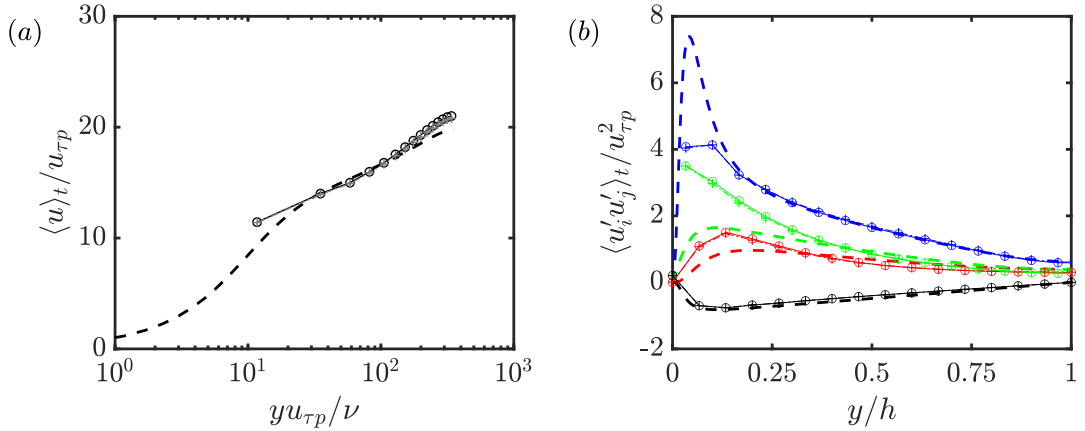


**Figure 6.5:** The time-averaged mean (a) velocity profiles and (b) Reynolds stresses. Dashed lines correspond with the DNS of Weng et al. (2016) for  $Re_\tau = 350$  with pulsations, circles with solid connecting lines correspond with LES with the multi-timescale wall model, and plus symbols with dashed-dot connecting lines correspond with LES with the EQWM. In panel (b),  $\langle u' u' \rangle_t$ ,  $\langle v' v' \rangle_t$ ,  $\langle w' w' \rangle_t$ , and  $\langle u' v' \rangle_t$  are shown with blue, red, green, and black lines, respectively. For the LES, only the high frequency case ( $\omega_f^+ = 0.04$ ) is shown since the time averaged velocity and Reynolds stress profiles are independent of the pulsation frequency.

as shown in table 6.1. Therefore we will simply use the Stokes solution as the “laminar channel flow solution”, which is

$$\tilde{u}/U_{cl} = a_{cl} \left[ \sin(\omega_f t) - e^{-y/l_f} \sin(\omega_f t - y/l_f) \right]. \quad (6.9)$$

Figure 6.6 shows the amplitude and phase of the periodic velocity for the six lowest forcing frequencies. The Stokes solution curve is also shown for reference. In the figures it is clear that for the lowest frequency, the DNS and LES deviate from the Stokes solution significantly and thus a quasi-laminar state is not achieved. However for the highest frequency shown, the DNS and LES follow the Stokes solution very closely, thus indicating that the flow is in a quasi-laminar state. Generally the LES agrees closely with the DNS. The MTS wall model and EQWM produce similar results with the greatest

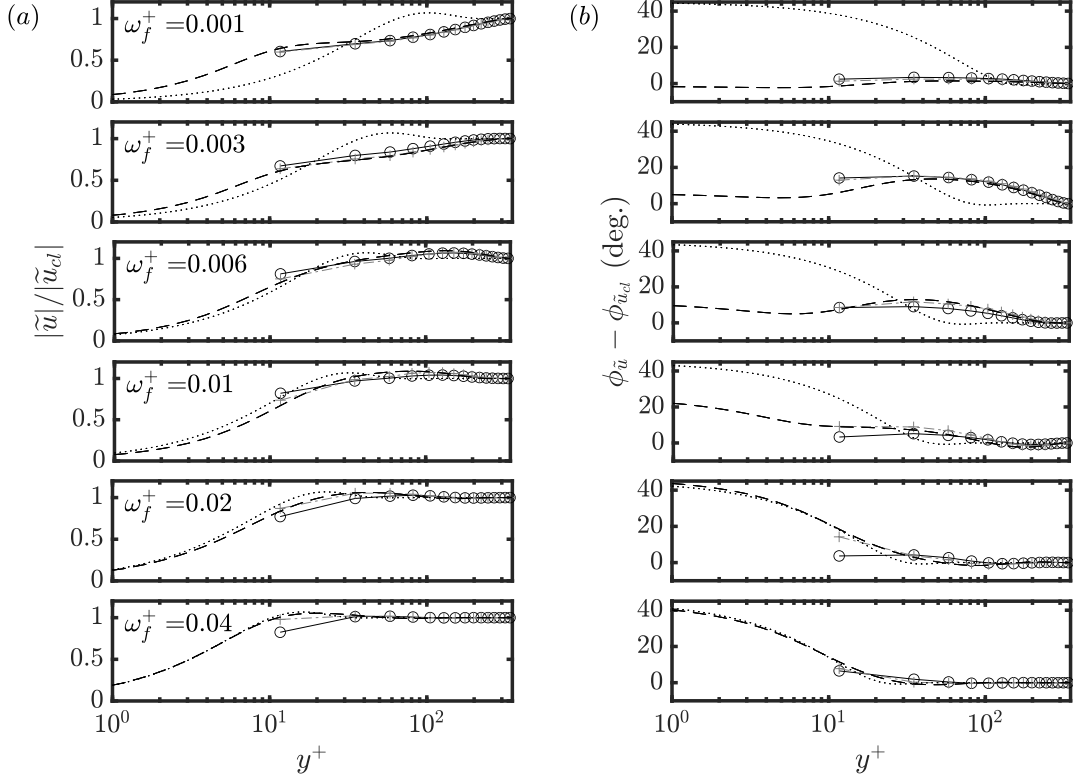


**Figure 6.6:** (a) amplitude and (b) phase lead of the periodic velocity for six forcing frequencies  $\omega_f^+ = 0.001, 0.003, 0.006, 0.01, 0.02, 0.04$ . The DNS of Weng et al. (2016), the LES with the MTS wall model, the LES with the EQWM, and the Stokes solution are shown with dashed black lines, open circles connected with solid black lines, gray plus symbols connected with gray dashed-dot lines, and dotted black lines, respectively.

discrepancies between the two occurring in the first few grid points away from the wall. These grid points are more sensitive to the wall model since they are more directly affected by the wall-stress.

Figures 6.7-6.10 show how the periodic wall-stress changes with frequency where figures 6.7 and 6.8 show the periodic wall-stress time signals and figures 6.9 and 6.10 show the periodic wall-stress amplitude and phase as a function of frequency. Figure 6.7 compares LES with the multi-timescale wall model

(solid black lines) against the DNS of Weng et al. (2016) (dashed black lines) and the LES with the EQWM (dashed-dot gray lines). The figure shows that the MTS wall model and EQWM perform similarly well for low frequencies but as the frequency is increased the EQWM degrades in performance whereas the MTS wall model follows the trends of the DNS quite well. This is expected since the EQWM is based on equilibrium assumptions and therefore cannot properly capture the non-equilibrium dynamics of the high frequency test cases. Figure 6.8 shows the different wall-stress contributions in the multi-timescale wall model for the (a) low, (b) intermediate and (c) high frequencies. This figure demonstrates why the MTS wall model can capture the trends of the DNS and highlights the usefulness of such an approach. For the low, intermediate, and high frequencies the dominant contributors to the periodic wall-stress are the quasi-equilibrium (LaRTE), turbulent non-equilibrium, and laminar non-equilibrium components, respectively. This is consistent with the length and timescale schematic in figure 5.3, where each component of the multi-timescale wall model targets dynamics within a range of timescales. Using table 6.1, we see the flow dynamics relative to the relaxation timescale (the frequencies in figure 6.8) are of the orders (a)  $T_f/T_s \gg 1$ , (b)  $T_f/T_s \sim 1$ , and (c)  $T_f/T_s < 1$  which again is consistent with the model picture in figure 5.3. Note that in this flow the scale separation between the laminar viscous time scale,  $t_v$  and the relaxation time scale,  $T_s$ , is not very large (from the caption in table 6.1 we see that  $\langle t_v \rangle_t / \langle T_s \rangle_t = 0.16$ ). This is a direct result of the low Reynolds number of the flow considered. As seen from the expression  $t_v/T_s = (l_s^+)^2/f(\Delta^+)\Delta^+$ , the numerator is constant while the denominator (and thus the scale ratio) typically increases with increasing Reynolds number.

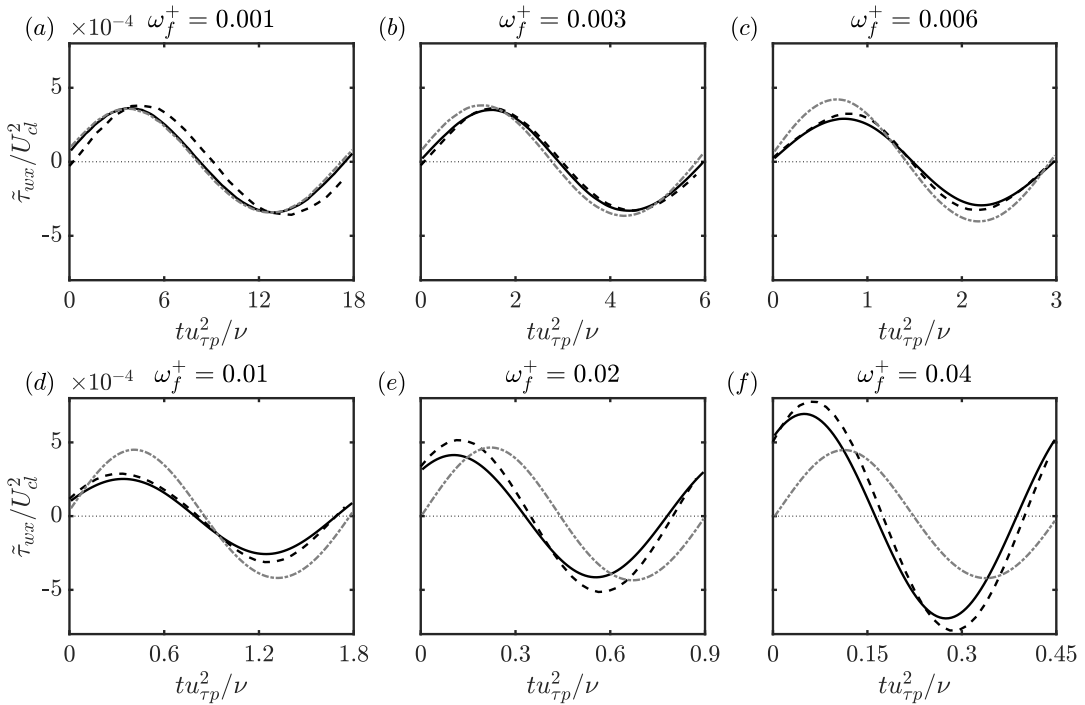


**Figure 6.7:** Single period time evolution of the periodic streamwise wall-stress  $\tilde{\tau}_{wx}$  for several forcing frequencies,  $\omega_f^+ = 0.001, 0.003, 0.006, 0.01, 0.02, 0.04$  (subplots (a-f), respectively). Line types correspond with LES using the multi-timescale wall model (thick solid black), LES using the EQWM (thick dashed-dot gray), and DNS from Weng et al. (2016) (thick dashed black). The phase within the cycle is based on the imposed forcing frequency.

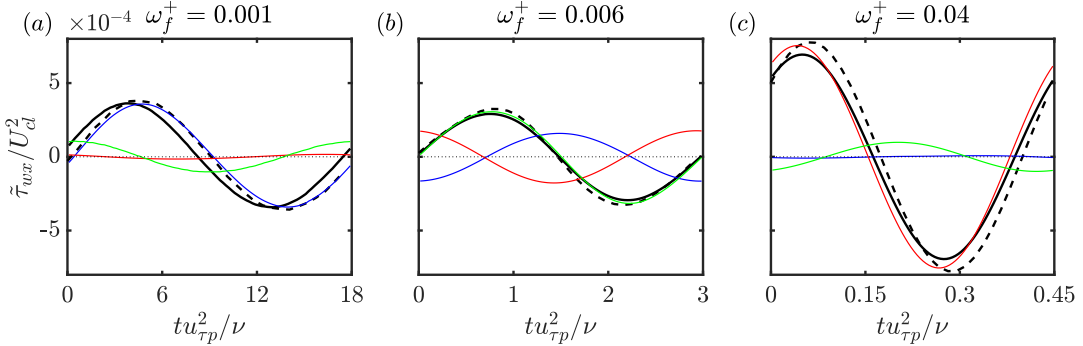


**Figure 6.8:** Single period time evolution of the periodic streamwise wall-stress  $\tilde{\tau}_{wx}$  for low, intermediate, and high forcing frequencies:  $\omega_f^+ = 0.001, 0.006, 0.04$  (subplots (a-c), respectively). Line types correspond with LES using the multi-timescale wall model (thick solid black) with LaRTE (thin solid blue), lamNEQ (thin solid red), and turbNEQ (thin solid green) parts and DNS from Weng et al. (2016) (thick dashed black). The phase within the cycle is based on the imposed forcing frequency.

Figures 6.9 and 6.10 show the periodic wall-stress amplitude and phase. They provide the same information as figures 6.7 and 6.8 but in a more succinct manner allowing trends to become more obvious. In general, as the forcing frequency increases, the wall-stress amplitude (normalized with the Stokes solution amplitude) decreases and the wall-stress phase (relative to the centerline velocity phase) increases until they reach their Stokes limit values of 1 and 45 degrees, respectively. Figure 6.9 clearly demonstrates that the EQWM is unable to capture the non-equilibrium effects caused by the high frequency pressure gradient pulsations. The wall-stress amplitude continues to decrease past its Stokes limit value while the phase remains relatively constant. The multi-timescale wall model, on the other hand, agrees quite well with DNS trends. It even captures the non-monotonic behavior in the intermediate frequency range where the periodic wall-stress amplitude falls beneath the Stokes amplitude. The wall model's ability to capture the full

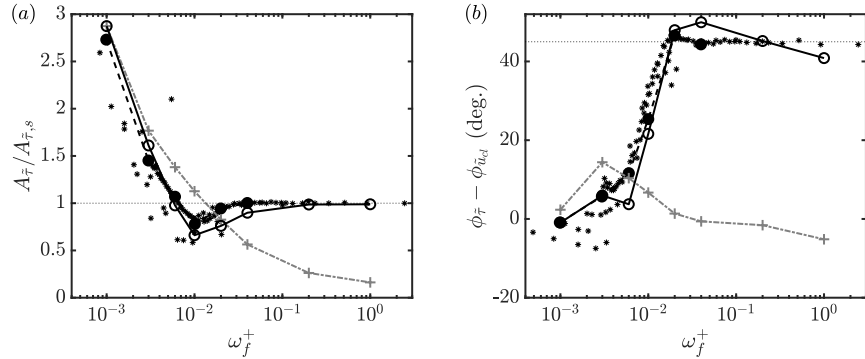


**Figure 6.9:** (a) The periodic wall-stress amplitude normalized by the Stokes solution amplitude and (b) the periodic wall-stress phase relative to the centerline velocity phase. Asterisks correspond with outside experimental, LES, or DNS data from Ronneberger & Ahrens (1977) (experimental), Tardu et al. (1994) (experimental), Scotti & Piomelli (2001) (LES), and Weng et al. (2016) (DNS). The DNS data of Weng et al. (2016) are emphasized with filled circles and connected with thick dashed black lines. LES using the MTS wall model is shown with open circles and connected with thick solid black lines. LES using the EQWM is shown with plus symbols and connected with thick dashed-dot gray lines. The thin dotted horizontal black lines correspond with the Stokes solution.

spectrum of frequencies, from quasi-equilibrium conditions to Stokes limit conditions, is due to the separate modeling of quasi-equilibrium and non-equilibrium effects. This is most clearly observed in figure 6.10 where the model's decomposition into quasi-equilibrium, laminar non-equilibrium, and turbulent non-equilibrium parts is shown. The periodic wall-stress, which is the wall-stress deviation from equilibrium conditions, is captured best by the LaRTE model for low frequencies, the laminar non-equilibrium model for high frequencies, and the turbulent non-equilibrium model for intermediate frequencies (since the LaRTE and laminar non-equilibrium models become out of phase with each other). These models effectively turn on or off depending on if the conditions consistent with these models are met. This is an important quality to have to capture both extremes of non-equilibrium.

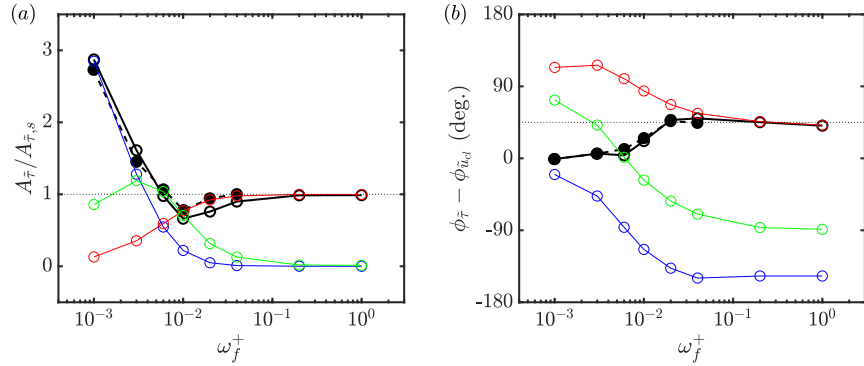


**Figure 6.10:** (a) The periodic wall-stress amplitude normalized by the Stokes solution and (b) the periodic wall-stress phase relative to the centerline velocity phase. Line types correspond with the DNS of Weng et al. (2016) (filled circles connected with thick dashed black lines) and LES using the MTS wall model (open circles connected with thick solid black lines), LaRTE (open circles connected with thick solid blue lines), laminar non-equilibrium (open circles connected with thick solid red lines), and turbulent non-equilibrium (open circles connected with thick solid green lines) components. The thin dotted horizontal black lines correspond with the Stokes solution.

Figures 6.11-6.15 show the periodic Reynolds stresses as a function of height and phase for several forcing frequencies. In order to compare LES with DNS, the subgrid scale (SGS) stresses are included for the shear-stress component, although the SGS contribution is negligible relative to the resolved stresses. Figure 6.11 shows  $\widetilde{u'v'}$  profiles at different times (where time is indicated by a shift in the vertical direction) whereas figure 6.12 shows the  $\widetilde{u'v'}$  amplitude and phase. For succinctness, only the amplitude and phase plots are shown for the normal stresses. Unlike the time-averaged Reynolds stress profiles in figure 6.5, the periodic Reynolds stresses for the WMLES do exhibit a dependency on the wall model choice. For instance, in figure 6.12(c) the EQWM agrees well with the DNS whereas the multi-timescale wall model significantly underpredicts the amplitude. This discrepancy (for this

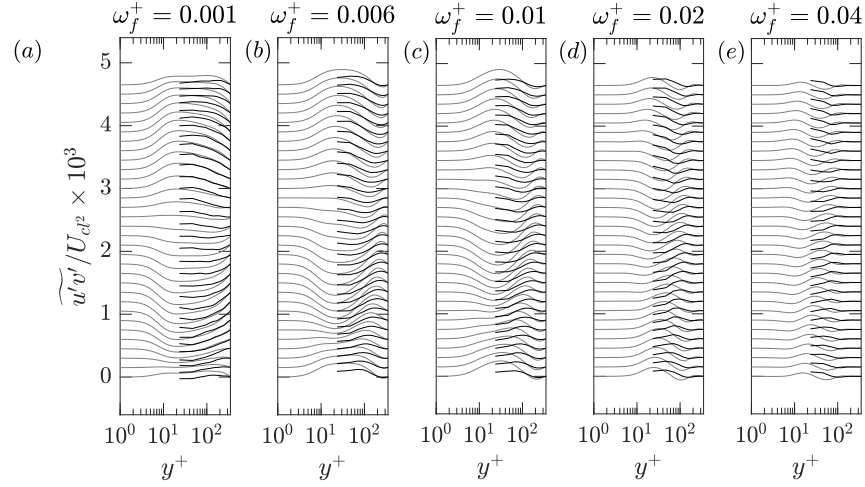


**Figure 6.11:** The time evolution of  $\widetilde{u'v'}$  at different phases of the wave cycle for different forcing frequencies:  $\omega_f^+ = 0.001, 0.006, 0.01, 0.02$ , and  $0.04$ . The profiles are  $T_f/32$  apart, and are offset by  $1 \times 10^{-1}$  units in the vertical direction. Gray lines correspond with the DNS of Weng et al. (2016). Black lines correspond with LES using the multi-timescale wall model.

particular frequency) is discussed in detail further below. Overall, the LES with the EQWM appears to agree with the DNS better than the multi-timescale wall model for the  $\widetilde{u'v'}$  and  $\widetilde{u'u'}$  components however the reverse is true for the  $\widetilde{v'v'}$  and  $\widetilde{w'w'}$  components where the EQWM tends to overpredict the amplitudes. It is interesting to note that the discrepancy between the MTS wall model and the EQWM is greatest for the intermediate frequencies and not for the highest frequency. This might be explained by the fact that for these frequencies the Stokes length is roughly the same height as the height of the first LES grid point which is the most sensitive point to the wall model.

The periodic Reynolds stress sensitivity to the wall model may further understood by examining the different contributions to the phase-averaged,

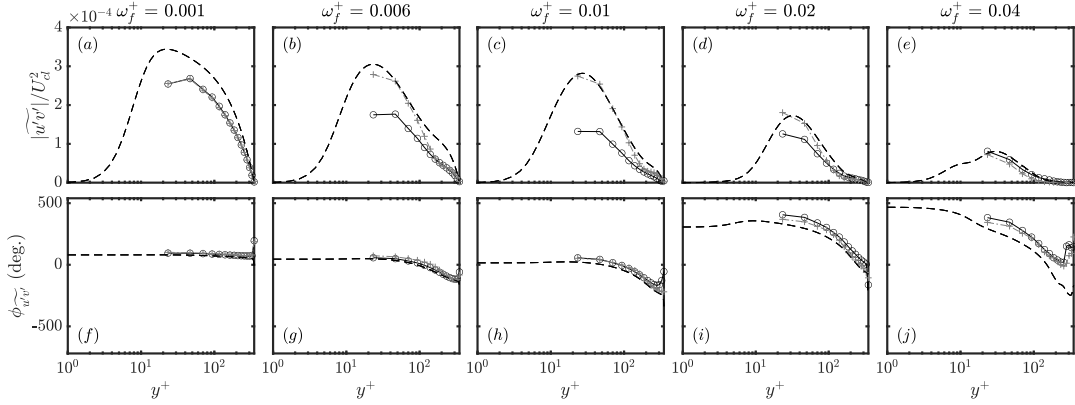


**Figure 6.12:** (a-e) amplitude and (f-j) phase lead of  $\widetilde{u'v'}$  for five forcing frequencies  $\omega_f^+ = 0.001, 0.006, 0.01, 0.02, 0.04$ . The DNS of Weng et al. (2016), the LES with the multi-timescale wall model, and the LES with the EQWM are shown with dashed lines, open circles with solid black connecting lines, and plus signs with gray dashed-dot connecting lines respectively.

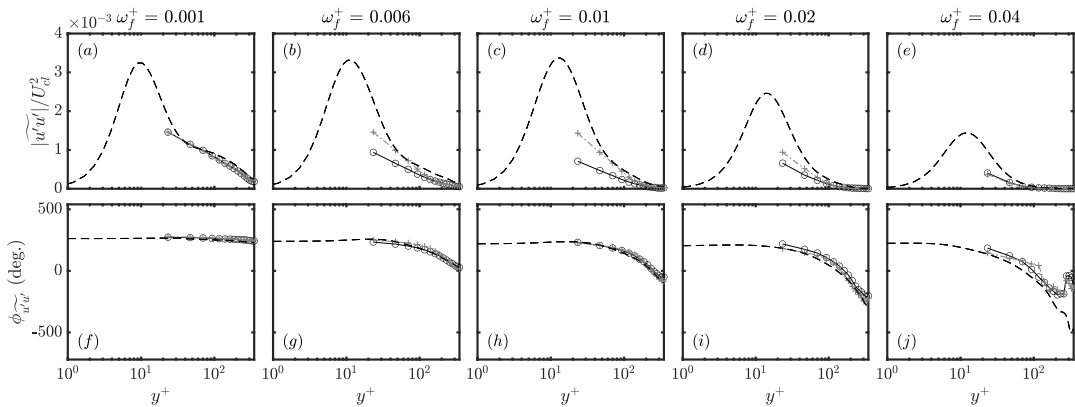


**Figure 6.13:** (a-e) amplitude and (f-j) phase lead of  $\widetilde{u'u'}$  for five forcing frequencies  $\omega_f^+ = 0.001, 0.006, 0.01, 0.02, 0.04$ . Line types are the same as in figure 6.12.

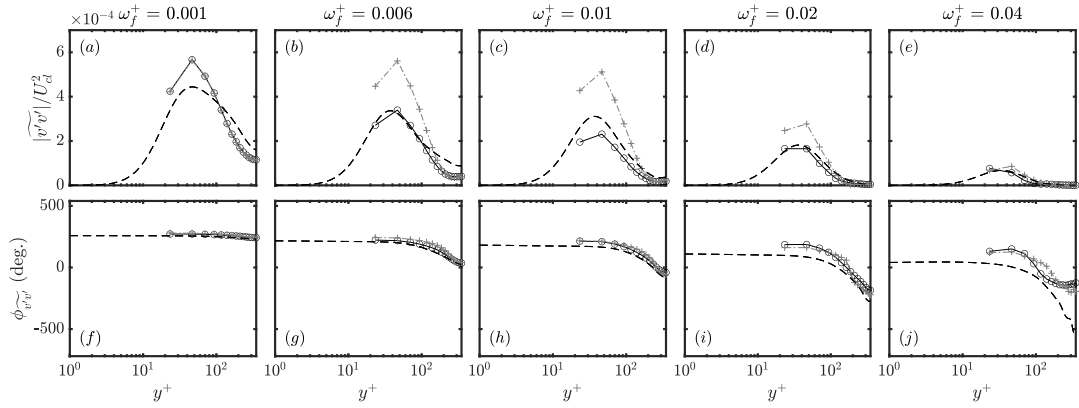


**Figure 6.14:** (a-e) amplitude and (f-j) phase lead of  $\widetilde{v'v'}$  for five forcing frequencies  $\omega_f^+ = 0.001, 0.006, 0.01, 0.02, 0.04$ . Line types are the same as in figure 6.12.

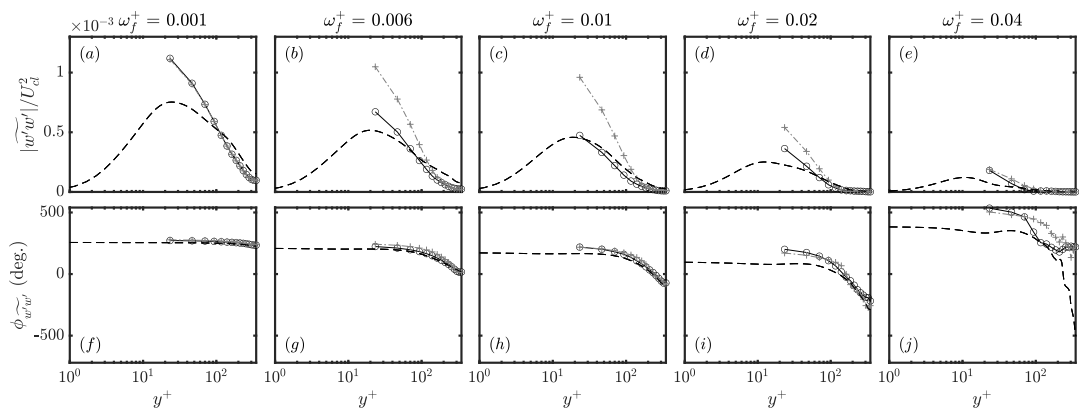


**Figure 6.15:** (a-e) amplitude and (f-j) phase lead of  $\widetilde{w'w'}$  for five forcing frequencies  $\omega_f^+ = 0.001, 0.006, 0.01, 0.02, 0.04$ . Line types are the same as in figure 6.12.

integrated momentum budget. These are related by

$$\int_0^y \frac{\partial \langle u \rangle}{\partial t} dy' = -\frac{y}{\rho} \frac{\partial \langle p \rangle}{\partial x} + \nu \frac{\partial \langle u \rangle}{\partial y} - \langle u'v' \rangle - \langle \tau_{wx} \rangle \quad (6.10)$$

where angled brackets represent phase averaging. Figure 6.16 shows the time signals of the different terms in equation (6.10) at three heights for the intermediate frequency  $\omega_f^+ = 0.01$ . Although the MTS wall model predicts the wall-stress much better than the EQWM, small discrepancies in the  $\partial_t \langle u \rangle$  term are correlated with noticeable discrepancies in the Reynolds stress since the Reynolds stress oscillation amplitude is small relative to the  $\partial_t \langle u \rangle$  term. This figure highlights the intricate relationship between each term in the momentum balance. Instead of focusing on how a wall model might be able to capture these details (i.e. how wall-stress fluctuations can affect the near wall turbulence), we give a greater focus on capturing the mean wall-stress behavior which is arguably the most important feature in wall modeling since an accurate skin friction prediction is usually the goal. We have shown in figures 6.7-6.10 that the MTSWM is more successful than the EQWM at achieving this goal.

### 6.3 Linearly accelerating channel flow

Wall modeled LES were also conducted for a turbulent channel flow which is accelerated linearly over a ramp time,  $T$ . The flow setup is based on the DNS study of S. Y. Jung and Kim (2017). In their work, the linear acceleration is imposed by modifying the pressure gradient forcing. The governing equation for the pressure gradient is found by integrating the ensemble-averaged

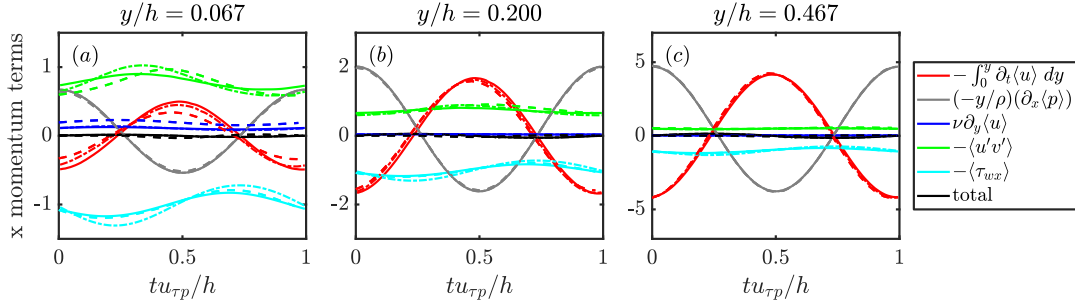


**Figure 6.16:** Time signals of budget terms for  $\omega_f^+ = 0.01$  in the integrated, phase-averaged x-momentum equation for different integration heights. Line types correspond with the DNS of Weng et al. (2016)(dashed lines), LES with the MTS wall model (solid lines), and LES with the EQWM (dashed-dot lines). Line colors correspond with different terms in the budget as indicated in the figure legend.

streamwise momentum equation in the wall normal direction over the entire channel. This yields

$$-\frac{1}{\rho} \frac{\partial \langle p \rangle^*}{\partial x}(t^*) = \frac{1}{2Re_{\tau,i}} \frac{dRe_m(t^*)}{dt^*} + \left( \frac{Re_\tau(t^*)}{Re_{\tau,i}} \right)^2 \quad (6.11)$$

where a star indicates normalization with  $h$  and  $u_{\tau p,i} \equiv \sqrt{-h\rho^{-1}(\partial_x \langle p \rangle)_i}$  (the friction-velocity based on the pressure gradient forcing before acceleration),  $Re_{\tau,i} \equiv u_{\tau p,i} h / \nu$  is the initial friction Reynolds number, and  $Re_m \equiv U_m 2h / \nu$  is the bulk mean Reynolds number with  $U_m$  being the bulk mean velocity (averaged over the entire channel). Each term on the right hand side of equation (6.11) is modeled since they are not known a-priori. A benefit of this approach is that the pressure gradient remains unaffected by the LES wall model and the LES has the exact same pressure gradient forcing as used in the DNS of S. Y. Jung and Kim (2017). If  $t^* = 0$  marks the beginning of the

acceleration, then  $Re_m$  is set according to

$$Re_m(t^*) = Re_{m,i} \quad t^* < 0 \quad (6.12)$$

$$Re_m(t^*) = Re_{m,i} + \frac{t^*}{T^*} (Re_{m,f} - Re_{m,i}) \quad 0 \leq t^* < T^* \quad (6.13)$$

$$Re_m(t^*) = Re_{m,f} \quad t^* \geq T^* \quad (6.14)$$

where the initial and final bulk mean Reynolds numbers,  $Re_{m,i}$  and  $Re_{m,f}$  respectively, are estimated to give the correct initial and final friction Reynolds numbers. For all simulations considered in this study, the initial and final friction Reynolds numbers are  $Re_{\tau,i} = 180$  and  $Re_{\tau,f} = 395$  to match those of S. Y. Jung and Kim (2017). Since these are low Reynolds numbers, following S. Y. Jung and Kim (2017) we use the empirical relationship given by Dean (1978) to relate the bulk mean Reynolds number with the friction Reynolds number:  $C_f \equiv \tau_w / \frac{1}{2} U_m^2 \approx 0.073 Re_m^{-1/4}$ . To obtain the  $Re_{m,i}$  and  $Re_{m,f}$  as a function of  $Re_{\tau,i}$  and  $Re_{\tau,f}$ , respectively, we use  $Re_m = (8/0.073)^{4/3} Re_{\tau}^{8/3}$ . Then once  $Re_m(t)$  has been obtained from equations (6.12-6.14), we use the inverse relation  $Re_{\tau} = (0.073/8)^{1/2} Re_m^{3/8}$  to substitute  $Re_{\tau}(t)$  into equation (6.11) to obtain the pressure gradient forcing.

Table 6.2 shows the acceleration rates considered and their corresponding flow regimes. The flow regime classification is based on the work of S. Y. Jung and Kim (2017) and the trends observed for the skin friction. A flow is considered “transitional” if laminar-like behavior is observed initially (e.g. through the skin friction) which breaks down into a new turbulent state as turbulent spots form. A flow is considered “quasi-steady” if the skin friction

does not deviate far from its steady value at a given flow rate (i.e. agrees with “Dean’s correlation” specified above). The “intermediate” flow doesn’t exhibit transitional characteristics yet its skin friction differs enough from its steady value that it cannot be labeled quasi-steady.

Large eddy simulations were performed with the MTS wall model and compared against LES with the EQWM. The domain length, resolution, and other simulation details are the same as the pulsatile channel flow, specified in §6.2. Again, a constant CFL of 0.05 was used which gives an initial time step size around  $\delta t^* \approx 4.6 \times 10^{-4}$  and a final time step size (long after the acceleration) around  $\delta t^* \approx 1.9 \times 10^{-4}$ . Note the time step size decreases as the flow accelerates to achieve a constant CFL. This time step size is several orders of magnitude smaller than the fastest acceleration rate thus ensuring all dynamics are well resolved temporally.

Figure 6.17 shows time signals of the imposed pressure gradient forcing and the resulting bulk mean Reynolds numbers for each of the acceleration rates. The pressure gradient forcing is designed to be the same between the LES and the DNS of S. Y. Jung and Kim (2017) which is observed in figure 6.17(a). However, the mean Reynolds number is not directly controlled so there can be discrepancies between the LES and DNS which we see in figure 6.17(b). The acceleration rates match well between the DNS and the LES with largest deviations occurring for the slowest acceleration rate ( $T^* = 10$ ) at the end of the acceleration period. This is caused by a combination of factors with the primary contributors being the performance of the wall model and the SGS model.

$T^* \equiv Tu_{\tau p,i}/h$	flow regime
0.1	transitional
1.0	transitional
3.0	intermediate acceleration
5.0	quasi-steady
10.0	quasi-steady

**Table 6.2:** The acceleration/ramp rates simulated and the flow regime classification. For comparison, the relevant wall modeling time scales are  $T_s^* = 2.20$ ,  $t_v^*/h = 0.80$  and  $T_\Delta^* = 1.22$  where the timescales are computed before the flow is accelerated (i.e.  $t^* \leq 0$ ).

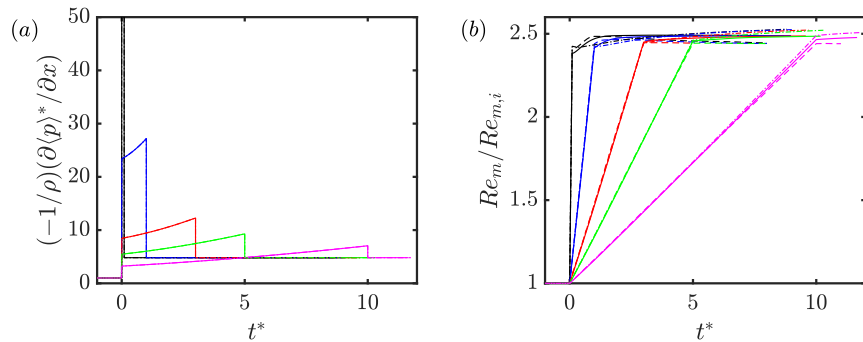


**Figure 6.17:** Time signals of (a) the pressure gradient forcing and (b) the mean Reynolds number ( $Re_m = 2hU_m/\nu$ ) divided by the initial mean Reynolds number,  $Re_{m,i}$ , for different acceleration ramp rates. Ramp rates of  $T^* = 0.1, 1.0, 3.0, 5.0, 10.0$  correspond with black, blue, red, green, and magenta lines, respectively. Line types for the DNS of S. Y. Jung and Kim (2017), LES with the multi-timescale wall model, and LES with the EQWM are dashed, solid, and dashed-dot, respectively.

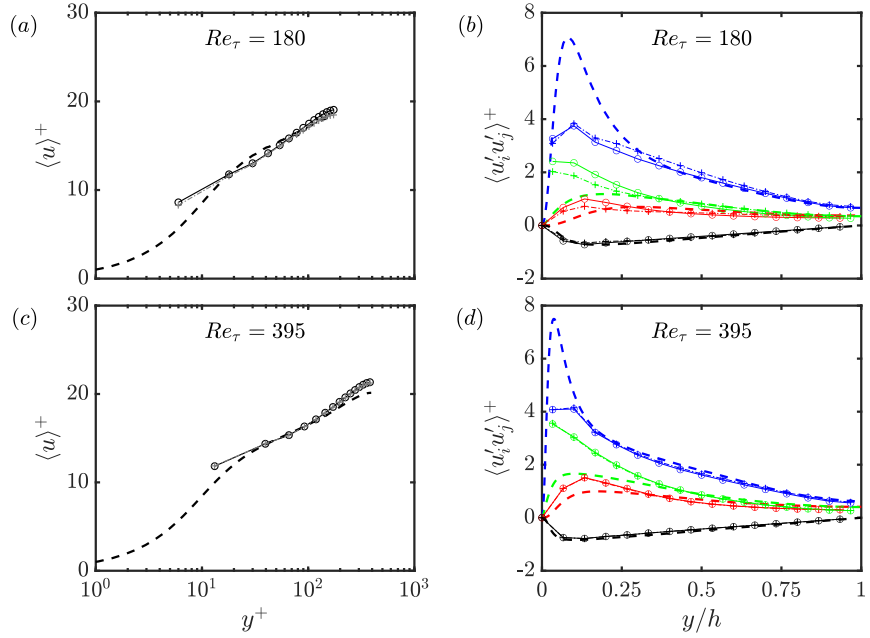


**Figure 6.18:** The mean velocity profiles and Reynolds stresses (a, b) before acceleration and (c, d) after acceleration once the flow has achieved its new steady state. Dashed lines correspond with the DNS of Moser et al. (1999), circles with solid connecting lines correspond with LES with the MTS wall model, and plus signs with dashed-dot connecting lines correspond with LES with the EQWM. In panels (b, d),  $\langle u'v' \rangle$ ,  $\langle v'w' \rangle$ , and  $\langle w'u' \rangle$  are shown with blue, red, green, and black lines, respectively.

Figure 6.18 shows the mean velocity (left column) and mean Reynolds stresses (right column) before the acceleration (top row) and long after the acceleration once the flow has reached its new steady-state (bottom row). The LES and DNS agree reasonably well, with overall trends similar to those observed and discussed for the time-averaged profiles of pulsating channel flow (figure 6.5). Note that the slight over-prediction of the velocity near the center of the channel causes the over-prediction of the mean Reynolds number after the acceleration period seen in figure 6.17(b).

Time signals of the planar-averaged wall-stress for each of the acceleration rates considered are shown in figures 6.19 and 6.20. We first show the results

in terms of the skin friction coefficient,  $C_f \equiv 2\tau_w/U_m^2$  in figure 6.19, in order to highlight the evolution during what is often termed a “turbulent to turbulent transition”. The acceleration process is marked by an initial fast increase in the skin friction where a laminar Stokes layer develops; the skin friction then decays until the transition time where (in the DNS) turbulent streaks would start developing and ultimately increase the skin friction to a new turbulent state at a higher Reynolds number. For example, He, Ariyaratne, and Vardy (2011) identify three acceleration stages for the wall-stress with the following characteristics: (1) the turbulence remains “frozen” and the wall-stress is governed by a laminar solution, (2) the wall-stress increases rapidly with many signatures of a transition-like process, (3) the wall-stress asymptotically approaches its quasi-steady value. Across each of these stages the velocity deviation from its initial value (ensemble averaged) is governed by the equation

$$\frac{\partial \langle u \rangle^\wedge}{\partial t} = -\frac{1}{\rho} \frac{\partial \langle p \rangle^\wedge}{\partial x} + \nu \frac{\partial^2 \langle u \rangle^\wedge}{\partial y^2} - \frac{\partial \langle u'v' \rangle^\wedge}{\partial y} \quad (6.15)$$

where angled brackets represents ensemble averaging and  $F^\wedge \equiv F(t) - F(t < 0)$  (for any variable  $F$ ) indicates the change in a variable from its initial value before the acceleration. The Reynolds shear stress deviation is typically neglected during the first stage because the turbulence is assumed to be “frozen” (He, Ariyaratne, & Vardy, 2011). These arguments lead to a laminar solution to equation (6.15) (Sundstrom & Cervantes, 2018c):

$$\langle u_{lam} \rangle^\wedge = U_m \left[ 1 - (1 + 2\eta^2) \operatorname{erfc}(\eta) + \frac{2}{\sqrt{\pi}} \eta e^{-\eta^2} \right] \quad \text{where } \eta = \frac{y}{\sqrt{4\nu t}} \quad (6.16)$$

which has the corresponding wall-stress

$$\langle \tau_{w,lam} \rangle^\wedge = 2 \frac{dU_m}{dt} \sqrt{\frac{\nu t}{\pi}}. \quad (6.17)$$

The thin dotted line in figure 6.19 shows the laminar analytical solution during this initial acceleration stage (shifted to have an initial wall-stress of  $u_{\tau p,i}^2$ ). The DNS of S. Y. Jung and Kim (2017) is shown with the thick dashed line. All acceleration rates have a brief period where DNS wall-stress closely follows the laminar solution. However, for  $T^* = 0.1$  and  $T^* = 1$  the laminar solution persists longer (relative to the acceleration rate) and there is a distinctive time where the skin friction quickly increases, departing from this laminar state. This is a feature of stage 2, and is indicative of a transition-like process occurring. S. Y. Jung and Kim (2017) identified these two acceleration rates as having a bypass-like transition. The rest of the acceleration rates are in a state of quasi-equilibrium where the wall-stress does not differ far from its steady value at the instantaneous Reynolds number.

For the slowest acceleration case considered ( $T^* = 10$ ), the MTS wall model and the EQWM show little difference between them over the entirety of the acceleration. This trend is expected since the flow is in a state of quasi-equilibrium and equilibrium assumptions made by the EQWM are a good approximation. Note both LES skin frictions differ from the DNS long after the acceleration because of the overpredicted velocity in the wake region as seen in figure 6.18(c). For the faster acceleration rates, the EQWM performs very poorly relative to the DNS. The EQWM is unable to capture the quick increase in the skin friction caused by the developing laminar Stokes layer. The EQWM

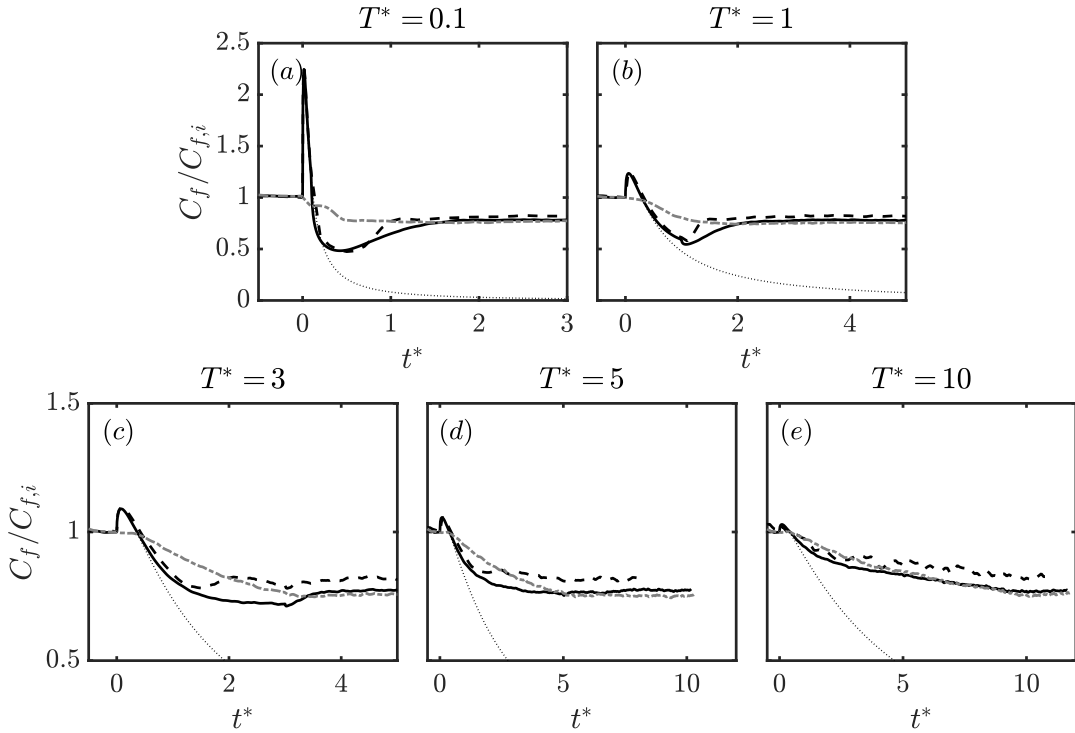


**Figure 6.19:** Time signals of the skin friction coefficient for different acceleration ramp rates. Ramp rates of  $T^* = 0.1, 1.0, 3.0, 5.0, 10.0$  correspond with panels (a), (b), (c), (d), and (e), respectively. The curves compared are the DNS of Weng et al. (2016) (thick dashed black line), LES with the EQWM (thick dashed-dot gray line), and LES with the multi-timescale wall model (thick solid black line). The thin black dotted line is the laminar solution given by equation (6.17).

also overpredicts the skin friction once the flow starts transitioning to its new turbulent state. During this time, the EQWM incorrectly attributes the increase in velocity to an increase in the wall-stress. This undesired effect justifies the use of a velocity correction in the equilibrium closure for the MTS wall model, as introduced in §5.2.2.

The MTS wall model, on the other hand, does quite well over each of the acceleration rates considered. It is able to capture the wide range of flow features, from the rapid increase in  $C_f$  initially, to the transition between

turbulent states. Figure 6.20 shows the different contributions to the MTS wall-stress so we may clearly see how each component behaves during the different stages of the flow. For all of the acceleration rates, the lamNEQ wall model is dominant when the flow first accelerates. This response allows the MTS wall model to capture the sharp initial increase in the wall-stress, which the EQWM is unable to do. Conversely, the LaRTE wall model has a delayed response to the acceleration because of its inherent relaxation dynamics. Without the velocity correction, however, the LaRTE model responds too quickly causing the wall-stress to be overpredicted initially. Also as expected, after the flow has accelerated and approaches its new steady state, the LaRTE model is the primary contributor to the wall-stress. In between these two extremes (after the lamNEQ contribution decays, but before the LaRTE model responds) the turbNEQ response is the most prominent. This also happens to be the time when the turbulent-to-turbulent transition occurs. Figures 6.20(a) and (b) show the turbNEQ model helps speed-up the wall-stress response during this transition stage.

Further insights can be obtained by focusing on the relationship between the LES velocity at the wall model point and the wall-stress evolution and fluctuations. According to the turbNEQ model equations (5.1) and (5.3), an increase in  $\tau'_{wx}$  means that the LES velocity is increasing faster than the quasi-equilibrium velocity obtained from LaRTE, thus leading to a velocity deviation  $u'_\Delta$  (see figure 6.21 for time signals of this velocity as well as other model contributions to the LES velocity). For channel flow with a constant pressure gradient, this velocity deviation may be explained by turbulent

fluctuations. However, for linearly accelerating channel flow, this velocity deviation has a non-zero average which can be explained as follows. As the flow accelerates, the initial growth in  $U_{LES}$  is accounted for by the laminar contribution,  $u''_\Delta$ , and the turbulent contribution,  $u'_\Delta$ , is small. However, near the flow transition time, the laminar Stokes layer decays as it interacts with the ‘outside’ turbulence and there is no change in the pressure gradient to drive its growth. This occurs around the time  $t = t_v$  since this timescale is defined as the time for a Stokes layer to grow from the wall to the edge of the laminar viscous sublayer. After this time, there is a difference between the turbulent state away from the wall and near the wall. In DNS studies, this leads to the generation of near wall streaks and a breakdown to a new turbulent state (He & Seddighi, 2013, 2015). In LES with the MTS wall model, this is measured through  $u'_\Delta$  and the turbNEQ model attempts to account for the expected increase in the wall-stress during transition. In practice, the turbNEQ model responds less quickly than desirable, as seen by the difference between the DNS and LES curves after transition in figure 6.20. A possible explanation is that the breakdown to turbulence caused by near-wall streak instabilities is a rapid phenomenon (Hack & Zaki, 2014) that is not detected by the first LES-velocity point which is too far from the wall. The turbNEQ model relies solely on LES velocity information and therefore cannot account for this subtle effect whose modeling requires more detailed future efforts.

Single-point time signals (no planar averaging) of the different modelled components of the LES velocity are shown in figure 6.21. The LES velocity ( $U_{LES}$  shown in gray) is decomposed according to equation (5.1) with

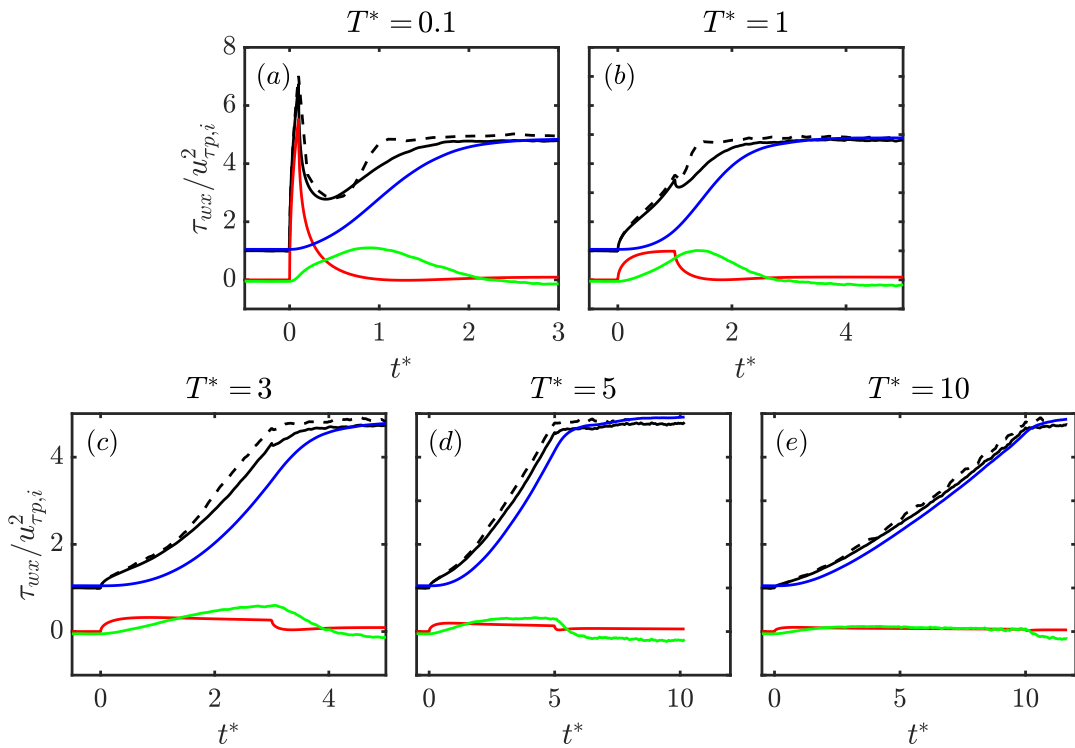


**Figure 6.20:** Time signals of the wall-stress for different acceleration ramp rates. Ramp rates of  $T^* = 0.1, 1.0, 3.0, 5.0, 10.0$  correspond with panels (a), (b), (c), (d), and (e), respectively. The curves compared are the DNS of Weng et al. (2016) (thick dashed black line) and the LES with the MTS wall model (thick solid black line) with LaRTE (thick blue line), lamNEQ (thick red line), and turbNEQ (thick green line) components.

LaRTE ( $u_\tau f(\Delta^+)$  shown in blue), lamNEQ ( $u'_\Delta$  shown in red), and turbNEQ ( $u''_\Delta$  shown in green) contributions. It is clear from the figure that the LaRTE portion effectively filters out the large LES velocity fluctuations due to the relaxation dynamics of LaRTE. It also captures the mean value before and after the linear acceleration. The lamNEQ portion captures the initial linear behavior of the velocity as soon as the flow accelerates. The turbNEQ contribution is twofold. On the one hand, it is responsible for capturing the majority of the LES velocity fluctuations. On the other hand, it captures the behavior of the velocity in response to transition, as discussed previously. Figure 6.21 demonstrates the usefulness of decomposing a complicated flow into its constitutive parts, as is possible with the multi-timescale wall model.

Figure 6.22 shows time signals of the (planar averaged) velocity perturbation at different heights for a fast acceleration case ( $T^* = 0.1$ ) and a slow acceleration case ( $T^* = 5$ ). For the fast accelerating case, the LES for both wall models gives the correct linear trend during the accelerating phase. However, after the acceleration is over the LES predicts a decrease in the velocity perturbation too soon (with the exception of the channel centerline) with the EQWM generally giving a larger drop in the velocity perturbation than the MTS wall model, the latter therefore being closer to the DNS data. For the slow acceleration case, the LES and the DNS agree well over all times. This is expected since the flow is in a state of quasi-equilibrium and thus both wall models yield similar mean wall-stresses.

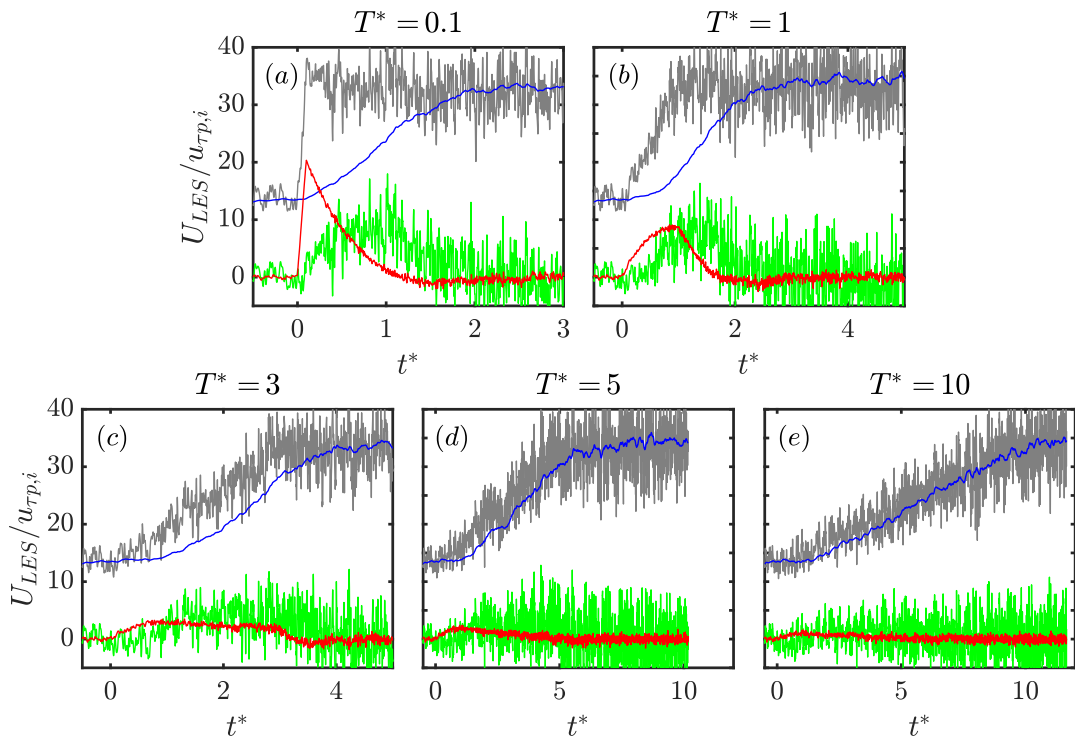


**Figure 6.21:** Time signals at a representative single point  $(x, y, z) = (L_x/2, \Delta, L_z/2)$  of the different modeling components of the LES velocity for several acceleration ramp rates. Ramp rates of  $T^* = 0.1, 1.0, 3.0, 5.0, 10.0$  correspond with panels (a), (b), (c), (d), and (e), respectively. The different lines correspond to  $U_{LES}$ ,  $u_{\tau f}(\Delta^+)$ ,  $u'_{\Delta}$ , and  $u''_{\Delta}$ , shown in gray, blue, green, and red, respectively.

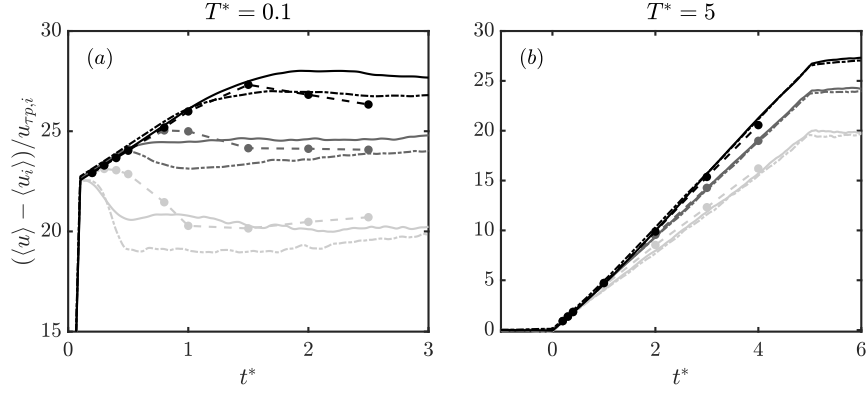


**Figure 6.22:** Time signals of the velocity perturbation (from the initial condition) at several heights for (a)  $T^* = 0.1$  and (b)  $T^* = 5.0$ . From light to dark lines, the heights correspond with  $y/h = 0.167, 0.5, 0.967$  which are the third, eighth, and centerline LES grid points, respectively. The DNS (from S. Y. Jung and Kim (2017)), the LES with the multi-timescale wall model, and the LES with the EQWM correspond with dashed lines with filled circles, solid lines, and dashed-dot lines, respectively. The circles correspond with the sample times given for the DNS.

## 6.4 The MTS wall model in the limit of instantaneous relaxation

A possible variant of the MTS wall model is now explored by considering the limit of a vanishingly small relaxation time scale, i.e.,  $T_s \rightarrow 0$ . In that limit the friction velocity from LaRTE is equal to its equilibrium value (i.e.  $\mathbf{u}_\tau = \bar{\boldsymbol{\tau}}_w^{\text{eq}} / (\bar{\tau}_w^{\text{eq}})^{1/2}$  with the corresponding wall-stress  $u_\tau \mathbf{u}_\tau = \bar{\boldsymbol{\tau}}_w^{\text{eq}}$ ) and the quasi-equilibrium velocity becomes  $\bar{\mathbf{u}}_\Delta = \mathbf{u}_\tau f(\Delta^+)$ , since  $\mathbf{u}_\tau$  is obtained from the equilibrium model that uses  $\bar{\mathbf{u}}_\Delta$  as input velocity. Therefore, according to equation (5.1),  $\mathbf{u}'_\Delta = 0$  and the turbulent turbNEQ portion is subsumed into the equilibrium wall model contribution. The total wall-stress for the MTS wall model in the limit  $T_s \rightarrow 0$  is then simply

$$\boldsymbol{\tau}_w = \bar{\boldsymbol{\tau}}_w^{\text{eq}} + \boldsymbol{\tau}_w'' \quad (6.18)$$

where  $\bar{\tau}_w^{\text{eq}}$  is evaluated according to the fit from equation 5.9 and  $\tau_w''$  is governed by equation 3.5. The MTS wall model in the limit of instantaneous relaxation, governed by equation 6.18, is referred to as the equilibrium MTS (EQMTS) wall model. It is important to note that the quasi-equilibrium velocity input still contains the velocity correction to the LES velocity (equations 5.11 and 5.12) to account for changes in the LES velocity caused by the laminar Stokes layer. For succinctness, the equilibrium model component,  $\bar{\tau}_w^{\text{eq}}$ , with a corrected velocity input is referred to as the “corrected equilibrium” model.

We now apply this model to pulsating and linearly accelerating channel flow. Representative resulting stress evolution plots are shown in figures 6.23-6.25. For pulsating channel flow, the EQMTS wall model is nearly identical to the EQWM for the two lowest frequencies ( $\omega_f^+ = 0.001, 0.003$ ). For low frequencies the laminar non-equilibrium contribution is relatively small, meaning the corrected equilibrium wall-stress is dominant. Additionally, while  $T_f \gg T_\Delta$ , the velocity correction has a negligible impact and the corrected equilibrium wall model thus behaves similarly to the standard EQWM (e.g. see figure 6.24(a) where the corrected equilibrium wall-stress component and EQWM curves are nearly indistinguishable). These two effects cause the EQMTS wall model to behave similarly to the EQWM for low frequencies where performance is good.

Most evident in figure 6.23(d), the total EQMTS wall-stress is not sinusoidal. From figure 6.24 we see this is caused by the corrected equilibrium model component which becomes non-sinusoidal as frequency is increased. This must be caused by the velocity correction since this is the only difference

between the corrected equilibrium and EQWM models. The model equation 5.11 shows  $\mathbf{u}_\Delta''$  evolves at timescale  $T_\Delta$ . When subtracted from the LES velocity (which evolves at the forcing period,  $T_f$ ), the quasi-equilibrium velocity input becomes distorted and non-sinusoidal if  $T_f$  and  $T_\Delta$  are of similar order. This occurs in the intermediate and high frequency regime.

For high frequencies, the EQMTS wall model behaves similar to the regular MTS wall model. This is primarily because the lamNEQ model is dominant here which is shared between the two models and therefore any differences between the corrected equilibrium model and the LaRTE+turbNEQ stresses (figure 6.24(c)) are small relative to the total wall-stress. At high frequencies ( $\omega_f^+ \geq 0.04$ ) the velocity correction effectively filters out the corresponding high frequency content of the LES velocity which causes the equilibrium portion of the equilibrium MTS wall model to respond slowly, similar to the LaRTE model. Without the velocity correction, the total wall-stress for the EQMTS wall model is simply the lamNEQ wall-stress plus the EQWM wall-stress. This leads to an overprediction of the total wall-stress, thus showing the necessity of the velocity correction for non-equilibrium flows.

For linearly accelerating channel flow, the EQMTS wall model is able to achieve some of the same trends in the skin friction as the full MTS wall model (e.g. the sharp increase in the skin friction initially), although it tends to over predict the skin friction after the laminar stage of the acceleration. The velocity correction allows the EQMTS model to have a delayed response to changes in the pressure gradient so that the lamNEQ model can capture the non-equilibrium response to fast changes in the pressure gradient. However

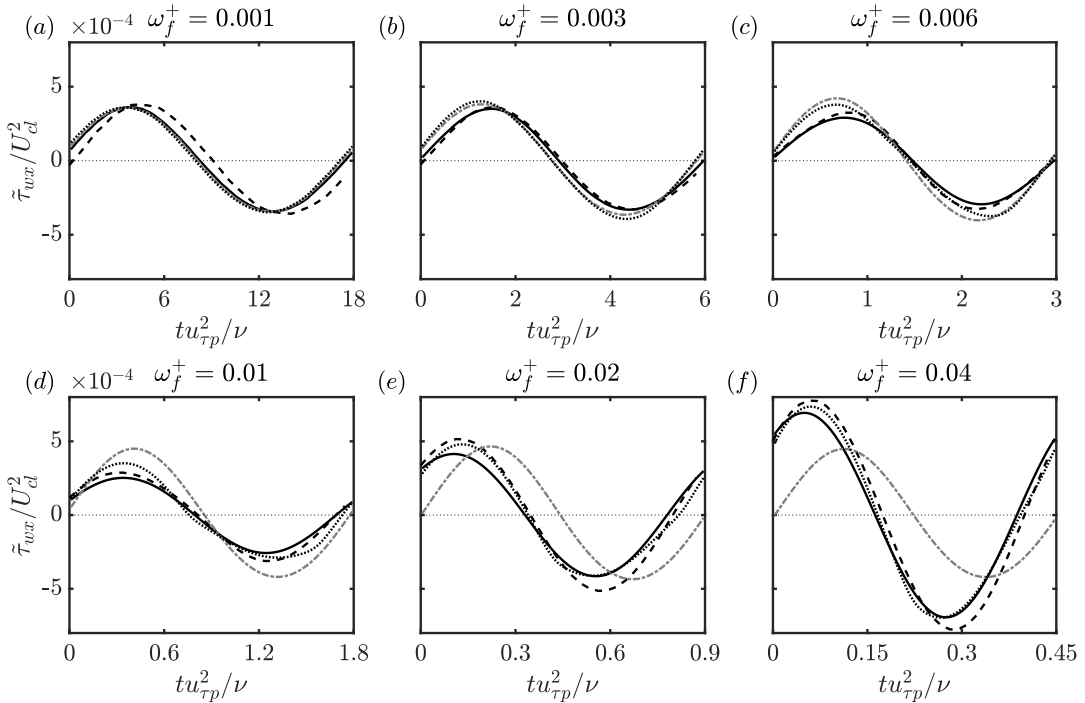


**Figure 6.23:** Single period time evolution of the periodic streamwise wall-stress  $\tilde{\tau}_{wx}$  for several forcing frequencies,  $\omega_f^+ = 0.001, 0.003, 0.006, 0.01, 0.02, 0.04$  (subplots (a-f), respectively). Line types correspond with LES using the multi-timescale wall model (thick solid black), LES using the EQWM (thick dashed-dot gray), LES using the equilibrium MTS wall model (thick dotted black) and DNS from Weng et al. (2016) (thick dashed black). The phase within the cycle is based on the imposed forcing frequency.

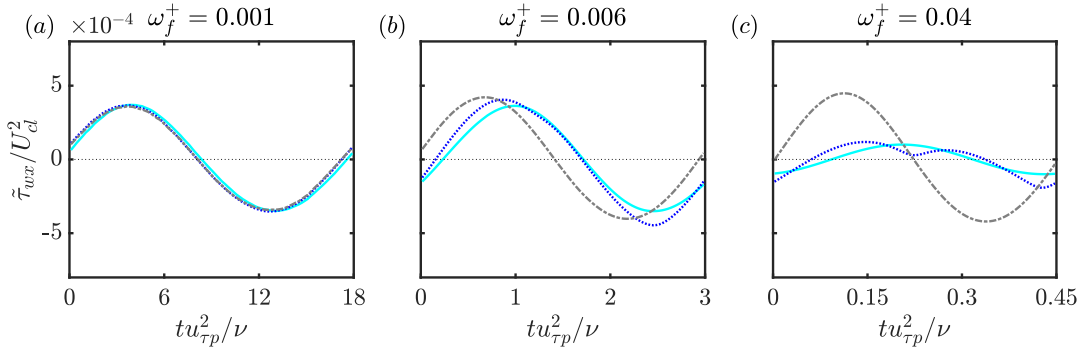


**Figure 6.24:** Single period time evolution of the periodic streamwise wall-stress  $\tilde{\tau}_{wx}$  for low, intermediate, and high forcing frequencies:  $\omega_f^+ = 0.001, 0.006, 0.04$  (subplots (a-c), respectively). Curves shown include the corrected equilibrium component of the EQMTS wall model (dotted blue), the EQWM wall-stress (dashed-dot gray), and the LaRTE+turbNEQ wall-stresses (solid cyan). The phase within the cycle is based on the imposed forcing frequency.

the velocity correction timescale,  $T_\Delta$ , appears to not be long enough for the EQMTS wall model to give the correct wall-stress since the skin friction begins to increase too early for all of the accelerations rates shown in figure 6.25. In fact, the EQMTS wall-stress even exceeds the EQWM wall-stress during portions of the flow acceleration for the slow acceleration cases. This must be caused by the slow decay of the lamNEQ wall-stress since the corrected equilibrium wall-stress  $\bar{\tau}_w^{\text{eq}}$  can never be greater than the EQWM wall-stress (since it is essentially just a delayed version of it).

We now briefly comment on the differences in computational cost between the wall models considered. For all wall modeled LES considered here, the computational cost remains insignificant compared to wall-resolved LES because the wall models do not require solving equations on a fine, near-wall mesh (see e.g. Choi and Moin (2012) and X. I. A. Yang and Griffin (2021) for more details). For pulsatile channel flow, the average percent of time spent

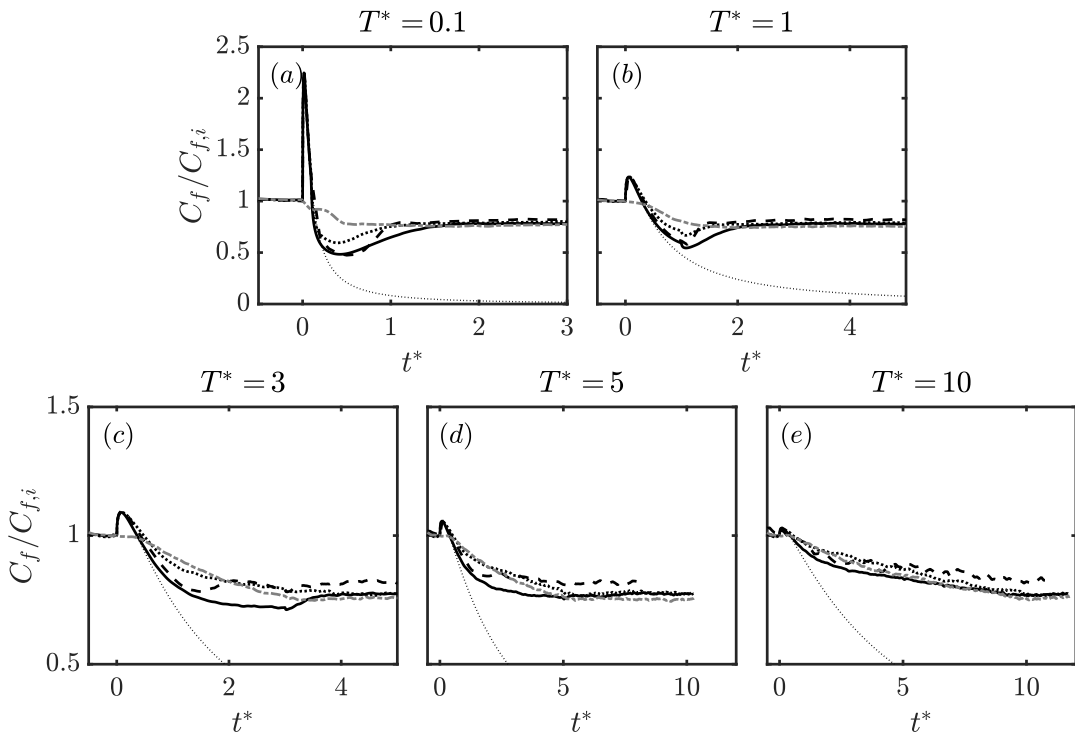


**Figure 6.25:** Time signals of the skin friction coefficient for different acceleration ramp rates. Ramp rates of  $T^* = 0.1, 1.0, 3.0, 5.0, 10.0$  correspond with panels (a), (b), (c), (d), and (e), respectively. The curves compared are the DNS of Weng et al. (2016) (thick dashed black line), LES with the EQWM (thick dashed-dot gray line), LES with the EQMTS wall model (thick dotted black line), and LES with the MTS wall model (thick solid black line). The thin black dotted line is the laminar solution given by equation 6.17.

in the wall model function call (over the total time spent per time step) was measured to be 18.973% for the MTS wall model, 16.373% for the EQMTS wall model, and 3.390% for the EQWM. Similar percentages were found for the linearly accelerating channel flow. The  $\sim 3\%$  of time spent for the EQWM is consistent with expectations since 30 grid points were used in the wall normal direction and wall model computations are done over a single horizontal plane. The additional  $\sim 15\%$  of time spent for the MTS and EQMTS wall models is a direct result of the additional 48 exponential terms (per point on the horizontal wall modeling plane) needed for the lamNEQ model. This increase in cost is expected since  $N_{exp}$  times more computations were used for the lamNEQ model. However it is clear from the present results that the lamNEQ model plays a critical role in properly modeling the wall-stress in instances of high non-equilibrium, therefore no effort was made to reduce  $N_{exp}$  to decrease the computational cost. It is possible that further gains in efficiency could be made by reducing  $N_{exp}$  following a careful study of loss of accuracy versus computational efficiency. In this work we opted to keep the model highly accurate since the overall cost increase was relatively small. Finally, the minor difference in cost between the MTS and EQMTS wall models shows that the additional complexity of the LaRTE model does not equate with a significant increase in computational time.

Overall, the EQMTS wall model is able to capture several of the important features in non-equilibrium flows (since the lamNEQ model captures the majority of these dynamics) while maintaining some of the simplicity of the EQWM. While the full MTS model agrees somewhat better with the DNS for

the majority of the non-equilibrium flows tested, the EQMTS wall model can be considered as a simpler alternative since it does not require the solution of the LaRTE friction-velocity transport equation.

## 6.5 Summary

A multi-timescale wall model for large eddy simulations has been developed and applied to a wide variety of flows from quasi-equilibrium to non-equilibrium conditions. The MTS wall model consists of LaRTE, lamNEQ, and turbNEQ components which allow the wall model to capture the full range of timescales necessary to model non-equilibrium flows. Figure 5.3 presents the various length and timescales included in the MTS wall model. The LaRTE+lamNEQ model has been augmented to represent additional physical effects not included before. For the LaRTE model, this includes a newly added “velocity correction” to the LES velocity input to the equilibrium closure and inclusion of the full pressure gradient term in the closure (both discussed in §5.2). The velocity correction allows for a more accurate prediction of  $\bar{\tau}_\Delta$  when using an equilibrium closure. And, to represent the contributions from unresolved turbulent eddies, we introduced the turbNEQ term which models the wall-stress response to velocity fluctuations around their quasi-equilibrium value (see equation 5.1). It is worthwhile pointing out that the quasi-equilibrium portion of the MTS model bears resemblance to behavior of slow, large-scale outer boundary layer motions that have been observed to cause amplitude modulation of near wall, small-scale turbulence

(Mathis et al., 2009). Amplitude modulation is a phenomenon that has received considerable attention over the past decade (Marusic & Monty, 2019). In future work, it would be of interest to explore the relationship between the LaRTE inherent timescale  $T_s$  and the characteristic timescale of the modulating motions identified in the work of Mathis et al. (2009).

First, in §6.1, the equilibrium/stationary channel flow and sudden spanwise pressure gradient (SSPG) test cases from chapter 4 are repeated for the MTS wall model. The streamwise wall-stress PDFs for the equilibrium channel flow actually improve relative to the original LaRTE+lamNEQ wall model. This is primarily due to the turbNEQ model which dominates wall-stress fluctuations for the MTS wall model. The spanwise wall-stress variance is over-predicted, however, which appears to be related to the over-prediction of the spanwise resolved velocity fluctuation variance in the LES due to the SGS closure as mentioned in §6.2. For the SSPG flow, the MTSWM shows good agreement with the DNS for the spanwise component of the wall-stress, similar to what was seen in the LaRTE+lamNEQ model in chapter 4. The streamwise wall-stress component, however, shows an increased delayed response to the SSPG and still cannot predict the short drop in  $\tau_{wx}$  caused by the scrambling of momentum carrying turbulent structures which would require further modeling.

The multi-timescale wall model was then applied to two distinct non-equilibrium flows, namely pulsating channel flow in §6.2 and linearly accelerating channel flow in §6.3. For pulsating channel flow, the forcing frequency was varied to achieve conditions ranging from quasi-equilibrium to

non-equilibrium. As expected, for low frequencies the MTS wall model and EQWM are very similar and agree well with the DNS of Weng et al. (2016). However, as the frequency is increased the EQWM progressively departs from the DNS results whereas the MTS wall model displays good agreement with the DNS. Time signals of the different components of the MTS wall model show that the LaRTE, turbNEQ, and lamNEQ wall-stresses are most dominant for low, intermediate, and high frequencies, respectively. This is consistent with the length and time scale schematic of figure 5.3. Amplitude and phase plots of the periodic velocity show little difference between the MTS wall and the EQWM over all of the frequencies tested. However, amplitude and phase plots of the periodic Reynolds stresses show a dependency on the wall model with complicated trends that have so far eluded any straightforward explanation.

For linearly accelerating flow, the acceleration rate was varied from very rapidly accelerating, non-equilibrium conditions (where bypass transition-like behaviour is observed in the DNS) to slow accelerating, quasi-steady conditions. The MTS wall model performs significantly better than the EQWM for the majority of the acceleration rates (except for the slowest  $T^* = 10$  case where performance is similar). Time signals of the various constitutive components of the MTS wall model show that different terms are dominant during each stage of the flow acceleration. During the laminar, transition, and quasi-steady stages the lamNEQ, turbNEQ, and LaRTE components, respectively, provide the largest contribution to the wall-stress response to acceleration. These trends are, again, consistent with the situation illustrated

in figure 5.3.

Finally, motivated by practical considerations, we explore the MTS wall model in the limit of instantaneous relaxation called the equilibrium multi-timescale wall model (EQMTS). This approach keeps some of the simplicity of the traditional EQWM while maintaining most of the accuracy of the full MTS wall model during non-equilibrium conditions. It leverages the observation that the EQWM with velocity correction behaves similarly to the LaRTE+turbNEQ models. For both pulsating and linearly accelerating channel flow, the EQMTS wall model captures the majority of the mean wall-stress time evolution. The most noticeable differences between EQMTS and the full MTS wall models include non-sinusoidal behavior during intermediate forcing frequencies and an over-prediction of the skin friction during the transition stage for the two fastest flow accelerations considered.

The next chapter will focus on developing and testing the MTS wall model for flows with non-equilibrium in space instead of the temporal non-equilibrium conditions considered in this chapter. The shear stress closure for  $\bar{\tau}_\Delta$  already contains weak effects of non-equilibrium since the fit  $Re_{\tau_\Delta}^{\text{pres}}$  incorporates the LES pressure gradient information in estimating the local shear stress. However, further testing is needed to ascertain the performance of the MTS model for spatial non-equilibrium where “history effects” are significant, or cases with separation where the wall-stress is zero locally.

# Chapter 7

## The MTSWM applied to streamwise developing flows

### 7.1 Introduction

In chapter 6, the MTSWM was applied to flows with a wide range temporal non-equilibrium. The tests demonstrate the MTSWM's capability to model complex unsteady wall bounded flows. However these flows were homogeneous in the horizontal plane (channel flows). In this chapter, we now explore the performance of the MTSWM for flows with spatial non-equilibrium. Figures 7.1 and 7.2 show the two flows of interest in this chapter. These flows include (1) a zero pressure gradient (ZPG) flat plate turbulent boundary layer over a wide range of Reynolds numbers treated in §7.3 and (2) a weakly separated boundary layer induced by suction and blowing on the top surface treated in §7.4. The ZPG boundary layer serves as a canonical flow check, similar to what was done with the statistically stationary channel flow, to ensure the code behaves as expected and predicts realistic flow statistics. Here the EQWM and MTSWM are expected to perform similarly and so the focus

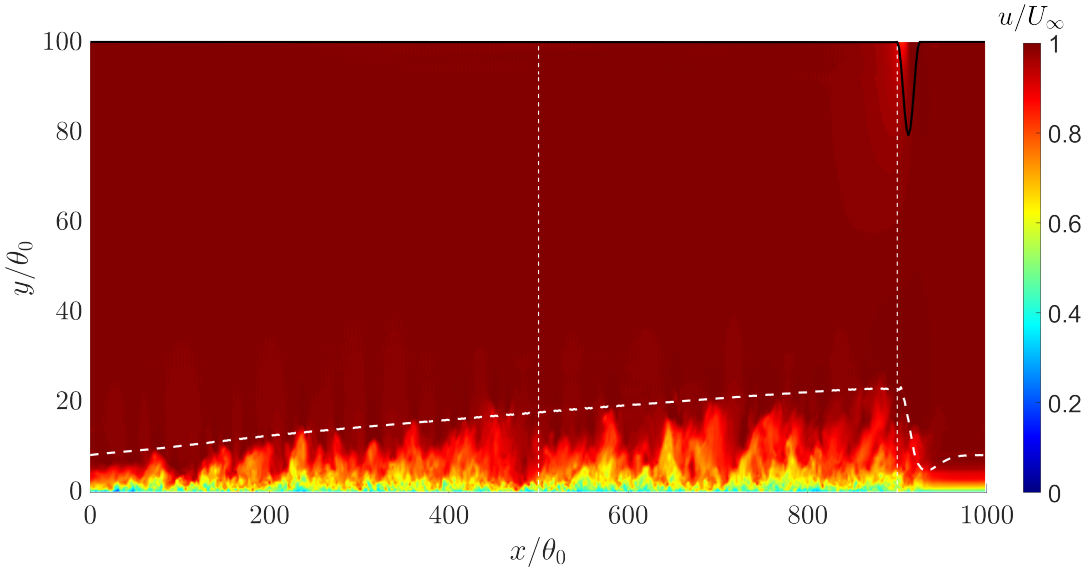


**Figure 7.1:** Contour plot of the instantaneous streamwise velocity field for the ZPG boundary layer. The thick dashed line corresponds with the  $\delta_{99}$  boundary layer thickness and the vertical dashed lines correspond with the sample plane (left) and start of the fringe region (right), respectively. The black solid line on the top surface corresponds with the prescribed vertical velocity boundary condition scaled by a factor of 100. The plot aspect ratio is stretched 5 times in the vertical direction.

remains on the performance of the code for this type of flow. The section also serves to show how the code performs for simulations over a vast range of Reynolds numbers up to values which are only reachable by wall modeled LES. Finally in §7.4, a separated boundary layer is simulated to test the MTSWM's ability to handle flows with large spatial non-equilibrium including separation. Here the performance of the MTSWM is compared against the EQWM and details regarding the wall model's behavior are highlighted.

First we describe code developments needed to simulate these flows using the LESGO pseudo-spectral code, which has been used in the previous simulations in this dissertation. Because LESGO is periodic in the streamwise direction, major modifications are needed to adapt it to developing flows.

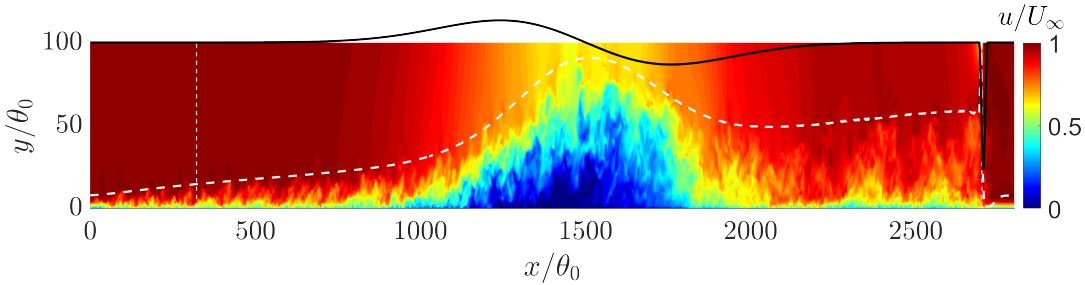


**Figure 7.2:** Contour plot of the streamwise instantaneous velocity field for the separated boundary layer. The thick dashed line corresponds with the  $\tilde{\delta}_{995}$  ([§7.4](#)) boundary layer thickness and the vertical dashed lines correspond with the sample plane (left) and start of the fringe region (right). The black solid line on the top surface corresponds with the prescribed vertical velocity boundary condition scaled by a factor of 100. The plot aspect ratio is stretched 5 times in the vertical direction.

One such adaptation is introducing a fringe region at the end of the domain which forces the flow to a desired inflow velocity. The target inflow velocity is determined according to a modified version of the rescale-recycle method developed by Lund et al. ([1998](#)) where the mean velocity is known from a composite ZPG boundary layer profile developed by Monkewitz et al. ([2008](#)) and velocity fluctuations are added which are obtained at a sample plane downstream of the inlet and then rescaled at the inlet. A schematic representing both the fringe region and the rescale-recycle method is shown in figure [7.3](#). The details regarding the fringe region and the rescale-recycle method are discussed in [§7.2](#) below.

## 7.2 Code development

### 7.2.1 Fringe region

To allow for periodic boundary conditions a fringe region must be used at the end of the domain, as portrayed in figure [7.3](#), located at  $L_x - L_f \leq x \leq L_x$

where  $L_f$  is the length of the fringe region. A body force is applied inside the fringe region to force the flow towards the target inflow velocity. This force is evaluated as

$$\mathbf{f}(\mathbf{x}, t) = \frac{\beta(x)}{T_f} (\mathbf{u}^t - \mathbf{u}^n) \quad (7.1)$$

where  $\mathbf{u}^n$  is the LES velocity at the current time step,  $n$ ;  $\mathbf{u}^t$  is the target velocity the body force drives the flow to;  $T_f$  is the fringe force time scale (evaluated as  $T_f = aL_f/U_\infty$  for some constant  $a$ ); and  $\beta(x)$  is the weighting function of the form

$$\begin{aligned} \beta &= \frac{1}{2} \left[ 1 - \cos \left( \pi \frac{x - x_f}{L_\beta} \right) \right] && \text{for } x_f \leq x \leq x_f + L_\beta \\ \beta &= 1 && \text{for } x_f + L_\beta \leq x \leq L_x \end{aligned} \quad (7.2)$$

where  $x_f \equiv L_x - L_f$  is the position of the start of the fringe region and  $L_\beta$  is the length of the region over which  $\beta$  changes from zero to one (typically  $L_\beta = 0.75L_f$ ). Equation 7.1 was motivated by the fringe force outlined in Chevalier et al. (2007) although here we use it for a desired turbulent desired instead of a laminar Blasius boundary layer.

Existing versions of LESGO have used a fringe region before (see Stevens et al. (2014) for more information). In these implementations the fringe region is enforced implicitly through direct modification of the LES velocity after the projection step. This method has the benefit of exactly prescribing the inflow velocity but with the caveat that the flow may not satisfy mass conservation within the fringe region. This effect is not significant when the fringe force is

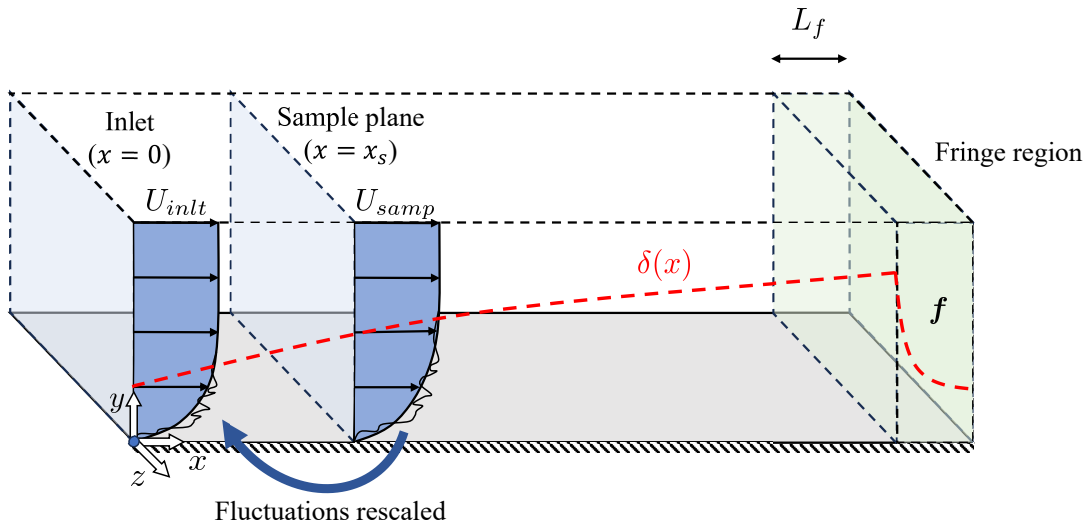


**Figure 7.3:** Schematic of the modified rescaling-recycling method and the fringe region.

small, however, when the fringe force is large (as needed to re-scale a developing boundary layer), violating mass conservation can generate a large pressure gradient region which can affect the flow and wall model downstream of the inlet. The method outlined here (where a body force is enforced explicitly in the momentum balance) satisfies continuity which in turn reduces the magnitude of the pressure gradient in the fringe region, but the inlet velocity may not be exactly prescribed. Through many numerical experiments, we have concluded that it is more important to reduce the pressure gradient inside the fringe region than having exact control of the velocity inside the fringe region, thus the presented method, with an explicitly applied body force, is the preferred method.

### 7.2.2 Rescale-recycle method

A turbulent boundary layer inflow velocity profile ( $\mathbf{u}^t$  in equation 7.1) is computed using a modified version of the turbulent inflow generation method developed by Lund et al. (1998), referred to as the rescale-recycle method here. In this method, the velocity is extracted at a sample plane located downstream of the inlet which is then rescaled and re-introduced (or recycled) at the inlet. The method of Lund et al. (1998) decomposes the sampled velocity into a mean and fluctuating component and rescales each of these components. The modified version used here utilizes the composite boundary layer velocity profile developed in Monkewitz et al. (2008) for prescribing the mean velocity and then only the fluctuations are rescaled, as schematically shown in figure 7.3. The rescaling-recycling method is as follows. The velocity profile at the inlet is

$$(u_i)_{inlt} = (U_i)_{inlt} + (u'_i)_{inlt}^{inner}[1 - W(\eta_{inlt})] + (u'_i)_{inlt}^{outer}W(\eta_{inlt}) \quad (7.3)$$

where the weighting function  $W(\eta)$  merges the inner and outer velocity fluctuation profiles according to

$$W(\eta) = \frac{1}{2} \left\{ 1 + \tanh \left[ \frac{\alpha(\eta - b)}{(1 - 2b)\eta + b} \right] / \tanh(\alpha) \right\} \quad (7.4)$$

with the constants  $\alpha = 4$  and  $b = 0.2$ . The mean velocity at the inlet,  $(U_i)_{inlt}$ , is prescribed using the mean velocity outlined in appendix (§9.3) based on the composite velocity profile of Monkewitz et al. (2008). Prescribing the mean velocity at the inlet eliminates numerical instabilities observed by others when using the traditional rescaling-recycling method of Lund et al. (1998). It

does reduce the applicability to more complex inflows, however, we are only concerned with flows with a ZPG turbulent boundary layer inflow thus opt for the present method due to its stability and relative ease of implementation.

The inlet velocity fluctuations are computed using the typical rescaling procedure. First, the velocity fluctuations at the sample plane,  $x = x_s$ , must be measured according to

$$(u'_i)_{samp} = (u_i)_{samp} - (U_i)_{samp} \quad (7.5)$$

where the mean velocity at the sample plane is computed using temporal and spanwise averaging

$$(U_i)_{samp}^n = \frac{\delta t}{T} \langle (u_i)_{samp}^n \rangle_z + \left(1 - \frac{\delta t}{T}\right) (U_i)_{samp}^{n-1} \quad (7.6)$$

where  $T$  is a specified averaging time scale,  $n$  is the time step index, and  $\langle \cdot \rangle_z$  denotes averaging in the spanwise direction. Note running time averaging is achieved if  $T = t^n - t^0$  where  $t^n$  is the current simulation time and  $t^0$  is the time when averaging was initiated.

The inner and outer solutions for the fluctuating components are related to the sample velocity fluctuations according to

$$(u'_i)_{inlt}^{inner} = \gamma (u'_i)_{samp} (y_{inlt}^+, z, t) \quad (7.7)$$

$$(u'_i)_{inlt}^{outer} = \gamma (u'_i)_{samp} (\eta_{inlt}, z, t) \quad (7.8)$$

where  $\gamma$  is the ratio between the inlet and sample friction velocities

$$\gamma = \left( \frac{u_{\tau,inlt}}{u_{\tau,samp}} \right). \quad (7.9)$$

$y_{inlt}^+ = yu_{\tau,inlt}/\nu$  and  $\eta_{inlt} = y/\delta_{inlt}$  are the inner and outer vertical coordinates at inlet plane. The friction velocities and the boundary layer thicknesses at the inlet and sample planes are the same as computed in the velocity initialization routine described in appendix §9.3. Again, this approach eliminates numerical instabilities and other problems we have observed if we were to instead dynamically compute them. Note evaluating  $(u'_i)_{samp}$  at  $y_{inlt}^+$  and  $\eta_{inlt}$  requires interpolation since  $(u'_i)_{samp}$  is only recorded at discrete points for  $y_{samp}^+ = yu_{\tau,samp}/\nu$  and  $\eta_{samp} = y/\delta_{samp}$ . Simple linear interpolation is used here to achieve this. Once the inlet velocity fluctuations have been computed, the total velocity at the inflow can be solved for using equation 7.3. This velocity is then implicitly enforced at the inflow by setting  $\mathbf{u}^t = \mathbf{u}_{inlt}$  in the fringe body force, equation 7.1.

### 7.3 Zero pressure gradient flat plate turbulent boundary layer

LES of a zero pressure gradient flat plate turbulent boundary layer were performed over a wide range of Reynolds numbers using the EQWM and the MTSWM. The simulations were motivated by Inoue and Pullin (2011). The Reynolds numbers covered include  $Re_{\theta_0} = 8 \times 10^2, 2 \times 10^2, 8 \times 10^3, 2 \times 10^4, 2.5 \times 10^4, 8 \times 10^4, 1.25 \times 10^5, 5 \times 10^5, 1.25 \times 10^6, 5 \times 10^6, 1.25 \times 10^7, 5 \times 10^7, 1.25 \times 10^8, 5 \times 10^9$  named as A0-A13, respectively, where  $Re_{\theta_0}$  is the prescribed inlet Reynolds number. Simulations are performed using LESGO, modified according to §7.2 so that LESGO has the ability to perform developing boundary layer simulations. The domain size, number of grid points, and resolution

are  $(L_x, L_y, L_z)/\theta_0 = (1000, 100, 120)$ ,  $(N_x, N_y, N_z)/\theta_0 = (480, 200, 76)$ , and  $(\Delta_x, \Delta_y, \Delta_z)/\theta_0 = (2.0833, 0.5, 1.5789)$ , respectively, for all of the simulations. The fringe region has the size  $L_f/\theta_0 = 100$  at the end of the domain where blowing is applied within the first quarter of this region for mass conservation and a body force is applied to force the flow to a desired inflow velocity, as described in §7.2.1. The target inflow velocity is specified according to the modified rescale-recycle method described in §7.2.2 with the sample plane location  $x_s/\theta_0 = 500$ . The sample plane is located far enough downstream to where it is not affected by the numerical disturbances caused the fringe region. LES simulations are performed with the EQWM and MTSWM, described in chapter 5, with the second grid point used as the wall modeling height ( $\Delta/\theta_0 = 0.75$ ). The equilibrium fit used is the updated  $Re_{\tau\Delta}^{pres}$  fit (algorithm 2) which corrects the sharp transition in the original fit between favorable and adverse pressure gradients. The fringe region causes the development of a very large pressure gradient at the inlet. To prevent this large pressure gradient from further affecting the wall model, the pressure gradient input to the wall models (both EQWM and MTSWM) is zeroed out until  $x/\theta_0 = 100$ . Details regarding this behavior are explained in this section below. The subgrid stress model used is the Lagrangian scale-dependent model from Bou-Zeid et al. (2005). Time advancement is done using an Adams-Bashforth method with a varying time step size to achieve a constant Courant-Friedrichs-Lowy (CFL) value of 0.1. This gives an average time step size around  $\delta t U_\infty/\theta_0 = 0.19$  for all Reynolds numbers.

Figure 7.4 shows several velocity profiles over the full range of Reynolds

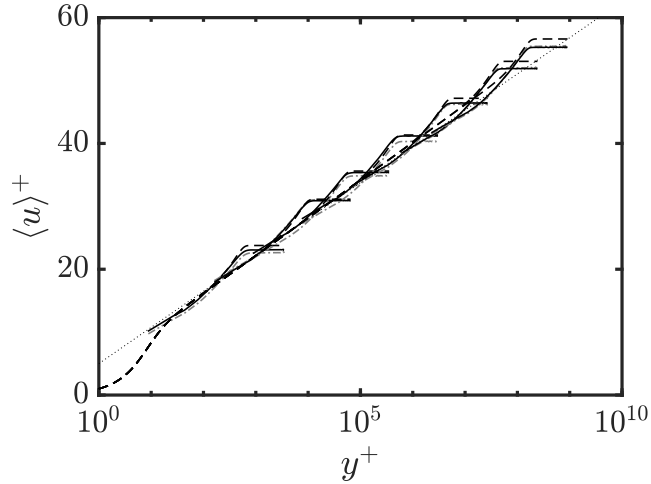


**Figure 7.4:** Mean velocity profiles for simulations A0, A3, A6, A8, A10, A12, and A13 at  $x/\theta_0 = 500$ . LES with the EQWM and the MTSWM are shown with dashed-dotted gray lines and solid black lines, respectively. Dashed lines correspond with the Monkewitz fit (equation 9.4) and dotted lines correspond with the log profile  $\langle u \rangle^+ = \frac{1}{\kappa} \log y^+ + B$  with  $\kappa = 0.4$  and  $B = 5.0$ .

numbers simulated. The EQWM and MTSWM results are compared against the Monkewitz fit described in the appendix according to equation 9.4. The LES and the Monkewitz fit agree fairly well with the worst agreement occurring at the highest Reynolds number considered,  $Re_{\theta_0} = 500E7$ . At this Reynolds number, the velocity is significantly underpredicted in the log-layer. The EQWM and MTSWM give very similar velocity profiles for the highest Reynolds numbers but differ from each other (in a non-monotonic way) for lower Reynolds numbers. For all Reynolds numbers the shape of the velocity profiles are quite good. However, the skin friction displays some differences, discussed in more detail below.

Figure 7.5 shows profiles of the streamwise and spanwise turbulence intensities normalized in outer units (panel (a)) and normalized in inner units (panel (b)). For the the outer units normalization, the EQWM and MTSWM

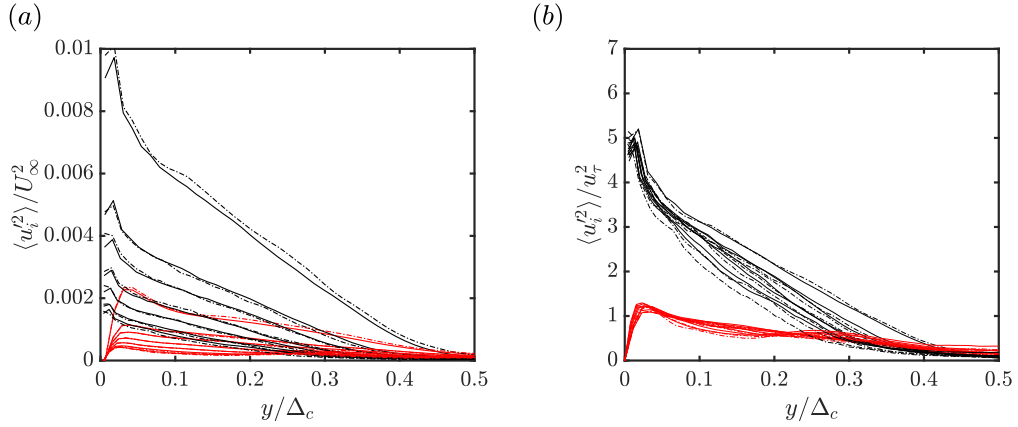


**Figure 7.5:** Turbulence intensities in (a) outer units and (b) inner units. Line colors correspond with  $\langle u'^2 \rangle$  (black) and  $\langle v'^2 \rangle$  (red). Line types correspond with LES using the EQWM (dashed-dot) and LES using the MTSWM (solid). The simulations shown are the same as in figure 7.4, again at  $x/\theta_0 = 500$ .  $\Delta_c = U_\infty^+ \delta^*$  is the Rotta-Clauser outer length scale.

results give very similar predictions, however, the curves do not collapse on top of each other. Panel (b) demonstrates the friction velocity is a much more appropriate velocity scale since the profiles collapse better over all the Reynolds numbers simulated. There still however is some Reynolds number dependence of the streamwise turbulence intensity, particularly in the outer regions of the boundary layer for  $y/\Delta_c > 0.1$ . This was not observed by Inoue and Pullin (2011) and suggests that the discrepancy may be related to the LES features unrelated to the wall model (i.e. the performance of the SGS model, the choice of keeping grid resolution constant with  $\theta_0$ , fringe region related disturbances, etc.).

The skin friction and  $U_\infty^+$  are shown in figure 7.6 for all Reynolds numbers considered. They are compared against the “Coles-Fernholz 2” empirical

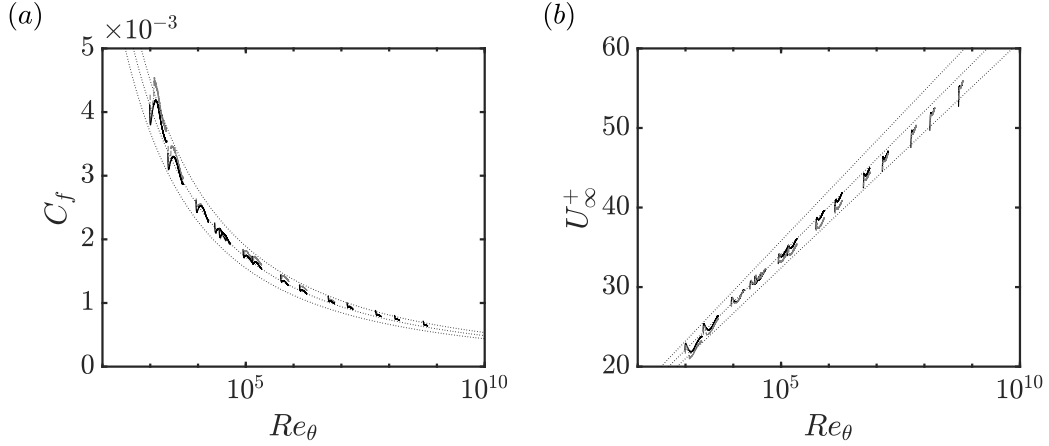


**Figure 7.6:** (a)  $C_f$  and (b)  $U_\infty^+$  vs  $Re_\theta$  for all Reynolds numbers. LES with the EQWM and the MTSWM are shown with dashed-dotted gray lines and solid black lines, respectively. Dotted lines are the Coles–Fernholz 2 curve ( $\pm 10\%$  for  $C_f$  and  $\pm 5\%$  for  $U_\infty$ ).

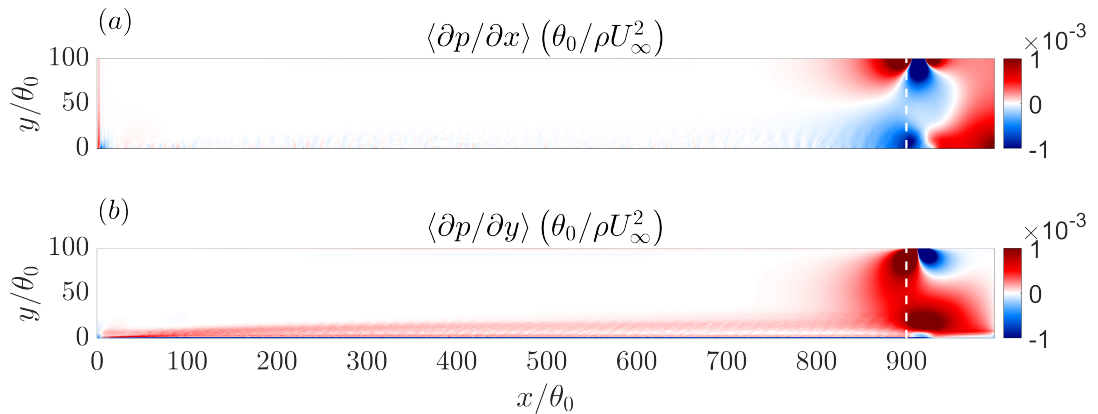


**Figure 7.7:** Mean pressure gradient plots for simulation A0 using the EQWM. Vertical dashed lines show the start of the fringe region.

relation from Nagib et al. (2007):

$$U_\infty^+ = \frac{1}{\kappa} \log(Re_\theta) + C \quad \text{where} \quad \kappa = 0.384, \quad C = 4.127 \quad (7.10)$$

or alternatively in terms of the skin friction

$$C_f = 2 \left[ \frac{1}{\kappa} \log(Re_\theta) + C \right]^{-2}. \quad (7.11)$$

The LES falls within 10% of  $C_f$  and within 5% of  $U_\infty^+$  for this empirical relation over all of the Reynolds numbers considered. Generally the EQWM tends to predict a higher skin friction than the MTSWM. Figure 7.6 clearly shows that there are some entrance effects that persist long into the domain. These entrance effects have been found to be caused by large pressure gradients appearing at the inlet. Figure 7.7 most clearly demonstrates this effect. We can see a large pressure region with gradients in both the streamwise and vertical direction develops inside of the fringe region. This large region of pressure is needed to shrink the boundary layer down to its height at the inlet (see figure 7.1 to see how the boundary layer height shrinks as it enters the fringe region). This is one of the primary challenges of simulating a developing boundary layer with a code that is periodic in the streamwise direction. Since pressure is non-local, the large pressure gradient generated in the fringe region carries into the inlet. This generates an adverse then favorable pressure gradient near the wall that further affects the wall model and thus the skin friction. In response to this we have zeroed out the pressure gradient input to the wall model up to  $x/\theta_0 = 100$  since by then the large pressure gradient generated by the fringe region has died out. However, the LES velocity is still directly

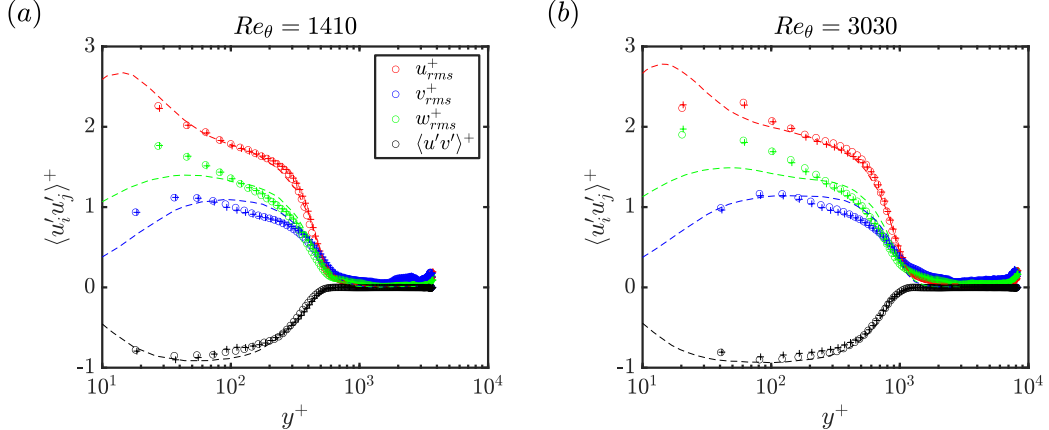


**Figure 7.8:** Reynolds stresses in inner units at (a)  $Re_\theta = 1410$  and (b)  $Re_\theta = 3030$ . Statistics are taken using simulation (a) A0 at the location  $x/\theta_0 = 227$  and (b) A1 at the location  $x/\theta_0 = 185$ . Line colors correspond with the different Reynolds stress components as indicated in the figure legend in panel (a). Line types correspond with LES using the EQWM (plus symbols), LES using the MTSWM (circles), and the DNS of J. Lee et al. (2017).

affected by this pressure gradient which then goes into the wall model. In figure 7.7(a), this is observed by the large dip downwards and then sudden increase upwards in the skin friction. It takes roughly  $200\theta_0$  (at low Reynolds numbers) for these fringe region disturbances to die out. Thus, in the following section we nominally consider up to  $x/\theta_0 = 200$  as part of the fringe region despite the fringe body force being zero here.

Continuing now with the presentation of flow statistics for the ZPG developing boundary layer, figure 7.8 shows the Reynolds stresses at two Reynolds numbers (within the Reynolds numbers expected for the separated flow in §7.4) compared with the DNS data of J. Lee et al. (2017). Overall the LES agrees quite well with the DNS. The turbulent stresses appear to not be sensitive to the wall model since the EQWM and MTSWM results are nearly identical.

The Reynolds shear stress agrees very well with the DNS with only slight discrepancies around  $y^+ = 100$ . The streamwise normal stress peak is slightly underpredicted for the higher Reynolds number, although the rest of the profile agrees well with the DNS. The spanwise normal stress is overpredicted in the near wall region. This is consistent with other Reynolds stress plots shown for channel flow and is likely an issue specific to the combination of SGS model, grid configuration, and numerics used in LESGO. The vertical normal stress is slightly under predicted for  $y^+ > 100$  and overpredicted in the buffer layer for the lower Reynolds number. All profiles tend to decay well to zero at the edge of the boundary layer, however, there does appear to be some level of fluctuations in the free stream at the top of the domain. These fluctuations should not affect the boundary layer behavior near the wall.

## 7.4 Separation induced by suction and blowing

The last test case considered is a separated turbulent boundary layer induced by suction and blowing on the top surface of the domain. The simulation set-up is based on the work by Coleman et al. (2018). The vertical velocity on the top surface,  $V_{top} \equiv v(y = L_y)$ , is prescribed according to

$$V_{top}(x) = -\sqrt{2}V_{max} \left[ \frac{x - x_c}{\sigma} \right] \exp \left( \frac{1}{2} - \left[ \frac{x - x_c}{\sigma} \right] \right) + \phi_{top} \quad (7.12)$$

where  $V_{max}$  controls the strength of the suction and blowing,  $\sigma$  controls the width,  $x_c$  marks the center of the suction and blowing, and  $\phi_{top}$  is a constant suction velocity to give roughly zero pressure gradient before the suction and after the blowing. This gives four regions within the domain caused by the

prescribed vertical velocity on the top surface, summarized in table 7.1. In addition to the prescribed vertical velocity on the top surface, the horizontal velocities are prescribed to give an irrotational transpiration boundary condition on the top surface. The boundary condition on the top surface ( $y = L_y$ ) is then

$$v(x, L_y, z) = V_{top}(x), \quad \frac{\partial u}{\partial y} \Big|_{(x, L_y, z)} = \frac{dV_{top}}{dx}, \quad \frac{\partial w}{\partial y} = 0. \quad (7.13)$$

The parameters in equation 7.12 are chosen to match that of “Case C” in Coleman et al. (2018). This case has the highest Reynolds number we could obtain for DNS with this type of flow, thus making it most ideal for wall modeling. However the Reynolds number is still relatively low (for typical wall modeling applications) and the separated region is quite small, thus presenting some difficulties for analyzing the performance of the wall models tested, as discussed further in this section. From the DNS, the parameters fixed for this simulation are  $Re_Y \equiv L_y U_\infty / \nu = 80000$ ,  $V_{max}/U_\infty = 0.1333$ ,  $\sigma/L_y = 3.66$ , and  $\phi_{top}/U_\infty = 0.0034$  (note the DNS uses the domain height as the normalization length scale). Since all LESGO simulation quantities are normalized with the inlet momentum thickness,  $\theta_0$ , the inlet Reynolds number  $Re_{\theta_0}$  must first be determined since  $L_y/\theta_0 = Re_Y/Re_{\theta_0}$ . Coleman et al. (2018) use a linear fit for the ZPG region before suction to give an estimate for  $Re_\theta$  at the center of the suction and blowing. We use this same fit to estimate  $Re_{\theta_0}$ . If the linear fit is given by  $Re_\theta(x) = m(x'/L_y) + b$  where  $x' = x - x_c$  is the DNS position, then the inlet Reynolds number is given by

$$Re_{\theta_0} = b \left[ 1 + \left( \frac{m}{Re_Y} \right) \left( \frac{x_c}{\theta_0} \right) \right]^{-1} \quad (7.14)$$

where  $m = 156.7829$  and  $b = 3142.2$  are the linear fit's slope and intercept, respectively, for the case of interest. The center of suction and blowing,  $x_c$ , must still be specified. However, this again implicitly depends on  $Re_{\theta_0}$ . One can solve for  $Re_{\theta_0}$  as a function of the known parameters (i.e.  $Re_Y$ ,  $\sigma/L_y$ , etc.) however it is simpler to just "guess and check" to get an appropriate  $Re_{\theta_0}$  and corresponding  $x_c/\theta_0$ . For  $x_c/\theta_0 = 1500$ , equation 7.14 gives  $Re_{\theta_0} \approx 800$ , and  $\sigma/\theta_0 = 366$  which allows for a sufficiently extended ZPG region before the suction. With  $Re_{\theta_0} = 800$  and  $x_c/\theta_0 = 1500$  chosen, the domain size is set to  $(L_x, L_y, L_z)/\theta_0 = (2800, 100, 120)$  with the corresponding number of grid points  $(N_x, N_y, N_z) = (1350, 200, 76)$  and resolution  $(\Delta_x, \Delta_y, \Delta_z)/\theta_0 = (2.074, 0.5, 1.58)$ . The simulation parameters are very similar to the ZPG simulation A0 ( $Re_{\theta_0} = 800$ ) from §7.3, apart from the significantly larger length of the domain. The fringe region has a similar size,  $L_f/\theta_0 = 107.8$ , and is denoted as region F in table 7.1. The sample plane is slightly closer to the inlet,  $x_s/\theta_0 = 322$  to avoid being affected by the blowing region although it is far enough downstream to where it is not affected by the numerical disturbances caused by the fringe region (region F0 in table 7.1). The same SGS and wall models (EQWM and MTSWM) as in §7.3 are used here. Time advancement is done using an Adams-Bashforth method with a varying time step size to achieve a constant Courant-Friedrichs-Lowy (CFL) value of 0.1. This gives an average time step size of  $\delta t U_\infty / \theta_0 = 7.04 \times 10^{-2}$ .

First, we show plots of time and spanwise averaged statistics. In this section angled brackets represent spanwise and time averaging occurring over a time period of  $\sim 2800\theta_0/U_\infty$  which corresponds to one flow through time.

Region Name	Location	Description
F0	$0 \leq x/\theta_0 \leq 200$	fringe region ( $f = 0$ )
ZPG1	$200 \leq x/\theta_0 \leq 700$	ZPG before suction
suction	$700 \leq x/\theta_0 \leq 1500$	suction
blowing	$1500 \leq x/\theta_0 \leq 2300$	blowing
ZPG2	$2300 \leq x/\theta_0 \leq 2700$	ZPG after blowing
F	$2700 \leq x/\theta_0 \leq 2800$	fringe region ( $f \neq 0$ )

**Table 7.1:** Summary of the different regions within the separated flow.

Figure 7.9 shows the vertical and streamwise mean velocity on the top surface of the domain,  $y = L_y$ . The vertical velocity is imposed by equation 7.12 except in the fringe region where blowing is done to achieve mass conservation. Figure 7.9(a) shows that the vertical velocity is being properly prescribed on the top surface to match that of the DNS. One can also see the short but strong blowing in the first quarter of the fringe region to achieve mass conservation. The streamwise velocity shown in figure 7.9 is not the actual velocity but rather the “generalized velocity” first proposed by Lighthill (1963) and used by the DNS of Coleman et al. (2018) which we are comparing. The generalized velocity is needed because the free stream has non-zero shear in the suction and blowing regions which disagrees with traditional definitions used for ZPG boundary layers. The generalized velocity is based on the integral of the spanwise vorticity

$$\tilde{U}(x, y) = - \int_0^y \langle \omega_z \rangle(x, y') dy' \quad (7.15)$$

which has the corresponding top surface value  $\tilde{U}_{top} = \tilde{U}(x, L_y)$ . From this, different boundary layer thickness definitions may be formed, similar to traditional boundary layer thicknesses, such as  $\tilde{\delta}_{995}$  which corresponds to the

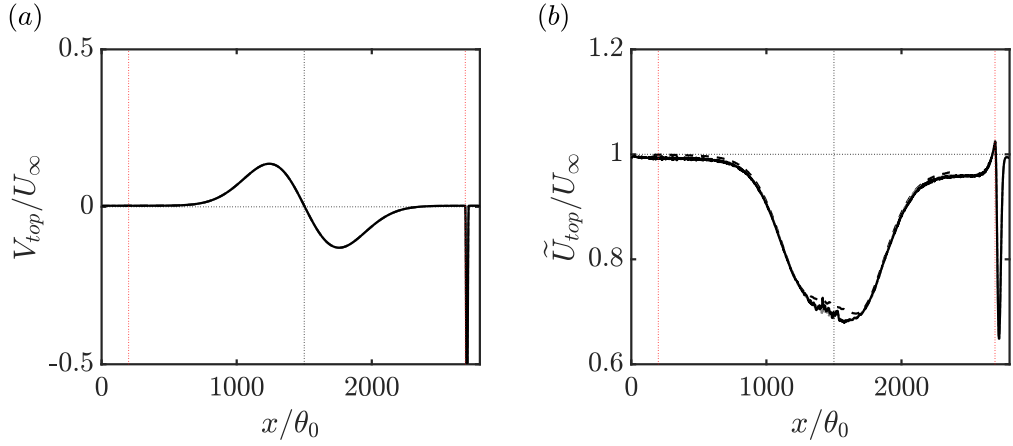


**Figure 7.9:** Mean (a) vertical and (b) streamwise velocity on the top surface of the domain. Line types correspond with LES using the EQWM (dashed-dot gray), LES using the MTS wall model (solid black), and the DNS of Coleman et al. (2018) (dashed black). Black dotted vertical lines show the center of the suction and blowing and red dotted vertical lines show the boundaries of the fringe region.

height when  $\tilde{U}/\tilde{U}_{top} = 0.995$  or the displacement thickness

$$\tilde{\delta}^* = \frac{-1}{\tilde{U}_{top}} \int_0^{L_y} y \langle \omega_z \rangle dy \quad (7.16)$$

and the momentum thickness

$$\tilde{\theta} = \frac{-2}{\tilde{U}_{top}^2} \int_0^{L_y} y \tilde{U} \langle \omega_z \rangle dy - \tilde{\delta}^*. \quad (7.17)$$

It can easily be shown that these definitions resort to the traditional definitions when  $\langle \omega_z \rangle \rightarrow -\partial_y \langle u \rangle$  which is true for ZPG boundary layers. Figure 7.9(b) shows that the LES for both wall models agree well with the DNS except for a slight underprediction around the separation. This discrepancy may be explained by differences in the degree of separation predicted by DNS and LES. This issue is described in more detail throughout this section.

Figure 7.10 shows the various boundary layer thickness lengths based

on the generalized velocity presented in equation 7.15. Again note the good agreement between the LES and DNS in the ZPG regions. Only the momentum thickness is overpredicted in the separation region. This leads to an underpredicted shape factor near the center of the suction and blowing. For Coleman et al. (2018), separation occurs when  $H \equiv \tilde{\delta}^*/\tilde{\theta} = 3.25$ , as shown by the horizontal dashed line in panel (c).

Figure 7.11 shows the skin friction  $C_f \equiv \langle \tau_w \rangle / 0.5U_\infty^2$ , the wall pressure coefficient  $(\langle p_w \rangle - \langle p_\infty \rangle) / 0.5\rho U_\infty^2$ , and the fraction of reversed wall stress,  $\gamma_r$ . The skin friction for the LES agrees relatively well with the DNS over most of the domain except in the last half of the blowing region. In the ZPG regions the EQWM gives a higher skin friction than the MTSWM. For region ZPG1 the EQWM agrees better with the DNS, however, in ZPG2 the MTSWM agrees better with the DNS. Both the EQWM and MTSWM do not predict mean flow separation although  $C_f$  is nearly zero for both the EQWM and the MTSWM at the center of suction and blowing. For  $C_p$ , the two wall models given nearly identical results and agree well with the DNS with the largest discrepancies occurring at the center of the suction and blowing.  $\gamma_r$ , the fraction of reversed wall stress, can provide information about the wall stress fluctuations and can even be used to characterize separation better than negative mean stress (Coleman et al. (2018) found a very close agreement between the  $C_f = 0$  and  $\gamma_r = 0.5$  locations).  $\gamma_r$  remains finite even in the ZPG regions for the DNS whereas for the LES there are locations within the domain where the wall stress is never negative. This is expected since DNS (non-filtered) generally has wider wall stress probability density functions than LES, and thus large

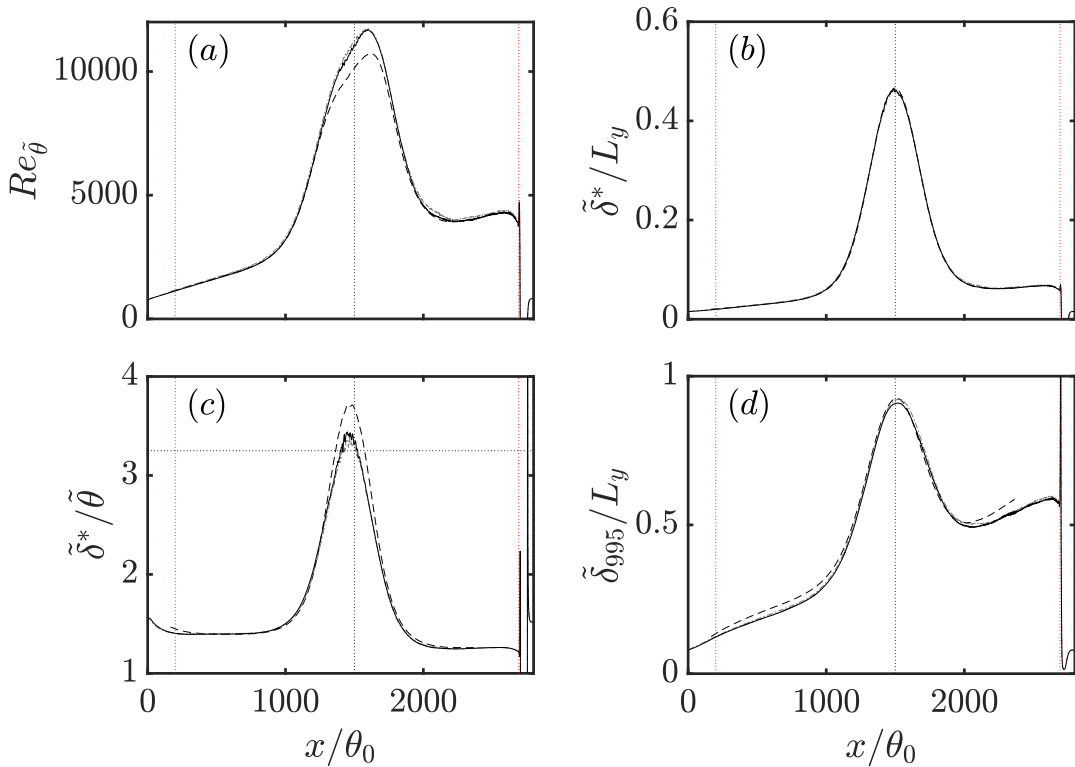


**Figure 7.10:** Different boundary layer thicknesses including (a) the Reynolds number based on the momentum thickness, (b) the displacement thickness, (c) the shape factor, and (d) the boundary layer thickness based on when the velocity is 99.5% of its top surface value. Line types correspond with LES using the EQWM (dashed-dot gray), LES using the MTS wall model (solid black), and the DNS of Coleman et al. (2018) (dashed black). Black dotted vertical lines show the center of the suction and blowing and red dotted vertical lines show the boundaries of the fringe region. The horizontal dotted line in (c) corresponds with the shape factor separation occurs for the DNS ( $H = 3.25$ ).

wall stress fluctuation events (where the fluctuation exceed the mean value) occur for the DNS but not the LES. Using the same logic, this is why the MTSWM has a wider  $\gamma_r$  curve than the EQWM since it has a flatter wall stress PDF (see figures 4.8 and 6.1 for these PDFs).

Figures 7.12-7.14 show the velocity profiles (and Reynolds shear stresses for figures 7.13(b) and 7.14(b)) at different streamwise positions in the domain. Figure 7.13 shows the velocity and Reynolds stress profiles in the ZPG regions immediately before and after suction and blowing. In figure 7.13(a) it is clear that the velocity profile prediction is poor in the buffer layer and the beginning of the log layer. This might be explained by the underprediction of the Reynolds shear stress peak, as seen in figure 7.13(b) especially in the ZPG1 region. In the ZPG2 region, the underprediction of the velocity profile in the inner log layer is even more pronounced than the ZPG1 region. This is the primary cause for the overprediction of  $C_f$  right before ZPG2 as seen in figure 7.11(a). Also note the constant shift upwards in the velocity profiles for the EQWM versus the MTSWM. Again, this is consistent with the higher  $C_f$  for the EQWM in the ZPG regions in figure 7.11(a). Figure 7.14 shows velocity and Reynolds shear stress profiles (in outer units) inside the suction and blowing region. In the near-wall region, we can see the LES for both the EQWM and MTSWM overpredicts the velocity which in turn leads to no mean flow separation. It is important to note that the size and magnitude of the separation bubble is quite small. For the DNS, separation occurs at  $x/\theta_0 = 1355$  and then reattaches at  $x/\theta_0 = 1540$  with the separation bubble reaching a maximum height of  $2.78\theta_0$  and having a minimum backflow velocity of  $-0.0076U_\infty$ . This

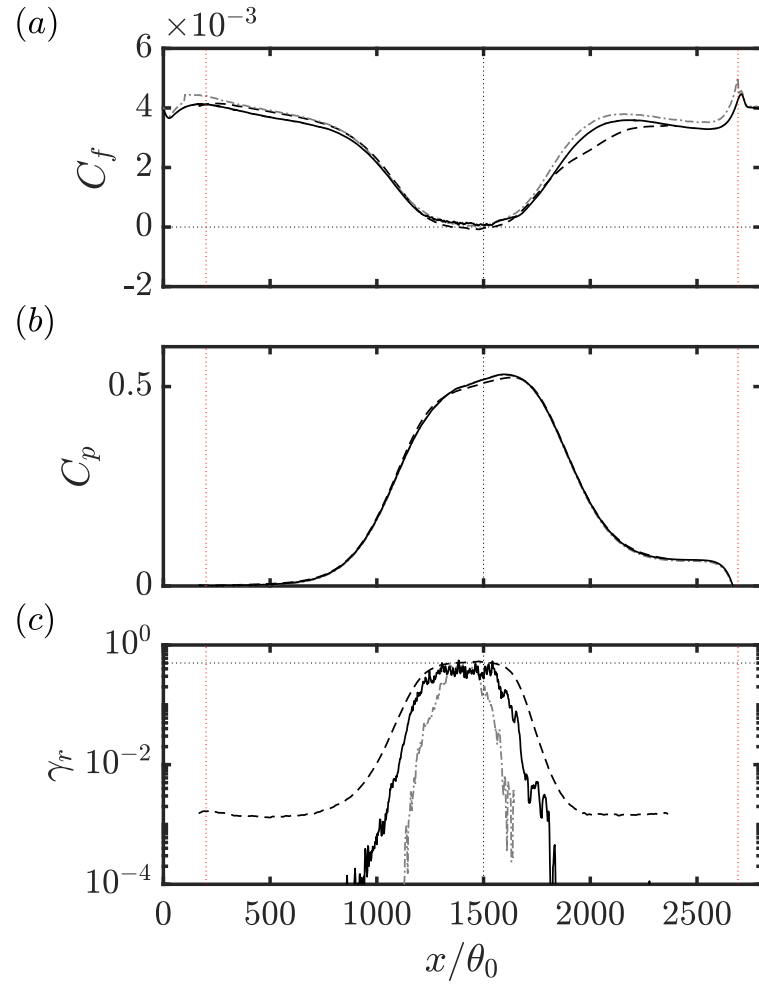


**Figure 7.11:** (a) Skin friction, (b) wall pressure coefficient, and (c) fraction of reversed wall stress. Line types correspond with LES using the EQWM (dashed-dot gray), LES using the MTSWM (solid black), and the DNS of Coleman et al. (2018) (dashed black). Black dotted vertical lines show the center of the suction and blowing and red dotted vertical lines show the boundaries of the fringe region. The horizontal dotted line in (c) denote the  $\gamma_r = 0.5$  threshold for separation.

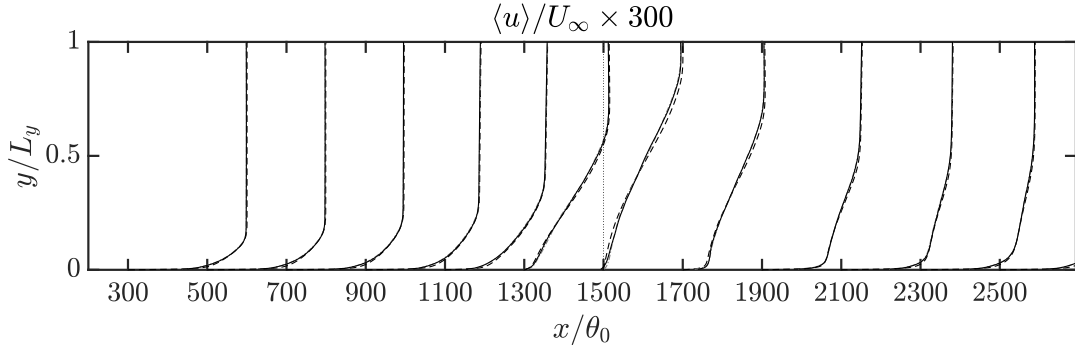


**Figure 7.12:** Mean velocity profile at different streamwise locations. Velocity profiles start at  $x/\theta_0 = 300$ , end at  $x/\theta_0 = 2500$ , and are spaced  $200\theta_0$  with tick marks showing the locations of the start of the profiles. Line types correspond with LES using the EQWM (dashed-dot), LES using the MTSWM (solid), and the DNS of Coleman et al. (2018) (dashed). The vertical dotted line shows the center of suction and blowing.

means there are roughly a maximum of six vertical grid points within the LES domain for the same size separation bubble. The LES also does not experience backflow at the wall model height until  $x/\theta_0 = 1355$ . This is one of the major faults of the traditional EQWM (without pressure gradient inputs) because it will always predict separation too late. However, because this separation bubble is so small it is difficult to attribute the overprediction of  $C_f$  near separation to wall modeling errors instead of for other errors in the LES (e.g. the role of the SGS model, the inflow generation method, grid resolution, etc.).

Figure 7.15 shows the different wall stress components (both mean and RMS) of the MTSWM along with the EQWM results. From panel (a) it is clear that the turbNEQ model is reducing the mean wall stress for the MTSWM in the ZPG regions. This is an unexpected and detrimental feature since it brings the skin friction away from the DNS results, as observed in figure 7.11(a). It is unexpected because the turbNEQ model (governed by equation 5.3) should respond to velocity fluctuations around the LaRTE value and thus

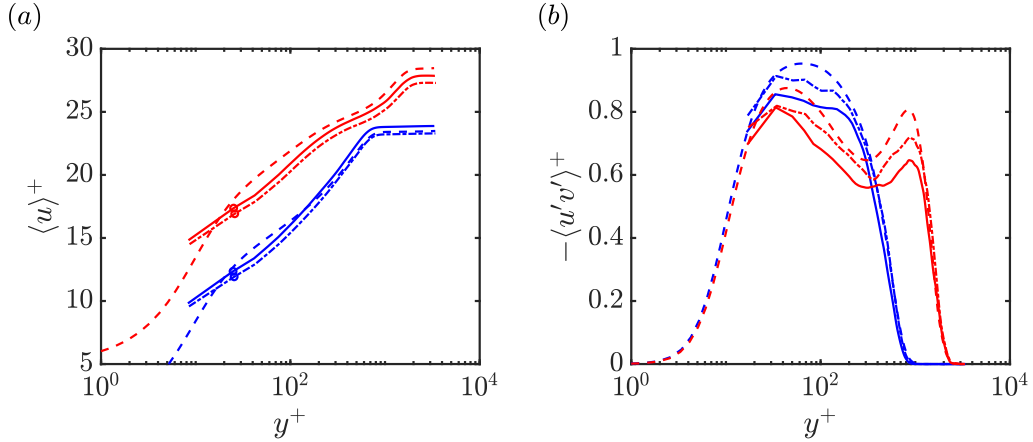


**Figure 7.13:** (a) Velocity and (b) Reynolds shear stress profiles at the ZPG regions before ( $x/\theta_0 = 700$ ) and after ( $x/\theta_0 = 2300$ ) separation. Line types correspond with LES using the EQWM (dashed-dot), LES using the MTSWM (solid), and the DNS of Coleman et al. (2018) (dashed). Before and after separation are indicated with blue and red lines, respectively, where the velocity profiles after separation are shifted five units vertically. The circles in (a) mark the wall modeling height.

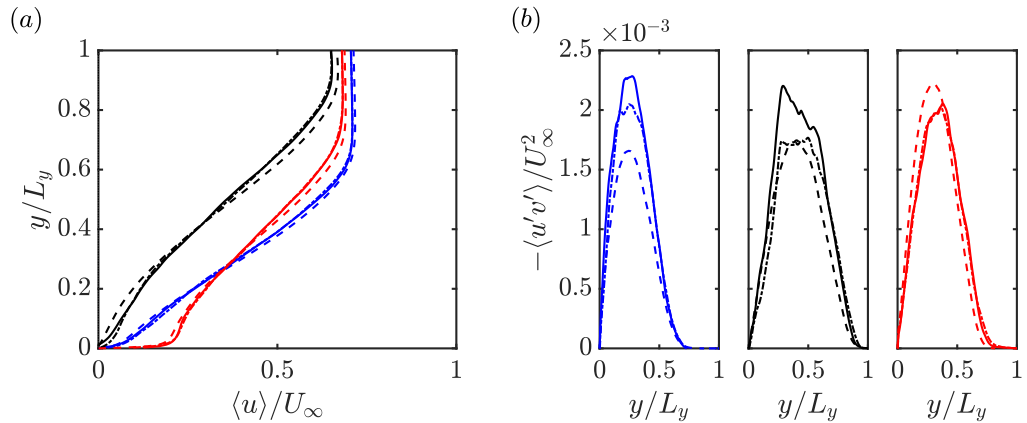


**Figure 7.14:** (a) Velocity and (b) Reynolds shear stress profiles in the suction and blowing region in the middle of the suction (blue lines,  $x/\theta_0 = 1300$ ), at the center of the suction and blowing (black lines,  $x/\theta_0 = 1500$ ), and in the middle of blowing (red lines,  $x/\theta_0 = 1700$ ). Line types correspond with LES using the EQWM (dashed-dot), LES using the MTSWM (solid), and the DNS of Coleman et al. (2018) (dashed).

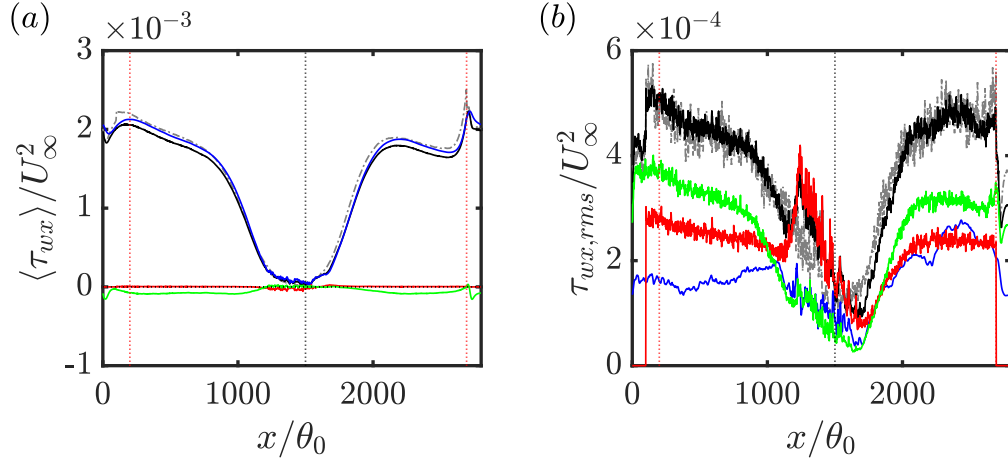


**Figure 7.15:** Wall stress (a) mean and (b) RMS with each component shown for the MTSWM. LES using the EQWM is shown with gray dashed-dot lines and LES using the MTWSM is shown with black solid lines with its LaRTE, lamNEQ, and turbNEQ components shown with blue, red, and green solid lines, respectively. Black dotted vertical lines show the center of the suction and blowing and red dotted vertical lines show the boundaries of the fringe region.

give zero mean. The lamNEQ model on the other hand does have a zero mean wall stress throughout the domain, as expected. The LaRTE model has a very similar wall stress value to the EQWM but with a slightly more delayed response to changes in the  $x$ -direction such as the onset of suction at  $x/\theta_0 = 700$  and the onset of blowing at  $x/\theta_0 = 1500$ . This is expected since the LaRTE wall stress relaxation is Lagrangian by design and thus exhibits a delayed response in both  $t$  and  $x$ . However, it is important to note that the EQWM results in figure 7.15 (gray dashed-dotted lines) are an entirely separate simulation from MTSWM lines in this figure, and thus the LaRTE model does not necessarily relax to this stress.

Figure 7.15(b) shows the wall stress RMS as a function of streamwise position for the different components of the MTSWM. The same information as

well as related conclusions may be gathered from figures 7.16 and 7.17, which show wall stress PDFs, and figures 7.18 and 7.19, which show instantaneous wall stress contour plots, thus these figures will be discussed together. First we focus our attention to the ZPG regions (ZPG1 and ZPG2 in table 7.1). In the ZPG regions, wall stress fluctuations are primarily dominated by the turbNEQ model. This is consistent with the PDFs for stationary channel flow presented in figure 6.1 before. In figure 7.19(d) we can see that these are fine structures with shape similar to the LES velocity input (not shown here). The lamNEQ fluctuations are the next largest in the ZPG regions. The Reynolds number is small enough to where these fluctuations are still comparable to the turbNEQ model since  $\tau_w''$  scales with  $\sqrt{\nu}$ . The structure of the fluctuations are similar to those observed in previous studies (e.g. steady channel flow or the SSPG flow first presented in chapter 4). Finally, the LaRTE model yields the lowest wall stress fluctuations in the ZPG regions, again consistent with PDFs from previous studies of stationary channel flow. Interestingly, the RMS is higher in ZPG2 than ZPG1 as seen in figures 7.15(b) and 7.16(b). The wall stress structures are also slightly wider in ZPG2 as seen in figure 7.19(b). The total wall stress for the MTSWM (LaRTE+lamNEQ+turbNEQ) has a similar RMS as the EQWM in the ZPG regions.

Very distinct behavior from the MTSWM appears in the suction region, particularly from the lamNEQ model. In this region, the lamNEQ wall stress RMS spikes up very rapidly (see figure 7.15(b)) and we can see very large (in size and magnitude) wall stress fluctuations in the contour plot of figure 7.19(c). Figure 7.20 shows  $t_v$  spikes up very rapidly in the suction region by several

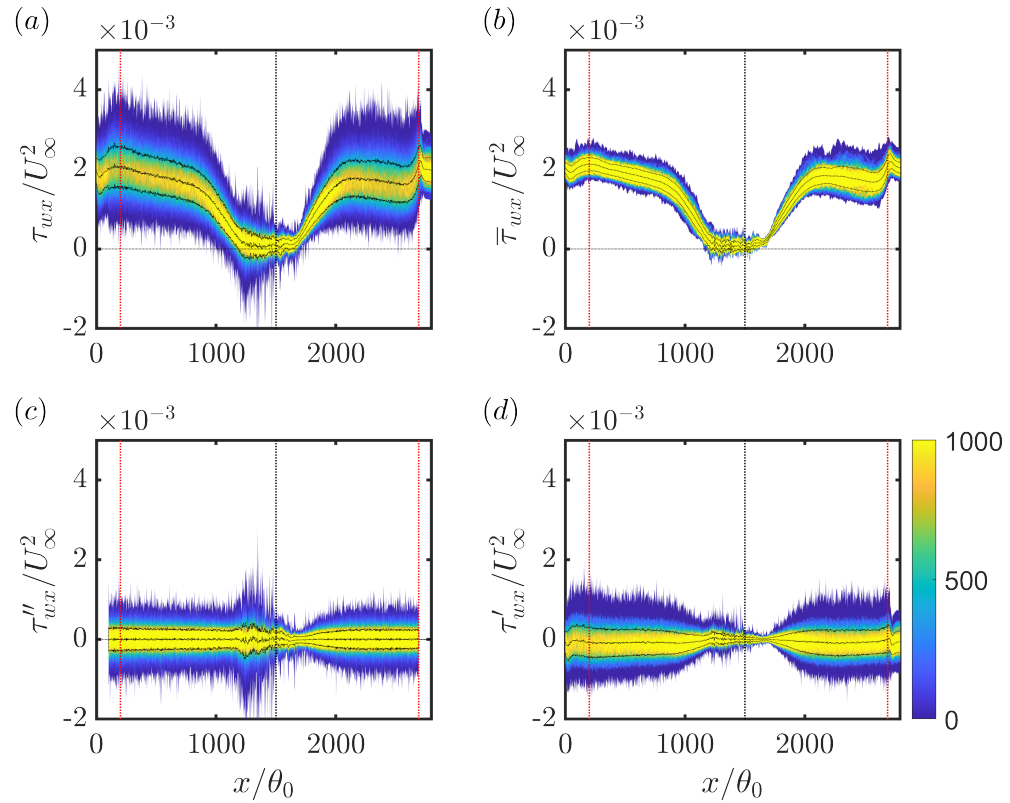


**Figure 7.16:** Wall stress PDFs for the MTSWM. Each panel corresponds to the (a) total, (b) LaRTE, (c) lamNEQ, or (d) turbNEQ wall stress. PDFs correspond with each streamwise location (i.e. the integral of the contour at each  $x$  is one). Dotted lines inside the contour show the mean  $\pm$  RMS. Black dotted vertical lines show the center of the suction and blowing and red dotted vertical lines show the boundaries of the fringe region.

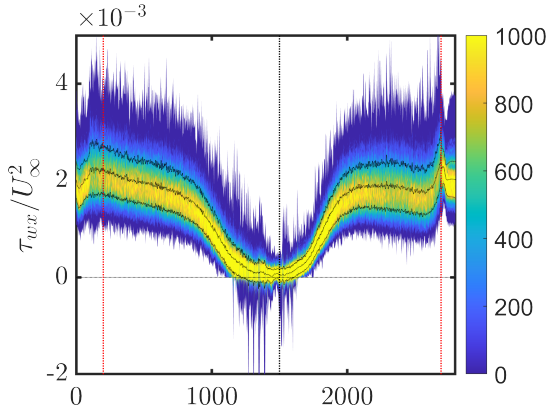


**Figure 7.17:** Wall stress PDFs for the EQWM. Dotted lines inside the contour show the mean  $\pm$  RMS. Black dotted vertical lines show the center of the suction and blowing and red dotted vertical lines show the boundaries of the fringe region.

orders of magnitude. One would expect, according to equations 5.7 and 5.6 for  $\nabla_h p''$ , that this means more LES pressure fluctuations go into the lamNEQ model thereby increasing it's wall stress fluctuations. However, figure 7.21 shows that  $\nabla_h p''$  already contained the largest LES pressure gradients and that the magnitude of these fluctuations actually decreases. Figure 7.22 shows that the time scale of these pressure gradient fluctuations decreases in the suction region. A potential explanation is that the lamNEQ model, which is governed by a non-local fractional derivative in time, has enough time for the pressure gradient fluctuations to build up in the history term and yield larger wall stress fluctuations. However, the behavior of such non-local operators is complex and it is still unclear why the model performs this way in this region. In terms of the other components of the MTSWM in the suction region, the turbNEQ model yields a zero mean wall stress and the fluctuations drop significantly in magnitude. The drop in the turbNEQ wall stress fluctuations is a response to the drop in the LES fluctuations in the suction and blowing

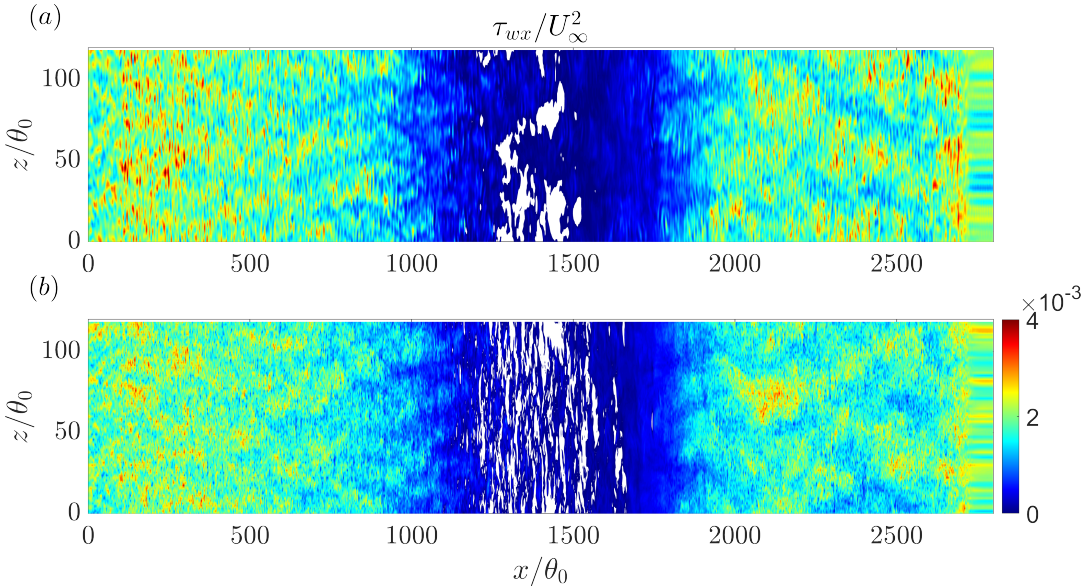


**Figure 7.18:** Instantaneous total wall stress contour for the (a) EQWM and (b) MTSWM. The  $z/\theta_0$  axis is stretched by a factor of five. White regions corresponds to negative wall stress.

region, which can be observed clearly in figure 7.24(a). This also causes the drop in the LaRTE wall stress fluctuations in the suction region. The EQWM has interesting behavior when intermittent separation begins ( $\tau_{wx} < 0$  instantaneously). In comparison to the full MTSWM, intermittent separation is predicted earlier for the MTSWM primarily due to the large spike in the lamNEQ wall stress fluctuations, as discussed earlier.

The blowing region has distinctly different wall stress behavior than the suction region. This is because the flow has slowed down so much that many of the turbulent fluctuations have died off that go into the model. The result is a continued decline in the RMS of all components of the MTSWM until around  $x/\theta_0 = 1650$  where the wall stress RMS increases quite rapidly for all components. The EQWM on the other hand does not exhibit the same trend.

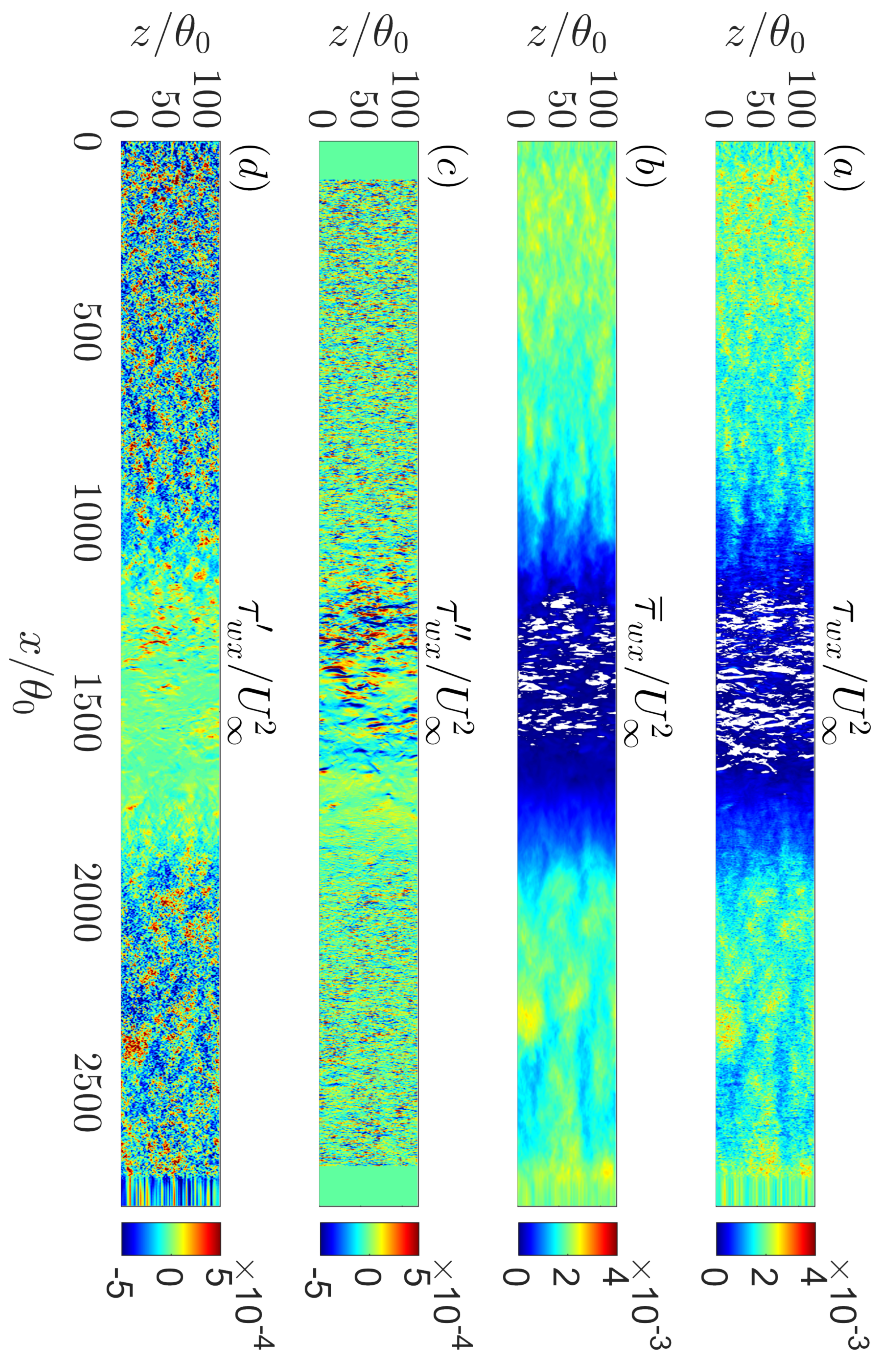


**Figure 7.19:** Instantaneous wall stress contour plots for the MTSWM with each of its wall stress components including the (a) total, (b) LaRTE, (c) lamNEQ, and (d) turbNEQ wall stress. The  $z/\theta_0$  axis is stretched by a factor of two. White regions corresponds to negative wall stress in panels (a) and (b).

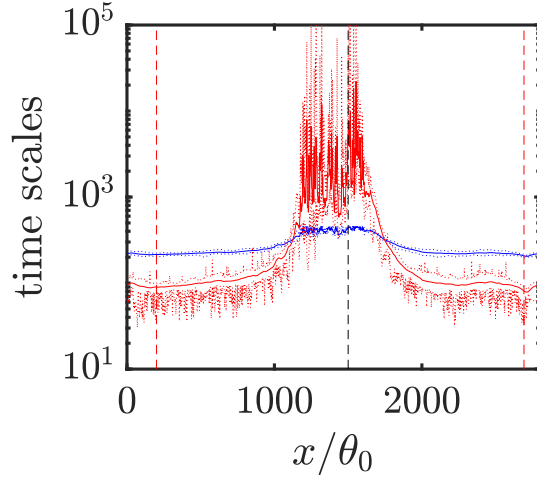


**Figure 7.20:** The MTSWM time scales  $T_s$  (blue) and  $t_v$  (red) normalized with  $U_\infty$  and  $\theta_0$ . Solid lines correspond with the mean and dotted lines correspond with the minimum and maximum values. Black dashed vertical lines show the center of the suction and blowing and red dashed vertical lines show the boundaries of the fringe region.

As soon as blowing is applied, the wall stress fluctuations start increasing.

Figures 7.23 and 7.24 provide additional insights into the LaRTE model behavior. Figure 7.23 shows the LaRTE model inputs and outputs (with mean, maximum, and minimum values) as a function of streamwise location and figure 7.24 shows time signals of the LaRTE model inputs at select streamwise locations (in regions ZPG1, suction,  $x = x_c$ , blowing, and ZPG2). In figure 7.23, panels (a) and (b) correspond with the velocity and pressure gradient inputs to the equilibrium stress closure fit and panel c shows the corresponding output to the fit with pressure gradient input  $Re_{\tau\Delta}^{pres}$  (red lines) and without pressure gradient input  $Re_{\tau\Delta}^{fit}$  (red lines). Similar information is contained in figure 7.24. As expected, in the ZPG regions there is no difference between the two fit outputs. In the suction region  $\psi_p > 0$  and  $Re_{\tau\Delta}^{pres} < Re_{\tau\Delta}^{fit}$  whereas in the blowing region  $\psi_p < 0$  and  $Re_{\tau\Delta}^{pres} > Re_{\tau\Delta}^{fit}$ . This is observed in

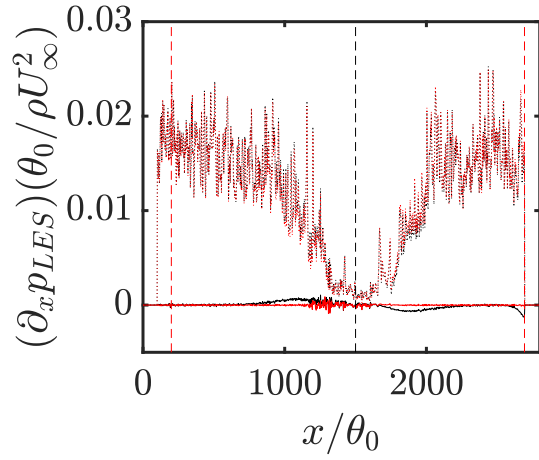


**Figure 7.21:** The MTSWM pressure gradients  $\partial_x p_{LES}$  (black) and  $\partial_x p''$  (red). Solid lines correspond with the mean and dotted lines correspond with the maximum values. Black dashed vertical lines show the center of the suction and blowing and red dashed vertical lines show the boundaries of the fringe region.

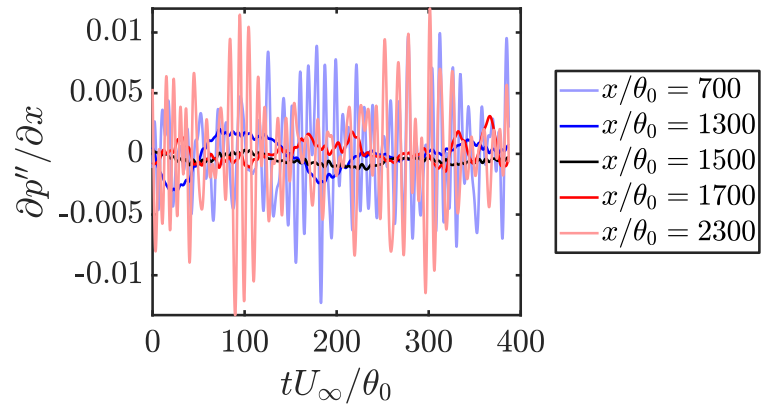


**Figure 7.22:** Time signals of the lamNEQ pressure gradient at the locations  $x/\theta_0 = 700, 1300, 1500, 1700, 2300$  (see figure legend for corresponding line colors).

both figures, although the pressure gradient magnitude is not large enough to strongly affect  $Re_{\tau\Delta}$ . Panel (d) shows the corresponding equilibrium wall stress (gray lines in figure 7.23 and dashed-dot lines in figure 7.24). In terms of mean value, the LaRTE wall stress slightly lags its equilibrium value, as seen in figure 7.23. This is because the LaRTE friction velocity relaxes in a Lagrangian manner to its equilibrium value, as was mentioned earlier in this section. If the advection term were to be removed (i.e. Eulerian relaxation) then it is expected that the corresponding wall stress would have the same mean as the equilibrium wall stress at any given location. In figure 7.24(d) we can see that the LaRTE wall stress is effectively a time filtered version the equilibrium wall stress, as has been pointed out before, where the filtering time scale is the relaxation time scale,  $T_s$ . From figure 7.20 we see that  $215 \leq T_s U_\infty / \theta_0 \leq 425$  which agrees well with the time scale of fluctuations filtered out in 7.20(d) by the LaRTE model.

## 7.5 Summary

In this chapter, the MTSWM is applied to streamwise developing flows such as ZPG turbulent boundary layers over a wide range of Reynolds numbers and a separated turbulent boundary layer induced by a suction and blowing transpiration boundary condition on the top surface. To enable LESGO to handle these flows several modifications are done including the addition of a fringe body force at the end of the domain to force the flow to a desired inflow velocity and a modified version of the rescale-recycle method by Lund et al. (1998) is used to prescribe the inflow velocity. For the simulations of the ZPG

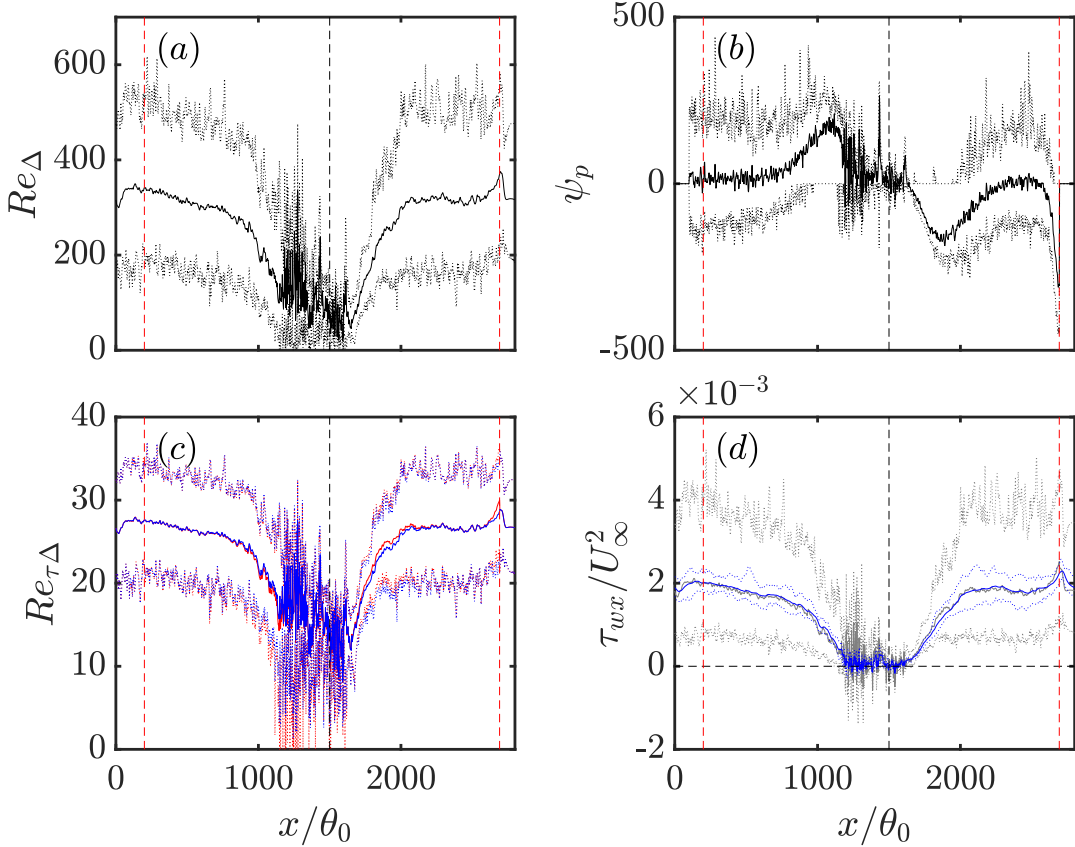


**Figure 7.23:** Inputs and outputs for the LaRTE model versus streamwise location. Panels correspond to (a)  $Re_\Delta$  the velocity input to the equilibrium wall stress fit, (b)  $\psi_p$  the pressure gradient input to the equilibrium wall stress fit, (c) the equilibrium fit output with the pressure gradient input  $Re_{\tau_\Delta}^{pres}$  (red lines) and without the pressure gradient input  $Re_{\tau_\Delta}^{fit}$  (blue lines), and (d) the equilibrium wall stress  $\tau_{wx}^{eq}$  (gray lines) and the LaRTE wall stress  $\bar{\tau}_{wx}$  (blue lines). Solid lines correspond with the mean and dotted lines correspond with the minimum and maximum values. Black dashed vertical lines show the center of the suction and blowing and red dashed vertical lines show the boundaries of the fringe region.

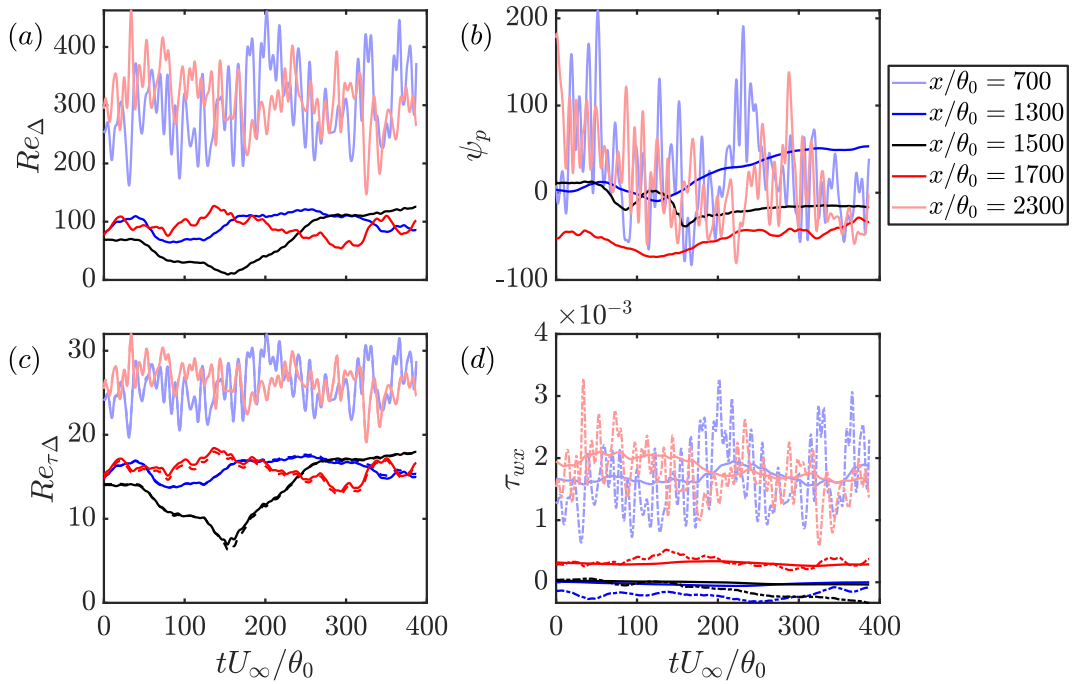


**Figure 7.24:** Time signals of the inputs and outputs for the LaRTE model at the locations  $x/\theta_0 = 700, 1300, 1500, 1700, 2300$  (see figure legend for corresponding line colors). Panels correspond to (a)  $Re_{\Delta}$  the velocity input to the equilibrium wall stress fit, (b)  $\psi_p$  the pressure gradient input to the equilibrium wall stress fit, (c) the equilibrium fit output with the pressure gradient input  $Re_{\tau_{\Delta}}^{pres}$  (solid lines) and without the pressure gradient input  $Re_{\tau_{\Delta}}^{fit}$  (dashed lines), and (d) the equilibrium wall stress  $\tau_{wx}^{eq}$  (dashed-dot lines) and the LaRTE wall stress  $\bar{\tau}_{wx}$  (solid lines).

boundary layers, LES using the MTSWM and EQWM gives reasonable results for the velocity profiles, Reynolds stress profiles, and skin friction. Briefly, the impacts of the fringe region and the challenges associated with simulating turbulent boundary layers for a streamwise periodic code are discussed. The fringe region generates a large region of pressure which in turn creates a large streamwise pressure gradient at the inlet. This pressure gradient in turn affects the LES velocity and thus the skin friction, causing the flow to evolve in an incorrect until some distance far enough downstream from the inlet. Many attempts to reduce the impact of this “fringe region effect” have been made but no satisfactory solution has been found to fix this issue. Nevertheless, flow statistics such as mean velocity and Reynolds shear stress profiles agree well with DNS and are considered good enough to move onto the primary flow of this chapter, a weakly separated turbulent boundary layer.

A separation bubble is generated through modification of the top vertical velocity. The domain is divided up into four regions based on this vertical velocity (ZPG1, suction, blowing, and ZPG2). Plots of different boundary layer thicknesses, the skin friction, and the wall pressure coefficient agree well with the DNS for both the EQWM and MTSWM. Generally, the EQWM predicts a slightly higher (and better) skin friction than the MTSWM in the ZPG regions. We later see that it is the negative turbNEQ velocity in this region that causes this underprediction in the total wall stress for the MTSWM. Significantly, neither of the LES predicts mean flow separation. The separation bubble studied is only weakly separated and thus any slight deviations can cause the separation in the resulting mean flow to be missed. A plot of the

“fraction of reversed wall stress” shows that the intermittent separation region is larger and in closer agreement to DNS for the MTSWM than the EQWM. This behavior can be understood through analysis of plots of the wall stress RMS, wall stress PDFs at different streamwise locations, and instantaneous wall stress contour plots for the different components the MTSWM. The lamNEQ velocity experiences a large increase in fluctuations in the suction region, possibly explained by the change in time scale for the pressure gradient fluctuations in this region. Conversely, the turbNEQ contribution disappears in the suction and blowing regions but remain significant in the ZPG regions. Plots (versus time and streamwise location) of the various LaRTE inputs (velocity and pressure gradient) and outputs (the LaRTE wall stress and corresponding equilibrium stress) show the pressure gradient does not play a significant role in the equilibrium stress closure. The time signals of the different LaRTE inputs show both the velocity and pressure gradient fluctuate much more rapidly in the ZPG regions than the suction and blowing regions. Finally, plots of the LaRTE wall stress and corresponding equilibrium stress show the LaRTE model relaxes to its equilibrium value in a Lagrangian manner. For time signals this just appears as filtering. For plots of the wall stress versus streamwise position, this is apparent as the wall stress having a lagged response to changing conditions (i.e. in the blowing region the equilibrium stress decreases more rapidly than the LaRTE wall stress).

# **Chapter 8**

## **Summary, conclusions, and future directions**

This dissertation deals with the development of improved wall modeling concepts and tools for Large Eddy Simulations of turbulent flows. In chapter 2 the “Lagrangian Relaxation Towards Equilibrium” (LaRTE) wall model is introduced. The main ansatz for the model is that slow, quasi-equilibrium velocity behavior follows the law of the wall. The governing equation for the LaRTE model is derived by substituting the law of the wall velocity profile into a RANS-like momentum balance for the quasi-equilibrium velocity, vertically integrating from the wall to the wall model height, and then simplifying terms to get an evolution equation for the friction velocity vector, from which the corresponding wall stress can be obtained. The underlying behavior of this friction velocity can be described as a Lagrangian relaxation towards its equilibrium value, thus it is dubbed the Lagrangian relaxation towards equilibrium wall model, or LaRTE for short. The Lagrangian relaxation occurs at a rate corresponding to the relaxation time scale which is formally derived. The primary term to be closed in the model is the total shear stress at the

wall model height,  $\bar{\tau}_\Delta$ . The simplest consistent way to connect known LES inputs (such as the velocity and pressure gradient) to this stress is through an equilibrium stress closure. This type of closure worked well for the flows discussed in chapter 4, however, modifications were needed in chapter 5 for the model work well for the more challenging flows in chapter 6. In future work, it may be interesting and useful to explore alternative closure models. In §2.4, an a-priori test reveals that the relaxation time scale is consistent with idea of quasi-equilibrium. This is done by showing that DNS velocities filtered using the relaxation time scale collapse to the law of the wall.

The LaRTE model, although well motivated conceptually, does not offer inherent advantages to wall modeling when considered as a standalone wall model. This is because the EQWM already captures the mean wall stress well for quasi-steady flows and the LaRTE model by itself cannot properly model non-equilibrium wall stress behavior. The real advantage the LaRTE model offers is the ability to extract the quasi-equilibrium dynamics from LES inputs (which can be highly non-equilibrium in nature) so that more complex non-equilibrium dynamics can be modeled separately. The first example of this is the introduction of the laminar non-equilibrium (lamNEQ) model in chapter 3. The lamNEQ model predicts the wall stress response to rapid changes in the LES pressure gradient. It was physically motivated by the observation in experimental and DNS studies that the wall stress follows laminar trends for an array of complex non-equilibrium flows.

The lamNEQ wall stress is found to be governed by a non-local convolutional-type operator (with a  $t^{-1/2}$  kernel) of the fast, lamNEQ pressure gradient

fluctuations. It can be directly related to the “Caputo fractional derivative”. This type of operator is expensive (both in storage and number of computations) to evaluate through traditional methods. This motivated the use of the “sum-of-exponentials” method already developed by Jiang et al. (2017) to approximate the kernel with a series of exponential terms. This method is able to significantly reduce the storage and work requirements needed for evaluating the operator, compared with alternative methods, thus enabling it to be practical for wall modeling. However, most testing and simulations done were with 48 exponential terms which is certainly not a small number. Attempts were made at reducing the number of exponential terms (not shown), however, it is difficult to ensure accuracy for a variety of non-equilibrium flows since the accuracy is dependent on the behavior of input signal. Thus, a large number of terms were used so accuracy of the numerical method would not be a concern when validating the model. In the future it would be useful to more rigorously quantify the accuracy of this model so that fewer exponential terms could be used with confidence.

The LaRTE and lamNEQ models are then combined (LaRTE+lamNEQ) and tested in chapter 4 for stationary channel flow and channel flow with a sudden spanwise pressure gradient (SSPG) to understand the wall model’s behavior and performance under non-equilibrium conditions. For stationary channel flow, plots of the mean velocity and Reynolds stress profiles show good agreement with DNS, however, with some discrepancies not attributed to the wall model (since the EQWM and LaRTE+lamNEQ wall model give identical results here). This includes an overprediction of the velocity in the wake region

(and buffer region, not shown here but in later sections) and an overprediction of the spanwise normal Reynolds stress in the near-wall region. This behavior is consistently observed (for a wide range of flows) and is attributed to code and SGS model specific issues and future work should focus on understanding and reducing these discrepancies. Interestingly, the LaRTE model yields large, streamwise elongated wall stress structures which advect down stream due to the inherent Lagrangian nature of LaRTE. When switched to Eulerian relaxation, these structures thin out unrealistically. Streamwise wall stress PDFs are underpredicted by the LaRTE+lamNEQ model, suggesting there is some “missing physics” of the model to capture these turbulent fluctuations. This later motivated the development of the turbNEQ model in §5.1. For the SSPG flow, the LaRTE+lamNEQ shows an improved spanwise wall stress response (relative to the EQWM) due to the lamNEQ model which is able to capture the quick rise in the spanwise wall stress immediately after the SSPG.

Chapter 5 introduces the final ingredients needed to form the multi-time-scale wall model (MTSWM). First the turbNEQ model is introduced. It is motivated by the underpredicted wall stress PDFs for the LaRTE+lamNEQ model, attributed to the missing physics of the model for turbulence dynamics operating at intermediate time scales between the relaxation time scale and a laminar viscous diffusion time scale associated with the lamNEQ model. The turbNEQ model utilizes the identification of velocity fluctuation (measured as the difference between the LaRTE velocity input and output) to connect turbulence occurring at the wall model height with corresponding wall stress fluctuations, and may be physically explained by the wall attached

eddy hypothesis. The turbNEQ model offers ample opportunity for future development. The proposed model connects the turbulent velocity fluctuation with the wall stress by assuming they are connected via a linear + plug flow velocity profile in the near wall region. Alternative methods for connecting the velocity profile to the wall stress could be explored in the future.

After the turbNEQ model is introduced in chapter 5, modifications to the LaRTE model are outlined. The original LaRTE model did not account for contributions of the laminar Stokes layer to the velocity and pressure gradient at the LES wall model height. A velocity correction model was developed to account for the contribution of the laminar Stokes to the LES velocity so the equilibrium stress closure could continue to be used. The final MTSWM thus includes the LaRTE model (with the velocity correction model and pressure gradient decomposition modification) to capture the slow quasi-equilibrium wall stress dynamics, the lamNEQ model to capture the wall stress dynamics responding to fast changes in the LES pressure gradient, and the turbNEQ model to capture the wall stress fluctuations associated with LES velocity fluctuations formed by near-wall attached turbulent eddies.

In chapter 6, the MTSWM is tested for channel flows with a wide range of time scale dynamics such as pulsating and linearly accelerating channel flow. Revisiting stationary channel flow shows the introduction of the turbNEQ significantly improves the streamwise wall stress PDFs. For pulsatile channel flow, the MTSWM is able follow the DNS wall stress trends over all of the forcing frequencies whereas the EQWM is unable to properly model the wall stress for high frequencies where a laminar Stokes layer is observed. For low,

intermediate, and high forcing frequencies the LaRTE, turbNEQ, and lamNEQ models are dominant, respectively, in the MTSWM. For linearly accelerating channel flow, the MTSWM gives good skin friction predictions compared with the DNS over all acceleration rates whereas the EQWM is unable to predict the sharp rise in skin friction immediately after acceleration for the fast acceleration cases. Looking at the different MTSWM components shows the lamNEQ model captures this quick rise in  $C_f$  associated with a developing laminar Stokes layer, the turbNEQ model effectively speeds up the wall stress response during the “transition” stage, and the LaRTE model captures the correct mean wall stress before and after the acceleration. Finally, the MTSWM in the limit of “instantaneous relaxation” is explored and the corresponding model, the EQMTSWM, is tested for the pulsating and linearly accelerating channel flows. For these flows, the EQMTSWM yields similar results as the full MTSWM but with non-sinusoidal behavior during intermediate forcing frequencies and an over-prediction of the skin friction during the transition stage for the two fastest flow accelerations considered.

In chapter 7, the MTSWM is applied to streamwise developing flows such as ZPG turbulent boundary layers over a wide range of Reynolds numbers and a separated turbulent boundary layer induced by a suction and blowing transpiration boundary condition on the top surface. These flows are tested to see wall model (and code) performance for spatial non-equilibrium, since temporal non-equilibrium has been exclusively studied so far. Several modifications to LESGO are needed to enable it to handle these types of flows. These modifications include adding a fringe body force at the end of the domain to

force the flow to a desired inflow velocity (this is needed because LESGO is periodic in  $x$ ) and a modified version of the rescale-recycle method by Lund et al. (1998) is used to prescribe the inflow velocity. For the simulations of the ZPG boundary layers, LES using the MTSWM and EQWM gives reasonable results for the velocity profiles, Reynolds stress profiles, and skin friction. Some negative fringe region effects are observed such as a large pressure gradient being generated at the inlet which in turn affects the skin friction evolution downstream of the inlet. Future work should focus on developing different fringe region strategies to reduce errors arising from the large inlet pressure gradient. Despite these issues, however, the flow statistics obtained in WMLES were considered sufficiently accurate to apply the MTSWM to a more complex case, a separated turbulent boundary layer. The separation bubble is generated through modification of the top vertical velocity. The domain is divided up into four regions based on this vertical velocity (ZPG1, suction, blowing, and ZPG2). The EQWM and MTSWM give very similar and reasonably accurate skin friction, wall pressure coefficient, and boundary layer thickness predictions compared with the DNS reference data. In the ZPG regions the EQWM agrees slightly better than the MTSWM with the latter underpredicting the skin fregion due to a negative mean turbNEQ wall stress in the ZPG regions. The MTSWM gives a wider “fraction of reversed wall stress” than the EQWM, more consistent with the DNS. Subsequent analysis shows this is primarily caused by the lamNEQ model which predicts large wall stress fluction in the blowing region. Neither wall models are able to predict mean flow separation, primarily because the size of the separation is so small that minor discrepancies can lead to missing it. Future tests should

involve flows with a larger separation bubble so that wall model performance can be quantified with more certainty.

In summary, in this dissertation we have developed a multi-time-scale wall model that captures the full spectrum of time scales relevant for the modeling of non-equilibrium flows. The components of the model have been rigorously developed and tested for a wide range of non-equilibrium conditions. The MTSWM was tested for streamwise homogeneous flows such as stationary channel flow, channel flow with a sudden spanwise pressure gradient, pulsating channel flow, and linearly accelerating channel flow. Unlike the classical EQWM, the MTSWM is able to capture the proper wall stress behavior for all these flows. Analysis of its constituent parts shows the model components are “engaged” or “disengaged” depending on the time scale of the flow dynamics. This highlights the usefulness of the MTS wall modeling approach, since it is simpler to model dynamics through its constituent parts as opposed to all at once which is what is traditionally done. Finally, the MTSWM was applied to flows with spatial non-equilibrium, mainly a separated boundary layer, to test its performance and understand its behavior for this other class of flows. MTSWM results are good compared with DNS although similar to the traditional EQWM. Future efforts should focus on continuing developing and testing the MTSWM for flows not previously tested. Some examples include wall bounded flows with roughness, flows with a greater degree of separation than the one studied here, and flows with combined temporal and spatial non-equilibrium. Applications to flows over rough walls will likely require modification of the MTSWM model equations. The current LaRTE model was

derived for smooth walls where the law of the wall for the quasi-equilibrium behavior is well established. For rough walls, dependence on a roughness length must be included. New ways for modeling the turbNEQ portion also remain an open challenge for future development. The goal is to continue improving the wall model so that wall modeled LES can become a high-fidelity, robust and generally applicable prediction tool for a broad community of engineers and researchers.

# Chapter 9

## Appendix

### 9.1 Fits for $f(\Delta^+)$ , cell thickness scales, and $Re_{\tau\Delta}$

Here we provide details how the cell thickness scales  $\delta_\Delta^*$  and  $\theta_\Delta$ , and law of the wall quantities  $f(\Delta^+)$  and  $Re_{\tau\Delta}$ , are evaluated. We begin with the velocity profile fit to the numerically obtained solution to the “full equilibrium” streamwise momentum equation with a prescribed eddy viscosity. As in Meneveau (2020), a mixing length model with the van-Driest damping function is used. All variables are non-dimensionalized in inner units such that we can obtain  $u^+ = f(y^+)$ , i.e. the law of the wall. We then develop a fit for this velocity profile as a function of the wall-model height in inner units  $\Delta^+ \equiv u_\tau \Delta / \nu$  where  $u_\tau$  is the friction velocity magnitude obtained from the quasi-equilibrium wall model (its value at the previous time-step is used for explicit evaluation).

$$f(\Delta^+) = \left[ \frac{1}{\kappa} \log(\kappa_2 + \Delta^+) + B \right] \left[ 1 + (\kappa_1^{-1} \Delta^+)^{-\beta} \right]^{-\frac{1}{\beta}}. \quad (9.1)$$

We set  $\kappa = 0.4$  and other fitting parameters are chosen to minimize the error between the fit and the numerical solution. This yields

$$B = 4.95, \kappa_2 = 9.753, \beta = 1.903, \kappa_1 = \frac{1}{\kappa} \log(\kappa_2) + B,$$

where the last choice is required to ensure the near-wall viscous layer asymptote  $f(\Delta^+) = \Delta^+$ . The fit has an error, relative to the numerical solution, of less than one percent for  $\Delta^+ > 5$  and an error less than 2.25% for  $0 \leq \Delta^+ \leq 5$ . Other fits could also be used, such as the traditional Reichardt fit (Reichardt, 1951):  $f(\Delta^+) = \kappa^{-1} \log(1 + \kappa \Delta^+) + 7.3[1 - \exp(-\Delta^+/11) - (\Delta^+/11) \exp(-\Delta^+/3)]$ . But it yields over 3% relative error near  $\Delta^+ \sim 10$ , so we prefer to use equation 9.1 instead.

From the numerical solution of the velocity profile we can obtain the cell thickness scales from their definitions in Eqs. 2.8 and 2.18 through numerical integration. We then provide fits for these scales (non-dimensionalized by  $\Delta$ ) to eliminate the need for numerical integration while implementing the wall model. The fits were developed by analytically determining the length scales when  $\Delta$  lies in the viscous sublayer or when  $\Delta$  lies in the log-layer and then using a merger function to create a function valid for any  $\Delta$  within the range of  $\Delta^+$  considered. The log-layer solutions are denoted with superscript “log”. The cell displacement thickness fit is

$$\frac{\delta_\Delta^*}{\Delta} = \frac{1}{2}\gamma_1 + (1 - \gamma_1)^{C_3} \left( \frac{\delta_\Delta^{*log}}{\Delta} \right) \quad (9.2)$$

where

$$\frac{\delta_{\Delta}^{*log}}{\Delta} = \frac{C_1}{Re_{\Delta}} + \frac{1}{\kappa} \frac{\Delta^+}{Re_{\Delta}}, \quad \gamma_1 = \frac{1}{1 + C_2 Re_{\Delta}^{C_4}},$$

$$C_1 = 23.664, C_2 = 0.0016, C_3 = 1.516, C_4 = 1.177$$

Similarly, the cell momentum thickness fit is

$$\frac{\theta_{\Delta}}{\Delta} = \frac{1}{6} \gamma_2 + (1 - \gamma_2)^{C_8} \left( \frac{\theta_{\Delta}^{log}}{\Delta} \right) \quad (9.3)$$

where

$$\frac{\theta_{\Delta}^{log}}{\Delta} = \frac{1}{Re_{\Delta}} \left( C_5 + \frac{\Delta^+}{\kappa} \right) + \frac{\Delta^+}{Re_{\Delta}^2} \left( C_6 - \frac{2\Delta^+}{\kappa^2} \right), \quad \gamma_2 = \frac{1}{1 + C_7 Re_{\Delta}},$$

$$C_5 = -103.5, C_6 = 2586, C_7 = 0.00154, C_8 = 2.475$$

For both fits,  $Re_{\Delta} = \Delta^+ f(\Delta^+)$  and  $\kappa = 0.4$ . The fitting functions from Eqs. 9.2 and 9.3 have a maximum error of 0.5 percent over (over the range  $10^{-1} \leq \Delta^+ \leq 10^5$ ) compared to the numerical solutions obtained by integrating the velocity profile. Note Eqs. 9.2 and 9.3 require the fit  $f(\Delta^+)$  given by equation 9.1. Figure 9.1 displays the results as well as the associated cell shape factor  $H_{\Delta} = \delta_{\Delta}^*/\theta_{\Delta}$ . Note that its low Reynolds number limit is not the traditional Blasius profile value, but  $H_{\Delta} \rightarrow 3$  associated with a linear profile.

Furthermore, to evaluate  $\bar{\tau}_{\Delta}$  according to equation 5.9 in terms of  $Re_{\tau\Delta}^{pres}$ , we use the fitting function provided in Meneveau (2020) reproduced here for completeness. Since the applications in the present paper only deal with smooth surfaces the merging with rough wall parameterizations treated in Meneveau (2020) is omitted. Mean pressure gradients are included, however,

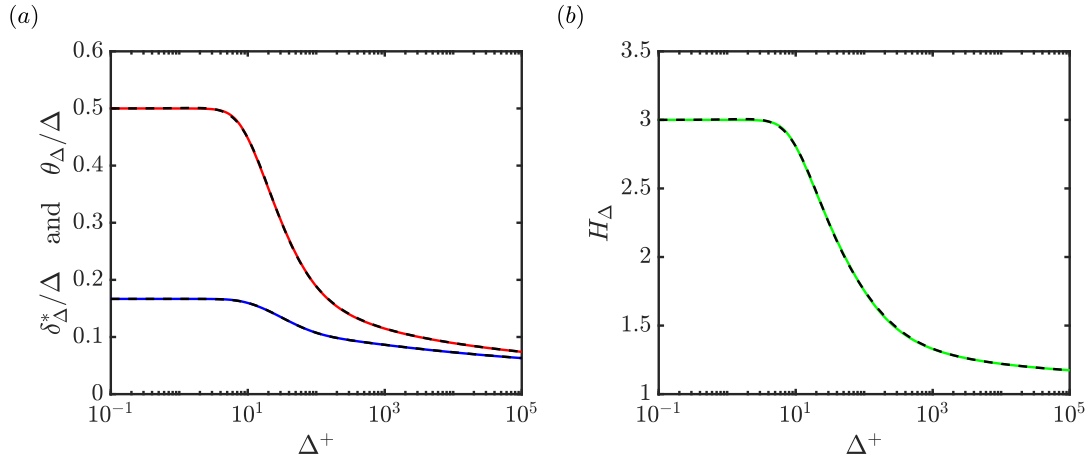


**Figure 9.1:** (a) Numerical evaluation of the cell displacement thickness (—), cell momentum thickness (—), (b) cell shape factor (—), and their corresponding fits (---).

and so we use  $Re_{\tau\Delta}^{\text{pres}}$  that generalizes  $Re_{\tau\Delta}^{\text{fit}}$  to include pressure gradients. The inputs are  $Re_\Delta = U_{\text{LES}}\Delta/\nu$  and  $\psi_p = \rho^{-1}(\nabla_h P \cdot \hat{e}_u)\Delta^3/\nu^2$ , and the fitting function Meneveau (2020) is provided in algorithm 1.

Recently, it was discovered that the  $Re_{\tau\Delta}^{\text{pres}}$  fit in algorithm 1 changes too sharply between favorable and adverse pressure gradients. The fit has since been updated to more gradually change between these conditions and is reflected in algorithm 2. Only the adverse pressure gradient side of the fit has been modified. Algorithm 2 is only used in chapter 7. Algorithm 1 is used everywhere else in this dissertation.

---

**Algorithm 1:**  $Re_{\tau\Delta}^{\text{pres}} = Re_{\tau\Delta}^{\text{pres}}(Re_{\Delta}, \psi_p)$  where  $0 < Re_{\Delta} < 10^7$  and  $|\psi_p| < 2 \times 10^7$ . This is the original algorithm for the fit.

---

$$\beta_1 = [1 + 0.155/Re_{\Delta}^{0.03}]^{-1}, \quad \beta_2 = 1.7 - [1 + 36/Re_{\Delta}^{0.75}]^{-1},$$

$$\kappa = 0.4, \quad \kappa_3 = 0.005, \quad \kappa_4 = \kappa_3^{\beta_1-1/2},$$

$$Re_{\tau\Delta}^{\text{fit}} = \kappa_4 Re_{\Delta}^{\beta_1} [1 + (\kappa_3 Re_{\Delta})^{-\beta_2}]^{(\beta_1-1/2)/\beta_2}$$

**if**  $\psi_p < 0$  **then**

$$Re_{\tau\Delta-\min}(\psi_p) = 1.5(-\psi_p)^{0.39} \left[ 1 + \left( \frac{1000}{-\psi_p} \right)^2 \right]^{-0.055},$$

$$p(\psi_p) = 2.5 - 0.6 [1 + \tanh(2(\log_{10}(-\psi_p) - 6))],$$

$$Re_{\tau\Delta}^{\text{pres}} = ((Re_{\tau\Delta-\min})^p + (Re_{\tau\Delta}^{\text{fit}})^p)^{1/p}$$

**else**

$$Re_{\Delta-\min}(\psi_p) = 2.5\psi_p^{0.54} \left( 1 + \left[ \frac{30}{\psi_p} \right]^{1/2} \right)^{-0.88}$$

**if**  $Re_{\Delta} > Re_{\Delta-\min}$  **then**

$$| Re_{\tau\Delta}^{\text{pres}} = Re_{\tau\Delta}^{\text{fit}} (1 - (1 + \log[Re_{\Delta}/Re_{\Delta-\min}])^{-1.9})$$

**else**

$$| Re_{\tau\Delta}^{\text{pres}} = 0 \text{ (flow separation)}$$

**end**

**end**

---

---

**Algorithm 2:**  $Re_{\tau\Delta}^{\text{pres}} = Re_{\tau\Delta}^{\text{pres}}(Re_{\Delta}, \psi_p)$  where  $0 < Re_{\Delta} < 10^7$  and  $|\psi_p| < 2 \times 10^7$ . This is the updated algorithm for the fit.

---

$$\beta_1 = [1 + 0.155/Re_{\Delta}^{0.03}]^{-1}, \quad \beta_2 = 1.7 - [1 + 36/Re_{\Delta}^{0.75}]^{-1},$$

$$\kappa = 0.4, \quad \kappa_3 = 0.005, \quad \kappa_4 = \kappa_3^{\beta_1-1/2},$$

$$Re_{\tau\Delta}^{\text{fit}} = \kappa_4 Re_{\Delta}^{\beta_1} [1 + (\kappa_3 Re_{\Delta})^{-\beta_2}]^{(\beta_1-1/2)/\beta_2}$$

**if**  $\psi_p < 0$  **then**

$$Re_{\tau\Delta-\min}(\psi_p) = 1.5(-\psi_p)^{0.39} \left[ 1 + \left( \frac{1000}{-\psi_p} \right)^2 \right]^{-0.055},$$

$$p(\psi_p) = 2.5 - 0.6 [1 + \tanh(2(\log_{10}(-\psi_p) - 6))],$$

$$Re_{\tau\Delta}^{\text{pres}} = ((Re_{\tau\Delta-\min})^p + (Re_{\tau\Delta}^{\text{fit}})^p)^{1/p}$$

**else**

$$a = 12.38(1.0 + 20.3Re_{\Delta})^{-1} \text{ if } Re_{\tau\Delta}^{\text{fit}} - a\psi_p > 0 \text{ then}$$

$$| Re_{\tau\Delta}^{\text{pres}} = Re_{\tau\Delta}^{\text{fit}} - a\psi_p$$

**else**

$$| Re_{\tau\Delta}^{\text{pres}} = 0 \text{ (flow separation)}$$

**end**

**end**

---

## 9.2 Sum of exponentials (SOE) constants used for the lamNEQ model

$\omega_m$	$s_m$	$\omega_m$	$s_m$
1.3898757483451424e-01	7.5282266941433940e-01	1.5527017883648535e+00	9.3954363832858405e+01
1.2060529793429185e-01	5.6673908971466702e-01	1.7895412273724953e+00	1.2480278190206187e+02
1.0555353081992419e-01	4.2637779056655817e-01	2.0625066760812811e+00	1.6577978643123276e+02
1.0260701642375072e-01	3.1612785829153345e-01	2.3771085705165462e+00	2.2021093737118954e+02
1.1978321072028018e-01	2.1598964664056086e-01	2.7396978742194036e+00	2.9251368928511243e+02
1.4109533658267584e-01	1.2172750553149388e-01	3.1575942870675360e+00	3.8855589754363325e+02
1.5672901568060668e-01	4.6830157099149762e-02	3.6392340102692207e+00	5.1613203431577790e+02
1.6481868095304203e-01	5.3781334349654710e-03	4.1943400505072308e+00	6.8559576249136285e+02
1.6018785097424312e-01	1.0000000000000000e+00	4.8341185012138190e+00	9.1070020516985505e+02
1.8462190588734567e-01	1.3283340635894432e+00	5.5714847633662217e+00	1.2097141042450137e+03
2.1278297902227652e-01	1.7644713844920430e+00	6.4213242725902608e+00	1.6069044518732414e+03
2.4523956647496567e-01	2.3438074442496064e+00	7.4007929959489198e+00	2.1345059203567503e+03
2.8264687918732784e-01	3.1133592666912668e+00	8.5296637646353481e+00	2.8353369229432074e+03
3.257600698860445e-01	4.1355811661378592e+00	9.8307254340931181e+00	3.7662746164983369e+03
3.7544947759177760e-01	5.4934333357198710e+00	1.1330242929529694e+01	5.0028708659270051e+03
4.3271819739031103e-01	7.2971146258944870e+00	1.3058487463901008e+01	6.6454837869500625e+03
4.9872233024201951e-01	9.6930059234923824e+00	1.5050347632037740e+01	8.8274224832371328e+03
5.7479432152857068e-01	1.2875549946749178e+01	1.7346033717255416e+01	1.1725765978179188e+04
6.6246985953317794e-01	1.7103031581714173e+01	1.9991889428498453e+01	1.5575734370493623e+04
7.6351887684418329e-01	2.2718539440636977e+01	2.3041327454801390e+01	2.0689778529747542e+04
8.7998128051923397e-01	3.0177809813998348e+01	2.6555907723388167e+01	2.7482937589185152e+04
1.0142081323056815e+00	4.0086212740457803e+01	3.0606580128531345e+01	3.6506522167217408e+04
1.1689091102347560e+00	5.3247881863443240e+01	3.5275116818514498e+01	4.8492856937897959e+04
1.3472072097110654e+00	7.0730975293198128e+01	4.0655762954707924e+01	6.4414713711379489e+04

**Table 9.1:** SOE constants. Computed using  $\delta t = 0.0004$ ,  $T = 1$ ,  $\epsilon = 10^{-9}$ . There are a total of  $N_{exp} = 48$  exponential terms.

## 9.3 ZPGBL velocity field initialization and fits

The velocity initial condition must be modified within LESGO, otherwise, it can take a significant amount of computational time until the flow reaches stationary conditions. Therefore the initialization routine has been modified to give a realistic zero pressure gradient boundary layer (ZPGBL) mean velocity profile plus random fluctuations such that stationary conditions can be achieved quickly from initialization. The mean velocity from this initialization

routine is also used in the modified rescaling-recycling method presented in §7.2.2. The mean velocity is computed using the composite (inner plus outer) fit of Monkewitz et al. (2008). The mean streamwise velocity is

$$U_{comp} = \begin{cases} u_\tau \left[ U_{inner}^+(y^+) + \frac{2\Pi}{\kappa} \mathcal{W}_{exp} \left( \frac{y^+}{\delta^+} \right) \right] & \text{if } 0 \leq y^+ \leq \delta^+ \\ U_\infty & \text{if } y^+ \geq \delta^+ \end{cases} \quad (9.4)$$

with the inner profile

$$\begin{aligned} U_{inner}^+ = & \frac{1}{\kappa} \log \left( \frac{y^+ + a_0}{a_0} \right) \\ & + \frac{\alpha_0}{a_0 + 4\alpha_0} \left\{ (a_0 - 4\alpha) \log \left[ \frac{a_0 [(y^+ - \alpha)^2 + \beta^2]}{2\alpha_0 (y^+ + a_0)^2} \right] \right. \\ & + \frac{2\alpha(5a_0 - 4\alpha_0)}{\beta_0} \left[ \arctan \left( \frac{y^+ - \alpha_0}{\beta_0} \right) \right. \\ & \left. \left. + \arctan \left( \frac{\alpha}{\beta} \right) \right] \right\} \end{aligned} \quad (9.5)$$

and with the outer profile

$$\begin{aligned} \mathcal{W}_{exp}(Y) = & \left[ 1 - \frac{1}{2\Pi} \log(Y) \right] \\ & \times \frac{1 - \exp \{ Y^4 [a_1 (Y - \frac{5}{4}) + a_2 (Y^2 - \frac{3}{2}) + a_3 (Y^3 - \frac{7}{4})] \}}{1 - \exp \left[ -\frac{1}{4} (a_1 + 2a_2 + 3a_3) \right]} \end{aligned} \quad (9.6)$$

where the various constants and coefficients in equations 9.4-9.6 are  $\kappa = 0.384$ ,  $\Pi = 0.446$ ,  $\alpha_0 = 0.5(a_0 - 1/\kappa)$ ,  $\beta_0 = (2a_0\alpha_0 - \alpha_0^2)^{0.5}$ ,  $a_0 = 10.306$ ,  $a_1 = 132.8410$ ,  $a_2 = -166.2041$ , and  $a_3 = 71.9114$ . The mean streamwise velocity is first computed at the inlet since this is where the boundary layer profile is fixed. This is done by specifying the inlet Reynolds number  $Re_{\theta_0} \equiv U_\infty \theta_0 / \nu$

with  $U_\infty = 1$  and  $\theta_0 = 1$  such that all simulation variables are normalized with these two quantities (thus the molecular viscosity controls the inlet Reynolds number). To evaluate equation 9.4,  $u_\tau$  and  $\delta^+$  must then be solved in an iterative manner achieve the target Reynolds number. An initial guess for  $\delta^+$  is made using a linear fit to equation 9.4 over a wide range of Reynolds numbers

$$\delta_{fit}^+ = 0.3851 Re_\theta^t + 72.1823 \quad (9.7)$$

where  $Re_\theta^t$  is the known target Reynolds number. Then  $u_\tau$  may be computed using the definition of  $\delta^+$ ,  $u_\tau = U_\infty / U_{comp}(\delta^+)$  since  $U_\infty$  is prescribed. Equation 9.4 is then used to compute  $U$  for the current iteration. The momentum thickness must then be computed to compare with its target value. This is done using a “near-wall corrected” version of its definition

$$\theta(x) = \int_0^{L_y} \frac{U(x, y)}{U_\infty} \left( 1 - \frac{U(x, y)}{U_\infty} \right) dy \quad (9.8)$$

$$= \int_0^\Delta \frac{U}{U_\infty} \left( 1 - \frac{U}{U_\infty} \right) dy + \int_\Delta^{L_y} \frac{U}{U_\infty} \left( 1 - \frac{U}{U_\infty} \right) dy \quad (9.9)$$

$$= \Delta \frac{U_\Delta}{U_\infty} \left[ \left( 1 - \frac{U_\Delta}{U_\infty} \right) \left( 1 - \frac{\delta_\Delta^*}{\Delta} \right) + \frac{U_\Delta \theta_\Delta}{U_\infty \Delta} \right] + \int_\Delta^{L_y} \frac{U}{U_\infty} \left( 1 - \frac{U}{U_\infty} \right) dy \quad (9.10)$$

where the first term of equation 9.10 is a modeled term which assumes the velocity profile follows the law of the wall (see the fits in the appendix for more information) and the second term is evaluated numerically using trapezoidal integration. Once the momentum thickness has been computed the next

iteration for  $\delta^+$  is determined using a Newton-Raphson method

$$\delta_{k+1}^+ = \delta_k^+ - \frac{Re_\theta(\delta_k^+) - Re_\theta^t}{\left. \frac{dRe_\theta}{d\delta^+} \right|_{\delta_k^+}} \quad (9.11)$$

where  $k$  is the iteration number. This iterative procedure is repeated until the computed  $Re_\theta$  is within some small  $\epsilon$  of  $Re_\theta^t$

Once the inlet velocity has been computed, the momentum thickness at the next grid point is estimated using the integrated momentum equation for a ZPGLB

$$\theta(x_i) = \theta(x_{i-1}) + \int_{x_{i-1}}^{x_i} (U_\infty^+)^{-2} dx \quad (9.12)$$

$$\approx \theta(x_{i-1}) + \Delta_x (U_\infty^+(x_{i-1}))^{-2}. \quad (9.13)$$

Then equation 9.4 can be solved for the streamwise velocity, again iterating using equation 9.11 with the updated  $Re_\theta^t$  from equation 9.12.

The mean vertical velocity can be computed by applying continuity

$$V(x, y) = - \int_0^y \partial_x U(x, y') dy' \quad (9.14)$$

where  $\partial_x U$  is computed using finite differencing and the integral is computed using trapezoidal integration. For ZPG boundary layer simulations, the computed vertical velocity on the top surface is used as a boundary condition. However, in order to enforce global mass conservation, blowing on the top surface must be added such that the top surface has zero flow rate. This must be done smoothly otherwise Gibbs phenomenon becomes severe. Two cosine functions work well to achieve this goal. The vertical velocity is then modified

according to

$$V(x, L_y) = \begin{cases} a_1 \left( \cos \left[ \frac{2\pi(x-x_1)}{L_b} \right] - 1 \right) + V(x_1, L_y) & \text{if } x_1 \leq x \leq x_1 + \frac{L_b}{2} \\ a_2 \left( \cos \left[ \frac{2\pi(x-x_2)}{L_b} \right] - 1 \right) + V(x_2, L_y) & \text{if } x_1 + \frac{L_b}{2} \leq x \leq x_2 \end{cases} \quad (9.15)$$

where  $x_1$  and  $x_2$  are the beginning and end positions, respectively, of the blowing,  $L_b \equiv x_2 - x_1$  is the length of the blowing, and the amplitudes are

$$a_1 = \frac{Q_{out}}{L_b} + \frac{1}{4}V(x_1, L_y) + \frac{3}{4}V(x_2, L_y) \quad (9.16)$$

$$a_2 = \frac{Q_{out}}{L_b} + \frac{3}{4}V(x_1, L_y) + \frac{1}{4}V(x_2, L_y) \quad (9.17)$$

where

$$Q_{out} = \int_0^{x_1} V(x, L_y) dx + \int_{x_2}^{L_x} V(x, L_y) dx \quad (9.18)$$

is the flow rate on the top surface (excluding the region of blowing).

Finally, random fluctuations are added to the mean velocity to perturb the flow to a ZPG turbulent boundary layer. The fluctuations are just a rescaled version of what is currently implemented in LESGO where  $u_\tau(x)$  and  $\delta(x)$  are the rescaling velocity and length scales, respectively, known from the mean velocity initialization routine. The velocity fluctuations have the form

$$u'_i = \begin{cases} \frac{u_{rms}}{\sigma_{rv}} (\text{rand} - 0.5) \left(1 - \frac{y}{\delta}\right) \frac{u_\tau}{u_{\tau,chan}} & \text{for } y \leq \delta \\ 0 & \text{for } y > \delta \end{cases} \quad (9.19)$$

where  $u_{rms} = 3U_\infty$ ,  $\sigma_{rv} = 0.289$ ,  $u_{\tau,chan} = U_\infty$ , and  $\text{rand}$  is a random variable uniformly distributed between 0 and 1.

# Bibliography

- Abe, H. (2020). Direct numerical simulation of a non-equilibrium three-dimensional turbulent boundary layer over a flat plate. *Journal of Fluid Mechanics*, 902, A20. <https://doi.org/10.1017/jfm.2020.488>
- Bae, H. J., Lozano-Durán, A., Bose, S. T., & Moin, P. (2019). Dynamic slip wall model for large-eddy simulation. *Journal of Fluid Mechanics*, 859, 400–432. <https://doi.org/10.1017/jfm.2018.838>
- Balaras, E., Benocci, C., & Piomelli, U. (1996). Two-layer approximate boundary conditions for large-eddy simulations. *AIAA Journal*, 34(6), 1111–1119. <https://doi.org/10.2514/3.13200>
- Bose, S. T., & Moin, P. (2014). A dynamic slip boundary condition for wall-modeled large-eddy simulation. *Physics of Fluids*, 26(1), 015104. <https://doi.org/10.1063/1.4849535>
- Bose, S., & Park, G. (2018). Wall-modeled large-eddy simulation for complex turbulent flows. *Annual Review of Fluid Mechanics*, 50(1), 535–561. <https://doi.org/10.1146/annurev-fluid-122316-045241>
- Bou-Zeid, E., Meneveau, C., & Parlange, M. B. (2005). A scale-dependent Lagrangian dynamic model for large eddy simulation of complex turbulent flows. *Physics of Fluids*, 17, 025105.
- Cheng, Z., Jelly, T., Illingworth, S., Marusic, I., & Ooi, A. (2020). Forcing frequency effects on turbulence dynamics in pulsatile pipe flow. *International Journal of Heat and Fluid Flow*, 82, 108538. <https://doi.org/https://doi.org/10.1016/j.ijheatfluidflow.2020.108538>
- Chevalier, M., Schlatter, P., Lundbladh, A., & Henningson, D. S. (2007). Simson : A pseudo-spectral solver for incompressible boundary layer flows.
- Choi, H., & Moin, P. (2012). Grid-point requirements for large eddy simulation: Chapman's estimates revisited. *Physics of Fluids*, 24, 1–6. <https://doi.org/10.1063/1.3676783>
- Chung, D., & Pullin, D. (2009). Large-eddy simulation and wall modelling of turbulent channel flow. *Journal of fluid mechanics*, 631, 281–309.

- Coleman, G. N., Kim, J., & Le, A.-T. (1996). A numerical study of three-dimensional wall-bounded flows. *International Journal of Heat and Fluid Flow*, 17(3), 333–342. [https://doi.org/https://doi.org/10.1016/0142-727X\(96\)00042-2](https://doi.org/https://doi.org/10.1016/0142-727X(96)00042-2)
- Coleman, G. N., Rumsey, C. L., & Spalart, P. R. (2018). Numerical study of turbulent separation bubbles with varying pressure gradient and reynolds number. *Journal of Fluid Mechanics*, 847, 28–70. <https://doi.org/10.1017/jfm.2018.257>
- Dean, R. B. (1978). Reynolds number dependence of skin friction and other bulk flow variables in two-dimensional rectangular duct flow. *Journal of Fluids Engineering*, 100(2), 215–223. <https://doi.org/10.1115/1.3448633>
- Deardorff, J. W. (1970). A numerical study of three-dimensional turbulent channel flow at large reynolds numbers. *Journal of Fluid Mechanics*, 41(2), 453–480. <https://doi.org/10.1017/S0022112070000691>
- de Wiart, C. C., Larsson, J., & Murman, S. (2018). Validation of wmls on a periodic channel flow featuring adverse favorable pressure gradients. *Tenth International Conference on Computational Fluid Dynamics*.
- Fowler, M., Zaki, T. A., & Meneveau, C. (2022). A lagrangian relaxation towards equilibrium wall model for large eddy simulation. *Journal of Fluid Mechanics*, 934, A44. <https://doi.org/10.1017/jfm.2021.1156>
- Fowler, M., Zaki, T. A., & Meneveau, C. (2023). A multi-time-scale wall model for large-eddy simulations and applications to non-equilibrium channel flows. *Journal of Fluid Mechanics*, 974, A51. <https://doi.org/10.1017/jfm.2023.585>
- Graham, J., Kanov, K., Yang, X., Lee, M., Malaya, N., Lalescu, C., Burns, R., Eyink, G., Szalay, A., Moser, R., et al. (2016). A web services accessible database of turbulent channel flow and its use for testing a new integral wall model for LES. *Journal of Turbulence*, 17(2), 181–215.
- Greenblatt, D., & Moss, E. A. (2004). Rapid temporal acceleration of a turbulent pipe flow. *Journal of Fluid Mechanics*, 514, 65–75. <https://doi.org/10.1017/S0022112004000114>
- Hack, M. P., & Zaki, T. A. (2014). Streak instabilities in boundary layers beneath free-stream turbulence. 741, 280–315. <https://doi.org/http://dx.doi.org/10.1017/jfm.2013.677>
- Hansen, C., Yang, X. I., & Abkar, M. (2023). A pod-mode-augmented wall model and its applications to flows at non-equilibrium conditions. *Journal of Fluid Mechanics*, 975, A24. <https://doi.org/10.1017/jfm.2023.857>

- He, S., & Ariyaratne, C. (2011). Wall shear stress in the early stage of unsteady turbulent pipe flow. *Journal of Hydraulic Engineering*, 137, 606–610. [https://doi.org/10.1061/\(ASCE\)HY.1943-7900.0000336](https://doi.org/10.1061/(ASCE)HY.1943-7900.0000336)
- He, S., Ariyaratne, C., & Vardy, A. (2011). Wall shear stress in accelerating turbulent pipe flow. *Journal of Fluid Mechanics*, 685, 440–460. <https://doi.org/10.1017/jfm.2011.328>
- He, S., Ariyaratne, C., & Vardy, A. E. (2011). Wall shear stress in accelerating turbulent pipe flow. *Journal of Fluid Mechanics*, 685, 440–460. <https://doi.org/10.1017/jfm.2011.328>
- He, S., Ariyaratne, C., & Vardy, A. (2008a). A computational study of wall friction and turbulence dynamics in accelerating pipe flows. *Computers & Fluids*, 37, 674–689. <https://doi.org/10.1016/j.compfluid.2007.09.001>
- He, S., Ariyaratne, C., & Vardy, A. (2008b). A computational study of wall friction and turbulence dynamics in accelerating pipe flows. *Computers & Fluids*, 37(6), 674–689. <https://doi.org/https://doi.org/10.1016/j.compfluid.2007.09.001>
- He, S., & Jackson, J. D. (2000). A study of turbulence under conditions of transient flow in a pipe. *Journal of Fluid Mechanics*, 408, 1–38. <https://doi.org/10.1017/S0022112099007016>
- He, S., & Seddighi, M. (2013). Turbulence in transient channel flow. *Journal of Fluid Mechanics*, 715, 60–102. <https://doi.org/10.1017/jfm.2012.498>
- He, S., & Seddighi, M. (2015). Transition of transient channel flow after a change in reynolds number. *Journal of Fluid Mechanics*, 764, 395–427. <https://doi.org/10.1017/jfm.2014.698>
- Inoue, M., & Pullin, D. I. (2011). Large-eddy simulation of the zero-pressure-gradient turbulent boundary layer up to  $Re_\theta = O(10^{12})$ . *Journal of Fluid Mechanics*, 686, 507–533. <https://doi.org/10.1017/jfm.2011.342>
- JHTDB. (2021). Webpage \NoCaseChange{<http://turbulence.pha.jhu.edu>}.
- (seen 06/06/2021).
- Jiang, S., Zhang, J., Zhang, Q., & Zhang, Z. (2017). Fast evaluation of the caputo fractional derivative and its applications to fractional diffusion equations. *Communications in Computational Physics*, 21(3), 650–678. <https://doi.org/10.4208/cicp.OA-2016-0136>
- Joel Sundstrom, L., & Cervantes, M. J. (2018). Laminar similarities between accelerating and decelerating turbulent flows. *International Journal of Heat and Fluid Flow*, 71, 13–26. <https://doi.org/https://doi.org/10.1016/j.ijheatfluidflow.2018.03.005>

- Jung, S. Y., & Chung, Y. M. (2012). Large-eddy simulation of accelerated turbulent flow in a circular pipe. *International Journal of Heat and Fluid Flow*, 33(1), 1–8. <https://doi.org/https://doi.org/10.1016/j.ijheatfluidflow.2011.11.005>
- Jung, S. Y., & Kim, K. (2017). Transient behaviors of wall turbulence in temporally accelerating channel flows. *International Journal of Heat and Fluid Flow*, 67, 13–26. <https://doi.org/https://doi.org/10.1016/j.ijheatfluidflow.2017.06.012>
- Jung, W. J., Mangiavacchi, N., & Akhavan, R. (1992). Suppression of turbulence in wall-bounded flows by high-frequency spanwise oscillations. *Physics of Fluids A: Fluid Dynamics*, 4(8), 1605–1607. <https://doi.org/10.1063/1.858381>
- Karniadakis, G., & Choi, K.-S. (2003). Mechanisms on transverse motions in turbulent wall flows. *Annual Review of Fluid Mechanics*, 35(1), 45–62. <https://doi.org/10.1146/annurev.fluid.35.101101.161213>
- Larsson, J., Kawai, S., Bodart, J., & Bermejo-Moreno, I. (2016). Large eddy simulation with modeled wall-stress: Recent progress and future directions. *Mechanical Engineering Reviews*, 3, 15–00418–15–00418. <https://doi.org/10.1299/mer.15-00418>
- Lee, J., Sung, H. J., & Zaki, T. A. (2017). Signature of large-scale motions on turbulent/non-turbulent interface in boundary layers. *Journal of Fluid Mechanics*, 819, 165–187.
- Lee, M., & Moser, R. D. (2015). Direct numerical simulation of turbulent channel flow up to  $Re_\tau \approx 5200$ . *Journal of Fluid Mechanics*, 774, 395–415.
- LESGO. (2021). Github webpage \NoCaseChange{<https://lesgo.me.jhu.edu>}.
- (seen 06/06/2021).
- Li, C., & Zeng, F. (2015). *Numerical methods for fractional calculus*. Chapman; Hall/CRC.
- Lighthill, M. J. (1963). Introduction: Boundary layer theory. In L. Rosenhead (Ed.), *Laminar boundary layers* (p. 687). Oxford University Press.
- Lozano-Durán, A., & Bae, H. J. (2019). Error scaling of large-eddy simulation in the outer region of wall-bounded turbulence. *Journal of Computational Physics*, 392, 532–555.
- Lozano-Durán, A., Giometto, M. G., Park, G. I., & Moin, P. (2020). Non-equilibrium three-dimensional boundary layers at moderate Reynolds numbers. *Journal of Fluid Mechanics*, 883.

- Lund, T. S., Wu, X., & Squires, K. D. (1998). Generation of turbulent inflow data for spatially-developing boundary layer simulations. *Journal of Computational Physics*, 140(2), 233–258. <https://doi.org/https://doi.org/10.1006/jcph.1998.5882>
- Marusic, I., & Monty, J. P. (2019). Attached eddy model of wall turbulence. *Annual Review of Fluid Mechanics*, 51, 49–74.
- Mathis, R., Hutchins, N., & Marusic, I. (2009). Large-scale amplitude modulation of the small-scale structures in turbulent boundary layers. *Journal of Fluid Mechanics*, 628, 311–337.
- Meneveau, C. (2020). A note on fitting a generalised moody diagram for wall modelled large-eddy simulations. *Journal of Turbulence*, 21(11), 650–673.
- Meneveau, C., Lund, T., & Cabot, W. (1996). A Lagrangian dynamic subgrid-scale model of turbulence. *J. Fluid Mech.*, 319, 353–385.
- Moin, P., Shih, T.-H., Driver, D., & Mansour, N. N. (1990). Direct numerical simulation of a three-dimensional turbulent boundary layer. *Physics of Fluids A: Fluid Dynamics*, 2(10), 1846–1853. <https://doi.org/10.1063/1.857658>
- Monkewitz, P. A., Chauhan, K. A., & Nagib, H. M. (2008). Comparison of mean flow similarity laws in zero pressure gradient turbulent boundary layers. *Physics of Fluids*, 20(10), 105102. <https://doi.org/10.1063/1.2972935>
- Moser, R. D., Kim, J., & Mansour, N. N. (1999). Direct numerical simulation of turbulent channel flow up to  $Re_\tau = 590$ . *Physics of Fluids*, 11(4), 943–945. <https://doi.org/10.1063/1.869966>
- Nagib, H. M., Chauhan, K. A., & Monkewitz, P. A. (2007). Approach to an asymptotic state for zero pressure gradient turbulent boundary layers. *Philosophical Transactions: Mathematical, Physical and Engineering Sciences*, 365(1852), 755–770.
- Piomelli, U. (2008). Wall-layer models for large-eddy simulations. *Progress in Aerospace Sciences*, 44, 437–446. <https://doi.org/10.1016/j.paerosci.2008.06.001>
- Piomelli, U., & Balaras, E. (2002). Wall-layer models for large-eddy simulations. *Annual Review of Fluid Mechanics*, 34, 349–374. <https://doi.org/10.1146/annurev.fluid.34.082901.144919>
- Piomelli, U., Ferziger, J., Moin, P., & Kim, J. (1989). New approximate boundary conditions for large eddy simulations of wall-bounded flows. *Physics of Fluids A: Fluid Dynamics*, 1(6), 1061–1068. <https://doi.org/10.1063/1.857397>

- Quadrio, M., & Ricco, P. (2003). Initial response of a turbulent channel flow to spanwise oscillation of the walls. *Journal of Turbulence*, 4, 1–23.
- Reichardt, H. (1951). Vollständige darstellung der turbulenten geschwindigkeitsverteilung in glatten leitungen. *ZAMM-Journal of Applied Mathematics and Mechanics/Zeitschrift für Angewandte Mathematik und Mechanik*, 31(7), 208–219.
- Ricco, P., Ottonelli, C., Hasegawa, Y., & Quadrio, M. (2012). Changes in turbulent dissipation in a channel flow with oscillating walls. *Journal of Fluid Mechanics*, 700, 77–104. <https://doi.org/10.1017/jfm.2012.97>
- Schlichting, H., & Gersten, K. (2017). *Boundary-layer theory*. Springer Berlin Heidelberg.
- Schumann, U. (1975). Subgrid scale model for finite difference simulations of turbulent flows in plane channels and annuli. *J. Comp. Phys.*, 18, 376.
- Scotti, A., & Piomelli, U. (2001). Numerical simulation of pulsating turbulent channel flow. *Physics of Fluids*, 13. <https://doi.org/10.1063/1.1359766>
- Smits, A. J., McKeon, B. J., & Marusic, I. (2011). High-reynolds number wall turbulence. *Annual Review of Fluid Mechanics*, 43, 353–375.
- Staniforth, A., & Côté, J. (1991). Semi-lagrangian integration schemes for atmospheric models—a review. *Monthly Weather Review*, 119(9), 2206–2223. [https://doi.org/10.1175/1520-0493\(1991\)119<2206:SLISFA>2.0.CO;2](https://doi.org/10.1175/1520-0493(1991)119<2206:SLISFA>2.0.CO;2)
- Stevens, R. J., Graham, J., & Meneveau, C. (2014). A concurrent precursor inflow method for large eddy simulations and applications to finite length wind farms. *Renewable Energy*, 68, 46–50. <https://doi.org/https://doi.org/10.1016/j.renene.2014.01.024>
- Sundstrom, L., & Cervantes, M. (2017). The response of the wall shear stress in uniformly and nonuniformly accelerating pipe flows. : 1.
- Sundstrom, L., & Cervantes, M. (2018a). Characteristics of the wall shear stress in pulsating wall-bounded turbulent flows. *Experimental Thermal and Fluid Science*, 96, 257–265. <https://doi.org/https://doi.org/10.1016/j.expthermflusci.2018.02.036>
- Sundstrom, L., & Cervantes, M. (2018b). On the similarity of pulsating and accelerating turbulent pipe flows. *Flow, Turbulence and Combustion*, 100. <https://doi.org/10.1007/s10494-017-9855-5>
- Sundstrom, L., & Cervantes, M. (2018c). The self-similarity of wall-bounded temporally accelerating turbulent flows. *Journal of Turbulence*, 19(1), 49–60. <https://doi.org/10.1080/14685248.2017.1390239>

- Tang, Y., & Akhavan, R. (2016). Computations of equilibrium and non-equilibrium turbulent channel flows using a nested-les approach. *Journal of Fluid Mechanics*, 793, 709–748. <https://doi.org/10.1017/jfm.2016.137>
- Tardu, F. S., & Maestri, R. (2010). Wall shear stress modulation in a turbulent flow subjected to imposed unsteadiness with adverse pressure gradient. *Fluid Dynamics Research*, 42(3), 035510.
- Tardu, S., & da Costa, P. (2005). Experiments and modeling of an unsteady turbulent channel flow. *AIAA Journal*, 43(1), 140–148. <https://doi.org/10.2514/1.6332>
- Townsend, A. A. (1976). *Structure of turbulent shear flow*. Cambridge University Press.
- van Driest, E. R. (1956). On turbulent flow near a wall. *Journal of the Aeronautical Sciences*, 23(11), 1007–1011. <https://doi.org/10.2514/8.3713>
- Vardy, A. E., Brown, J. M. B., He, S., Ariyaratne, C., & Gorji, S. (2015). Applicability of frozen-viscosity models of unsteady wall shear stress. *Journal of Hydraulic Engineering*, 141(1), 04014064. [https://doi.org/10.1061/\(ASCE\)HY.1943-7900.0000930](https://doi.org/10.1061/(ASCE)HY.1943-7900.0000930)
- Vardy, A., & Brown, J. (2003). Transient turbulent friction in smooth pipe flows. *Journal of Sound and Vibration*, 259(5), 1011–1036. <https://doi.org/https://doi.org/10.1006/jsvi.2002.5160>
- Wang, L., Hu, R., & Zheng, X. (2020). A comparative study on the large-scale-resolving capability of wall-modeled large-eddy simulation. *Physics of Fluids*, 32(3), 035102. <https://doi.org/10.1063/1.5144669>
- Weng, C., Boij, S., & Hanifi, A. (2016). Numerical and theoretical investigation of pulsatile turbulent channel flows. *Journal of Fluid Mechanics*, 792, 98–133. <https://doi.org/10.1017/jfm.2016.73>
- Yang, X., Bose, S., & Moin, P. (2016). A physics-based interpretation of the slip-wall les model. *Annual Research Briefs*, 65–74.
- Yang, X., Sadique, J., Mittal, R., & Meneveau, C. (2015). Integral wall model for large eddy simulations of wall-bounded turbulent flows. *Physics of Fluids*, 27(2), 025112.
- Yang, X. I. A., & Griffin, K. P. (2021). Grid-point and time-step requirements for direct numerical simulation and large-eddy simulation. *Physics of Fluids*, 33(1), 015108. <https://doi.org/10.1063/5.0036515>
- Yang, X. I. A., Park, G. I., & Moin, P. (2017). Log-layer mismatch and modeling of the fluctuating wall stress in wall-modeled large-eddy simulations. *Phys. Rev. Fluids*, 2, 104601. <https://doi.org/10.1103/PhysRevFluids.2.104601>

Yao, J., Chen, X., & Hussain, F. (2019). Reynolds number effect on drag control via spanwise wall oscillation in turbulent channel flows. *Physics of Fluids*, 31(8), 085108. <https://doi.org/10.1063/1.5111651>